

**QUANTIFYING CARBON FLUXES AND ISOTOPIC SIGNATURE
CHANGES ACROSS GLOBAL TERRESTRIAL ECOSYSTEMS**

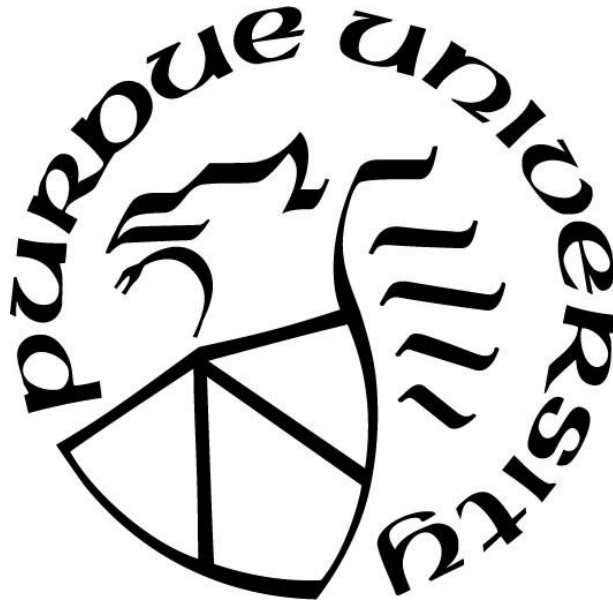
by
Youmi Oh

A Dissertation

Submitted to the Faculty of Purdue University

In Partial Fulfillment of the Requirements for the degree of

Doctor of Philosophy



Department of Earth, Atmospheric, and Planetary Sciences

West Lafayette, Indiana

August 2020

**THE PURDUE UNIVERSITY GRADUATE SCHOOL
STATEMENT OF COMMITTEE APPROVAL**

Dr. Qianlai Zhuang, Co-chair

Department of Earth, Atmospheric, and Planetary Sciences, and Agronomy

Dr. Lisa R. Welp-Smith, Co-chair

Department of Earth, Atmospheric, and Planetary Sciences

Dr. Jeffrey S. Dukes

Department of Forestry and Natural Resources, and Biological Sciences

Dr. Lori Bruhwiler

Global Monitoring Division, NOAA Earth System Research Laboratory

Approved by:

Dr. Daniel J. Cziczo

The completion of this thesis would not have been accomplished without the help and support from my advisors, Dr. Qianlai Zhuang and Dr. Lisa R. Welp-Smith. Dr. Zhuang inspired me to be positive and aim high when I felt discouraged. Dr. Welp has been committed to giving research and life advice over the last four years.

I also appreciate the academic and mental support from my EAPS colleagues, including Licheng Liu, Yang Qu, Mingyang Guo, Jie Chen, Jianghanyang (Ben) Li, Spencer J. Willem, Yongbo Hu, and Zhonghua He. I dedicate this work and give special thanks to my best friend and officemate, Alexandra L. Meyer, for her sincere friendship. I wish to thank my old and new friends for the last four years, especially Zhaoyi Shen, Juhyoung Ryu, Eun-Sol Her, Shinyoung Jun, Kate Yukyung Lee, Victoria Subin Hur, who all showed their trust in me when I went through hard times, Alex Woong Bae Kim who has been my emotional helper for the last year, and my Princeton, Purdue, and NOAA friends who supported me throughout this process.

I dedicate this dissertation to my family in Korea. During the last seven years when I was in the states for my master's and Ph.D. degree, my sister Yoojin had two lovely babies, Ahyun and Amin, who have been a great pleasure for my family. Without the consistent prayer of my family, I could not have achieved this milestone. Lastly, God has been a light and guide for my entire life. I do not know where He would lead me tomorrow, next week, or next year, but I will dedicate myself to walk humbly with Him. Soli Deo Gloria.

ACKNOWLEDGMENTS

This work was supported by NASA Earth and Space Science Fellowship Program (#80NSSC17K0368 P00001) and NASA Interdisciplinary Research in Earth Science (#NNX17AK20G). I thank the Purdue Climate Change Research Center for funding to support part of this work. I also appreciate the support from my department and Purdue university through many awards, including EAPS Henry Silver graduate award, EAPS outstanding graduate student award, EAPS graduate student EXPO outstanding talk award, and Andrews Purdue graduate fellowship. I thank all coauthors for providing observation data, model results, and valuable discussions.

TABLE OF CONTENTS

LIST OF TABLES	7
LIST OF FIGURES	9
ABSTRACT	18
CHAPTER 1. INTRODUCTION	20
CHAPTER 2. REDUCED NET METHANE EMISSIONS DUE TO MICROBIAL METHANE OXIDATION IN A WARMER ARCTIC.....	28
2.1 Abstract	28
2.2 Introduction.....	28
2.3 Methods.....	32
2.3.1 Model description	34
2.3.2 Model optimization.....	41
2.3.3 Simulation for the contemporary period.....	53
2.3.4 Simulation for future projection	63
2.4 Results.....	68
2.5 Discussion and Conclusion	89
CHAPTER 3. A MECHANISTIC WETLAND ISOTOPE MODEL IMPROVES UNDERSTANDING OF ATMOSPHERIC CH ₄ ISOTOPIC COMPOSITION.....	91
3.1 Abstract	91
3.2 Introduction.....	91
3.3 Methods.....	93
3.3.1 Model development	96
3.3.2 Model optimization.....	101
3.3.3 Simulation setup	106
3.3.4 Model data comparison.....	108
3.3.5 Forward modeling using TM5 chemical transport model	113
3.4 Results.....	119
3.5 Discussion and Conclusion	141

CHAPTER 4. CARBON ALLOCATION AFFECTS SEASONAL LEAF CARBON ISOTOPIC SIGNATURES AND INFERRED WATER USE EFFICIENCY OF TEMPERATE DECIDUOUS FORESTS.....	142
4.1 Abstract.....	142
4.2 Introduction.....	142
4.3 Materials and Methods.....	147
4.3.1 Study site and materials	147
4.3.2 Carbon isotope analysis.....	149
4.3.3 Modeling species-specific carbon allocation processes.....	150
4.4 Results.....	161
4.5 Discussion.....	177
CHAPTER 5. SUMMARY AND FUTURE WORK.....	181
REFERENCES	184
VITA.....	200
PUBLICATIONS.....	204

LIST OF TABLES

Table 2.1 Summary of the three models used in this study. The setup for XPTEM-XHAM is explained in details in Figure 2.1. For PTEM-HAM, methane production in wetlands is dependent on SOC derived from vegetation and thawing permafrost, and methane oxidation is by HAM, but $MIC_{biomass}$ changes are not explicitly simulated. In the TEM setup, methane production in wetlands is dependent on SOC derived from vegetation only, methane oxidation is by LAM, and $MIC_{biomass}$ changes are also not explicitly simulated.....	33
Table 2.2 Information about observation sites for model optimization.....	43
Table 2.3 Variable name, unit, upper and lower boundary of parameters.....	44
Table 2.4 Optimized parameters for PTEM-HAM.....	46
Table 2.5 Optimized parameters for XPTEM-XHAM	47
Table 2.6 Summary table of in-situ wetland methane emission and upland methane consumption measured in the Arctic from Emmerton et al. (2014) (Emmerton et al. 2014) and Lau et al. (2015) (Lau et al. 2015).....	55
Table 2.7 Summary table of observed regional estimation of net methane flux.	60
Table 2.8 Annual mean wetland methane emission, upland methane consumption, and net methane emission ($TgCH_4yr^{-1}$) with one standard deviation in 2000 – 2016 for low-Arctic (50-65 °N), high-Arctic (>65°N), and pan-Arctic (>50°N) estimated by TEM, PTEM-HAM, and XPTEM-XHAM.	70
Table 2.9 Model-data comparison of regional estimation of net methane flux with one standard deviation ($TgCH_4yr^{-1}$).	81
Table 3.1 Coefficients for multiple stepwise regression of the fraction of methanogenic community.	99
Table 3.2 Information about observation sites for model optimization.....	102
Table 3.3 Upper and lower limits of parameter range of fractionation factors (α), where AM=acetoclastic methanogenesis, HM=hydrogenotrophic methanogenesis, MO=methane oxidation, TP=plant-mediated transport, TE=ebullition transport, TD=diffusion.....	103
Table 3.4 Optimized Parameters related to methane fractionation factors in wetlands.....	104
Table 3.5 Site-level observations from Holmes <i>et al.</i> (2015) and Sherwood <i>et al.</i> (2017).	109
Table 3.6 Regional-level observation of Alaska airborne measurements from North-slope (N), interior (IN), and southwest (SW) Alaska in 2012-2013, and 2015.	112
Table 3.7 Data sources for total emissions and their spatiotemporal patterns used in building different emission scenarios for model simulations.....	115
Table 4.1 Species-specific model parameters for four tree species of this study.	152

Table 4.2 Phenology of Morgan Monroe State Forest in 2011 – 2013.....	152
Table 4.3 Details of parameter uncertainty tests.....	158
Table 4.4 Details of sensitivity tests.	160
Table 4.5 A final fraction of new carbon in leaf structural pool weighted by time-varying leaf growth in 2011-2013. Uncertainty represents one standard deviation of parameter uncertainty from 20 ensemble simulations.	174

LIST OF FIGURES

Figure 1.1 Schematic representation of the overall perturbation of global carbon cycle and terrestrial ecosystem caused by anthropogenic activities, averaged globally for the decade 2009–2018 in GtC per year, modified from Global Carbon Project (Friedlingstein et al. 2019). Bold arrows represent anthropogenic fluxes of fossil CO₂ (gray), land use change (yellow), land uptake by terrestrial ecosystem (green), and ocean uptake (teal), and atmospheric increase in anthropogenic carbon is in sky-blue color with plus (+) sign. Thin green arrows represent natural carbon cycling, and green round dots represent main carbon pools (permafrost, soils, and vegetation) in terrestrial ecosystems. The carbon fluxes interact with the atmosphere and dampen or amplify the feedback with climate..... 21

Figure 1.2 Summary of three articles and main chapters of this thesis. 21

Figure 1.3 The current state of the Arctic carbon cycle north of 45 °N based on a synthesis of the information presented in the review of McGuire et al., 2009. Values shown are the ranges of uncertainty..... 23

Figure 1.4 Global CH₄ budget for the 2008–2017 decade from Saunio et al., 2020. Both bottom-up (left) and top-down (right) estimates (TgCH₄ yr⁻¹) are provided for each emission and sink category, as well as for total emissions and total sinks..... 25

Figure 1.5 A schematic diagram of (A) surface energy fluxes, (B) hydrologic cycle, and (C) carbon cycle in terrestrial ecosystems modified from Bonan 2008..... 27

Figure 2.1 Schematic diagram of XPTEM-XHAM. The model simulates methane (CH₄) production by methanogens (MG), oxidation of CH₄ by Low Affinity Methanotrophs (LAM) in wetlands (panel a), and oxidation of atmospheric CH₄ ([CH₄]_{atm}) by High Affinity Methanotrophs (HAM) in uplands (panel b). We used a static inundation data (Matthews, E., and Fung 1987) to divide the Arctic landscape into wetland and upland regions but later varied the regions based on time-varying inundation data (Poulter et al. 2017; Lawrence et al. 2018). Changes in active biomass (*MIC_{biomass}*) of MG and HAM depend on microbial growth efficiencies (ϵ) and maintenance energy demand (m_E), and are tracked as a function of time, t. Permafrost SOC dynamics are added to account for accessible SOC from thawing permafrost when soil temperature at the corresponding depth becomes higher than 1°C. The dark blue arrow refers to permafrost SOC dynamics, dark red arrows refer to microbial dynamics, and grey arrows refer to processes from the original TEM..... 30

Figure 2.2 Model-data comparison of methane fluxes for XPTEM-XHAM model. (a-c) wetland methane emission and (d-f) upland methane consumption in mg m⁻² day⁻¹ for (a,d) alpine tundra, (b,e) wet tundra, and (c,f) boreal forest ecosystems 48

Figure 2.3 Box plot of normalized optimized parameters for XPTEM-XHAM model. (a-c) Normalized values of optimized parameters of (1) maximum methane production potential (*MGO*), (2) Q₁₀ temperature sensitivity of methane production (Q_{CH₄Q₁₀}), (3) Maximum potential of methane oxidation by LAM (*OXC*), and (4) reference temperature for methane production (*T_{PR}*). (d-f) Normalized values of optimized parameters with 1 standard deviation of (1) maximum potential of methane oxidation by HAM (*O_{max}*), (2) Q₁₀ temperature sensitivity of methane

oxidation(O_{CH_4Q10}), (3) Maximum soil moisture for methane oxidation (MV_{max}), (4) minimum soil moisture for methane oxidation (MV_{min}) and (5) optimum soil moisture for methane oxidation (MV_{opt}) for (a,d) alpine tundra, (b,e) wet tundra, and (c,f) boreal forests. On each box, the central mark indicates the median, and the bottom and top edges of the box indicate the 25th and 75th percentiles, respectively. The whiskers extend to the most extreme data points not considered outliers, and the outliers are plotted individually using the '+' symbol (Higham and Higham 2016).
 49

Figure 2.4 Model-data comparison of methane fluxes for PTEM-HAM model. (a-c) wetland methane emission and (d-f) upland methane consumption in $mg\ m^{-2}\ day^{-1}$ for (a,d) alpine tundra, (b,e) wet tundra, and (c,f) boreal forest ecosystems. 50

Figure 2.5 Box plot of normalized optimized parameters for PTEM-HAM model. (a-c) Normalized values of optimized parameters of (1) maximum methane production potential (MGO), (2) Q_{10} temperature sensitivity of methane production (Q_{CH_4Q10}), (3) Maximum potential of methane oxidation by LAM (O_{XIC}), and (4) reference temperature for methane production (T_{PR}). (d-f) Normalized values of optimized parameters with 1 standard deviation of (1) maximum potential of methane oxidation by HAM (O_{max}), (2) Q_{10} temperature sensitivity of methane oxidation(O_{CH_4Q10}), (3) Maximum soil moisture for methane oxidation (MV_{max}), (4) minimum soil moisture for methane oxidation (MV_{min}) and (5) optimum soil moisture for methane oxidation (MV_{opt}) for (a,d) alpine tundra, (b,e) wet tundra, and (c,f) boreal forests. On each box, the central mark indicates the median, and the bottom and top edges of the box indicate the 25th and 75th percentiles, respectively. The whiskers extend to the most extreme data points not considered outliers, and the outliers are plotted individually using the '+' symbol (Higham and Higham 2016).
 51

Figure 2.6 Model-data comparison of top soil temperature and moisture. (a,c, and e) daily top 10-cm soil temperature in °C and (b, d, and f) daily top 10-cm volumetric soil moisture in % volume for (a,b) alpine tundra in 2013, (c,d) wet tundra in 2012, and (e,f) boreal forest in 2012. 52

Figure 2.7 Seasonality of active microbial biomass for four soil depths. Changes in active microbial biomass ($nmol_{bioC}\ L_{soil}^{-1}$) of (a) methanogens in wetlands in a boreal forest in 2012 (Sellers et al. 1997) and (b) HAM in uplands in a dry tundra in 2013-2015 (D'Imperio et al. 2017) at 10, 50, 100, and 200 cm soil depths. 62

Figure 2.8 Inter-annual variability of soil temperature and moisture and atmospheric methane abundance during 2017 – 2100. Annual averaged estimates of pan-arctic (a) top 10-cm soil temperature in °C, (b) top 10-cm soil moisture in % volume, and (c) atmospheric methane abundance ($[CH_4]_{air}$) in ppb using RCP 2.6 (sky blue), RCP 4.5 (green), and RCP 8.5 (dark red) north of 50°N. 64

Figure 2.9 Effects of microbial dynamics of LAM to wetland methane emission for contemporary period and RCP 8.5 during 2017-2100 north of 50°N. Annual estimates of pan-Arctic net methane emission for XPTM-XHAM for (a) contemporary period in 2000-2016 (b) RCP 8.5 scenario in 2017-2100 without varying m_E (blue), XPTM-XHAM with physiological responses of MG and HAM to temperature change (skyblue), and sensitivity tests of varying microbial dynamics of LAM (red and yellow represent with and without varying m_E , respectively). The shaded error bars represent one standard deviation of model results determined by varying the optimized parameters from ensemble simulations. 67

Figure 2.10 Annual estimates of the Arctic methane budget by three models for 2000-2016. Annual estimates of (a) wetland methane emission, (b) upland methane consumption, and (c) net methane emission in $\text{TgCH}_4\text{yr}^{-1}$ averaged over 2000-2016 for TEM (red), PTEM-HAM (yellow), and XPTEM-XHAM (blue) for the pan-Arctic region (north of 50°N), including the low-Arctic between $50\text{--}65^\circ\text{N}$ and high-Arctic north of 65°N . The error bars represent one standard deviation of TEM, PTEM-HAM, and XPTEM-XHAM determined by varying the optimized parameters from ensemble simulations. The top-down inversion in panel (c) (grey) represents posterior estimates of mean and one standard deviation of net wetland methane fluxes by CarbonTracker- CH_4 in 2000-2010. 69

Figure 2.11 Pan-Arctic monthly mean methane fluxes for XPTEM-XHAM and PTEM-HAM from 2000-2016 north of 50°N . Estimates of pan-arctic (a,c) monthly wetland methane emission and (b,d) monthly upland methane consumption in $\text{mg m}^{-2} \text{day}^{-1}$ for (a,b) XPTEM-XHAM and (c,d) PTEM-HAM model. The blue line is monthly averages over 2000-2016, and grey lines represent values of each year. 71

Figure 2.12 Inter-annual variability of methane fluxes from 2000 – 2016 north of 50°N . (Left) Annual estimates of pan-arctic (a) wetland methane emission, (b) upland methane consumption, and (c) net methane emission for XPTEM-XHAM (blue line), PTEM-HAM (yellow line), and TEM (red line) in $\text{TgCH}_4\text{yr}^{-1}$ from 2000-2016. The shaded area represents one standard deviation of models determined by varying the optimized parameters. (Right) Mean and one standard deviation averaged over the simulation period for each metric are given by the bars. Panel (c) additionally shows mean and one standard deviation of previous estimates of net methane emission estimated by top-down inversions (times symbol) by the bars. 72

Figure 2.13 Spatial variability of soil and vegetation properties north of 50°N . (a) annual top 10-cm soil temperature in $^\circ\text{C}$, (b) annual top 10-cm soil moisture in % volume, (c) monthly net primary productivity in $\text{gC m}^{-2} \text{month}^{-1}$, and (d) permafrost SOC stored in the top 3-m in kg m^{-2} (Hugelius et al. 2013; Schuur et al. 2015). The soil temperature, moisture, and net primary productivity were averaged over the contemporary period during 2000-2016. The dotted longitudinal lines are at 30° intervals, and the latitudinal line is at 65°N 73

Figure 2.14 Inter-annual variability of top soil temperature and moisture. Estimates of pan-arctic (a) annual top 10-cm soil temperature in $^\circ\text{C}$ and (b) annual top 10-cm soil moisture in % volume for 2000-2016. 74

Figure 2.15 Spatial variability of methane fluxes north of 50°N . (a-b) Spatial variability of annual wetland methane emission ($\text{TgCH}_4\text{yr}^{-1}$) averaged over (a) 2000-2016 and (b) RCP 8.5 during 2017-2100 for XPTEM-XHAM model. (c-d) Spatial variability of annual upland methane consumption averaged over (c) 2000-2016 and (d) RCP 8.5 during 2017-2100 north of 50°N for XPTEM-XHAM model. The dotted longitudinal lines are at 30° intervals, and the latitudinal line is at 65°N 75

Figure 2.16 Inter-annual variability of methane fluxes using time-varying inundation fraction from 2000 – 2012 north of 50°N . Annual estimates of pan-arctic (a) net methane emission, (b) wetland methane emission, and (c) upland methane consumption for XPTEM-XHAM model using static inundation fraction (Matthews, E., and Fung 1987) (blue) and time-varying inundation fraction from SWAMPS-GLWD (Poulter et al. 2017) (green) in $\text{TgCH}_4\text{yr}^{-1}$. The shaded area represents one standard deviation determined by varying the optimized parameters. 76

Figure 2.17 Monthly averaged time-varying and static inundated area north of 50°N. Monthly inundated area from time-varying (SWAMPTS-GLWD (Poulter et al. 2017)) and a static estimates (Matthews&Fung, 1987 (Matthews, E., and Fung 1987)) in km² from 2000 – 2012..... 77

Figure 2.18 Sensitivity test of methane emission and consumption for XPTEM-XHAM. (a) Changes in pan-arctic wetland methane emission relative to a default simulation after varying temperature, water table, NPP, and permafrost SOC. (b) Changes in pan-arctic upland methane consumption relative to a default simulation after varying temperature, soil moisture, and atmospheric methane abundance ($[CH_4]_{atm}$). 78

Figure 2.19 Spatial variability of annual net methane flux north of 50°N for XPTEM-XHAM. The net methane fluxes are in TgCH₄yr⁻¹, positive for emission and negative for consumption, (a) averaged for the contemporary period during 2000-2016, and (b) difference between 2086-2100 for RCP 8.5 and 2000-2016. The dotted longitudes are at 30° intervals, and the dotted latitude is at 65°N. Panel (a) additionally shows five regions in black boxes used for regional model-data comparisons. 79

Figure 2.20 Model-data comparison of methane fluxes using site-level data. Comparison of (a) wetland methane emission and (b) upland methane consumption of data from 46 in-situ measurements (supplementary table 5) with simulation results from XPTEM-XHAM (blue), PTEM-HAM (yellow), and TEM (red)..... 80

Figure 2.21 Projected annual net Arctic methane emissions from 2016 to 2100. (Left) Annual estimates of pan-arctic net methane emission for (a) XPTEM-XHAM without varying m_E (baseline, blue), PTEM-HAM (yellow), and TEM (red), and (b) XPTEM-XHAM baseline (blue; same as in (a)), XPTEM-XHAM with physiological responses of MG and HAM to temperature change (green) based on RCP 2.6 (dotted), RCP 4.5 (dashed), and RCP 8.5 (solid). The shaded error bars represent one standard deviation of TEM, PTEM-HAM, and XPTEM-XHAM determined by varying the optimized parameters from ensemble simulations. (Right) Mean (symbols) and one standard deviation (bars) in 2100 for each metric. Panel (a) additionally shows mean (*) and one standard deviation (bars) of previous estimates of net methane emission estimated by process-based methane models (Lawrence et al. 2015; Koven et al. 2011; Schuur et al. 2013). 83

Figure 2.22 Spatial variability of top soil temperature and moisture averaged over 2017-2100 for RCP 8.5 north of 50°N. (a) Averaged annual top 10-cm soil temperature in °C and (b) averaged annual top 10-cm soil moisture in % volume. The dotted longitudinal lines are at 30° intervals, and the latitudinal line is at 65°N. 84

Figure 2.23 Inter-annual variability of methane fluxes during 2017 – 2100. (Left) Annual pan-arctic estimates of (a) wetland methane emission and (b) upland methane consumption for XPTEM-XHAM (blue), PTEM-HAM (yellow), and TEM (red) using RCP 2.6 (dotted), RCP 4.5 (dashed), and RCP 8.5 (solid) north of 50°N. The shaded error bars represent one standard deviation of model results determined by varying the optimized parameters from ensemble simulations. (Right) Mean (symbols) and one standard deviation (bars) in 2100 for each metric. 85

Figure 2.24 Inter-annual variability of methane fluxes for XPTEM-XHAM with its microbial physiology from 2017 – 2100. (Left) Annual estimates of pan-arctic (a) wetland methane emission and (b) upland methane consumption for XPTEM-XHAM without varying m_E (baseline, blue),

and XPTEM-XHAM with physiological responses of MG and HAM to temperature change with varying m_E (green) based on RCP 2.6 (dotted), RCP 4.5 (dashed), and RCP 8.5 (solid) north of 50°N. The shaded error bars represent one standard deviation of model results determined by varying the optimized parameters from ensemble simulations. (Right) Mean (symbols) and one standard deviation (bars) in 2100 for each metric. 86

Figure 2.25 Sensitivity of temperature and atmospheric methane abundance to projections of net methane emission for RCP 8.5 during 2017-2100 north of 50°N. Annual estimates of pan-Arctic net methane emission for XPTEM-XHAM without varying ϵ and m_E (solid blue), XPTEM-XHAM with physiological responses of MG and HAM to temperature change with varying m_E (solid green), and sensitivity tests of the two simulations to Q_{10} changes (dotted, dash-dot, and dashed lines for low, medium, and high Q_{10} setups, respectively) and atmospheric methane abundance to stay at 1.8 ppm (circle marker). 87

Figure 2.26 Inter-annual variability of methane fluxes using time-varying inundation fraction from 2017 – 2100 north of 50°N. Annual estimates of pan-arctic (a) net methane emission, (b) wetland methane emission, and (c) upland methane consumption for XPTEM-XHAM model using static inundation fraction (blue) and dynamic inundation fraction (green) in $TgCH_4yr^{-1}$ using RCP 2.6 (dotted), RCP 4.5 (dashed), and RCP 8.5 (solid). 88

Figure 2.27 Future arctic methane feedbacks (modified Fig. 5 of Oh et al., 2016 (Oh et al. 2016)). Previous studies predicted a positive feedback between temperature and methane emission (circles 1–2). However, because high-affinity methanotrophs may respond strongly to temperature and less strongly to soil moisture due to uncertain arctic hydrology (circles 3–4), this feedback loop may be partially suppressed. Moreover, explicit modeling of microbial dynamics (circle 5) will facilitate future model developments that include effects of microbial physiology. 90

Figure 3.1 Main configuration of isoTEM. Bold and dashed lines refer to chemical and transport processes, respectively. Precursor C_3/C_4 plant distribution (C_3/C_4) and fractionation factors related to methane production, oxidation, and transport processes (α_{HM} , α_{AM} , α_{MO} , α_{TP} , α_{TE} , α_{TD} .) were added for isoTEM. 95

Figure 3.2 The C_4 fraction of the vegetation (Still et al., 2003). 98

Figure 3.3 Multiple regression results between fraction of hydrogenotrophic methanogens (HM) and (a) step-wise latitude, (b) pH, and (c) total soils carbon. 100

Figure 3.4 Calibration results of seasonal methane emissions in $mg\ m^{-2}\ day^{-1}$ (a,b,e,f,i,j) and its carbon isotope changes in $\delta^{13}C-CH_4$ (c,d,g,h,k,l) for low-pH (a,c,e,g,i,k) and high-pH (b,d,f,h,j,l) system in boreal (a-d), temperate (e-h), and tropic (i-l) regions. Red error bars represent observation with standard deviation, and blue lines represent simulation results. 105

Figure 3.5 global soil wetland and pH map. (a) default wetland type map from Matthews and Fung (1987), where type 1 and 2 represent forested and non-forested bog, type 3 and 4 represent forested and non-forested swamp, and 5 represent alluvial wetlands. The wetland map was developed based on vegetation, soil properties, and fractional inundation, and yielded a global distribution of wetland sites identifies with in situ ecological and environmental characteristics. (b) filled wetland types assuming low-pH soils are in type 1 and high-pH soils are in type 2. (c) global soil pH map from (Carter and Scholes 2000). 107

Figure 3.6 (a) Bottom-up emissions for each category and (b) total emissions including soil sinks (negative) estimated by bottom-up (i.e., the total of a) and top-down approaches. The data sources can be found in Table 3.7.....	116
Figure 3.7 Bottom-up emissions for each category and scenario. (a) Bottom-up emissions for each category for static isoTEM scenario. Changes of emissions in (b) wetland, (c) ruminant, and (d) oil/gas for different scenarios of isoTEM with static inundation (blue), isoTEM with transient inundation (red), Ganesan <i>et al.</i> (2018) with static inundation (yellow), and Ganesan <i>et al.</i> (2018) with transient inundation (purple). The data sources can be found in Table 3.7.....	117
Figure 3.8 Global map of wetland methane carbon isotopic signatures ($\delta^{13}\text{C-CH}_4$) and its emissions. (a) (left) Modeled global wetland $\delta^{13}\text{C-CH}_4$ and (right) its latitudinal mean by flux not weighted (blue) and flux weighted (yellow). (b) (left) Modeled global wetland methane emissions by static inundation data from Matthews and Fung (1987) in $\text{Tg}_{\text{CH}_4} \text{yr}^{-1}$ and (right) its latitudinal sum. The error bars represent one standard deviation by varying the optimized parameters from ensemble simulations.	121
Figure 3.9 Wetland $\delta^{13}\text{C-CH}_4$ masked for grid cells using static inundation from Matthews and Fung (1987).....	122
Figure 3.10 Histogram of modeled global isotopic signatures of wetland $\delta^{13}\text{C-CH}_4$ by (a) Ganesan <i>et al.</i> (2018), and isoTEM with (b) flux not weighted and (c) weighted.	123
Figure 3.11 Global map of wetland $\delta^{13}\text{C-CH}_4$. Wetland $\delta^{13}\text{C-CH}_4$ by (a) isoTEM in July, 2000 and (b) Ganesan <i>et al.</i> (2018), and (c) their latitudinal gradients mean of wetland $\delta^{13}\text{C-CH}_4$ by isoTEM (blue) and Ganesan <i>et al.</i> (2018) (red).	124
Figure 3.12 Seasonality of (a) mean $\delta^{13}\text{C-CH}_4$ and (b) sum of methane fluxes for global (blue), boreal (green), temperate (yellow), and tropic (red) regions. The error bars represent one standard deviation by varying the optimized parameters from ensemble simulations.....	125
Figure 3.13 Latitudinal gradients of simulated $\delta^{13}\text{C-CH}_4$ and inter-annual variability of wetland emissions and $\delta^{13}\text{C-CH}_4$. (a) Flux-weighted mean latitudinal gradients of $\delta^{13}\text{C}$ of SOC (green), produced methane (red), methane after oxidized (yellow), and methane after transported to the soil surface (blue). The error bars represent one standard deviation by varying the optimized parameters from ensemble simulations. (b) inter-annual variability of global wetland emissions (skyblue), global mean wetland $\delta^{13}\text{C-CH}_4$ with flux weighted (maroon with cross symbol) and not weighted (maroon with circle symbol).	126
Figure 3.14 Site-level model-data comparison. (a-b) Comparison between observation and Ganesan <i>et al.</i> (2018) using 1:1 line with observation and (c-d) histogram of the difference between model and observation from the tropic (red), temperate (yellow), and boreal (blue) region.	128
Figure 3.15 Regional model-data comparison. Simulated wetland $\delta^{13}\text{C} (\text{CH}_4)$ by (a) Ganesan <i>et al.</i> (2018) and (b) isoTEM, and (c) their comparison with observation from NOAA Alaska aircraft data using Keeling and Miller-Tans plots.	129
Figure 3.16 Keeling and Miller-Tans plots of airborne measurements in 2012, 2013, and 2015 for North slope, interior, and southwest Alaska.	130

Figure 3.17 Spatial map of $\delta^{13}\text{C}$ simulated in isoTEM. Map of $\delta^{13}\text{C}$ of (a) SOC, (b) produced methane, (c) methane after oxidized, and (d) methane after transported to the soil surface. 132

Figure 3.18 Inter-annual variability of wetland emissions (skyblue), flux-integrated wetland $\delta^{13}\text{C}$ - CH_4 (Maroon), and fraction of plant-mediated transport over all three transport processes (green) for (a) global scale, (b) boreal, (c) temperate, and (d) tropic regions. 133

Figure 3.19 Long-term variability of atmospheric $[\text{CH}_4]$. Model-data comparison of long-term variability of atmospheric $[\text{CH}_4]$ (in ppb) by observation (grey) and simulations from uniform (yellow), Ganesan (red), isoTEM-static (blue), isoTEM-dynamic (skyblue) from 1984 to 2016 for scenarios using (a) static inundation from Matthews and Fung (1987) and (b) transient inundation from Poulter et al. (2017). 136

Figure 3.20 Inter-hemispheric gradients of atmospheric $[\text{CH}_4]$. Model-data comparison of global inter-hemispheric gradients of atmospheric $[\text{CH}_4]$ by observation (grey) and simulations from uniform (yellow), Ganesan (red), isoTEM-static (blue), isoTEM-dynamic (skyblue) scenarios in (a, d) 2005, (b, e) 2010, and (c, f) 2015 using (a-c) static and (d-f) dynamic inundation data from Matthews and Fung (1987) and Poulter et al. (2017), respectively. 137

Figure 3.21 Inter-hemispheric gradients of atmospheric $\delta^{13}\text{C}$ - CH_4 using static inundation. Model-data comparison of global inter-hemispheric gradients of atmospheric $\delta^{13}\text{C}$ - CH_4 by observation (grey) and simulations from uniform (yellow), Ganesan (red), isoTEM-static (blue), isoTEM-dynamic (skyblue) scenarios in (a) 2005, (b) 2010, and (c) 2015 using static inundation data from Matthews and Fung (1987). 138

Figure 3.22 Inter-hemispheric gradients of atmospheric $\delta^{13}\text{C}$ - CH_4 using dynamic inundation. Model-data comparison of global inter-hemispheric gradients of atmospheric $\delta^{13}\text{C}$ - CH_4 by observation (grey) and simulations from uniform (yellow), Ganesan (red), isoTEM-static (blue), isoTEM-dynamic (skyblue) scenarios in (a) 2005, (b) 2010, and (c) 2015 using dynamic inundation data from Poulter et al. (2017). 139

Figure 3.23 Comparisons of wetland (WL) emissions between static (red) and dynamic WL (blue) area maps for (a) annual emissions in Tg yr^{-1} , (b) seasonal cycle in Tg yr^{-1} and (c) latitude distribution in Tg yr^{-1} 140

Figure 4.1 A conceptual illustration of leaf carbon allocation processes. Trees produce newly assimilated carbon by photosynthesis (a) and input the new carbon to the non-structural carbon (NSC) pool in leaves. The NSC can be used for leaf growth and structural carbon pool (b), growth and maintenance respiration (c), or transported to stems through phloem (d). When leaf respiration costs outpace photosynthetic fluxes, the NSC from stems and roots is transported back to leaf (e). The color of the arrows represents drought/early growing season (red) and non-drought/mid to late growing season (blue) conditions and the size of arrows represents relative annual fluxes. 145

Figure 4.2 Inter- and intra-annual variability of environmental conditions in 2011–2013, 2017–2018. Seasonal changes of 10-day moving average of (a) air temperature, (b) net ecosystem CO_2 exchange (NEE), (c) vapor pressure deficit, and (d) soil moisture in the first 30 cm depth measured at the MMSF AmeriFlux site in 2011–2013, 2017–2018. 148

Figure 4.3 Observed seasonal leaf and annual tree ring $\delta^{13}\text{C}$ in 2011–2013, 2017–2018. Observed seasonal changes of bulk leaf $\delta^{13}\text{C}$ (‰) (open circles), early- and late-season averages of bulk leaf

$\delta^{13}\text{C}$ (‰) (up and down triangles), and annual tree ring cellulose (asterisk symbol) for (a) sugar maple, (b) tulip poplar, (c) sassafras, and (d) white oak in 2011–2013, 2017–2018. Left panels show bulk leaf $\delta^{13}\text{C}$ (‰) sampled throughout the growing season. Middle panels show early- and late-season averages of bulk leaf $\delta^{13}\text{C}$ (‰) based on the DOY 150 cutoff. Right panels show tree ring cellulose $\delta^{13}\text{C}$ plotted in 2011–2013. Error bars represent one standard deviation of each sampling/average period. 162

Figure 4.4 *Medlyn* stomatal conductance relationship using leaf gas exchange measurements in 2011–2013. The optimized linear relationship between g_s and $A/c_a D^{0.5}$, where A is photosynthesis rates in $\mu\text{mol m}^{-2} \text{s}^{-1}$, c_a is atmospheric CO_2 concentrations in $\mu\text{mol mol}^{-1}$, and D is VPD in kPa with R^2 for (a) sugar maple, (b) tulip poplar, (c) sassafras, and (d) white oak using leaf gas exchange measurements (open circles) (Medlyn et al. 2011). The filled circles represent average values of g_s and $A/c_a D^{0.5}$ in 2011 (green), 2012 (red), and 2013 (blue). 164

Figure 4.5 Model-data comparison of photosynthesis-related parameters. The model-data comparison of annual averages of (a) photosynthesis rate, (b) fraction of intercellular and atmospheric CO_2 concentrations (c_i/c_a), and (c) stomatal conductance rate during observation period of day of year (DOY) 195–235 in 2011(Δ), DOY 123–286 in 2012 (x), and DOY 135–270 in 2013 (o) for sassafras (red), sugar maple (blue), tulip poplar (green), and white oak (purple). Error bars represent one standard deviation of each measurement point, and an averaged root mean square error (RMSE) represents an absolute difference of the annual averages between model and observation. 165

Figure 4.6 Observed and simulated seasonal bulk leaf $\delta^{13}\text{C}$ in 2011–2013, 2017–2018. Observed (open circles) and simulated (lines) seasonal changes of bulk leaf $\delta^{13}\text{C}$ (‰) for (a) sugar maple, (b) tulip poplar, (c) sassafras, and (d) white oak, with carbon allocation in 2011–2013, 2017–2018 (solid lines) and with photosynthetic fractionation only in 2011–2013 (dashed lines) overlaid the observed bulk leaf $\delta^{13}\text{C}$ (open circle). The grey highlight represents the mean leaf growth period in 2011–2013. Shaded error bars represent one standard deviation of parameter uncertainty from 20 ensemble simulations. 166

Figure 4.7 Fraction of new carbon in the leaf NSC and structural pool. The simulated fraction of new carbon in the leaf NSC pool (solid lines) and structural carbon (SC) pool (dashed lines) for (a) sugar maple, (b) tulip poplar, (c) sassafras, and (d) white oak in 2011–2013. The grey highlight represents the leaf growth period. Shaded error bars represent one standard deviation of parameter uncertainty from 20 ensemble simulations. 168

Figure 4.8 Model-data comparison of leaf $\delta^{13}\text{C}$ in 2011–2013 and 2017–2018. The model-data comparison of the observed and carbon allocation simulated seasonal changes of bulk leaf $\delta^{13}\text{C}$ (‰) (a) sugar maple, (b) tulip poplar, (c) sassafras, and (d) white oak for trained years in 2011–2013 (black lines with circle symbols) and for tested years in 2017–2018 (grey lines with cross symbols). 169

Figure 4.9 Simulated photosynthesis rates in 2011 – 2013. The simulated daily-averaged photosynthesis rates ($\mu\text{mol m}^{-2} \text{s}^{-1}$) for (a) sugar maple, (b) tulip poplar, (c) sassafras, and (d) white oak in 2011 – 2013. 170

Figure 4.10 Simulated respiration rates in 2011 – 2013. The simulated daily-averaged respiration rates ($\mu\text{mol m}^{-2} \text{s}^{-1}$) for (a) sugar maple, (b) tulip poplar, (c) sassafras, and (d) white oak in 2011 – 2013..... 171

Figure 4.11 Simulated phloem loading rates in 2011 – 2013. The simulated daily-averaged phloem loading rates ($\mu\text{mol m}^{-2} \text{s}^{-1}$) for (a) sugar maple, (b) tulip poplar, (c) sassafras, and (d) white oak in 2011 – 2013..... 172

Figure 4.12 Simulated remobilization rates in 2011 – 2013. The simulated daily-averaged remobilization rates ($\mu\text{mol m}^{-2} \text{s}^{-1}$) for (a) sugar maple, (b) tulip poplar, (c) sassafras, and (d) white oak in 2011 – 2013..... 173

Figure 4.13 Estimation of iWUE. (a) Mean annual iWUE using five different methods in 2011–2012 for each of the 4 species studied with error bars. The horizontal bar in the middle of the *leaf* and *tree ring* $\delta^{13}\text{C}$ represents the adjustment in calculated iWUE between using the full Eq. 4.12a considering mesophyll conductance (g_m) rather than the simplified Eq. 4.12b (full bar height). This shows that the model derived from Licor observations (*Instantaneous Licor A/g_s*) can be partially reconciled with isotopic observations, but the ‘true’ iWUE, *GPP-weighted model A/g_s*, is lower than all the methods. (b) The difference in annual iWUE using five different methods between 2012 and 2011 showing that drought iWUE response varies by species and method. Error bars represent one standard deviation of parameter uncertainty from 20 ensemble simulations for *GPP-weighted* and *Instantaneous model A/g_s*, and one standard deviation of each sampling/average period for other methods..... 176

Figure 4.14 Model sensitivity test. Bar plot of the difference in RMSE between the observations and the model fits using the 1:1 line fit and the linear fit, compared to the RMSE of the optimal model (Table S2 and Supplementary Method 4). 178

ABSTRACT

This thesis is a collection of three research articles to quantify carbon fluxes and isotopic signature changes across global terrestrial ecosystems. Chapter 2, the first article of this thesis, focuses on the importance of an under-estimated methane soil sink for contemporary and future methane budgets in the pan-Arctic region. Methane emissions from organic-rich soils in the Arctic have been extensively studied due to their potential to increase the atmospheric methane burden as permafrost thaws. However, this methane source might have been overestimated without considering high affinity methanotrophs (HAM, methane oxidizing bacteria) recently identified in Arctic mineral soils. From this study, we find that HAM dynamics double the upland methane sink ($\sim 5.5 \text{ TgCH}_4\text{yr}^{-1}$) north of 50°N in simulations from 2000 to 2016 by integrating the dynamics of HAM and methanogens into a biogeochemistry model that includes permafrost soil organic carbon (SOC) dynamics. The increase is equivalent to at least half of the difference in net methane emissions estimated between process-based models and observation-based inversions, and the revised estimates better match site-level and regional observations. The new model projects double wetland methane emissions between 2017-2100 due to more accessible permafrost carbon. However, most of the increase in wetland emissions is offset by a concordant increase in the upland sink, leading to only an 18% increase in net methane emission (from 29 to 35 $\text{TgCH}_4\text{yr}^{-1}$). The projected net methane emissions may decrease further due to different physiological responses between HAM and methanogens in response to increasing temperature. This article was published in *Nature Climate Change* in March 2020.

In Chapter 3, the second article of this thesis, I develop and validate the first biogeochemistry model to simulate carbon isotopic signatures ($\delta^{13}\text{C}$) of methane emitted from global wetlands, and examined the importance of the wetland carbon isotope map for studying the global methane cycle. I incorporated a carbon isotope-enabled module into an extant biogeochemistry model to mechanistically simulate the spatial and temporal variability of global wetland $\delta^{13}\text{C}\text{-CH}_4$. The new model explicitly considers isotopic fractionation during methane production, oxidation, and transport processes. I estimate a mean global wetland $\delta^{13}\text{C}\text{-CH}_4$ of -60.78‰ with its seasonal and inter-annual variability. I find that the new model matches field chamber observations 35% better in terms of root mean square estimates compared to an empirical static wetland $\delta^{13}\text{C}\text{-CH}_4$ map. The model also reasonably reproduces the regional heterogeneity of

wetland $\delta^{13}\text{C-CH}_4$ in Alaska, consistent with vertical profiles of $\delta^{13}\text{C-CH}_4$ from NOAA aircraft measurements. Furthermore, I show that the latitudinal gradient of atmospheric $\delta^{13}\text{C-CH}_4$ simulated by a chemical transport model using the new wetland $\delta^{13}\text{C-CH}_4$ map reproduces the observed latitudinal gradient based on NOAA/INSTAAR global flask-air measurements. I believe this study is the first process-based biogeochemistry model to map the global distribution of wetland $\delta^{13}\text{C-CH}_4$, which will significantly help atmospheric chemistry transport models partition global methane emissions. This article is in preparation for submission to *Nature Geoscience*.

Chapter 4 of this thesis, the third article, investigates the importance of leaf carbon allocation for seasonal leaf carbon isotopic signature changes and water use efficiency in temperate forests. Temperate deciduous trees remobilize stored carbon early in the growing season to produce new leaves and xylem vessels. The use of remobilized carbon for building leaf tissue dampens the link between environmental stomatal response and inferred intrinsic water use efficiency (iWUE) using leaf carbon isotopic signatures ($\delta^{13}\text{C}$). So far, few studies consider carbon allocation processes in interpreting leaf $\delta^{13}\text{C}$ signals. To understand effects of carbon allocation on $\delta^{13}\text{C}$ and iWUE estimates, we analyzed and modeled the seasonal leaf $\delta^{13}\text{C}$ of four temperate deciduous species (*Acer saccharum*, *Liriodendron tulipifera*, *Sassafras albidum*, and *Quercus alba*) and compared the iWUE estimates from different methods, species, and drought conditions. At the start of the growing season, leaf $\delta^{13}\text{C}$ values were more enriched, due to remobilized carbon during leaf-out. The bias towards enriched leaf $\delta^{13}\text{C}$ values explains the higher iWUE from leaf isotopic methods compared with iWUE from leaf gas exchange measurements. I further showed that the discrepancy of iWUE estimates between methods may be species-specific and drought sensitive. The use of $\delta^{13}\text{C}$ of plant tissues as a proxy for stomatal response to environmental processes, through iWUE, is complicated due to carbon allocation and care must be taken when interpreting estimates to avoid proxy bias. This article is in review for publication in *New Phytologist*.

CHAPTER 1. INTRODUCTION

Human-induced perturbation has caused warming of the climate in the industrial era (Stocker et al. 2013). The anthropogenic activities caused the increase in atmospheric CO₂ by almost 50% from 280 ppm in the 1750s to 400 ppm in the 2010s (Friedlingstein et al. 2019), and the increase in atmospheric CH₄ by 150% from 720 ppb in the 1750s to 1850 ppb in the 2010s (Nisbet et al. 2019; Dlugokencky et al. 2011). The increase in greenhouse gases is due to carbon emissions from anthropogenic sources, such as fossil fuel burning (9.5 GtC yr⁻¹) and land use change (1.5 GtC yr⁻¹) (Fig. 1.1). More than 30% of the emissions are removed in the atmosphere by terrestrial ecosystems (3.2 GtC yr⁻¹), emphasizing the importance of terrestrial ecosystems in mitigating the climate change.

Despite the significant role as a major atmospheric carbon sink, terrestrial ecosystems are currently under tremendous pressure from climate change (Friedlingstein et al. 2019). The climate change may influence total carbon fluxes between the atmosphere and terrestrial ecosystems (120 GtC yr⁻¹) by altering photosynthesis, respiration, and nutrient uptake and release by microbes (Bonan 2008). Studies also address the vulnerability of carbon pools in terrestrial ecosystems as climate changes, which store up to 5,000 Pg of carbon (Turetsky et al. 2020; Wieder et al. 2013; Bonan 2008). The perturbations can further alter physical, chemical, and biological processes in terrestrial ecosystems that affect planetary energy fluxes and the hydrologic cycle (Bonan 2008). Depending on the mechanisms governing each process, the feedback between climate change and terrestrial ecosystems can be dampened or amplified.

This thesis summarizes three research articles that help to understand the processes governing the changes in three major carbon pools in terrestrial ecosystems: permafrost, wetland soils, and vegetation (Fig. 1.2). The first article studies soil CH₄ in Arctic permafrost, the second article studies CH₄ isotopes in global wetland soils, and the third article studies leaf carbon allocation and water use efficiency (WUE) in temperate forests.

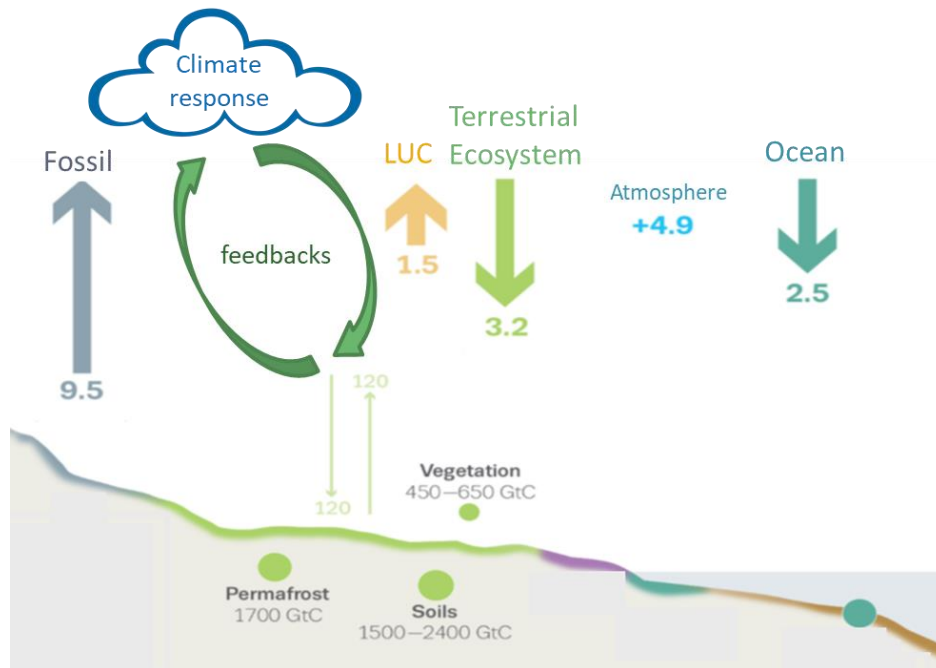


Figure 1.1 Schematic representation of the overall perturbation of global carbon cycle and terrestrial ecosystem caused by anthropogenic activities, averaged globally for the decade 2009–2018 in GtC per year, modified from Global Carbon Project (Friedlingstein et al. 2019). Bold arrows represent anthropogenic fluxes of fossil CO₂ (gray), land use change (yellow), land uptake by terrestrial ecosystem (green), and ocean uptake (teal), and atmospheric increase in anthropogenic carbon is in sky-blue color with plus (+) sign. Thin green arrows represent natural carbon cycling, and green round dots represent main carbon pools (permafrost, soils, and vegetation) in terrestrial ecosystems. The carbon fluxes interact with the atmosphere and dampen or amplify the feedback with climate.

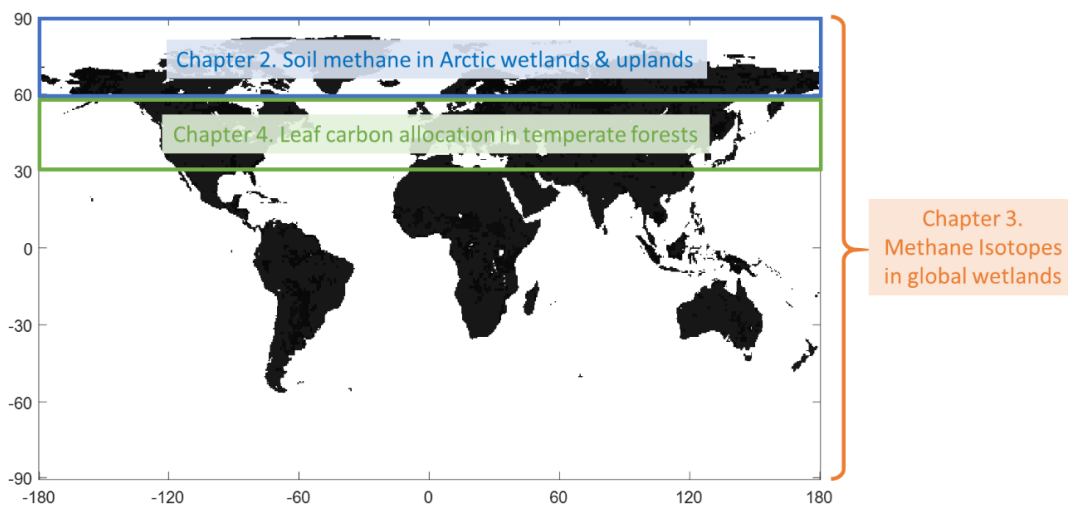


Figure 1.2 Summary of three articles and main chapters of this thesis.

Permafrost carbon cycle

The effects of climate change in the Arctic has been an interesting research topic as Arctic temperature has increased more rapidly than other regions. Studies revealed surface air temperature increases 0.6°C per decade since 1985 in the Arctic, twice the rate of the global increase (Stocker et al. 2013; McGuire et al. 2012). This rapid warming changes a broad spectrum of physical and ecological systems in the Arctic and causes a rapid thaw of permafrost soils (McGuire et al. 2009). Permafrost is ground that remains frozen for two or more consecutive years, which underlies 85% of Alaska, Greenland, Canada, and Siberia (Zimov et al. 2006). The Arctic permafrost was built up over thousands of years and stores up to 1,700 Pg of carbon (Fig. 1.3). This permafrost carbon pool is four times the carbon that has been released to the atmosphere due to human activities in the industrial era (Hugelius et al. 2013; Schuur et al. 2013).

The permafrost thaw may facilitate decomposition of the enormous carbon pool and release carbon into the atmosphere in the form of CO_2 and CH_4 (McGuire et al. 2018; Koven et al. 2011). It is crucial to understand the ratio between these two greenhouse gases, as CH_4 has 30 times stronger global warming potential over a 100-year period compared with CO_2 (Stocker et al. 2013). The ratio between CO_2 and CH_4 depends on the gradual or abrupt thaw of permafrost. For example, abrupt thaw may result in carbon release as mainly CH_4 due to associated changes in local hydrology (Turetsky et al. 2020). Current CH_4 emissions in the Arctic are estimated in a range of 31-100 $\text{TgCH}_4 \text{ yr}^{-1}$ (McGuire et al. 2009), but the emissions are expected to increase by 2-3 times or more by 2100, depending on the positive feedback between temperature and CH_4 due to more carbon from thawing permafrost (Koven et al. 2011; Lawrence et al. 2015).

However, in Chapter 2 and the first article of this thesis, I found a new perspective of the current understanding of the Arctic methane and permafrost feedback. I focused on the underestimated CH_4 soil sink that may help accurately estimate current CH_4 emissions and add a negative feedback between temperature and CH_4 in the Arctic. This study was published in *Nature Climate Change* in March 2020 (Oh et al. 2020).

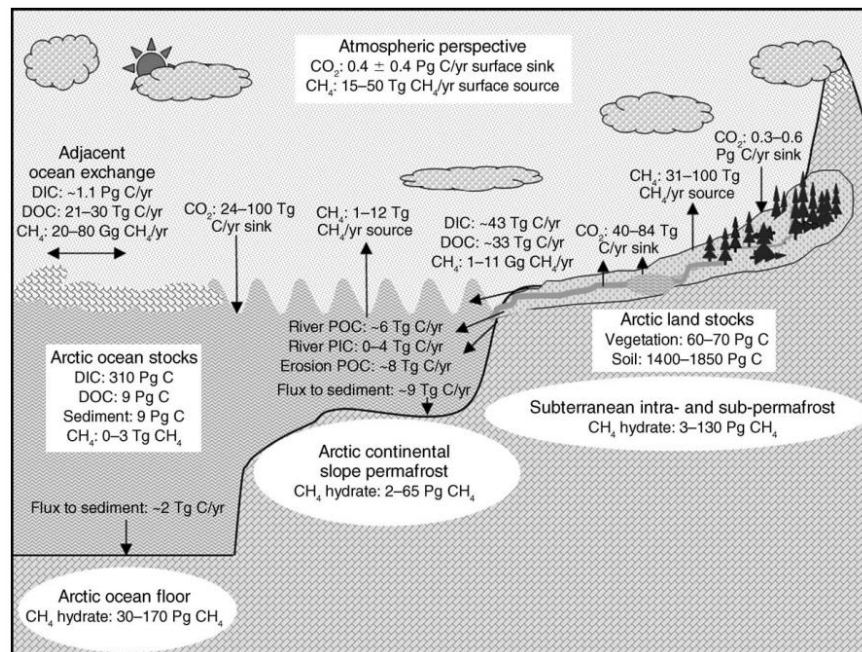


Figure 1.3 The current state of the Arctic carbon cycle north of 45 °N based on a synthesis of the information presented in the review of McGuire et al., 2009. Values shown are the ranges of uncertainty.

Uncertainty in wetland soils and the global methane cycle

Understanding and quantifying the global CH₄ budget is important in predicting future climate change (Saunio et al. 2020). The global CH₄ budget is determined by the balance of CH₄ sources and sinks (Fig. 1.4). CH₄ is emitted from three major sources through anthropogenic or natural processes: biogenic, thermogenic, and pyrogenic. The emitted CH₄ from three sources is oxidized by chemical reactants, mainly OH, in the atmosphere, and about 10% of the emissions are oxidized by soil methane oxidizing bacteria (Curry 2007).

Current synthesis analysis of the global CH₄ budget shows a huge discrepancy of over 200 TgCH₄ yr⁻¹ between the bottom-up and top-down estimates (Fig. 1.4) (Saunio et al. 2020). Bottom-up estimates of CH₄ emissions are derived from process-based, satellite-based, inventory, or observation-based upscaling models. Top-down estimates of CH₄ emissions are derived from an inversion approach of atmospheric observation of CH₄. The huge discrepancy is attributed to large natural emissions by bottom-up estimates in inland water systems (160 TgCH₄ yr⁻¹) (Saunio et al. 2020; DelSontro et al. 2018). It is expected that a better understanding of natural net methane emissions will help resolve the mechanisms responsible for long-term trends in atmospheric CH₄ and its carbon isotopic signatures ($\delta^{13}\text{C}$) (Nisbet et al. 2019).

Among the natural sources, wetlands are the largest and have a strong effect on atmospheric CH₄ and its $\delta^{13}\text{C}$ (Schwietzke et al. 2016). Since top-down estimates cannot distinguish CH₄ emissions between wetlands and other natural sources, the discrepancy in bottom-up and top-down estimates emphasizes the need of accurate estimation. The current estimation of wetland CH₄ emissions varies between 100 and 200 TgCH₄ yr⁻¹, and the wetland inundated area varies between 10 and 30 million km² (Melton et al. 2013; Wania et al. 2013).

Thus, in Chapter 3, the second article of this thesis, I develop and validate a first-of-its-kind process-based model to simulate $\delta^{13}\text{C}$ of CH₄ emitted from global wetlands, and examine the importance of the wetland $\delta^{13}\text{C}$ map for studying the global CH₄ cycle. I use stable isotope tracers as they are a useful tool in diagnosing a wide variety of mechanisms associated with determining CH₄ processes in wetlands (Chanton 2005). This article is in preparation for submission to *Nature Geoscience*.

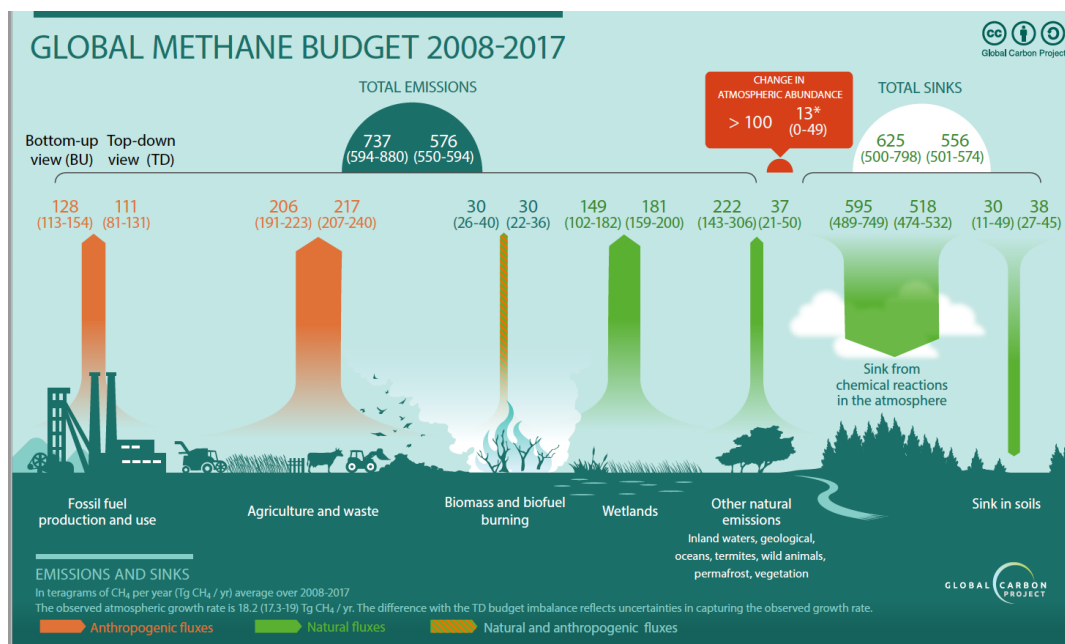


Figure 1.4 Global CH₄ budget for the 2008–2017 decade from Saunio et al., 2020. Both bottom-up (left) and top-down (right) estimates (TgCH₄ yr⁻¹) are provided for each emission and sink category, as well as for total emissions and total sinks.

Water use efficiency and global carbon cycle

Annually, about 60% of the total evapotranspiration of terrestrial ecosystems occurs as transpiration via plant stomata as a tradeoff of the carbon gain by photosynthesis (Schlesinger and Jasechko 2014; Bonan 2008). Thus, the terrestrial ecosystem's carbon and hydrologic cycles are intimately coupled by gas exchange through plant stomata. Water use efficiency (WUE) is a useful indication of the vegetation function that reflects the ratio between photosynthesis and transpiration (Medlyn et al., 2011). The changes in WUE have implications for the planetary energy, water, and carbon budgets, as photosynthesis is crucial to change atmospheric CO₂ to organic carbon, and transpiration is crucial to change sensible heat to latent heat and increase atmospheric water vapor (Fig. 1.5).

Due to the increase in atmospheric CO₂ and changes in precipitation in the industrial era, WUE has been widely studied to understand tree responses to climate change (Frank et al., 2015). The $\delta^{13}\text{C}$ in tree rings and leaves are used to estimate long-term changes in WUE, based on the assumption that $\delta^{13}\text{C}$ in plant tissues are governed by stomatal-controlled photosynthetic fractionation (Farquhar and Sharkey 1982; Farquhar et al. 1989). However, the $\delta^{13}\text{C}$ of plant tissues may not be explained solely by the photosynthetic fractionation. The $\delta^{13}\text{C}$ of plant tissues have been found to vary across different tissue types within the same plant (Badeck et al. 2005; Bowling et al. 2008), and there is a discrepancy in WUE estimation between the isotope-based and other methods (Medlyn et al. 2017). This discrepancy induces uncertainties in estimating future tree responses to climate change, as land surface models have incorporated $\delta^{13}\text{C}$ to improve model representation and prediction of terrestrial water and carbon fluxes (Raczka et al. 2016; Graven et al. 2017; Van Der Velde et al. 2013; Suits et al. 2005).

I argue that this discrepancy of isotope-based WUE may be resolved by improved understanding of leaf carbon allocation processes happening after photosynthesis in plant stomata. Thus, in the Chapter 4 of this thesis and the third article, I investigate the importance of leaf carbon allocation for seasonal leaf $\delta^{13}\text{C}$ changes and WUE in temperate forests. This article is in review for publication in *New Phytologist*.

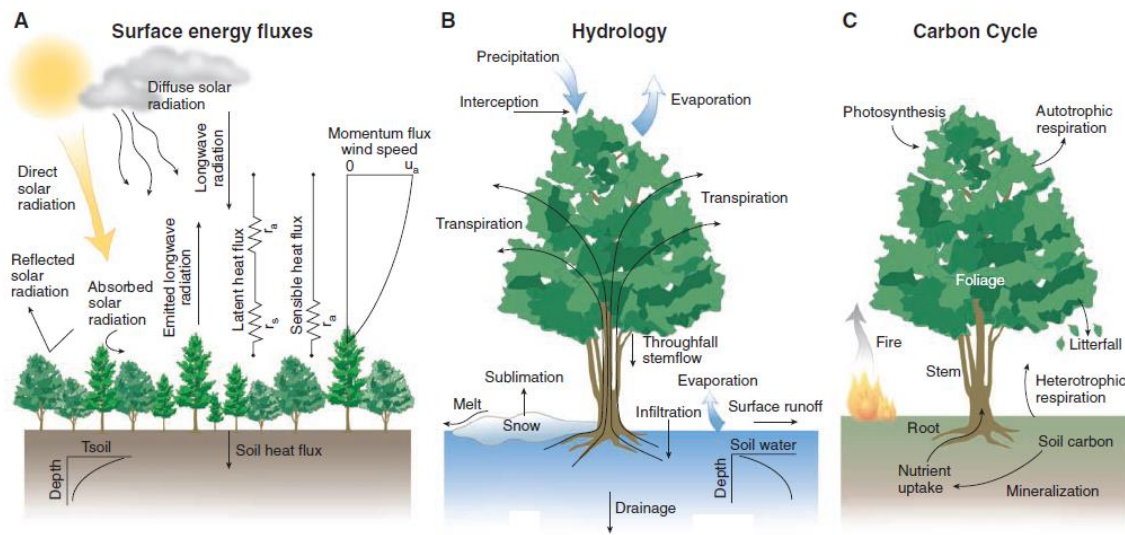


Figure 1.5 A schematic diagram of (A) surface energy fluxes, (B) hydrologic cycle, and (C) carbon cycle in terrestrial ecosystems modified from Bonan 2008.

CHAPTER 2. REDUCED NET METHANE EMISSIONS DUE TO MICROBIAL METHANE OXIDATION IN A WARMER ARCTIC

2.1 Abstract

Methane emissions from organic-rich soils in the Arctic have been extensively studied due to their potential to increase the atmospheric methane burden as permafrost thaws (McGuire et al. 2018; Schuur et al. 2013, 2015). However, this methane source might have been overestimated without considering high affinity methanotrophs (HAM, methane oxidizing bacteria) recently identified in Arctic mineral soils (Juncher Jørgensen et al. 2015; Lau et al. 2015; D'Imperio et al. 2017; Emmerton et al. 2014). Here, we find that HAM dynamics double the upland methane sink ($\sim 5.5 \text{ TgCH}_4\text{yr}^{-1}$) north of 50°N in simulations from 2000-2016 by integrating the dynamics of HAM and methanogens into a biogeochemistry model (Oh et al. 2016; Zhuang et al. 2004, 2013) that includes permafrost SOC dynamics (Schuur et al. 2015). The increase is equivalent to at least half of the difference in net methane emissions estimated between process-based models and observation-based inversions (Bruhwiler et al. 2014; Saunio et al. 2016), and the revised estimates better match site-level and regional observations (Emmerton et al. 2014; Lau et al. 2015; Bloom et al. 2010; Bohn et al. 2015; Miller et al. 2016). The new model projects doubled wetland methane emissions between 2017-2100 due to more accessible permafrost carbon (Hugelius et al. 2013; Koven et al. 2011; Lawrence et al. 2015). However, most of the increase in wetland emissions is offset by a concordant increase in the upland sink, leading to only an 18% increase in net methane emission (from 29 to 35 $\text{TgCH}_4\text{yr}^{-1}$). The projected net methane emissions may decrease further due to different physiological responses between HAM and methanogens in response to increasing temperature (Hagerty et al. 2014; Trimmer et al. 2015). This study was published in *Nature Climate Change* in March 2020 (Oh et al. 2020).

2.2 Introduction

Arctic soils are considered to be a significant net emission source of methane to the atmosphere. Current process-based biogeochemistry models and observation-based atmospheric inversions have estimated this source to be between 15 and 50 $\text{TgCH}_4\text{yr}^{-1}$, accounting for 20-25% of global natural methane emissions (Saunio et al. 2016). Furthermore, process-based models

predict 2-3 times larger methane emissions by 2100 (Koven et al. 2011; Lawrence et al. 2015; Schuur et al. 2013), as warmer temperature increases both rates of decomposition and availability of soil organic carbon (SOC) from permafrost-affected soils in addition to SOC from recently dead vegetation for decomposition (Hugelius et al. 2013; Schuur et al. 2009).

However, methane emissions are mainly confined to 13% of Arctic landscapes comprised of organic-rich soils where anaerobic processes dominate (Hugelius et al. 2013). The rest is comprised of mineral-rich soils where recent field studies have identified net annual methane sinks during growing seasons (Emmerton et al. 2014; Lau et al. 2015; D’Imperio et al. 2017; Juncher Jørgensen et al. 2015). This difference may be controlled by differences in methanotroph community composition (Fig. 2.1) (Christiansen et al. 2015). In wet organic soils, a fraction of methane produced by methanogenic archaea (methanogens, MG) is oxidized by methanotrophic bacteria (methanotrophs), and the remainder is mostly emitted into the atmosphere (Fig. 2.1a). The methanotrophs in these wet organic soils may be “low-affinity” methanotrophs (LAM) that require > 600 ppm of methane (by moles) for their growth and maintenance (Baani and Liesack 2008). But in dry mineral soils, the dominant methanotrophs are “high-affinity” methanotrophs (HAM), which can survive and grow at the level of atmospheric methane abundance ($[\text{CH}_4]_{\text{atm}}$) of about 1.8 ppm (Fig. 2.1b) (Tveit et al. 2019).

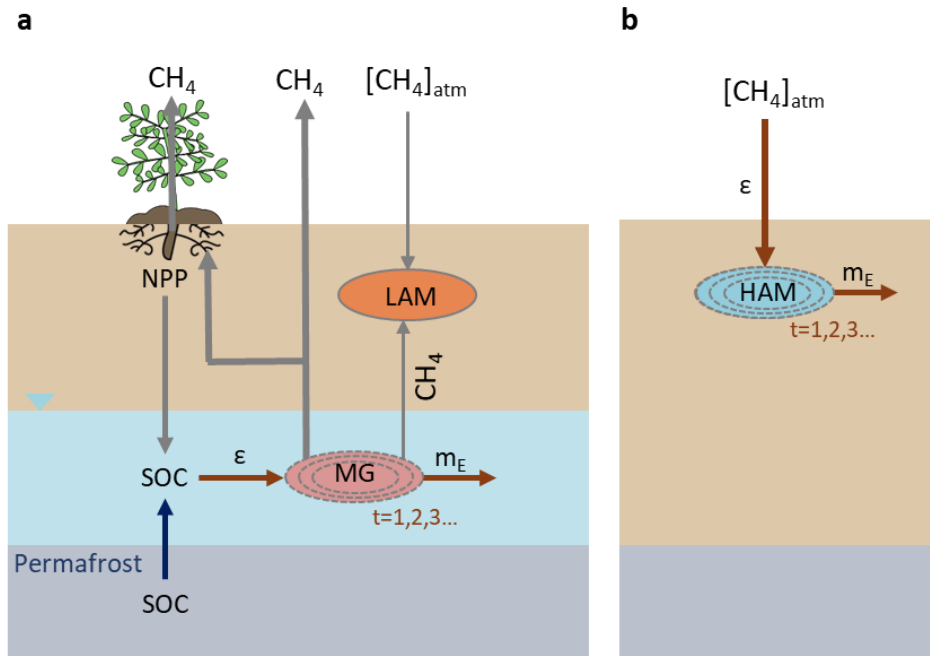


Figure 2.1 Schematic diagram of XPTEM-XHAM. The model simulates methane (CH₄) production by methanogens (MG), oxidation of CH₄ by Low Affinity Methanotrophs (LAM) in wetlands (panel a), and oxidation of atmospheric CH₄ ([CH₄]_{atm}) by High Affinity Methanotrophs (HAM) in uplands (panel b). We used a static inundation data (Matthews, E., and Fung 1987) to divide the Arctic landscape into wetland and upland regions but later varied the regions based on time-varying inundation data (Poulter et al. 2017; Lawrence et al. 2018). Changes in active biomass ($MIC_{biomass}$) of MG and HAM depend on microbial growth efficiencies (ϵ) and maintenance energy demand (m_E), and are tracked as a function of time, t . Permafrost SOC dynamics are added to account for accessible SOC from thawing permafrost when soil temperature at the corresponding depth becomes higher than 1°C. The dark blue arrow refers to permafrost SOC dynamics, dark red arrows refer to microbial dynamics, and grey arrows refer to processes from the original TEM

Quantification of the previously underestimated methane soil sink by HAM is needed to improve our understanding of Arctic methane budgets. Process-based methane models have overestimated Arctic methane emission by 5-10 TgCH₄yr⁻¹ when compared to observation-based atmospheric inversions (Bruhwiler et al. 2014; Saunio et al. 2016). Given that 87% of the Arctic is dominated by mineral-rich soils, the HAM-driven methane sink may greatly reduce current area-integrated net methane emissions. Furthermore, the positive feedbacks of methane emission due to additional accessible permafrost SOC may be partially suppressed by negative feedbacks from high activities of HAM at future increased surface temperatures and [CH₄]_{atm} (Oh et al. 2016).

Previous studies show that simulation of explicit microbial dynamics of MG and HAM improve model estimates of the magnitude and seasonality of methane sources and sinks (Oh et al. 2016; Segers 1998). Microbial dynamics may also cause additional complexity due to different microbial physiology between MG and HAM (Hagerty et al. 2014; Wieder et al. 2013). Recent laboratory and field studies show that microbial communities adjust their active microbial biomass ($MIC_{biomass}$) in warmer soils depending on microbial growth efficiency (ϵ) and maintenance energy (m_E) (Hagerty et al. 2014). ϵ represents growth efficiency of $MIC_{biomass}$ per unit of substrate consumed, and the ϵ of MG (0.05) is a factor of 10 smaller than that of HAM (0.5) (Von Stockar and Liu 1999; Trimmer et al. 2015). m_E , the rate of metabolic energy generation needed to maintain $MIC_{biomass}$, increases exponentially with temperature for all microbes, including MG and HAM, reflecting the fast turnover associated with cell mortality (Tijhuis et al. 1993; Hagerty et al. 2014). These processes are important for current and future Arctic methane budgets. However, current process-based methane models have not considered such microbial dynamics.

This study (1) estimates current pan-Arctic soil methane emissions and consumptions while accounting for microbial and permafrost SOC dynamics; (2) evaluates the magnitude and spatial variability of those estimates; and (3) projects pan-Arctic changes in soil methane emissions and consumptions through 2100. These projections include enhanced methane emissions due to increased available permafrost SOC and stimulated HAM activity due to increased surface temperatures and [CH₄]_{atm}, and different physiological responses of MG and HAM at warmer temperatures.

2.3 Methods

To address these objectives, we implemented explicit microbial dynamics for MG and HAM into a biogeochemistry model, the Terrestrial Ecosystem Model (TEM) (Fig. 2.1) (Zhuang et al. 2004, 2013). In wetland system, we simulated methane oxidation by LAM as a function of environmental parameters. We fixed $MIC_{biomass}$ of LAM due to the limited control of LAM $MIC_{biomass}$ on Arctic wetland methane emissions (Knoblauch et al. 2015; Throckmorton et al. 2016). Thus, we calculated changes in $MIC_{biomass}$ of MG and HAM as a function of ε , m_E , and environmental parameters, and set m_E as a constant with a temperature of 0°C (Hagerty et al. 2014; Tjhuis et al. 1993). To identify effects of permafrost SOC, we modified methane production to consider the amount of SOC from vegetation (Net Primary Productivity, NPP) and thawing permafrost in wetland ecosystems. The complete model with microbial and permafrost SOC dynamics is referred as eXplicit Permafrost TEM-eXplicit HAM model, XPTEM-XHAM (Fig. 2.1) (see Section 2.3.1).

To assess the effects of microbial and permafrost SOC dynamics, we conducted two additional sets of simulations for a factorial analysis (Table 2.1). First, we developed the Permafrost TEM-HAM model (PTEM-HAM), which considers HAM and permafrost SOC as XPTEM-XHAM but does not simulate explicit microbial dynamics of MG and HAM. Second, we used a version of TEM that simulates methane production and oxidation by MG and LAM, respectively, but does not consider HAM, permafrost nor microbial dynamics (TEM) (Zhuang et al. 2004, 2013). For XPTEM-XHAM and PTEM-HAM, we optimized key parameters of methane production and oxidation for alpine tundra, wet tundra, and boreal forest (see Section 2.3.2).

Table 2.1 Summary of the three models used in this study. The setup for XPTEM-XHAM is explained in details in Figure 2.1. For PTEM-HAM, methane production in wetlands is dependent on SOC derived from vegetation and thawing permafrost, and methane oxidation is by HAM, but $MIC_{biomass}$ changes are not explicitly simulated. In the TEM setup, methane production in wetlands is dependent on SOC derived from vegetation only, methane oxidation is by LAM, and $MIC_{biomass}$ changes are also not explicitly simulated.

Model Setup	XPTEM-XHAM	PTEM-HAM	TEM
Permafrost SOC Dynamics	ON	ON	OFF
High Affinity Methanotrophs (HAM)	ON	ON	OFF
Microbial Dynamics of HAM and MG	ON	OFF	OFF

The three models simulated methane dynamics north of 50°N, including low- (50-65°N) and high- (north of 65°N) Arctic regions at a spatial resolution of 0.5° latitude by 0.5° longitude. Gridded Climatic Research Unit (CRU) data were used as meteorological inputs for a contemporary simulation from 2000 to 2016 (Harris et al. 2014), and inputs from IPCC Representative Concentration Pathways (RCPs) 2.6, 4.5 and 8.5 were used for projections to 2100 (Meinshausen et al. 2011). For PTEM-HAM and XPTEM-XHAM, we used the Northern Circumpolar Soil Carbon Database version 2 (NCSCDv2) to estimate permafrost SOC at different soil depths (Hugelius et al. 2013). The simulated methane emission from wetlands and consumption from uplands were area-integrated for each grid cell based on static fractional inundation data (Matthews, E., and Fung 1987) (see Section 2.3.3).

For a sensitivity test of surface area of wetlands and uplands of XPTEM-XHAM, we used time-varying inundation data from the satellite-driven Surface Water Microwave Product Series-Global Lakes and Wetlands Database (SWAMPS-GLWD) during 2000-2012 (Poulter et al. 2017) and transient inundation fraction simulated by Community Land Model (CLM) version 5.0 during 2017-2100 (Lawrence et al. 2018). We further conducted XPTEM-XHAM sensitivity tests of wetland emission and upland consumption to changes in meteorology and substrate inputs during 2000-2016. For XPTEM-XHAM during 2017-2100, we varied m_E of MG and HAM to increase with temperature to model microbial physiological responses (equations (13), (14), and (19)). Lastly, for RCP 8.5 of XPTEM-XHAM, we varied Q_{10} of methane production and oxidation and fixed $[\text{CH}_4]_{\text{atm}}$ to the contemporary level (1.8 ppm) to test model sensitivity to temperature and $[\text{CH}_4]_{\text{atm}}$ changes (see Section 2.3.4).

2.3.1 Model description

We incorporated explicit microbial dynamics of high affinity methanotrophs (hereby, “HAM”) and methanogens (hereby, “MG”), including permafrost SOC dynamics, into a process-based biogeochemistry model, Terrestrial Ecosystem Model (TEM).

TEM

TEM is one of few biogeochemistry models that simulate methane consumption in Arctic mineral soils, and its methane, soil thermal, and hydrological dynamics have been evaluated in previous studies (Zhuang et al. 2004, 2013). The methane dynamics module of TEM simulates

methane production, oxidation, and three transport processes between soil and atmosphere. In a wetland system, changes in methane concentrations (C_M) at depth z and time t ($\partial C_M(z,t)/\partial t$) are governed by equation 2.1, where $M_P(z,t)$, $M_O(z,t)$, $R_P(z,t)$, and $R_E(z,t)$ are methane production, oxidation, plant-mediated transport, and ebullition rates, respectively, and $\partial F_D(z,t)/\partial z$ represents flux divergence due to gaseous and aqueous diffusion.

$$\frac{\partial C_M(z,t)}{\partial t} = M_P(z,t) - M_O(z,t) - \frac{\partial F_D(z,t)}{\partial z} - R_P(z,t) - R_E(z,t) \dots \text{Equation 2.1}$$

Methane is produced (M_P) in anaerobic soils and is calculated by the product of maximum potential production rate (M_{GO}) and limiting functions of substrate, soil temperature, pH, and redox potentials (S_{OM} , M_{ST} , pH and R_x , respectively) (equation 2.2). We used limiting factors of pH and R_x to consider enzymatic activity and the relative availability of electron acceptors (e.g., O_2 , NO_3^- , SO_4^{2-} , Fe^{+3} , Mn^{+4}) for methane production. The limiting function of substrate ($f(S_{OM}(z,t))$) is mainly dependent on soil organic carbon (SOC) derived from vegetation (Net Primary Productivity, NPP), where $NPP(mon)$ is monthly NPP ($gC\ m^{-2}\ month^{-1}$), NPP_{MAX} is ecosystem-specific maximum monthly NPP, and $f(C_{DIS}(z))$ describes the relative availability of organic carbon substrate at depth z (equation 2.3). For the substrate availability, we calculated changes in vegetation carbon using atmospheric CO_2 concentrations, transient temperature, precipitation, vapor pressure and soil texture (Zhuang et al. 2003).

$$M_{P,TEM}(z,t) = M_{GO}f(S_{OM}(z,t))f(M_{ST}(z,t))f(pH(z,t))f(R_x(z,t)) \dots \text{Equation 2.2}$$

$$f(S_{OM}(z,t)) = \left(1 + \frac{NPP(mon)}{NPP_{max}}\right)f(C_{DIS}(z)) \dots \text{Equation 2.3}$$

The produced methane diffuses into aerobic soils and is oxidized by low affinity methanotrophs (hereby, “LAM”), calculated by the product of the maximum potential oxidation rate (O_{MAX}) and limiting functions of methane concentration, soil temperature, soil moisture, redox potential, nitrogen deposition, diffusion limited by high soil moisture, and oxygen concentration

(C_M , T_{SOIL} , E_{SM} , R_{OX} , N_{DP} , D_{MS} , and C_{O_2} respectively) (equation 2.4). The Michaelis-Menten constant for methane oxidation was set to $5 \mu\text{M}$ ($k_{CH_4,LAM}$) (equation 2.5) (Baani and Liesack 2008).

$$M_{O,TEM}(z, t) = O_{MAX} f(C_M(z, t)) f(T_{SOIL}(z, t)) f(E_{SM}(z, t)) F(R_{OX}(z, t)) f(N_{dp}(z, t)) f(D_{ms}(z, t)) f(C_{O_2}(z))$$

... Equation 2.4

$$f(C_M(z, t)) = \frac{C_M(z, t)}{k_{CH_4,LAM} + C_M(z, t)} \quad \dots \text{Equation 2.5}$$

The residual methane is emitted to the surface through three transport processes. First, gaseous and aqueous diffusion (F_D) occur due to concentration gradients of methane ($\partial C_M(z, t)/\partial t$) following Fick's law through soil pores (equation 2.6). The molecular diffusion coefficient (D) in different soil layers was calculated based on soil texture and soil moisture. We also have a simple limitation of diffusion on temperature, that there will be no diffusion when temperature is below 0°C . Secondly, ebullition (R_E) occurs when methane bubble forms (i.e., when C_M is greater than $500 \mu\text{mol L}^{-1}$ in saturated soils); C_M is multiplied by a constant rate of 1.0 h^{-1} (K_e) (equation 2.7). Lastly, plant-mediated transport (R_p) occurs through the root systems of some plants that provide a direct conduit for methane to the atmosphere, and is functions of rate constant of 0.01 h^{-1} , vegetation type, root density, vegetation growth, and soil methane concentrations (K_p , TR_{veg} , f_{ROOT} , f_{GROW} , and C_M , respectively) (equation 2.8) (Walter and Heimann 2000). R_p depends on ecosystem-specific plant functional types and increases in a warmer soil due to the increase in vegetation growth. In both wetland and upland ecosystems, the soil profile was divided into 1-cm layers, and soil temperature, moisture, and methane dynamics of TEM were simulated at daily time steps (Zhuang et al. 2004).

$$F_D(z, t) = -D(z) \frac{\partial C_M(z, t)}{\partial t} \quad \dots \text{Equation 2.6}$$

$$R_E(z, t) = K_e f(C_M(z, t)) \quad \dots \text{Equation 2.7}$$

$$R_p(z, t) = K_p TR_{veg} f_{ROOT}(z) f_{GROW}(t) C_M(z, t) \dots \text{Equation 2.8}$$

Permafrost TEM-HAM model

We first revised TEM to consider permafrost SOC dynamics and HAM, but not active microbial biomass changes (Permafrost TEM-HAM model; “PTEM-HAM”). To consider atmospheric methane oxidation by HAM, we modified the Michaelis-Menten constant for methane oxidation from 5 to 0.11 μM ($k_{CH_4, HAM}$) (Baani and Liesack 2008; Zhuang et al. 2004) (equation 2.9). To account for permafrost SOC accessible as surface temperature increases and permafrost thaws, we set maximum lower boundary of soil layer from 1- to 3-m. We then added permafrost SOC dynamics by changing the main carbon source for MG to vegetation (NPP) and permafrost SOC (equation 2.10). $PSOC(z)$ represents permafrost soil organic carbon stored at depth z (g m^{-2}) and is available when soil temperature at the corresponding depth is greater than 1°C . We set $PSOC_{max}$ to be 300 kg m^{-2} for top 3-m soil, based on Northern Circumpolar Soil Carbon Database version 2 (NCSCDV2) (Hugelius et al. 2013). Accordingly, equations of methane production and oxidation for PTEM-HAM are similar to equations 2.2 and 2.4, but the $f(C_M)$ and $f(S_{OM})$ are replaced with $f_{new}(C_M)$ and $f_{new}(S_{OM})$, respectively (equations 2.11 and 2.12).

$$f_{new}(C_M(z, t)) = \frac{C_M(z, t)}{k_{CH_4, HAM} + C_M(z, t)} \dots \text{Equation 2.9}$$

$$f_{new}(S_{OM}(z, t)) = \left(\left(1 + \frac{NPP(mon)}{NPP_{max}} \right) f(C_{DIS}(z)) + \frac{PSOC(z)}{PSOC_{max}} \right) \dots \text{Equation 2.10}$$

$$M_{P, PTEM-HAM}(z, t) = M_{G0} f_{new}(S_{OM}(z, t)) f(M_{ST}(z, t)) f(pH(z, t)) f(R_x(z, t)) \dots \text{Equation 2.11}$$

$$M_{O, PTEM-HAM}(z, t) = O_{MAX} f_{new}(C_M(z, t)) f(T_{SOIL}(z, t)) f(E_{SM}(z, t)) f(R_{OX}(z, t)) f(N_{dp}(z, t)) f(D_{ms}(z, t)) \dots \text{Equation 2.12}$$

eXplicit Permafrost TEM-eXplicit HAM model

We further added explicit microbial dynamics of MG and HAM into PTEM-HAM (eXplicit Permafrost TEM-eXplicit HAM model; “XPTEM-XHAM”). The methane oxidation by LAM was simulated as a function of environmental parameters with fixed active microbial biomass ($MIC_{biomass}$), same as TEM and PTEM-HAM (equation 2.4 and 2.12), due to the limited control of LAM $MIC_{biomass}$ on Arctic wetland methane emissions (Knoblauch et al. 2015; Throckmorton et al. 2016). To clarify the role of LAM microbial dynamics in wetland methane emission for both contemporary period and future projection, we ran additional simulations by adding microbial dynamics of LAM into XPTEM-XHAM.

Methane production by MG ($M_{P,XPTEM-XHAM}$) and oxidation by HAM ($M_{O,XPTEM-XHAM}$) are calculated by the product of $MIC_{biomass}$ and methane production and oxidation of PTEM-HAM ($M_{P,PTEM-HAM}$ and $M_{O,PTEM-HAM}$), respectively (equation 2.13) (Oh et al. 2016; Lau et al. 2016). Active microbial biomass changes ($dMIC_{biomass}/dt$) are calculated thermodynamically by considering microbial growth efficiency (ϵ), maintenance energy (m_E), and Gibbs free energy (ΔG) of MG and HAM (equation 2.14). Here, the maximum methane production and oxidation potentials, M_{GO} and O_{max} respectively in equations 2.11 and 2.12, are multiplied by a geometric parameter ($\gamma_{geometric}$) and become M_{GO}' and O_{max}' ($M_{GO}' = M_{GO} \times \gamma_{geometric}$ and $O_{max}' = O_{max} \times \gamma_{geometric}$), where the units for M_{GO}' and O_{max}' are $\mu\text{M}_{\text{SOC}} / \mu\text{M}_{\text{bioC}}^{0.66} / \text{hr}$ and $\mu\text{M}_{\text{CH}_4} / \mu\text{M}_{\text{bioC}}^{0.66} / \text{hr}$, respectively.

$$M_{P,XPTEM-XHAM} = MIC_{biomass,MG}^{2/3} \times \gamma_{geometric} \times M_{P,PTEM-HAM} \dots \text{Equation 2.13a}$$

$$M_{O,XPTEM-XHAM} = MIC_{biomass,HAM}^{2/3} \times \gamma_{geometric} \times M_{O,PTEM-HAM} \dots \text{Equation 2.13b}$$

$$\frac{dMIC_{biomass,MG}}{dt} = \epsilon_{MG} \times \left(0.8 \times MIC_{biomass,MG}^{\frac{2}{3}} \times \gamma_{geometric} \times M_{P,PTEM-HAM} + MIC_{MG} \frac{m_E}{\Delta G_{r,MG}} \right)$$

... Equation 2.14a

$$\begin{aligned} & \frac{dMIC_{biomass,HAM}}{dt} \\ &= \varepsilon_{HAM} \times (0.8 \times MIC_{biomass,HAM}^{\frac{2}{3}} \times \gamma_{geometric} \times M_{O,PTEM-HAM} \\ &+ MIC_{HAM} \frac{m_E}{\Delta G_{r,HAM}}) \end{aligned}$$

... Equation 2.14b

Equations for changes in $MIC_{biomass}$ were derived from growth rate (ΔP) (Lau et al. 2016), which is proportional to the relative magnitude in the difference between maintenance energy demand and rate of energy delivery of a metabolic redox equation in equation 2.15, where ΔP is in $\text{kJ } \mu\text{mol}_{biomass}^{-1}\text{s}^{-1}$, ΔG_r is the free energy of the metabolic redox reaction at in-situ temperature, activities, and fugacities, which is usually negative, in $\text{kJ } \mu\text{mol}_{reactant}^{-1}$, M_P is the metabolic reaction rate in $\mu\text{mol}_{reactant} \mu\text{mol}_{biomass}^{-1} \text{s}^{-1}$, and m_E is the maintenance energy in $\text{kJ } \mu\text{mol}_{biomass}^{-1} \text{hr}^{-1}$. We assumed that only 80% of the free energy is available for metabolism and the rest is lost as heat (Lau et al. 2016).

$$\Delta P_{MG} = -0.8 \Delta G_{r,MG} M_{P,PTEM-HAM} - m_E \dots \text{Equation 2.15a}$$

$$\Delta P_{HAM} = -0.8 \Delta G_{r,HAM} M_{O,PTEM-HAM} - m_E \dots \text{Equation 2.15b}$$

The rate of increase or decrease of active biomass is governed by the fraction of ΔG_r that is directed to maintenance and the growth efficiency, so the active biomass increases according to equation 2.16, where $MIC_{biomass}$ is the active biomass concentration in $\mu\text{mol}_{biomass} \text{L}^{-1}$, and ε is the microbial growth efficiency in $\mu\text{mol}_{biomass} \mu\text{mol}_{substrate}^{-1}$.

$$\frac{dMIC_{biomass,MG}}{dt} = \frac{\varepsilon_{MG} \times MIC_{biomass,MG} \times \Delta P_{MG}}{-\Delta G_{r,MG}} \dots \text{Equation 2.16a}$$

$$\frac{dMIC_{biomass,HAM}}{dt} = \frac{\varepsilon_{HAM} \times MIC_{biomass,HAM} \times \Delta P_{HAM}}{-\Delta G_{r,HAM}} \dots \text{Equation 2.16b}$$

Here, ΔG_r is calculated using the net thermodynamic driving force (f) of the reaction in equation 2.17, where m is the number of moles of ATP generated per mole of reactant, and ΔG_p is the free energy for the phosphorylation reaction. At the point at which the thermodynamic drive vanishes, $\Delta G_r = -m \times \Delta G_p$. For methanotrophs, $\Delta G_{r,HAM} = -286 \times 2.8 \text{ kJ mol}_{\text{reactant}}^{-1} = -800.8 \text{ kJ mol}_{\text{reactant}}^{-1}$ (Stackhouse et al. 2015). Whereas for methanogens, the free energy of the metabolic redox reaction is much smaller, $\Delta G_{r,MG} = -25 \text{ kJ mol}_{\text{reactant}}^{-1}$ (Thauer et al. 2008).

$$f = -\Delta G_r - m \times \Delta G_p \dots \text{Equation 2.17}$$

Lastly in equations 2.13 and 2.14, we added the power of two thirds (2/3) to the active biomass term to account for substrate diffusion to the cell surface. Specifically, microbes rarely exist as single microbes in isolation, but rather as aggregates (Gottschalk 2012). As the availability of substrate is assumed to be positively correlated with diffusion, thus the rate of diffusion to the cell wall is determined by surface area (not cell volume). Based on this argument, since $MIC_{biomass}$ in equation 2.14 does not cancel out, we calculated the theoretical active microbial biomass at equilibrium, which is the maximum active microbial biomass for given environmental conditions when MG and MT are not limited by space (equation 2.18).

$$MIC_{biomass,MG} = \left(\frac{-0.8 \times \Delta G_{r,MG} \times M_{P,PTEM-HAM}}{m_E} \right)^3 \dots \text{Equation 2.18a}$$

$$MIC_{biomass,HAM} = \left(\frac{-0.8 \times \Delta G_{r,HAM} \times M_{O,PTEM-HAM}}{m_E} \right)^3 \dots \text{Equation 2.18b}$$

The active microbial biomass changes in equation 2.14 are dependent on ε and m_E . We set ε as 0.05 and 0.5 for MG and MT, respectively, defined from previous laboratory and experiment studies (Segers 1998; Von Stockar and Liu 1999; Von Stockar et al. 2006; Trimmer et al. 2015). The temperature sensitivity of m_E is derived from Tjihuis et al. (1993) (Tjihuis et al. 1993), who studied a large range of different organisms and found that maintenance energy is mainly influenced by temperature (T in °C) with energy of activation of 69 kJ mol^{-1} (equation 2.19).

$$m_E = 4.5 \times \exp\left(\frac{-6.94 \times 10^4}{R} \left(\frac{1}{T} - \frac{1}{298}\right)\right) \dots \text{Equation 2.19}$$

The initial $MIC_{biomass}$ of MG and HAM is estimated from metagenomic data (0.0002 and 0.0025 $\mu\text{mol}_{biomass} \text{L}_{soil}^{-1}$, respectively) (Stackhouse et al. 2015; Oh et al. 2016; Stackhouse et al. 2017). We set the maximum active microbial biomass of MG and HAM of each layer, as the maximum concentration of cells is 10^4 - 10^7 cells per gram of dry soil due to substrate availability and space limitation (Conrad 2009). Using conversion factors, 1 cell = 8×10^{-15} mol C, 1 L soil = 1500 g of dry soil, and the ratio of MT to MG in the total microbial composition from Stackhouse et al. (2015) (Stackhouse et al. 2015) (maximum 1.5% of total cells), we estimated that the maximum concentrations of both MG and HAM are 50,000 $\text{nmol}_{biomass} \text{L}_{soil}^{-1}$.

2.3.2 Model optimization

We optimized a total of 5 parameters for upland methane oxidation and 4 parameters for wetland methane production related to both PTEM-HAM and XPTM-XHAM (Table 2.2-2.3). All other parameters were set the same as in Zhuang et al. (2004) (Zhuang et al. 2004) for methane production and transport processes and as in Zhuang et al. (2013) (Zhuang et al. 2013) for methane oxidation. To optimize these parameters, we first collected observation data from six sites representing uplands and wetlands for alpine tundra, wet tundra, and boreal forest ecosystems (Sellers et al. 1997; Harazono et al.; D'Imperio et al. 2017; Juncher Jørgensen et al. 2015; Dinsmore et al. 2017) (Data from the *Greenland Ecosystem Monitoring Programme* were provided by the Department of Bioscience, Aarhus University, Denmark in collaboration with Department of Geosciences and Natural Resource Management, Copenhagen University, Denmark) (Table 2.2). Besides the observed meteorology from field sites, we also used CRU time-series data version 4.01 to fill missing meteorological inputs (Harris et al. 2014). We then used the Shuffled Complex Evolution Approach in R language (SCE-UA-R) to minimize the difference between simulated and observed methane emission and consumption rates (Duan et al. 1993). For each site, 40 ensembles were run using SCE-UA-R with 10,000 maximum loops per parameter ensemble, and all of them reached steady state before the end of the loops. Our optimization results show that

both XPTEM-XHAM and PTEM-HAM reasonably capture the magnitude and seasonality of observed soil methane fluxes (Figure 2.2 and 2.4).

The optimized parameters show maximum potential, temperature and moisture sensitivity of methane production and oxidation in different ecosystems (Table 2.4-2.5 and Figure 2.3 and 2.5). In wetlands, the temperature sensitivity of methane emission (P_{CH_4Q10}) ranges 2.5-9, corresponding to observations (Segers 1998; Roy C. et al. 2015). In boreal wetland ecosystems, methane emission is less sensitive to temperature (low P_{CH_4Q10}), and more oxidation occurs by LAM (high O_{XIC}), probably due to higher temperature throughout the growing season than in alpine and wet tundra ecosystems. In uplands, the temperature sensitivity (O_{CH_4Q10}) ranged from 1 to 6, also corresponding to observations (Lau et al. 2015). O_{CH_4Q10} was optimized to be lowest for upland wet tundra as our observation data from wet tundra showed consistent methane consumption throughout the growing season (Juncher Jørgensen et al. 2015) (Figure 2.2e and 2.4e). The optimal soil moisture (MV_{opt}) for methane consumption ranges between 0.35 to 0.55 v/v, corresponding to observations (Whalen and Reeburgh 1996). The parameter uncertainty is large for the reference temperature of methane production (T_{PR}) for wetland systems and is large for minimum soil moisture (MV_{min}) for upland systems (Figure 2.3 and 2.5).

Table 2.2 Information about observation sites for model optimization

No.	Vegetation Types	Latitude, Longitude	Meteorological Inputs	Observation Data	References
Uplands					
1	Alpine Desert	70, -53.5	Site observation	CH ₄ flux in 2013-2014	D'Imperio et al., 2016
2	Wet Tundra	74.5, -20.5	Site observation	CH ₄ flux in 2012	Jørgensen et al., 2015
3	Boreal Forest	67.5, 26.5	Site observation	CH ₄ flux in 2012	Dinsmore et al., 2017
Wetlands					
1	Alpine Desert	74.5, -20.5	Site observation	CH ₄ flux in 2010, 2012	<i>Greenland Ecosystem Monitoring Programme</i>
2	Wet Tundra	71, -156.5	CRU	CH ₄ flux in 2000-2001	Harazono et al., 2006
3	Boreal Forest	56, -98.5	Site observation	CH ₄ flux in 2012	Sellers et al., 1997

Table 2.3 Variable name, unit, upper and lower boundary of parameters

Symbol	Variable name	XPTEM-XHAM			PTEM-HAM		
		Unit	Upper Boundary	Lower Boundary	Unit	Upper Boundary	Lower Boundary
Wetlands							
M_{GO}	Maximum Potential of Methane Production	$\mu\text{M}_{\text{SOC}} / \mu\text{M}_{\text{bioC}}^{0.6} / \text{hr}$	0.05	0.001	$\mu\text{M}/\text{hr}$	5.0	0.1
Q_{CH4Q10}	Q ₁₀ temperature sensitivity	unitless	10.0	1.0	unitless	10.0	1.0
O_{XC}	Maximum Potential of methane oxidation by LAM	$\mu\text{M}/\text{hr}$	5.0	0.01	$\mu\text{M}/\text{hr}$	5.0	0.01
T_{PR}	Reference temperature for methane production	°C	5.0	-5.0	°C	0.01	-5.0
Uplands							
O_{max}	Maximum Potential of methane oxidation by HAM	$\mu\text{M}_{\text{CH4}} / \mu\text{M}_{\text{bioC}}^{0.6} / \text{hr}$	0.025	0.001	$\mu\text{M}/\text{hr}$	15.0	0.1

Table 2.3 continued

O_{CH4Q10}	Q ₁₀ temperature sensitivity	Unitless	10.0	0.5	Unitless	10.0	0.5
MV_{max}	Maximum Volumetric Soil Moisture	v/v	1.0	0.55	v/v	1.0	0.55
MV_{min}	Minimum Volumetric Soil Moisture	v/v	0.25	0.0	v/v	0.25	0.0
MV_{opt}	Optimum Volumetric Soil Moisture	v/v	0.55	0.25	v/v	0.55	0.25

Table 2.4 Optimized parameters for PTEM-HAM

Wetlands						
No.	Vegetation	M_{GO}	P_{CH4Q10}	O_{XIc}	T_{PR}	
1	Alpine Desert	0.280±0.094	8.034±1.928	0.028±0.055	2.154±1.908	
2	Wet Tundra	0.415±0.121	8.818±1.179	0.010±0.001	2.438±1.405	
3	Boreal Forest	0.504±0.140	6.296±1.873	0.211±0.194	2.827±1.287	
Uplands						
No.	Vegetation	O_{MAX}	O_{CH4Q10}	M_{Vmax}	M_{Vmin}	M_{Vopt}
1	Alpine Desert	3.755±0.487	6.240±1.119	0.818±0.818	0.226±0.052	0.541±0.019
2	Wet Tundra	2.422±0.149	2.864±0.925	0.614±0.058	0.134±0.071	0.464±0.032
3	Boreal Forest	0.813±0.188	4.192±0.758	0.853±0.057	0.124±0.067	0.431±0.082

Table 2.5 Optimized parameters for XPTEM-XHAM

Wetlands						
No	Vegetation	M_{Go}	P_{CH4Q10}	O_{XIc}	T_{PR}	
1	Alpine Desert	0.016±0.005	7.896±1.971	0.011±0.011	1.750±1.595	
2	Wet Tundra	0.014±0.005	7.985±1.832	0.010±0.000 2	1.920±1.529	
3	Boreal Forest	0.015±0.001	2.392±0.484	0.033±0.035	2.490±1.032	
Uplands						
No	Vegetation	O_{MAX}	O_{CH4Q10}	M_{vmax}	M_{vmin}	M_{vopt}
1	Alpine Desert	0.0034±0.00 02	6.1449±1.13 66	0.8090±0.18 06	0.1854±0.08 14	0.5259±0.03 11
2	Wet Tundra	0.0024±0.00 02	1.1762±0.12 37	0.7947±0.09 39	0.1349±0.06 88	0.4404±0.08 14
3	Boreal Forest	0.0022±0.00 05	3.7315±0.37 22	0.8553±0.06 13	0.1130±0.06 82	0.3603±0.08 11

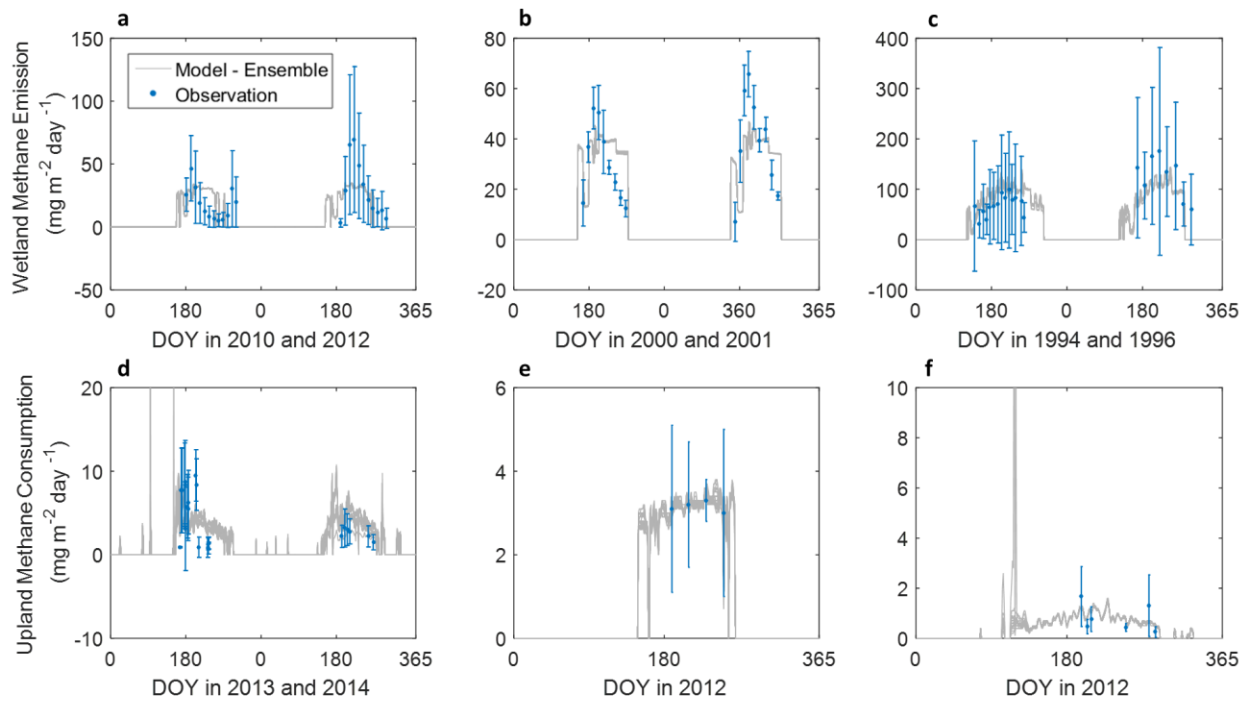


Figure 2.2 Model-data comparison of methane fluxes for XPTEM-XHAM model. (a-c) wetland methane emission and (d-f) upland methane consumption in $\text{mg m}^{-2} \text{ day}^{-1}$ for (a,d) alpine tundra, (b,e) wet tundra, and (c,f) boreal forest ecosystems

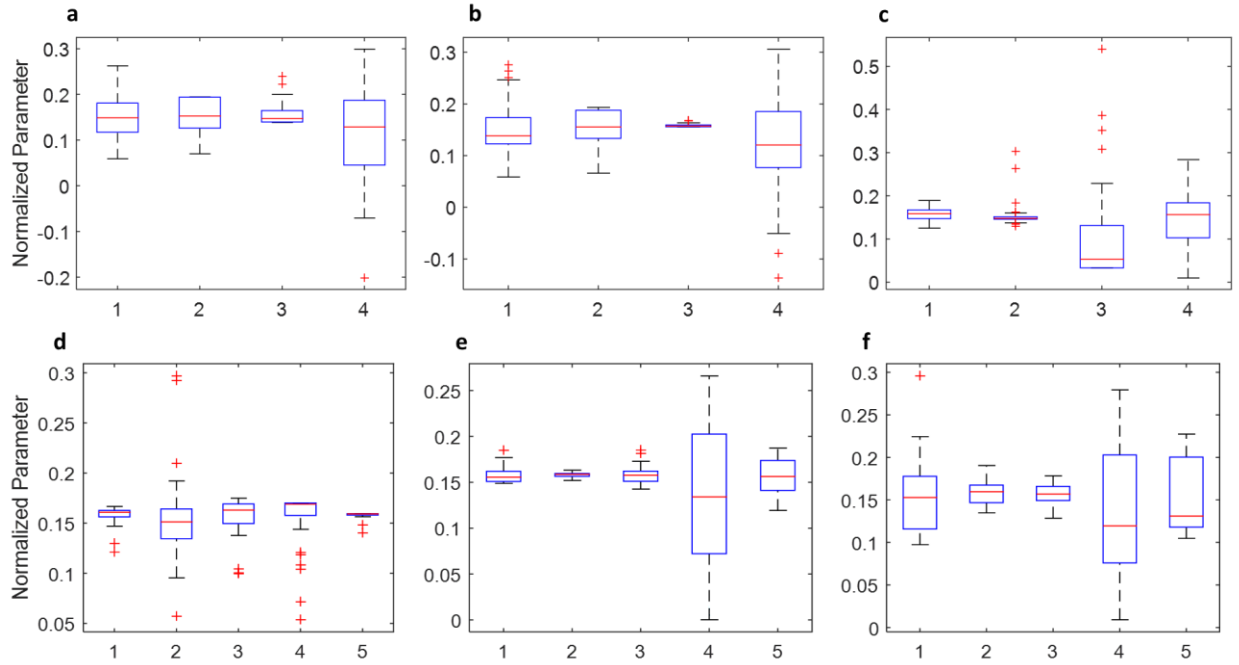


Figure 2.3 Box plot of normalized optimized parameters for XPTEM-XHAM model. (a-c) Normalized values of optimized parameters of (1) maximum methane production potential (MGO), (2) Q_{10} temperature sensitivity of methane production ($Q_{CH_4Q_{10}}$), (3) Maximum potential of methane oxidation by LAM (O_{XIC}), and (4) reference temperature for methane production (T_{PR}). (d-f) Normalized values of optimized parameters with 1 standard deviation of (1) maximum potential of methane oxidation by HAM (O_{max}), (2) Q_{10} temperature sensitivity of methane oxidation ($O_{CH_4Q_{10}}$), (3) Maximum soil moisture for methane oxidation (MV_{max}), (4) minimum soil moisture for methane oxidation (MV_{min}) and (5) optimum soil moisture for methane oxidation (MV_{opt}) for (a,d) alpine tundra, (b,e) wet tundra, and (c,f) boreal forests. On each box, the central mark indicates the median, and the bottom and top edges of the box indicate the 25th and 75th percentiles, respectively. The whiskers extend to the most extreme data points not considered outliers, and the outliers are plotted individually using the '+' symbol (Higham and Higham 2016).

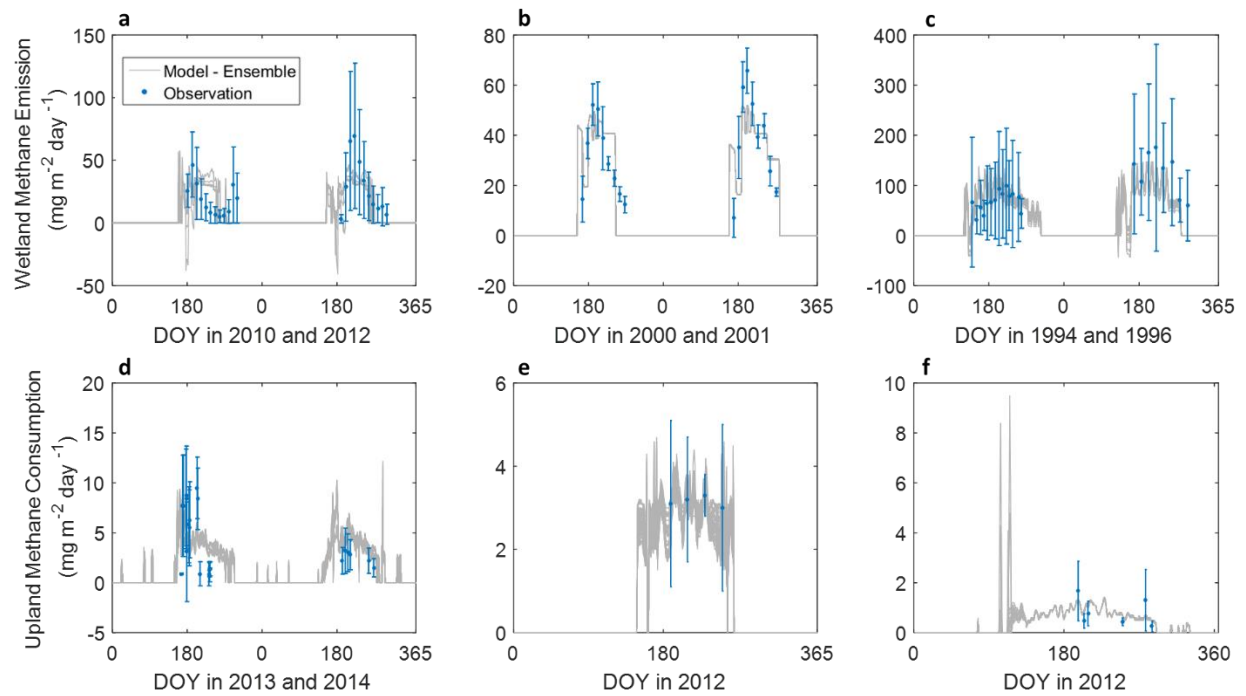


Figure 2.4 Model-data comparison of methane fluxes for PTEM-HAM model. (a-c) wetland methane emission and (d-f) upland methane consumption in $\text{mg m}^{-2} \text{day}^{-1}$ for (a,d) alpine tundra, (b,e) wet tundra, and (c,f) boreal forest ecosystems.

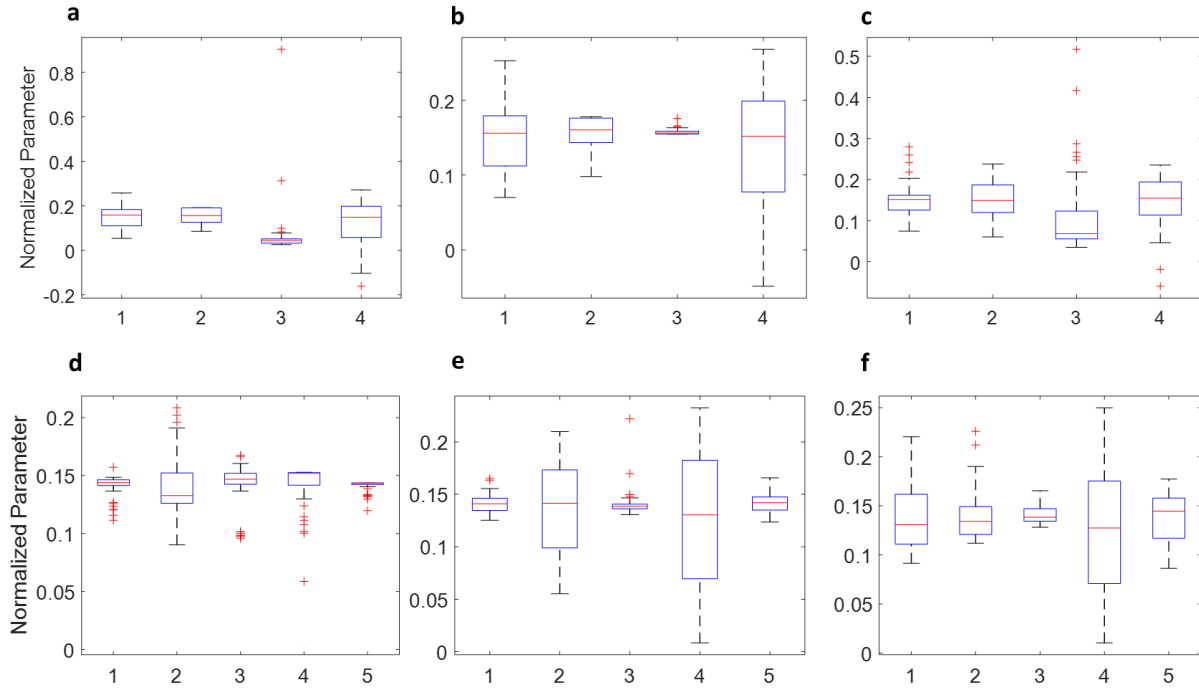


Figure 2.5 Box plot of normalized optimized parameters for PTEM-HAM model. (a-c) Normalized values of optimized parameters of (1) maximum methane production potential (MGO), (2) Q_{10} temperature sensitivity of methane production (Q_{CH_4Q10}), (3) Maximum potential of methane oxidation by LAM (O_{XI_C}), and (4) reference temperature for methane production (T_{PR}). (d-f) Normalized values of optimized parameters with 1 standard deviation of (1) maximum potential of methane oxidation by HAM (O_{max}), (2) Q_{10} temperature sensitivity of methane oxidation (O_{CH_4Q10}), (3) Maximum soil moisture for methane oxidation (MV_{max}), (4) minimum soil moisture for methane oxidation (MV_{min}) and (5) optimum soil moisture for methane oxidation (MV_{opt}) for (a,d) alpine tundra, (b,e) wet tundra, and (c,f) boreal forests. On each box, the central mark indicates the median, and the bottom and top edges of the box indicate the 25th and 75th percentiles, respectively. The whiskers extend to the most extreme data points not considered outliers, and the outliers are plotted individually using the '+' symbol (Higham and Higham 2016).

We validated soil temperature and moisture in the top 10-cm soil depth for alpine tundra, wet tundra, and boreal forest sites where we used the data from the sites for model optimization (Juncher Jørgensen et al. 2015; D’Imperio et al. 2017; Dinsmore et al. 2017). In general, soil thermal and hydrological modules of TEM simulate Arctic soil temperature and moisture reasonably well (Figure 2.6). The simulated soil temperature and moisture correspond well with observations, but with a slight under-estimation of temperature and over-estimation of moisture during the growing season.

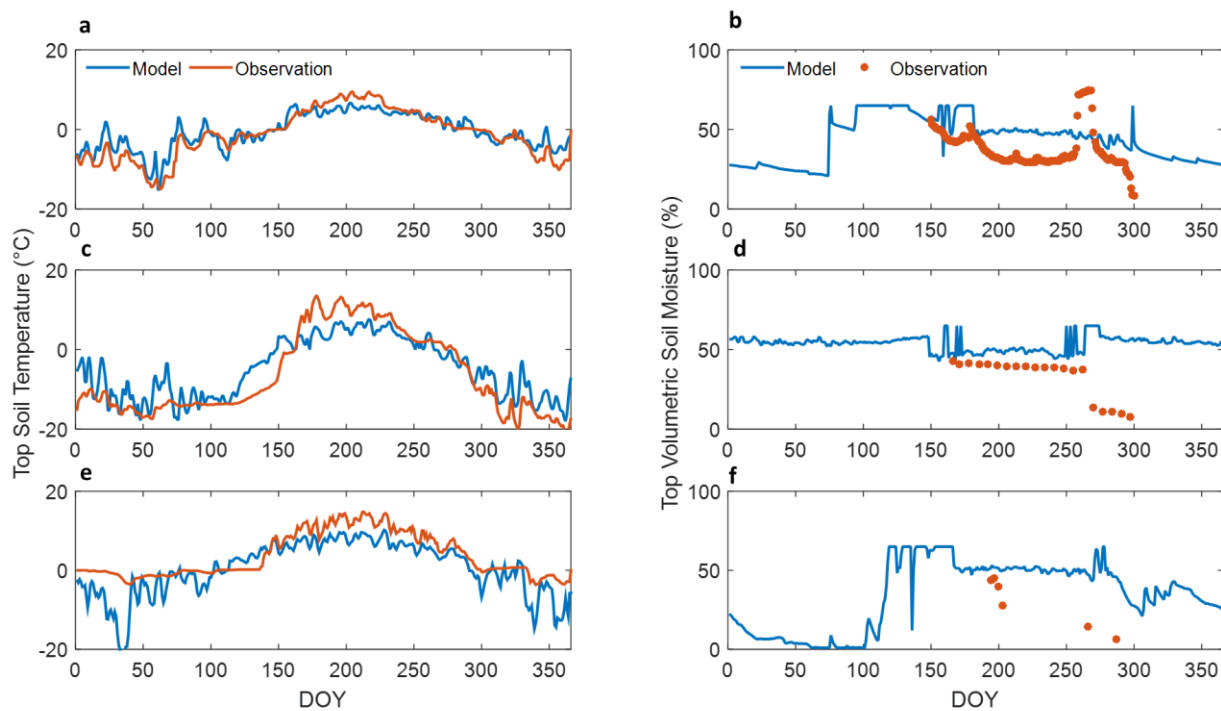


Figure 2.6 Model-data comparison of top soil temperature and moisture. (a,c, and e) daily top 10-cm soil temperature in °C and (b, d, and f) daily top 10-cm volumetric soil moisture in % volume for (a,b) alpine tundra in 2013, (c,d) wet tundra in 2012, and (e,f) boreal forest in 2012.

2.3.3 Simulation for the contemporary period

Setup

To make spatially- and temporally-varying estimates of methane emission and consumption in the Arctic, we used spatially explicit data of land cover, soil pH and textures, meteorology and leaf area index (LAI) (Zhuang et al. 2004). The vegetation and soil texture data sets were used to assign vegetation-specific and texture-specific parameters to a grid cell (Melillo et al. 1993; Zhuang et al. 2003). The soil-water pH data set was used to estimate methane production across the study region (Carter and Scholes 2000). Meteorological inputs were derived from historical air temperature, precipitation, vapor pressure, and cloudiness from gridded CRU time-series data, version 4.01 (Harris et al. 2014). We used monthly LAI data derived from satellite imagery (Myneni et al. 2002) to prescribe LAI for each 0.5° latitude and longitude grid cell. Lastly, for PTEM-HAM and XPTM-XHAM, we added the Northern Circumpolar Soil Carbon Database version 2 (NCSCDv2) to estimate permafrost SOC (Hugelius et al. 2013). Permafrost SOC of each 1-cm of soil layer depth was calculated using the NCSCDv2 data by dividing the permafrost SOC data of 1, 2, and 3m-depth equally to different depths.

The model was applied at the spatial resolution of 0.5° latitude by 0.5° longitude north of 50°N for both wetland and upland ecosystems with an hourly time-step for microbial dynamics and a daily time-step for other processes and modules during 2000-2016. A year of spin-up was used for methane equilibrium in soils for TEM and PTEM-HAM, and five years of spin up were used for biomass equilibrium in soils for XPTM-XHAM. Simulated ecosystem-specific methane emission from wetlands and consumption from uplands were then area weighted for each grid cell, as defined by the static fractional inundation data (Matthews, E., and Fung 1987).

Model-data comparison

i. Site-level

We compared our model results with data from 46 in-situ measurements organized by Emmerton et al. (2014) and Lau et al. (2015) (Table 2.6) (Emmerton et al. 2014; Lau et al. 2015). Specifically, Emmerton et al. (2014) summarized methane fluxes measured in high-, low- and sub-Arctic tundra for a portion of the northern growing season (May-October). Fluxes were organized by chamber and eddy covariance measurements and by terrestrial sites predominantly emitting or consuming methane. Lau et al. (2015) summarized methane emission and consumption in the

northern circumpolar permafrost region, organized by soil pH, moisture, temperature, SOC, and vegetation types for field measurements only. Due to a possible mismatch of soil and vegetation properties, and wetland distribution of grid cells between model and observation, we compared observed fluxes with simulated fluxes averaged over the growing season from 2000 to 2016 within two adjacent grid cells ($1^{\circ}\times 1^{\circ}$) of the observation.

ii. Regional-level

We compared model simulations of three regions with methane emission (Alaska, Hudson Bay Lowlands, West Siberian Lowlands) and two regions with consumption (Northeast and West Greenland) (Table 2.7). Regional estimates of methane consumption were calculated by extrapolating the measured consumption from fields to a regional level after considering the heterogeneity of land ecosystems (Juncher Jørgensen et al. 2015; D’Imperio et al. 2017). Regional estimates of methane emission of previous studies were calculated by combining field measurements with an atmospheric inversion (Bloom et al. 2010; Bohn et al. 2015; Miller et al. 2016).

iii. Pan-Arctic level

We compared the simulated net regional methane emission with results from a top-down inversion system, CarbonTracker-CH₄. CarbonTracker-CH₄ estimated anthropogenic and natural methane emission from 2000 through 2010 north of 50°N (Bruhwiler et al. 2014). To produce posterior flux estimates, CarbonTracker-CH₄ uses the ensemble Kalman smoother described by Peters et al. (2005) (Peters et al. 2005), and the TM5 transport model with driving meteorology from the European Centre for Medium-Range Weather Forecasting (ECMWF) (Krol et al. 2005). Air samples from 88 surface flask-air methane measurements from NOAA’s cooperative global air sampling and tall tower networks were used to constrain the flux estimates. Measurements of methane from flask-air samples collected from light aircraft were used to evaluate the inversion results.

Table 2.6 Summary table of in-situ wetland methane emission and upland methane consumption measured in the Arctic from Emmerton et al. (2014) (Emmerton et al. 2014) and Lau et al. (2015) (Lau et al. 2015).

Wetlands						
No	Location	Latitude (°)	Longitude (°)	Emission Flux (mg m⁻² day⁻¹)	Standard Deviation (mg m⁻² day⁻¹)	References
1	James Bay, CA	51.3	-80.3	34.0	18.0	Roulet et al., 1994, Moore et al., 1994
2	Hudson Bay lowlands, CA	53.0	-90.0	40.8	16.3	Picket-Heaps 2011
3	Schefferville, CA	54.5	-66.5	30.0	12.0	Bubier, 1995, Adamsen and King, 1993
4	Churchill, CA	58.5	-94.1	54.0	21.6	Roulet et al., 1994, Moore et al., 1994
5	Bethel, US	60.5	-161.5	58.0	28.0	Bartlett et al., 1992, Fan et al., 1992
6	Daring Lake, CA	64.5	-111.4	62.0	24.8	Wilson and Humphreys, 2012
7	Vorkuta, RU	67.2	63.4	44.0	39.0	Berestovakaya et al., 2005, Heikkinen et al., 2002a
8	Yamal, RU	68.1	71.4	58.0	23.2	Eheyer et al., 2002

Table 2.6 continued

9	Stordalen, SE	68.2	19.0	58.0	32.0	Oquiest and Svensson, 2002
10	Toolik, US	68.4	-149.4	41.5	36.5	King et al., 1998
11	Flakkerhuk, Disko Island, GL	69.0	-53.0	1.6	1.0	Johansen et al., 2011
12	Kaamanen, FI	69.1	27.2	48.5	20.0	Corradi et al., 2005
13	Cherskii, RU	69.4	161.2	223.0	58.0	Nakano et al., 2000
14	Indigirka, RU	70.5	147.3	83.0	20.0	Parmentier et al., 2011
15	Barrow, US	71.2	-156.4	37.0	7.3	Lara et al., 2012, Sturtevant et al., 2012
16	Tiski, RU	71.3	130.0	23.0	9.2	Nakano et al., 2000
17	Lena Delta, RU	72.2	126.3	20.5	10.5	Sachs et al., 2008
18	Northern RU	72.5	141.5	39.1	39.0	Christensen et al., 1995
19	Zackenberg Valley, GL	74.2	-21.0	26.5	5.5	Mastepanov 2008, Christensen 2000
20	Zackenberg, GL	74.3	-20.3	103.0	35.5	Strom et al., 2012

Table 2.6 continued

21	Alexandra Fjord, Ellesmere Island, CA	78.5	-75.6	1.5	6.4	Brummell et al., 2012
22	Ny-Ålesund, Svalbard	79.0	12.0	45.5	0.6	Adachi et al., 2006
23	Northern RU	72.5	141.5	39.0	39.0	Sachs et al., 2008
24	Alaska, US	69.0	-152.5	27.0	20.0	Morrissey and Livingston, 1992
25	Ellesmere I., CA	82.0	-71.2	0.7	0.5	Emmerton et al., 2014
26	Saskatchewan, CA	53.8	-104.6	189.2	34.7	Sellers et al., 1997
27	Manitoba, CA	55.9	-98.4	94.1	89.9	Seller et al., 1997
28	Poikovsky Bog, RU	56.9	82.9	173.9	157.7	Glagolev et al., 2011
29	Poikovsky Mire, RU	56.9	82.9	195.2	180.7	Glagolev et al., 2011
30	Khanty-Mansijsk, RU	60.9	68.7	78.6	47.1	Glagolev et al., 2011
Uplands						
No.	Location	Latitude	Longitude	Consumption Flux (mg m⁻² day⁻¹)	Standard Deviation (mg m⁻² day⁻¹)	References

Table 2.6 continued

1	Moscow, Puschino	54.5	37.37	0.31	0.1	Kizilova et al., 2013
2	Lipetsk, Danki	54.0	37.31	0.48	0.18	Kizilova et al., 2013
3	Schefferville, CA	54.5	-66.5	3.0	1.2	Bubier, 1995
4	Bonanza Creek, Alaska, US	64.5	-148.2	0.2	0.2	Whalen et al., 1992
5	Stordalen, SE	68.2	19.0	3.0	2.0	Jackowicz- Korczynski et al., 2010
6	Flakkerhuk, Disko Island, GL	69.0	-53.0	0.6	0.5	Johansen et al., 2011
7	Lena River Delta, RU	72.2	126.3	1.7	0.7	Liebner et al., 2011
8	Zackenberg Valley, GL	74.2	-21.0	0.02	0.01	Christensen 2000, Christensen 2012
9	Zackenberg, GL	74.3	-20.3	0.3	0.1	Ström et al., 2012
10	Okse Bay, Ellesmere Island, CA	77.8	-87.4	0.9	0.8	Brummell et al., 2014
11	Alexandra Fjord, Ellesmere Island, CA	78.5	-75.5	4.5	2.0	Brummell et al., 2012

Table 2.6 continued

12	Ny-Ålesund, Svalbard	79.0	12.0	2.4	1.7	Adachi et al., 2006
13	Expedition Fjord, Axel Heiberg Island, CA	79.2	-90.5	0.2	0.0	Allan 2014, Stackhouse 2016, Lau 2016
14	Patterson River, Ellesmere Island, CA	82.4	-63.5	0.2	0.0	Brummell et al., 2014
15	Ellesmere I., CA	80.0	-69.0	0.6	0.2	Lamb et al., 2011, Stewart et al., 2012
16	Ellesmere I., CA	82.0	-71.2	1.4	0.6	Emmerton et al., 2014

Table 2.7 Summary table of observed regional estimation of net methane flux.

Region	Latitude	Longitude	Net methane flux (TgCH₄yr⁻¹)	Methods	References
Upland					
NE Greenland	74 to 81	-30 to -15	1.3×10^{-3}	Field Study	Jørgensen et al., 2015
W Greenland	69 to 70	-52 to -55	15×10^{-9}	Field Study	D’Imperio et al., 2016
Wetland					
Hudson Bay Lowland	47 to 60	-100 to -80	3.5 – 6.5	Field Study and Inversion	Bloom et al., 2010
West Siberia	54 to 70	65 to 85	4.8 – 7.2	Field Study and Inversion	Bohn et al., 2015
Alaska	50 to 75	-160 to -120	1.48 – 2.0	Field Study and Inversion	Miller et al., 2016

Sensitivity test for XPTM-XHAM of contemporary period

We varied a transient wetland distribution using satellite-driven Surface Water Microwave Product Series- Global Lakes and Wetlands Database (SWAMPS-GLWD) during 2000-2012 for our sensitivity test (Poulter et al. 2017). We also conducted 8 sensitivity tests of wetland emission and 6 tests of upland consumption to changes in meteorology and substrate inputs. Specifically, we altered air temperature by $\pm 3^{\circ}\text{C}$, water table depth by ± 30 cm, and soil moisture, atmospheric methane abundance, permafrost SOC, and NPP by $\pm 30\%$, uniformly for each grid cell, while maintaining all other variables at their default XPTM-XHAM values.

Examples of seasonal changes in $MIC_{biomass}$ in soil columns

Figure 2.7 shows an example of seasonal changes in $MIC_{biomass}$ in wetland and upland systems at four soil depths. The simulated $MIC_{biomass}$ of MG and HAM are in a reasonable range of previous studies (Conrad 2007). The seasonal maximum of $MIC_{biomass}$ of MG and HAM are one to two months lagged behind the maximum of soil temperature (figure 2.7a), which extends the period of methane emission and consumption.

In a wetland system, $MIC_{biomass}$ of MG is higher at 50 and 100 cm depths (supplementary figure 6a), where the combined effects of soil temperature, moisture, pH, redox potential, and organic matter contents are optimal for methanogen (equation 2.14a). In an upland system, $MIC_{biomass}$ of HAM is highest at 10 cm depth and is negligible at 50, 100, and 200 cm depths due to the substrate depletion in deeper soils (figure 2.7b). The main energy source of HAM – methane and oxygen, mainly comes from the atmosphere, which reduces in concentration with depth as a result of diffusivity. The $MIC_{biomass}$ of HAM at deeper soils are thus negligible because most atmospheric methane is consumed by HAM at top soil layers (equation 2.14b).

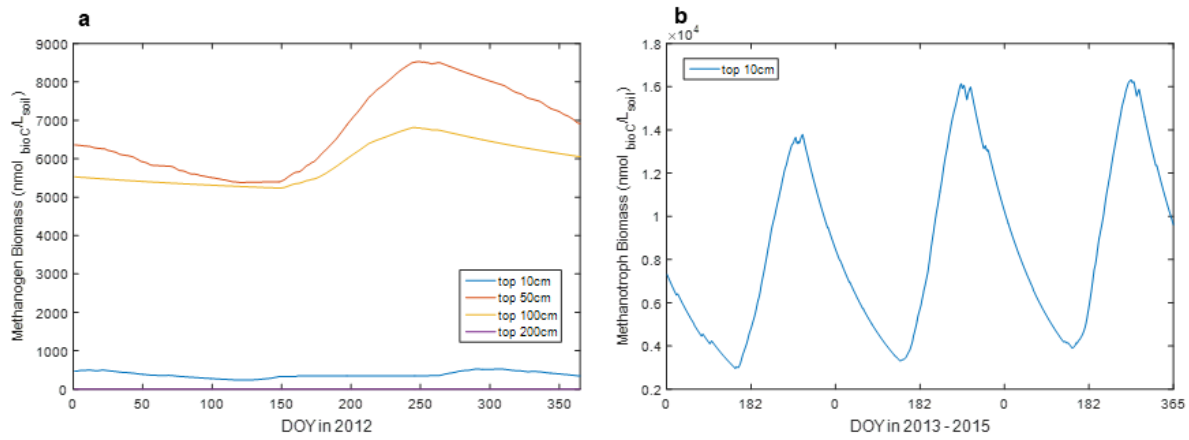


Figure 2.7 Seasonality of active microbial biomass for four soil depths. Changes in active microbial biomass ($\text{nmol}_{\text{bioC}} \text{L}_{\text{soil}}^{-1}$) of (a) methanogens in wetlands in a boreal forest in 2012 (Sellers et al. 1997) and (b) HAM in uplands in a dry tundra in 2013-2015 (D’Imperio et al. 2017) at 10, 50, 100, and 200 cm soil depths.

2.3.4 Simulation for future projection

Setup

From 2017 to 2100, we used the Intergovernmental Panel on Climate Change (IPCC) future climate scenarios from Representative Concentration Pathways (RCPs) climate forcing data sets, RCP 2.6, RCP 4.5, and RCP 8.5. RCPs 2.6, 4.5 and 8.5 are climate projections with a possible range of radiative forcing values of 2.6, 4.5 and 8.5 W m^{-2} , respectively, in the year 2100 (Meinshausen et al. 2011). Since RCP data sets did not provide water vapor pressure data, we used the specific humidity and sea level air pressure from the RCP data sets and elevation of surface to estimate the monthly surface vapor pressure (Seinfeld et al. 1998). Under those scenarios, the global climate was simulated with Hadley Centre Coupled Model version 3 at a 0.5° spatial resolution. Transient atmospheric methane data were obtained by linearly interpolating the decadal data for these future projections. Spatial data of vegetation, soil texture, soil pH, and LAI used in the 21st century were the same as in the simulation for the contemporary period. Models were then applied at a spatial resolution of 0.5° latitude by 0.5° longitude north of 50°N for both wetland and upland ecosystems from 2017 to 2100. Our simulation showed the largest increase in soil temperature and moisture for RCP 8.5 followed by RCP 4.5 and 2.6, but the soil moisture increase was not distinct (Figure 2.8).

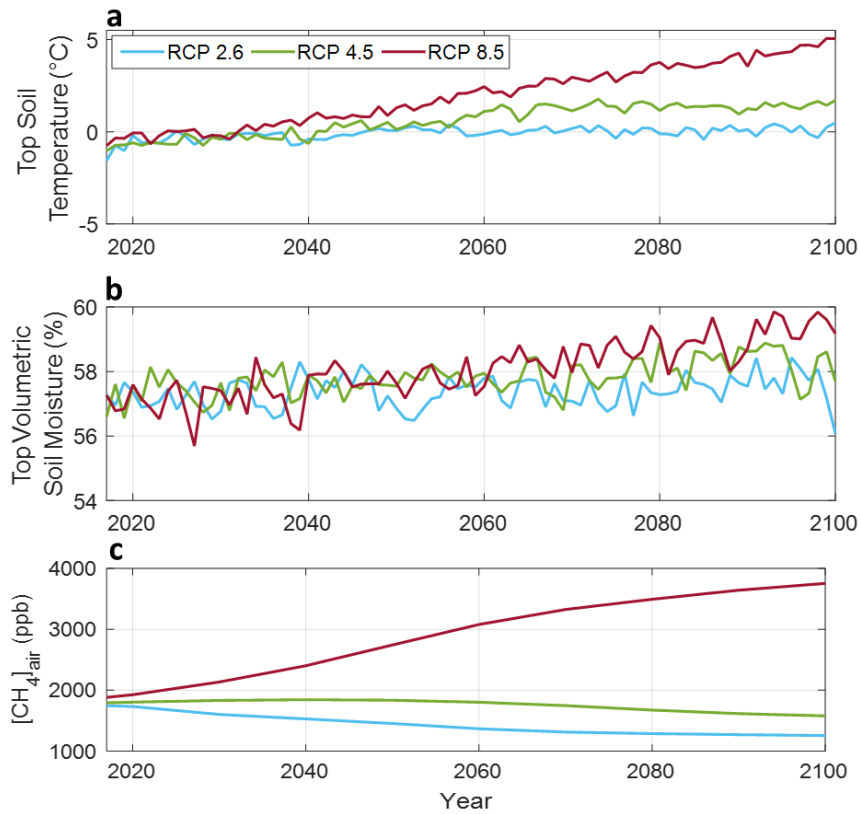


Figure 2.8 Inter-annual variability of soil temperature and moisture and atmospheric methane abundance during 2017 – 2100. Annual averaged estimates of pan-arctic (a) top 10-cm soil temperature in °C, (b) top 10-cm soil moisture in % volume, and (c) atmospheric methane abundance ($[\text{CH}_4]_{\text{air}}$) in ppb using RCP 2.6 (sky blue), RCP 4.5 (green), and RCP 8.5 (dark red) north of 50°N.

Microbial physiology

To elucidate effects of microbial physiological responses of MG and HAM to temperature increase, we conducted sensitivity tests by setting m_E as a function of temperature in Equation 2.19.

Sensitivity test for XPTM-XHAM for future projections

We used a static inundation map for our default simulation (Matthews, E., and Fung 1987) but applied the transient wetland inundation fraction data by setting the initial inundation fraction same as SWAMPS-GLWD but varying the seasonal and inter-annual fraction of each grid cell using normalized changes in the fraction simulated by the CLM 5.0 SSP3-7 deforestation scenario for a sensitivity test (Lawrence et al. 2018).

We acknowledge that different model structures and temperature sensitivity among models may cause potential biases in the projected methane emission as temperature increase (Xu et al. 2016). Thus, we used various Q_{10} of methanogenesis and methanotrophy for our sensitivity test of XPTM-XHAM for RCP 8.5 scenarios. We referred the temperature sensitivity test of CLM4Me (Riley et al. 2011) and varied the Q_{10} of methane production to 2, 3, and 4 with reference temperature of 3 °C for low, medium, and high setups, respectively. The Q_{10} of methane oxidation varied to 1, 2, and 3 with reference temperature of 5°C for low, medium, and high setups, respectively, which is smaller than Q_{10} of methane production but still is in a range of observation (Lau et al. 2015). Furthermore, to clarify the effect of projected increase in $[\text{CH}_4]_{\text{atm}}$ from 1.8 to 3.8 ppm for RCP 8.5 scenario (Figure 2.8), we conducted additional simulation where we keep $[\text{CH}_4]_{\text{atm}}$ to be same as the contemporary level, 1.8 ppm.

Importance of Microbial dynamics of LAM

We first need to acknowledge the limitation of observation data to optimize methane processes in wetlands. Most bottom-up methane models, including ours, use observed net wetland methane emissions to optimize methane production by MG and oxidation by LAM where the fraction of each is uncertain (Xu et al. 2016). Since methane oxidation by LAM is highly dependent on methane emission by MG due to its requirement of high methane concentrations (> 600ppm) for survival and growth (Baani and Liesack 2008), we assume that the observed net wetland methane emissions are mainly controlled by microbial dynamics of MG.

However, to clarify the role of LAM in wetland methane emission for both contemporary period and future projection, we ran additional simulations by adding microbial dynamics of LAM into XPTEM-XHAM. In specific, the methane oxidation and microbial biomass changes for LAM were simulated using Equations 2.13b and 2.14b but we set the Michaelis-Menten constant (k_{CH_4}) for LAM to be 5 μM (Equation 2.5), instead of 0.11 μM for HAM (Equation 2.9). For LAM physiology, microbial growth efficiency (ϵ) of LAM is set to be 0.5, same as HAM, and maintenance energy (m_E) exponentially increases, same as MG and HAM (Equation 2.19) (Trimmer et al. 2015; Tjihuis et al. 1993).

The results show that simulations with microbial dynamics of LAM for contemporary period in 2000-2016 are within the uncertainty range of the simulations without LAM microbial dynamics, reflecting the minor role of LAM $MIC_{biomass}$ in current wetland methane emissions (Figure 2.9a). For with and without physiology simulations of RCP 8.5 scenario, the wetland methane emissions may decrease by $\sim 5 \text{ Tgyr}^{-1}$ by 2100 after LAM microbial dynamics are included, although the difference is within the uncertainty ranges (Figure 2.9b). Thus, LAM microbial dynamics have a limited contribution to current wetland methane dynamics but may have a potential to decrease wetland emissions due to its increase in $MIC_{biomass}$ in a warmer Arctic.

To better constrain the methane pathways in Arctic wetlands, more observations of subsurface vertical processes using isotopic labeling analysis and inhibitor techniques are necessary (Pedersen et al. 2018). The future study shall factor the effects of diverse vertical methane pathways, including LAM microbial dynamics and physiology, when more data are available.

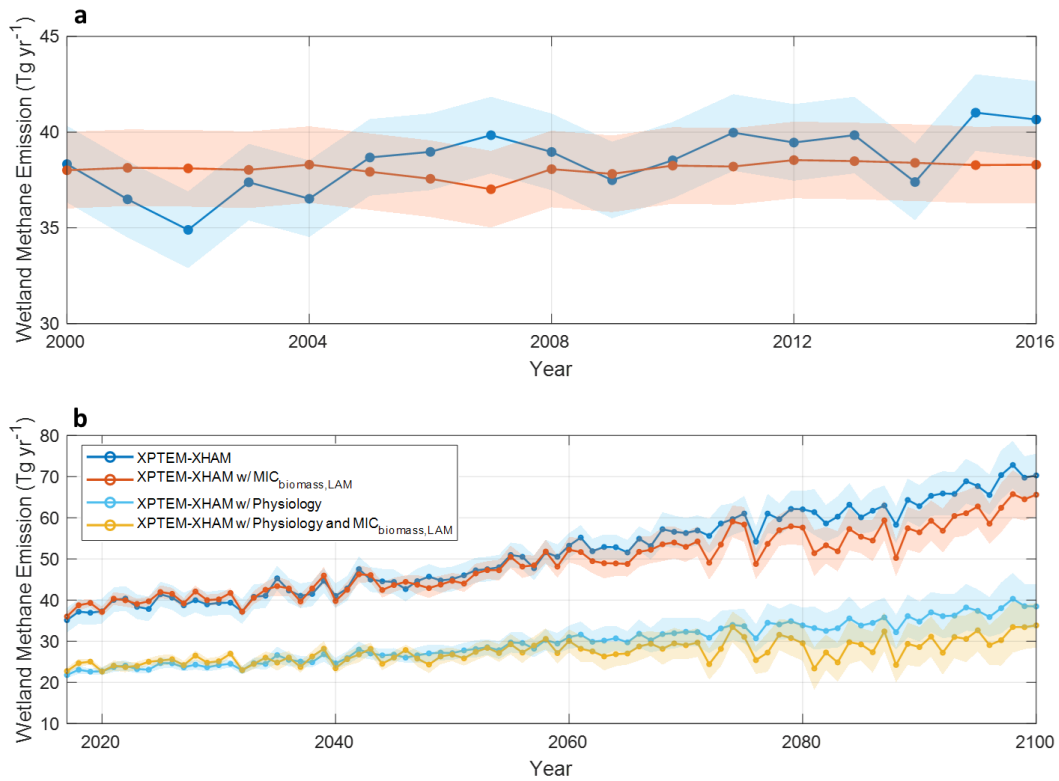


Figure 2.9 Effects of microbial dynamics of LAM to wetland methane emission for contemporary period and RCP 8.5 during 2017-2100 north of 50°N. Annual estimates of pan-Arctic net methane emission for XPTEM-XHAM for (a) contemporary period in 2000-2016 (b) RCP 8.5 scenario in 2017-2100 without varying m_E (blue), XPTEM-XHAM with physiological responses of MG and HAM to temperature change (skyblue), and sensitivity tests of varying microbial dynamics of LAM (red and yellow represent with and without varying m_E , respectively). The shaded error bars represent one standard deviation of model results determined by varying the optimized parameters from ensemble simulations.

2.4 Results

Our simulations during 2000-2016 show the effects of permafrost SOC and microbial dynamics on wetland methane emissions (Figures 2.10-15 and Table 2.8). Compared with PTEM-HAM, TEM estimates larger wetland methane emissions in the low-Arctic (37.70 vs. 26.83 $\text{TgCH}_4\text{yr}^{-1}$) but smaller emissions in the high-Arctic (3.73 vs. 6.76 $\text{TgCH}_4\text{yr}^{-1}$) (Fig. 2.10a). TEM simulates higher emissions in the low-Arctic as its parameterization on substrate depends on NPP only, which is higher in the low-Arctic (Figure 2.13c). For PTEM-HAM, methane emission is based on NPP and permafrost SOC, with more prevalent permafrost SOC in the high-Arctic (Extended Data

Figure 2.13d). Compared to PTEM-HAM, XPTEM-XHAM simulates larger methane wetland emissions in the low-Arctic (32.60 $\text{TgCH}_4\text{yr}^{-1}$) due to high $MIC_{biomass}$ of MG that persists late into the growing season, extending the period of methane emissions (Figure 2.11) (Segers 1998).

Comparing XPTEM-XHAM to TEM results, we more than double the upland methane sink by including microbially dynamic HAM (Figure 2.10b). TEM estimates upland sinks of 4.15 $\text{TgCH}_4\text{yr}^{-1}$ north of 50°N. After considering HAM and microbial dynamics, upland sinks for PTEM-HAM and XPTEM-XHAM increase to 6.14 and 9.52 $\text{TgCH}_4\text{yr}^{-1}$, respectively, consistent for both the low- and high-Arctic. This additional ~ 5.5 $\text{TgCH}_4\text{yr}^{-1}$ has not been accounted for in most current process-based methane models that do not consider microbial dynamics of HAM (McGuire et al. 2018; Koven et al. 2011; Lawrence et al. 2015).

By integrating wetland emission and upland consumption, net Arctic methane emission of XPTEM-XHAM and PTEM-HAM are closer to posterior fluxes estimated by an observation-based inversion, CarbonTracker-CH₄ (Figure 2.10c) (Bruhwiler et al. 2014). Starting with a prior estimate of 35 ± 10 $\text{TgCH}_4\text{yr}^{-1}$ for wetland emissions north of 50°N, CarbonTracker-CH₄ reduced net emission to 26 ± 5 $\text{TgCH}_4\text{yr}^{-1}$ during its optimization (Table 2.8). Our estimates of increased upland methane sinks are equivalent to at least half of the difference between prior and posterior estimates from the inversion (Bruhwiler et al. 2014; Saunio et al. 2016).

During 2000-2012, our XPTEM-XHAM sensitivity test using time-varying inundation data simulates less Arctic net methane emission due to smaller annual inundation fraction in SWAMPS-GLWD compared to the static map north of 50°N (Figure 2.16-17) (Matthews, E., and Fung 1987; Poulter et al. 2017). Additional sensitivity tests to meteorological and substrate changes show that

wetland emission is sensitive to temperature, NPP, permafrost SOC, and water table depth, and upland consumption is sensitive to temperature, soil moisture, and $[\text{CH}_4]_{\text{atm}}$ (Figure 2.18).

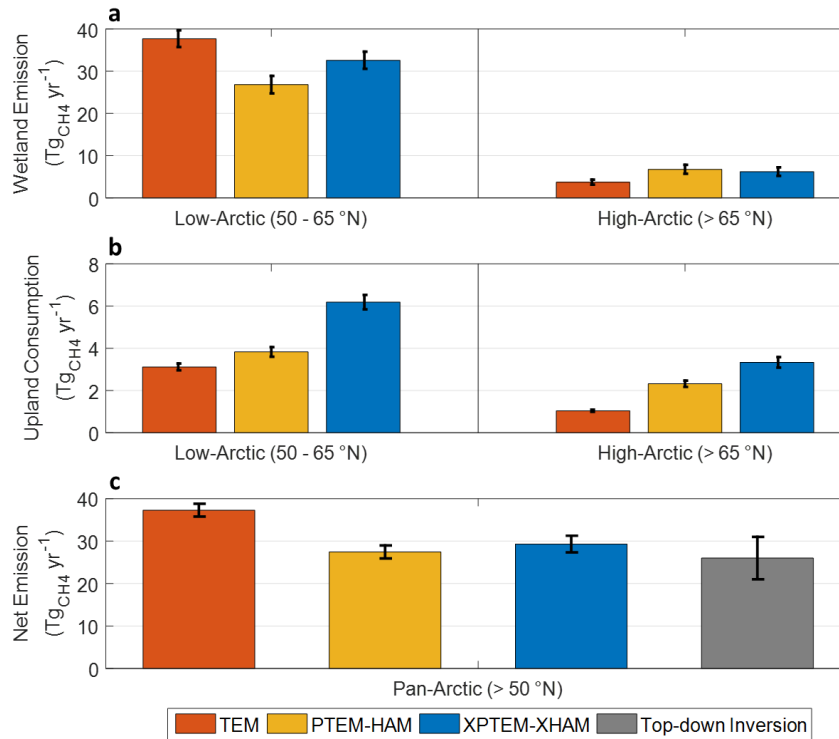


Figure 2.10 Annual estimates of the Arctic methane budget by three models for 2000-2016. Annual estimates of (a) wetland methane emission, (b) upland methane consumption, and (c) net methane emission in $\text{TgCH}_4\text{yr}^{-1}$ averaged over 2000-2016 for TEM (red), PTEM-HAM (yellow), and XPTEM-XHAM (blue) for the pan-Arctic region (north of 50°N), including the low-Arctic between $50\text{--}65^\circ\text{N}$ and high-Arctic north of 65°N . The error bars represent one standard deviation of TEM, PTEM-HAM, and XPTEM-XHAM determined by varying the optimized parameters from ensemble simulations. The top-down inversion in panel (c) (grey) represents posterior estimates of mean and one standard deviation of net wetland methane fluxes by CarbonTracker- CH_4 in 2000-2010.

Table 2.8 Annual mean wetland methane emission, upland methane consumption, and net methane emission ($\text{TgCH}_4\text{yr}^{-1}$) with one standard deviation in 2000 – 2016 for low-Arctic ($50\text{--}65^\circ\text{N}$), high-Arctic ($>65^\circ\text{N}$), and pan-Arctic ($>50^\circ\text{N}$) estimated by TEM, PTEM-HAM, and XPTEM-XHAM.

		Emission ($\text{TgCH}_4\text{yr}^{-1}$)	Consumption ($\text{TgCH}_4\text{yr}^{-1}$)	Net Emission ($\text{TgCH}_4\text{yr}^{-1}$)
TEM	Low-Arctic	37.70 ± 1.99	3.12 ± 0.16	34.58 ± 1.99
	High-Arctic	3.73 ± 0.60	1.04 ± 0.05	2.69 ± 0.60
	Pan-Arctic	41.43 ± 2.59	4.15 ± 0.21	37.27 ± 2.59
PTEM-HAM	Low-Arctic	26.83 ± 2.08	3.12 ± 0.23	23.00 ± 2.08
	High-Arctic	6.76 ± 1.05	1.04 ± 0.15	4.44 ± 1.05
	Pan-Arctic	33.59 ± 3.13	4.15 ± 0.38	27.44 ± 3.13
XPTEM-XHAM	Low-Arctic	32.60 ± 2.03	6.19 ± 0.34	26.41 ± 2.03
	High-Arctic	6.22 ± 1.00	3.33 ± 0.25	2.89 ± 1.00
	Pan-Arctic	38.82 ± 3.03	9.52 ± 0.59	29.3 ± 3.03

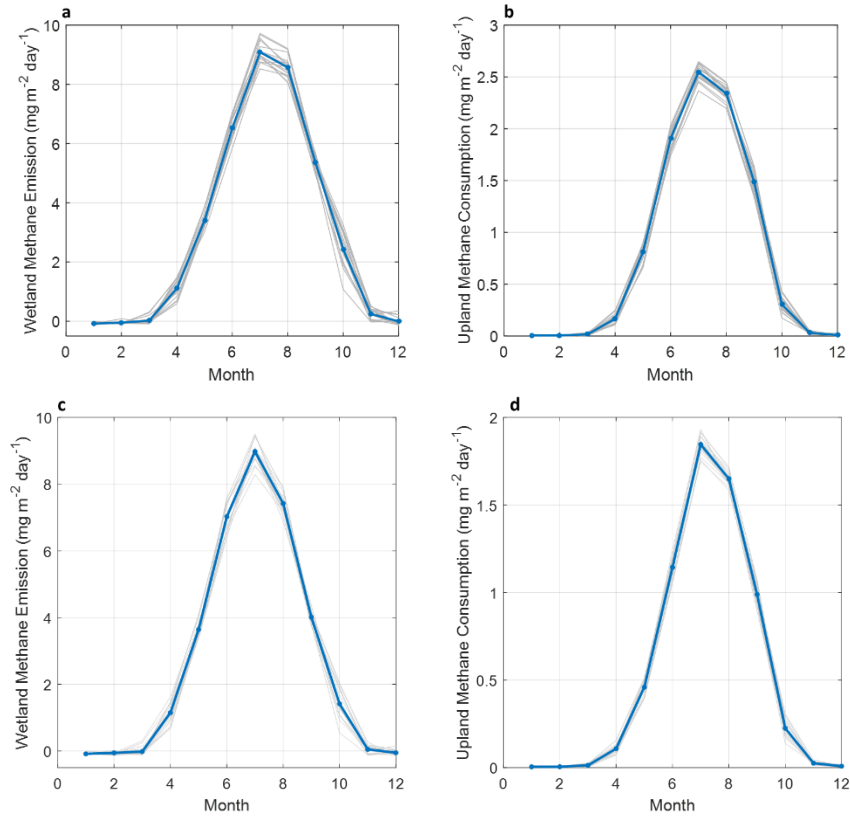


Figure 2.11 Pan-Arctic monthly mean methane fluxes for XPTM-XHAM and PTEM-HAM from 2000-2016 north of 50°N. Estimates of pan-arctic (a,c) monthly wetland methane emission and (b,d) monthly upland methane consumption in mg m⁻² day⁻¹ for (a,b) XPTM-XHAM and (c,d) PTEM-HAM model. The blue line is monthly averages over 2000-2016, and grey lines represent values of each year.

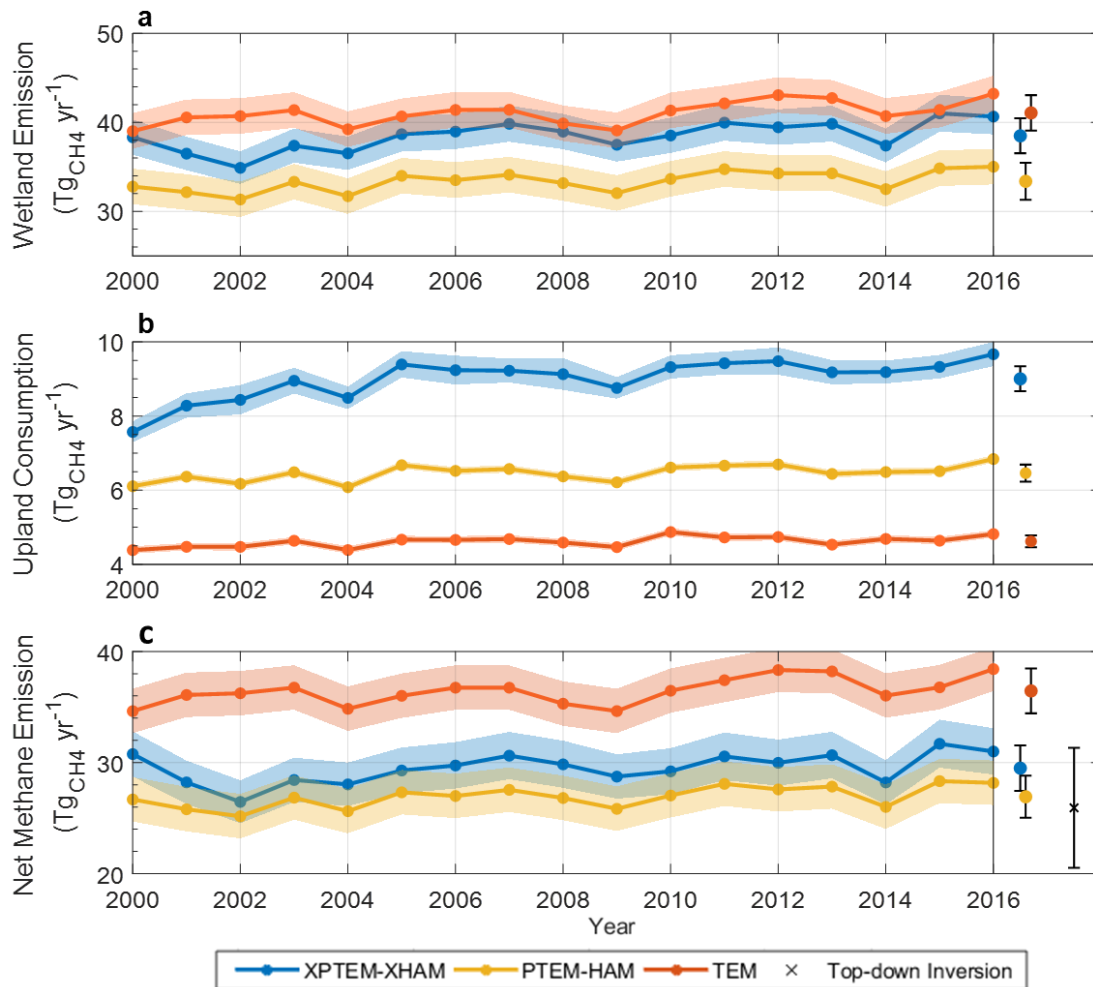


Figure 2.12 Inter-annual variability of methane fluxes from 2000 – 2016 north of 50°N. (Left) Annual estimates of pan-arctic (a) wetland methane emission, (b) upland methane consumption, and (c) net methane emission for XPTEM-XHAM (blue line), PTEM-HAM (yellow line), and TEM (red line) in TgCH₄yr⁻¹ from 2000-2016. The shaded area represents one standard deviation of models determined by varying the optimized parameters. (Right) Mean and one standard deviation averaged over the simulation period for each metric are given by the bars. Panel (c) additionally shows mean and one standard deviation of previous estimates of net methane emission estimated by top-down inversions (times symbol) by the bars.

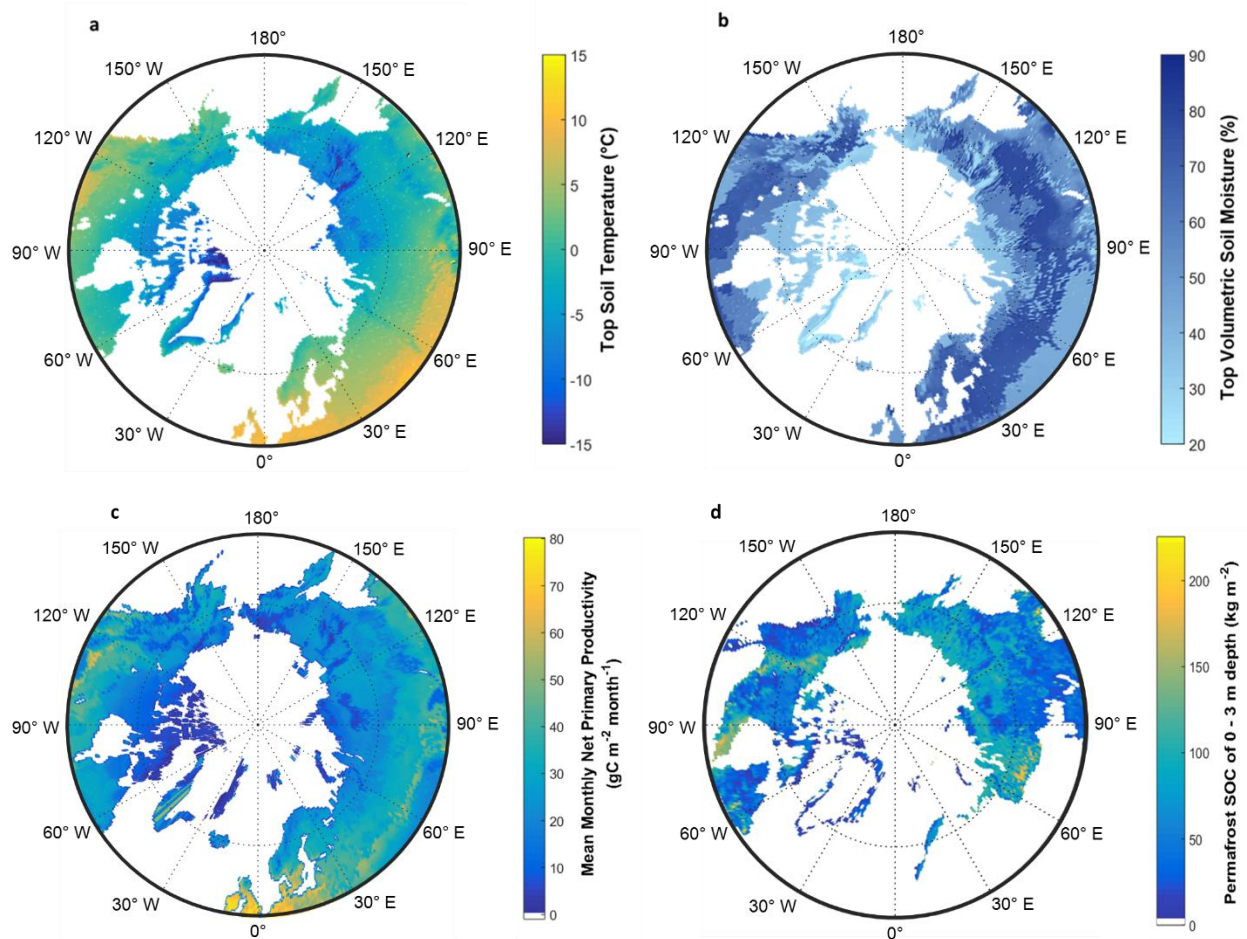


Figure 2.13 Spatial variability of soil and vegetation properties north of 50°N. (a) annual top 10-cm soil temperature in °C, (b) annual top 10-cm soil moisture in % volume, (c) monthly net primary productivity in $\text{gC m}^{-2} \text{ month}^{-1}$, and (d) permafrost SOC stored in the top 3-m in kg m^{-2} (Hugelius et al. 2013; Schuur et al. 2015). The soil temperature, moisture, and net primary productivity were averaged over the contemporary period during 2000-2016. The dotted longitudinal lines are at 30° intervals, and the latitudinal line is at 65°N.

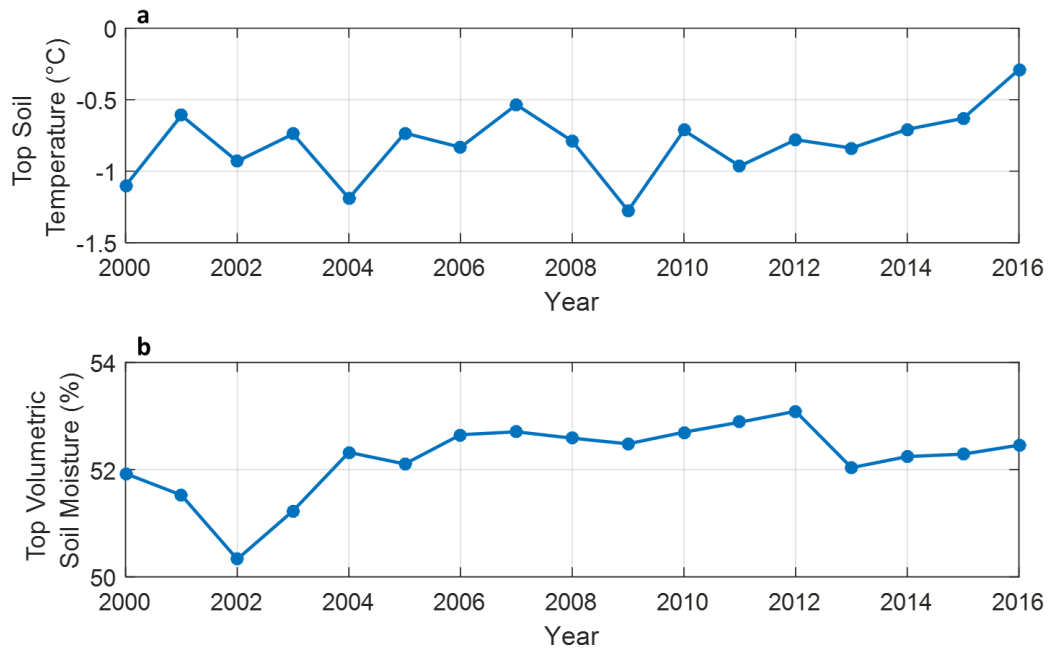


Figure 2.14 Inter-annual variability of top soil temperature and moisture. Estimates of pan-arctic (a) annual top 10-cm soil temperature in °C and (b) annual top 10-cm soil moisture in % volume for 2000-2016.

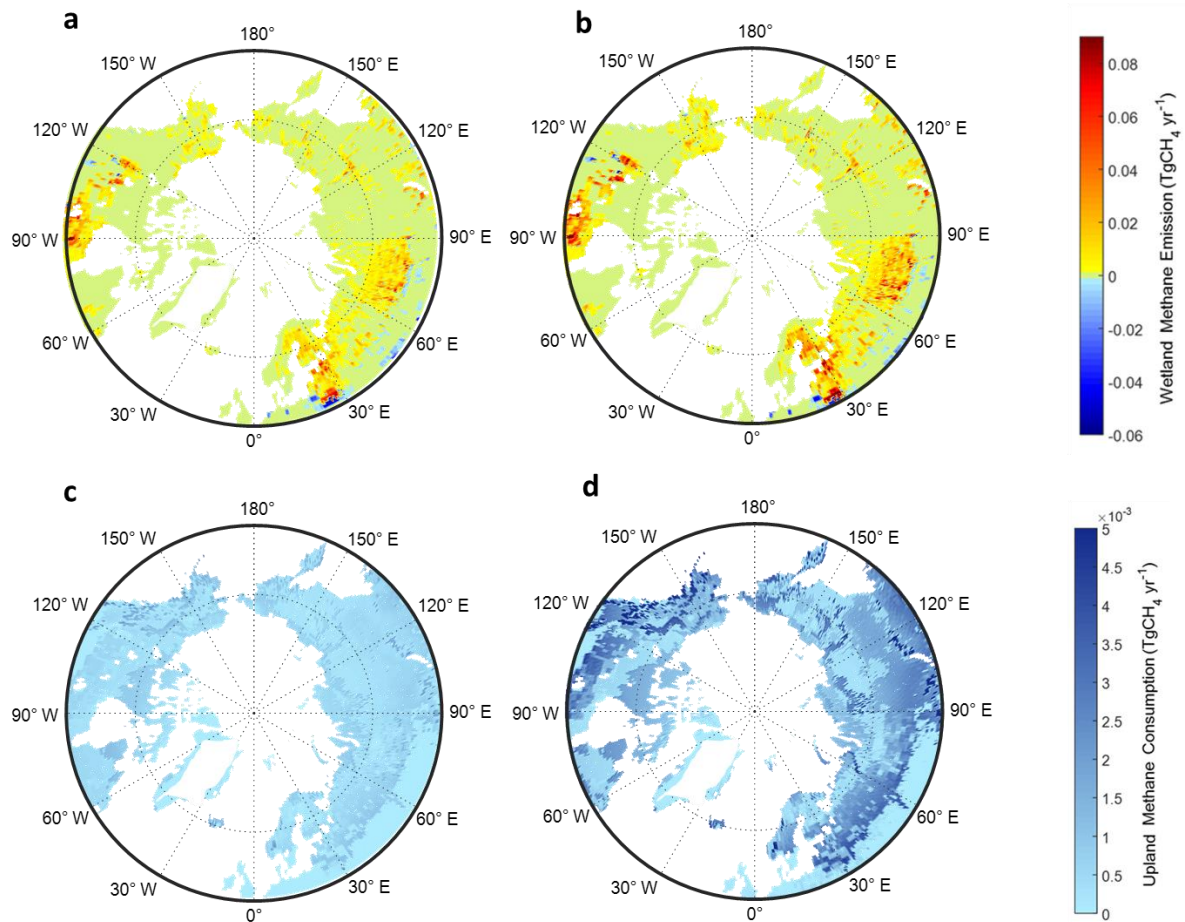


Figure 2.15 Spatial variability of methane fluxes north of 50°N. (a-b) Spatial variability of annual wetland methane emission ($\text{TgCH}_4\text{yr}^{-1}$) averaged over (a) 2000-2016 and (b) RCP 8.5 during 2017-2100 for XPTM-XHAM model. (c-d) Spatial variability of annual upland methane consumption averaged over (c) 2000-2016 and (d) RCP 8.5 during 2017-2100 north of 50°N for XPTM-XHAM model. The dotted longitudinal lines are at 30° intervals, and the latitudinal line is at 65°N.

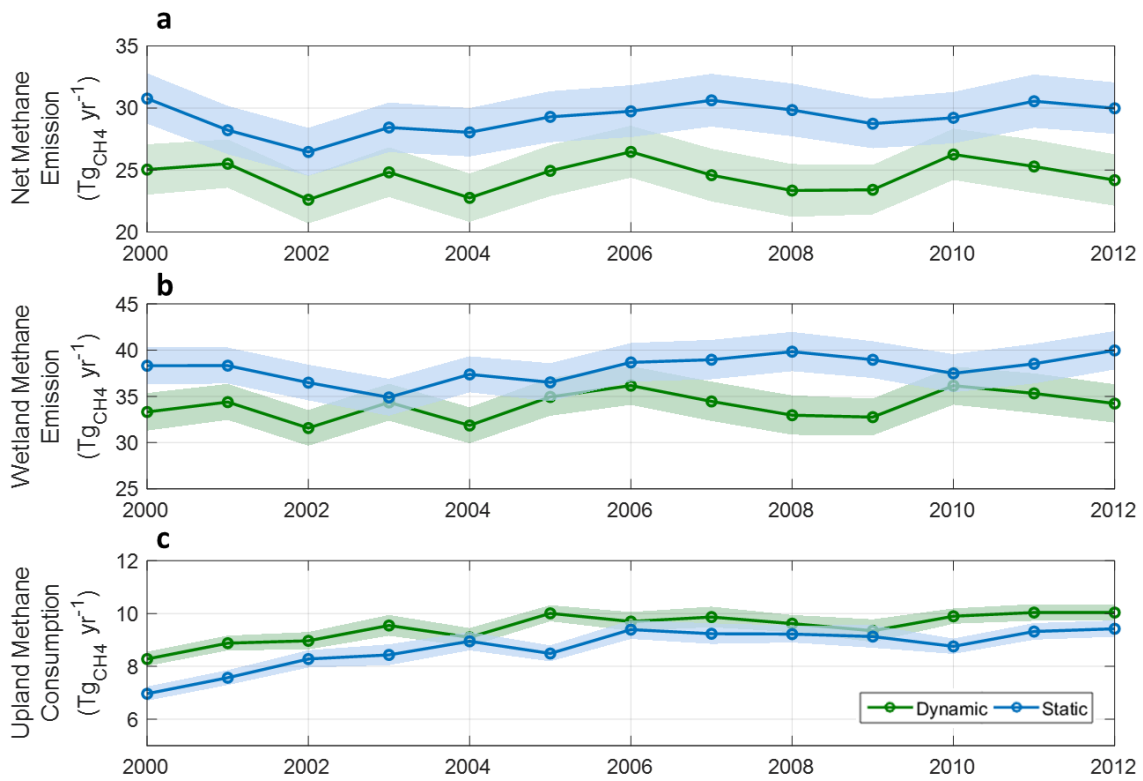


Figure 2.16 Inter-annual variability of methane fluxes using time-varying inundation fraction from 2000 – 2012 north of 50°N . Annual estimates of pan-arctic (a) net methane emission, (b) wetland methane emission, and (c) upland methane consumption for XPTM-XHAM model using static inundation fraction (Matthews, E., and Fung 1987) (blue) and time-varying inundation fraction from SWAMPS-GLWD (Poulter et al. 2017) (green) in $\text{Tg}_{\text{CH}_4}\text{yr}^{-1}$. The shaded area represents one standard deviation determined by varying the optimized parameters.

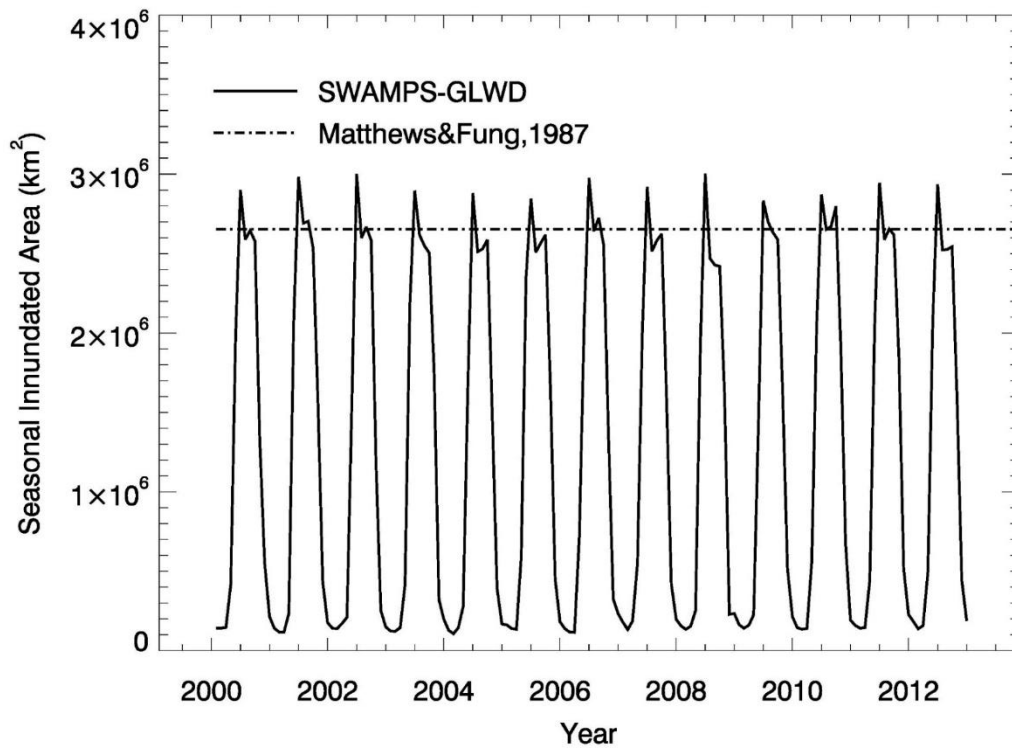


Figure 2.17 Monthly averaged time-varying and static inundated area north of 50°N. Monthly inundated area from time-varying (SWAMPTS-GLWD (Poulter et al. 2017)) and a static estimates (Matthews&Fung, 1987 (Matthews, E., and Fung 1987)) in km² from 2000 – 2012.

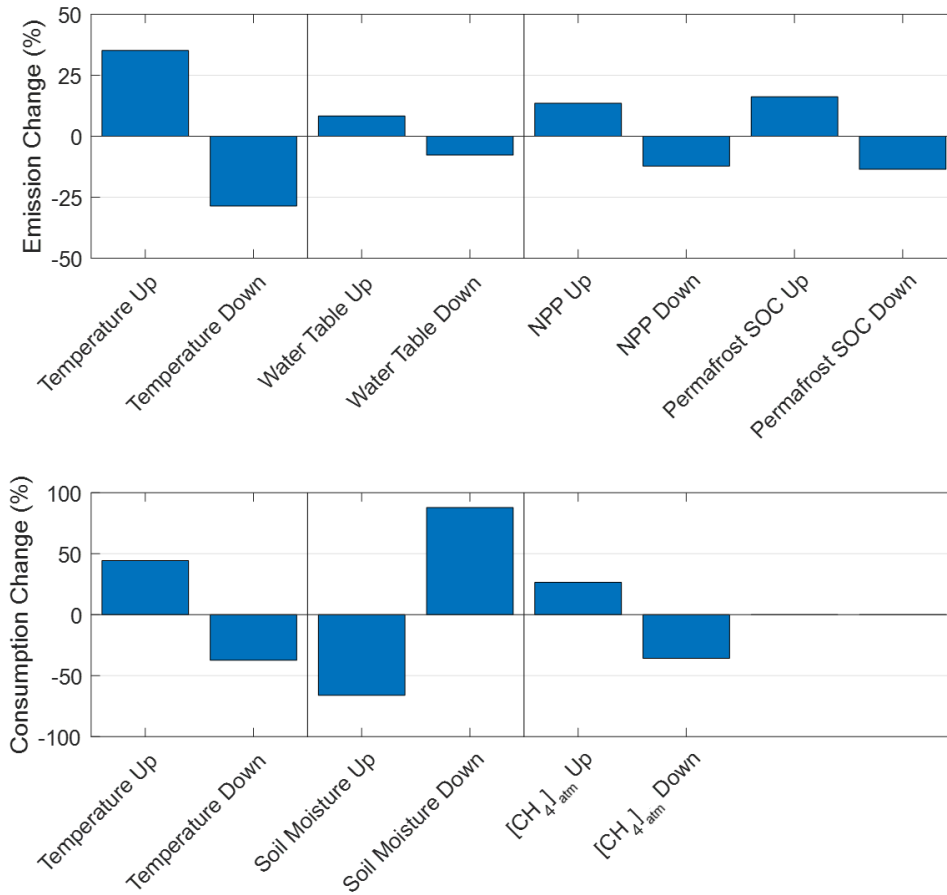


Figure 2.18 Sensitivity test of methane emission and consumption for XPTEM-XHAM. (a) Changes in pan-arctic wetland methane emission relative to a default simulation after varying temperature, water table, NPP, and permafrost SOC. (b) Changes in pan-arctic upland methane consumption relative to a default simulation after varying temperature, soil moisture, and atmospheric methane abundance ($[CH_4]_{atm}$).

We validated the magnitude and spatial variability of three models using site-level and regional observations. In-situ measurements from 46 flux observation sites confirm that XPTEM-XHAM reproduces both methane emission and consumption (R^2 of 0.65 and 0.87 and RMSE of 38.21 and 0.52 $\text{mgm}^{-2}\text{day}^{-1}$ for emission and consumption, respectively) (Figure 2.20) (Lau et al. 2015; Emmerton et al. 2014). Compared to XPTEM-XHAM, RMSEs in PTEM-HAM and TEM were 10% and 60% larger, respectively, on average for all sites. We also compared observed and simulated regional net methane emission for three regions for methane emission (Alaska, Hudson Bay Lowlands, West Siberian Lowlands) and two for consumption (Northeast and West Greenland) (Figure 2.19 and Table 2.9) (D’Imperio et al. 2017; Juncher Jørgensen et al. 2015; Bloom et al. 2010; Bohn et al. 2015; Miller et al. 2016). XPTEM-XHAM generally matched emission estimates for the West Siberian Lowlands and consumption in upland West Greenland, whereas PTEM-XHAM and TEM agreed poorly. All three models estimate less methane emissions from Alaska than observed (Miller et al. 2016), possibly because we did not consider methane emissions from aquatic sources such as thermokarst lakes (Sepulveda-Jauregui et al. 2015).

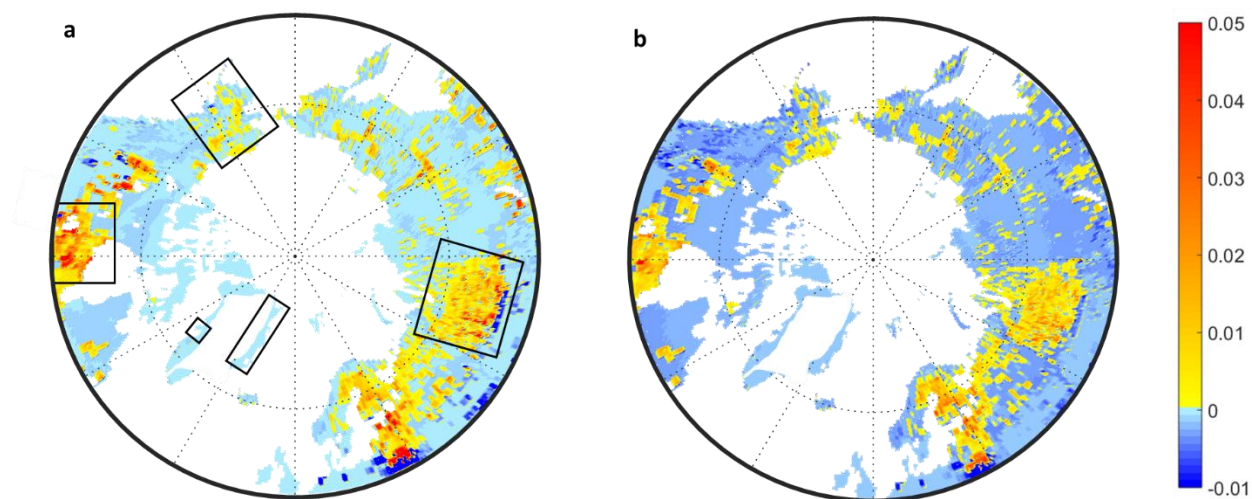


Figure 2.19 Spatial variability of annual net methane flux north of 50°N for XPTEM-XHAM. The net methane fluxes are in $\text{TgCH}_4\text{yr}^{-1}$, positive for emission and negative for consumption, (a) averaged for the contemporary period during 2000-2016, and (b) difference between 2086-2100 for RCP 8.5 and 2000-2016. The dotted longitudes are at 30° intervals, and the dotted latitude is at 65°N . Panel (a) additionally shows five regions in black boxes used for regional model-data comparisons.

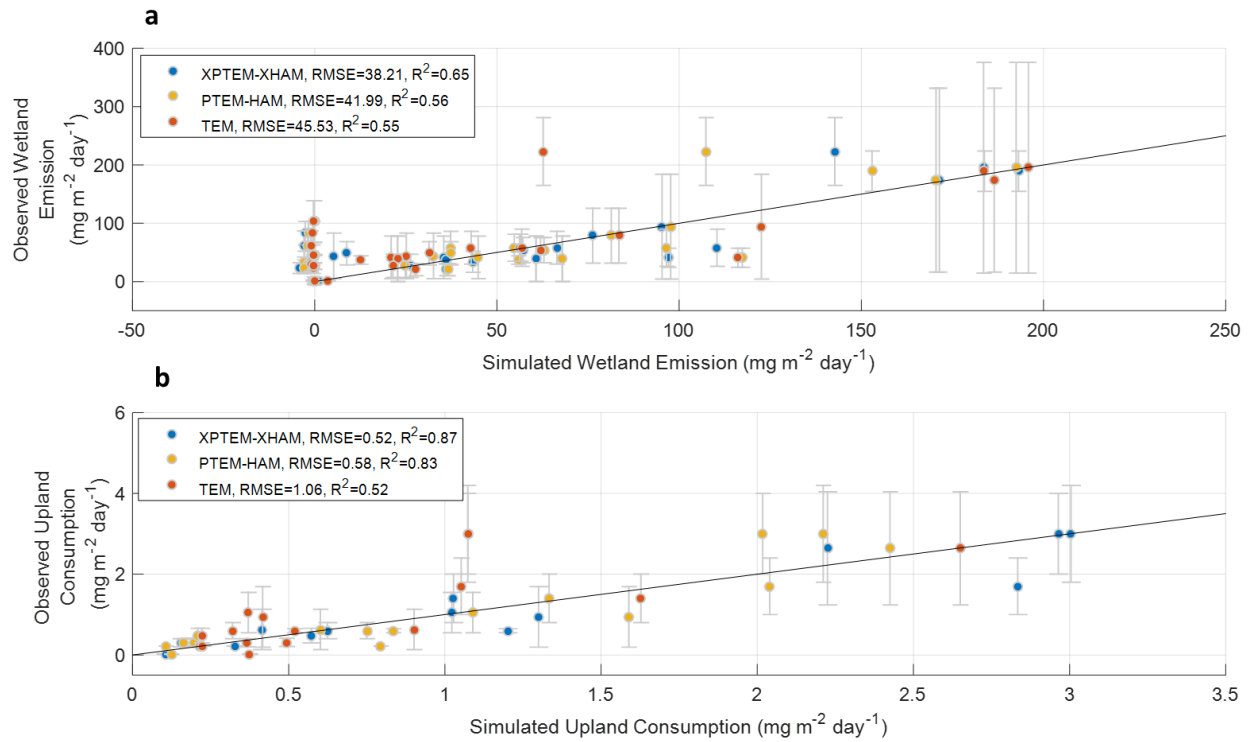


Figure 2.20 Model-data comparison of methane fluxes using site-level data. Comparison of (a) wetland methane emission and (b) upland methane consumption of data from 46 in-situ measurements (supplementary table 5) with simulation results from XPTEM-XHAM (blue), PTEM-HAM (yellow), and TEM (red).

Table 2.9 Model-data comparison of regional estimation of net methane flux with one standard deviation ($\text{TgCH}_4\text{yr}^{-1}$).

		Observation	XPTM-XHAM	PTEM-HAM	TEM
Upland					
1	NE Greenland	1.3×10^{-3}	1.0×10^{-3}	1.1×10^{-3}	0.2×10^{-3}
2	W Greenland	15×10^{-9}	13.5×10^{-9}	7.5×10^{-9}	7.5×10^{-9}
Wetland					
3	Hudson Bay Lowland	3.5 – 6.5	4.72 ± 0.21	3.97 ± 0.22	4.23 ± 0.20
4	West Siberia	4.8 – 7.2	6.69 ± 0.34	7.46 ± 0.22	8.03 ± 0.25
5	Alaska	1.48 – 2.0	0.88 ± 0.06	1.18 ± 0.03	0.66 ± 0.02

Our future simulation shows that both PTEM-HAM and XPTEM-XHAM project 70 and 100% increase in wetland methane emissions by 2100 for RCP 8.5, respectively, due to increased temperature and more accessible permafrost SOC (Figure 2.19 and 2.21a, and 2.22). This increase is larger than the 59% increase predicted by TEM. However, the increase in wetland emission is mostly compensated by an increase in upland consumption by 2100 (22 and 35 TgCH₄yr⁻¹ for PTEM-HAM and XPTEM-XHAM, respectively) due to increased HAM activity at increased temperature and [CH₄]_{atm} (Figure 2.23). This leads to a reduced increase in net methane emission by 2100 for XPTEM-XHAM and PTEM-HAM (35 TgCH₄yr⁻¹) than TEM (55 TgCH₄yr⁻¹) and other previous projections (40 to 120 TgCH₄yr⁻¹) (Schuur et al. 2013; Lawrence et al. 2015; Koven et al. 2011). The net methane emission increase is less for RCP 2.6 and 4.5 than for RCP 8.5 in all three models (Figure 2.21).

Furthermore, our simulation of XPTEM-XHAM with microbial physiology of MG and HAM shows that net Arctic methane emission can potentially decrease in the future (Figure 2.21b and 2.24). Increases in both methane production and oxidation are limited by decreases in *MIC_{biomass}* growth for MG and HAM, respectively, due to an exponential increase in *m_E* (equation 2.19) (Hagerty et al. 2014; Tjihuis et al. 1993). As *m_E* increases with temperature, growth in *MIC_{biomass}* slows more substantially for MG, because the ϵ of MG (0.05) is a factor of 10 smaller than the ϵ of HAM (0.5) (Von Stockar and Liu 1999; Trimmer et al. 2015). As a result, in our simulation, HAM survive better in the warmer Arctic due to their physiological response.

Our sensitivity test of XPTEM-XHAM using time-varying inundation simulated by CLM 5.0 does not change the projection significantly as the simulated inundation fraction increases only 5% between 2017-2100 (Figure 2.26) (Lawrence et al. 2018). XPTEM-XHAM also shows a sensitivity of net methane emissions to both temperature (5 TgCH₄yr⁻¹) and [CH₄]_{atm} (10 TgCH₄yr⁻¹) by 2100 for RCP 8.5 scenario (Figure 2.25).

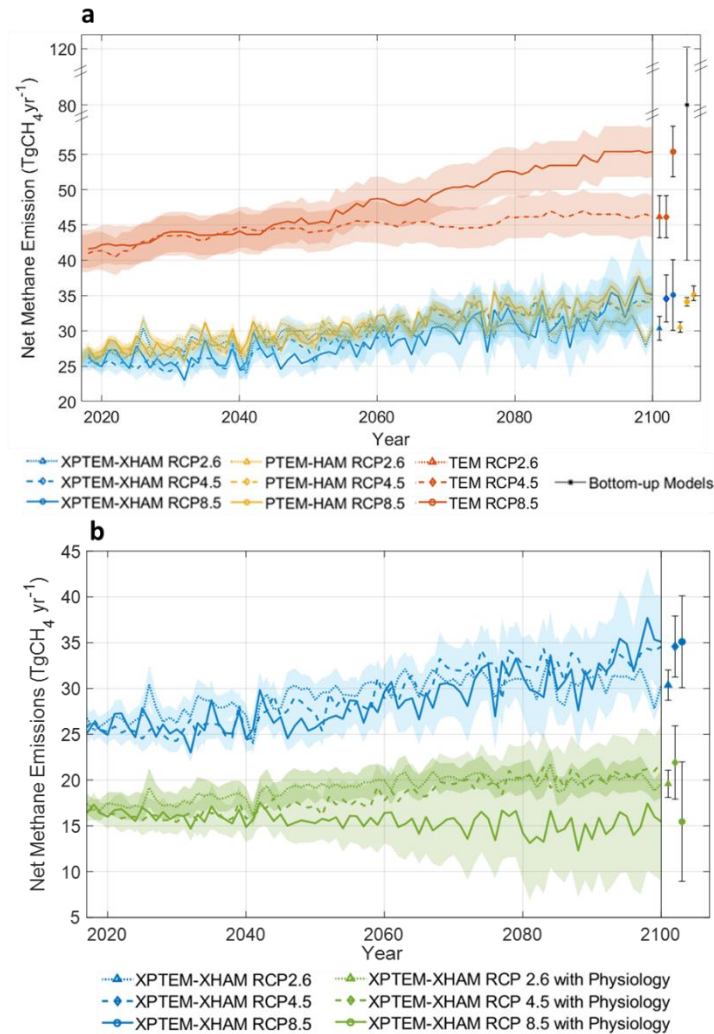


Figure 2.21 Projected annual net Arctic methane emissions from 2016 to 2100. (Left) Annual estimates of pan-arctic net methane emission for (a) XPTEM-XHAM without varying m_E (baseline, blue), PTEM-HAM (yellow), and TEM (red), and (b) XPTEM-XHAM baseline (blue; same as in (a)), XPTEM-XHAM with physiological responses of MG and HAM to temperature change (green) based on RCP 2.6 (dotted), RCP 4.5 (dashed), and RCP 8.5 (solid). The shaded error bars represent one standard deviation of TEM, PTEM-HAM, and XPTEM-XHAM determined by varying the optimized parameters from ensemble simulations. (Right) Mean (symbols) and one standard deviation (bars) in 2100 for each metric. Panel (a) additionally shows mean (*) and one standard deviation (bars) of previous estimates of net methane emission estimated by process-based methane models (Lawrence et al. 2015; Koven et al. 2011; Schuur et al. 2013).

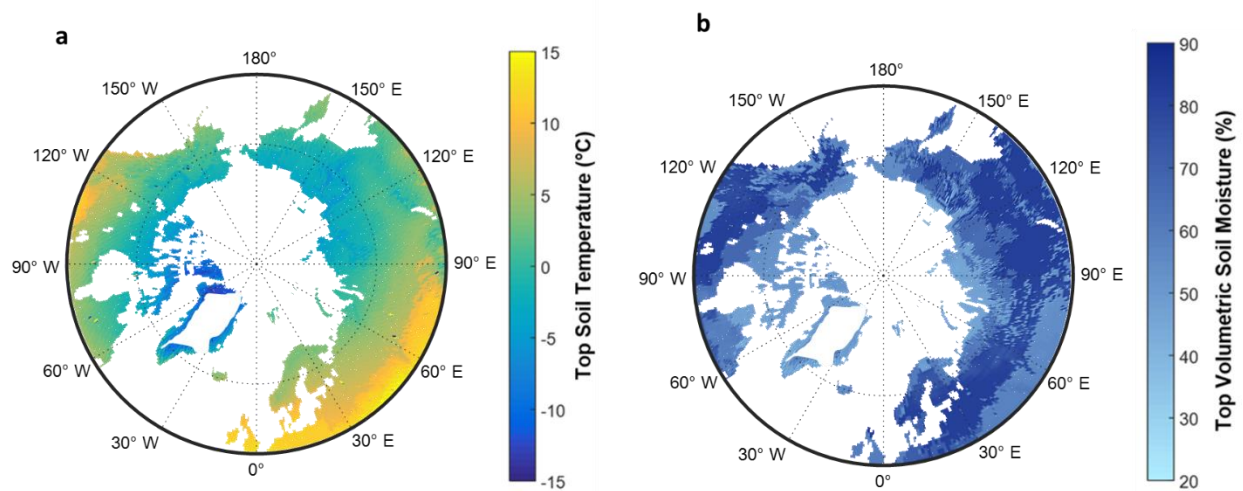


Figure 2.22 Spatial variability of top soil temperature and moisture averaged over 2017-2100 for RCP 8.5 north of 50°N. (a) Averaged annual top 10-cm soil temperature in °C and (b) averaged annual top 10-cm soil moisture in % volume. The dotted longitudinal lines are at 30° intervals, and the latitudinal line is at 65°N.

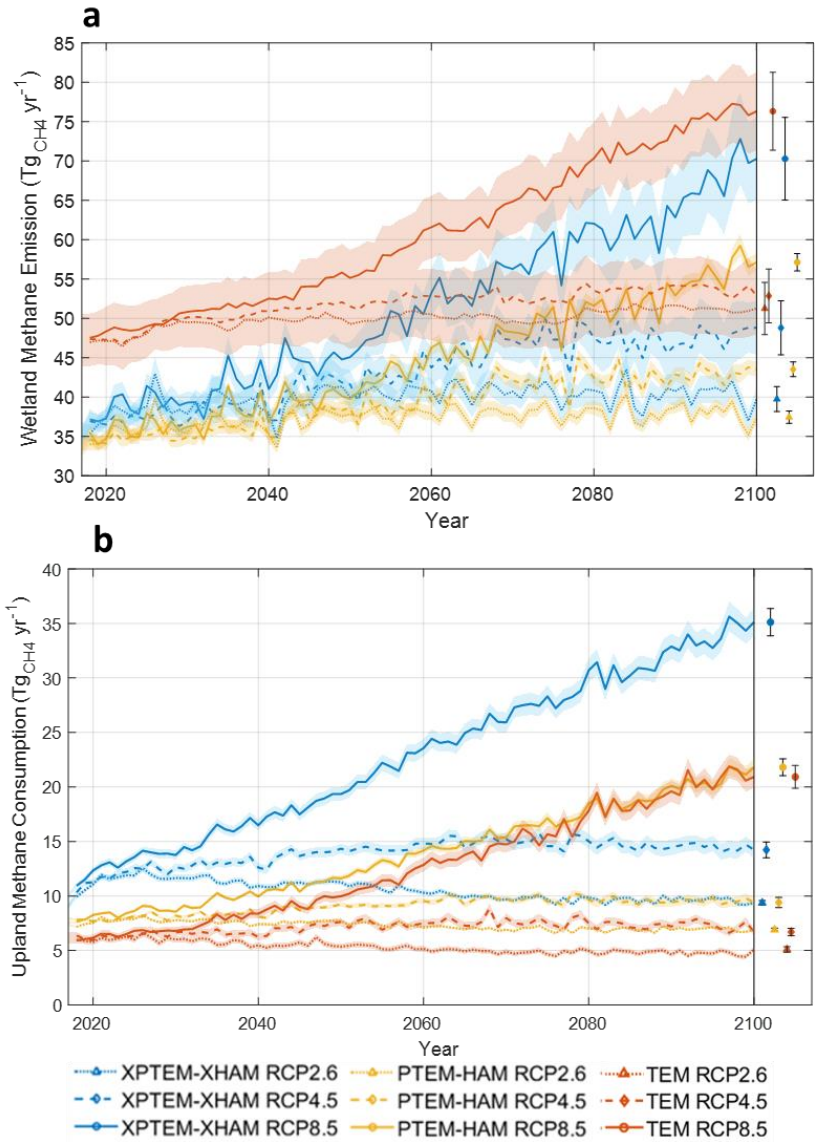


Figure 2.23 Inter-annual variability of methane fluxes during 2017 – 2100. (Left) Annual pan-arctic estimates of (a) wetland methane emission and (b) upland methane consumption for XPTEM-XHAM (blue), PTEM-HAM (yellow), and TEM (red) using RCP 2.6 (dotted), RCP 4.5 (dashed), and RCP 8.5 (solid) north of 50°N. The shaded error bars represent one standard deviation of model results determined by varying the optimized parameters from ensemble simulations. (Right) Mean (symbols) and one standard deviation (bars) in 2100 for each metric.

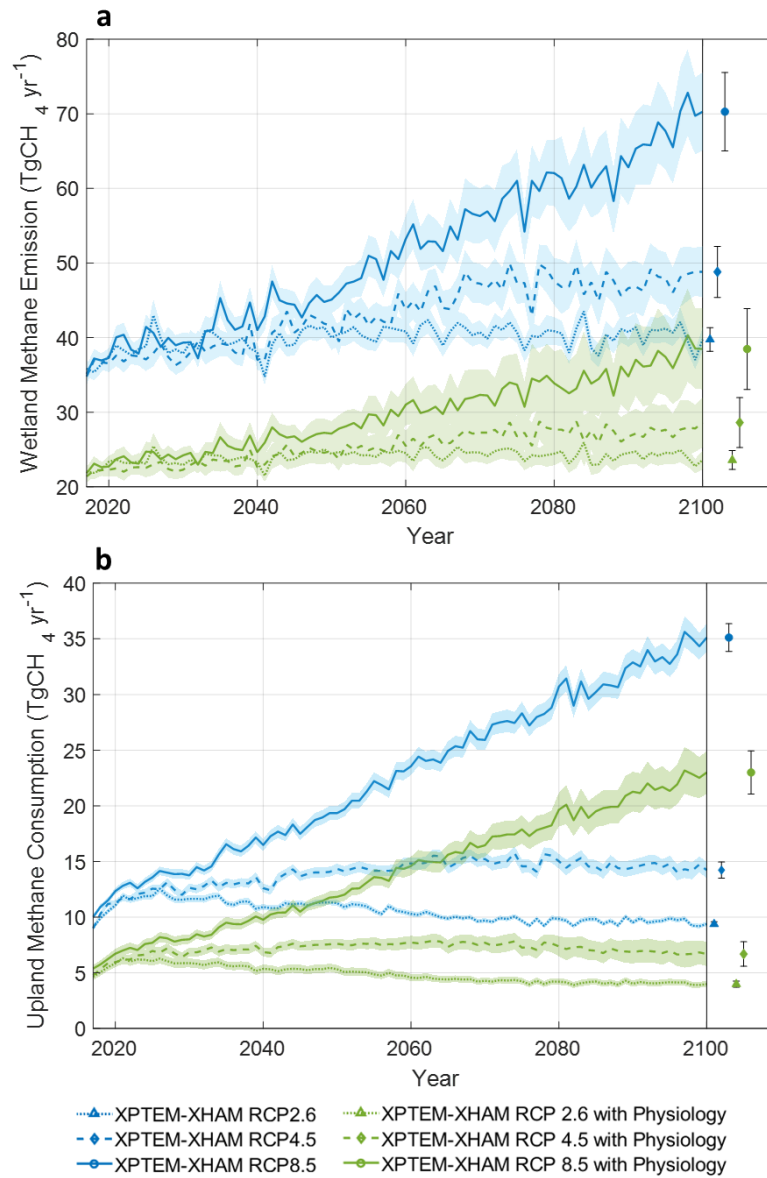


Figure 2.24 Inter-annual variability of methane fluxes for XPTEM-XHAM with its microbial physiology from 2017 – 2100. (Left) Annual estimates of pan-arctic (a) wetland methane emission and (b) upland methane consumption for XPTEM-XHAM without varying m_E (baseline, blue), and XPTEM-XHAM with physiological responses of MG and HAM to temperature change with varying m_E (green) based on RCP 2.6 (dotted), RCP 4.5 (dashed), and RCP 8.5 (solid) north of 50°N . The shaded error bars represent one standard deviation of model results determined by varying the optimized parameters from ensemble simulations. (Right) Mean (symbols) and one standard deviation (bars) in 2100 for each metric.

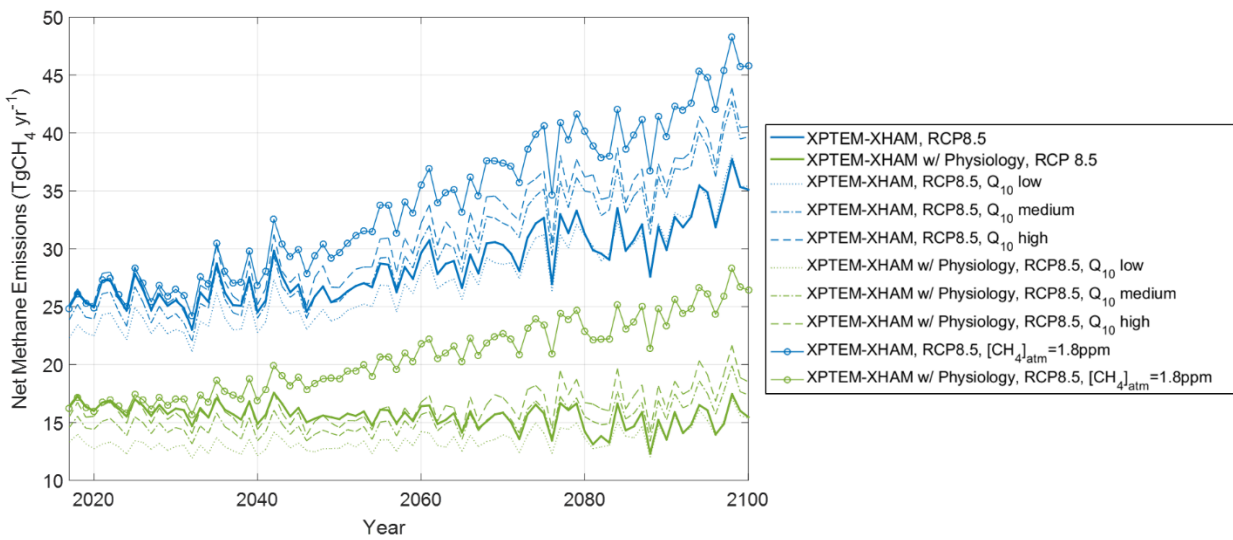


Figure 2.25 Sensitivity of temperature and atmospheric methane abundance to projections of net methane emission for RCP 8.5 during 2017-2100 north of 50°N. Annual estimates of pan-Arctic net methane emission for XPTEM-XHAM without varying ϵ and m_E (solid blue), XPTEM-XHAM with physiological responses of MG and HAM to temperature change with varying m_E (solid green), and sensitivity tests of the two simulations to Q_{10} changes (dotted, dash-dot, and dashed lines for low, medium, and high Q_{10} setups, respectively) and atmospheric methane abundance to stay at 1.8 ppm (circle marker).

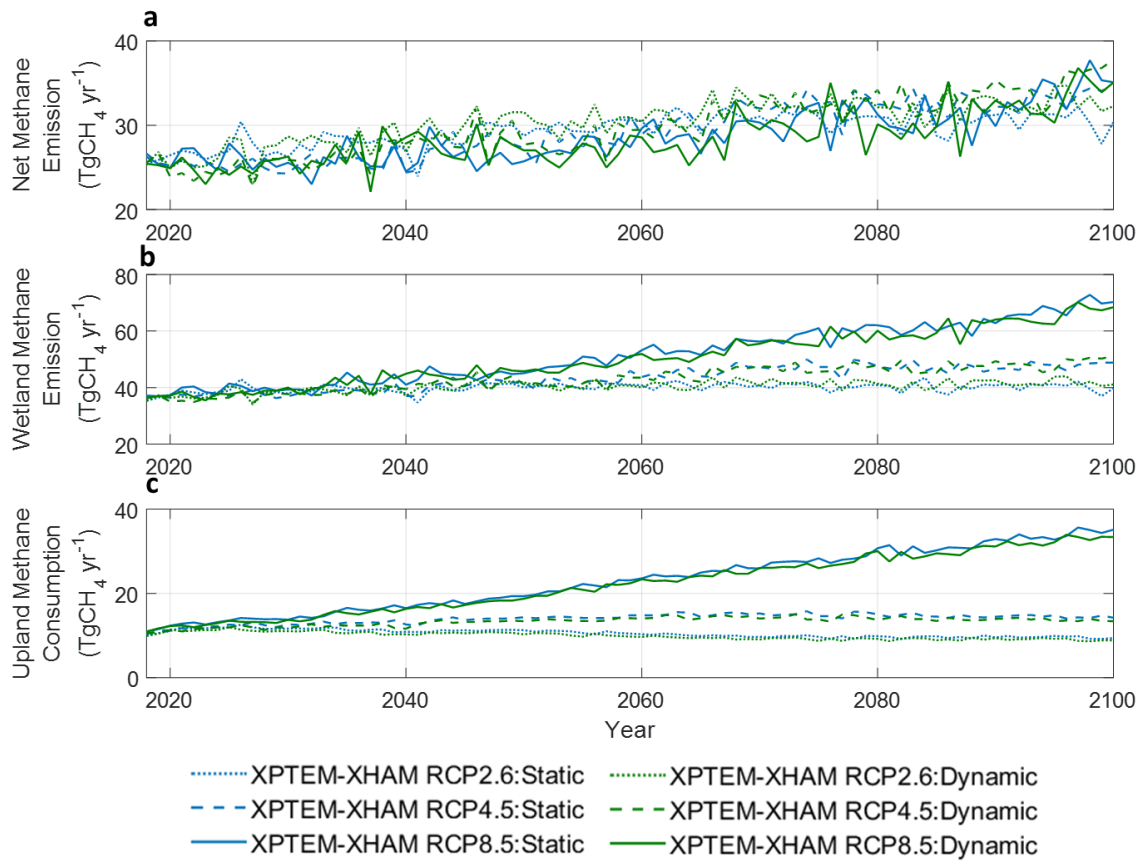


Figure 2.26 Inter-annual variability of methane fluxes using time-varying inundation fraction from 2017 – 2100 north of 50°N. Annual estimates of pan-arctic (a) net methane emission, (b) wetland methane emission, and (c) upland methane consumption for XPTEM-XHAM model using static inundation fraction (blue) and dynamic inundation fraction (green) in TgCH₄yr⁻¹ using RCP 2.6 (dotted), RCP 4.5 (dashed), and RCP 8.5 (solid).

2.5 Discussion and Conclusion

Our simulation emphasizes that the current understanding of Arctic methane feedback may be incomplete (Figure 2.27) (Oh et al. 2016). Previous studies predicted strong positive feedbacks between temperature and methane emission due to more accessible SOC from thawing permafrost. However, additional negative feedbacks between temperature and HAM may suppress this feedback loop. This study also shows we need more field and laboratory experiments to understand HAM and MG physiological responses to environmental changes (Christiansen et al. 2015; McCalley et al. 2014).

Although the new model significantly revises estimates of net Arctic methane emission, there are processes that current models, including ours, have not considered. We do not capture the complex Arctic hydrological and vegetation dynamics (Liljedahl et al. 2016; Nauta et al. 2015), which may influence our estimates of both methane production and consumption. We focused on terrestrial ecosystems without considering potential large methane emissions from aquatic systems, whose magnitude and spatial distribution may change (Sepulveda-Jauregui et al. 2015; Wik et al. 2016). We used observed wetland methane emissions to optimize methane production and oxidation where the fraction of each is uncertain (Segers 1998). More observations of subsurface vertical processes using isotopic labeling analysis and inhibitor techniques will better constrain future models (Pedersen et al. 2018).

In conclusion, we show HAM microbial dynamics are an important component of the current Arctic methane budget as our estimate more than doubles upland sinks. We also find our revised estimates with microbial and permafrost SOC dynamics better match site-level and regional observations and observation-based inversions. This model projects a smaller increase of net methane emission than previous models by 2100 as the increase in wetland emission due to more accessible permafrost SOC is mostly offset by the increase in upland consumption by HAM. A potential decrease in future net methane emission is projected after including microbial physiology of HAM and MG. This study highlights the need to incorporate more detailed microbial dynamics into process-based methane models to better constrain the Arctic methane budget.

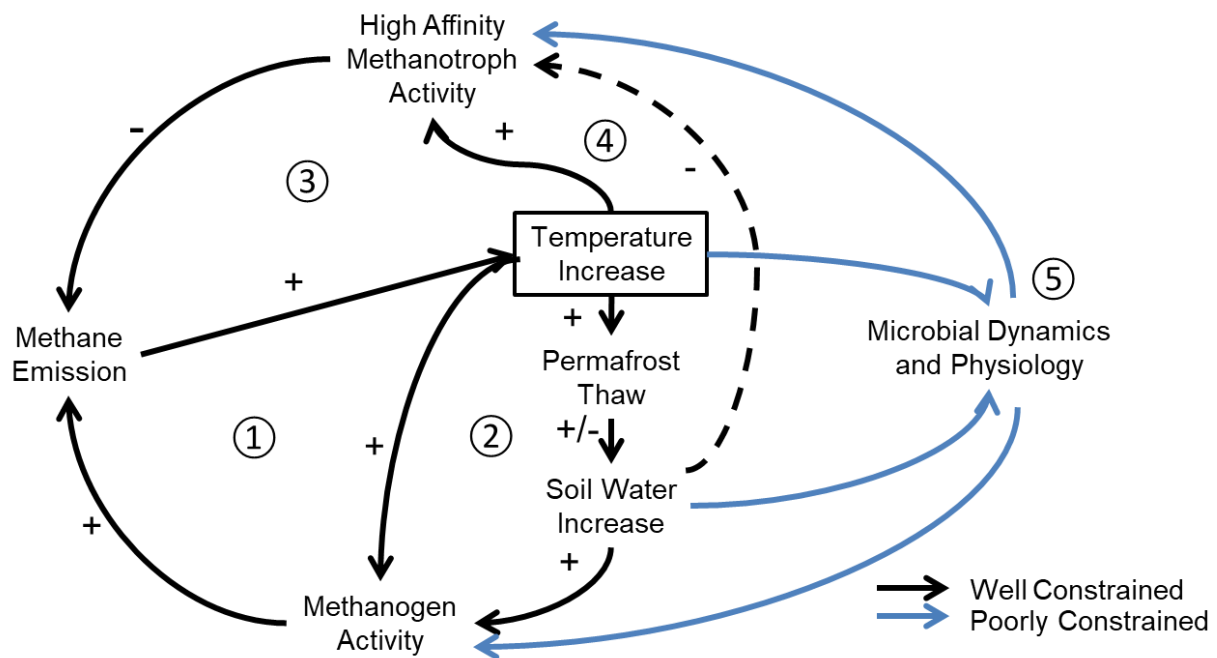


Figure 2.27 Future arctic methane feedbacks (modified Fig. 5 of Oh et al., 2016 (Oh et al. 2016)). Previous studies predicted a positive feedback between temperature and methane emission (circles 1–2). However, because high-affinity methanotrophs may respond strongly to temperature and less strongly to soil moisture due to uncertain arctic hydrology (circles 3–4), this feedback loop may be partially suppressed. Moreover, explicit modeling of microbial dynamics (circle 5) will facilitate future model developments that include effects of microbial physiology.

CHAPTER 3. A MECHANISTIC WETLAND ISOTOPE MODEL IMPROVES UNDERSTANDING OF ATMOSPHERIC CH₄ ISOTOPIC COMPOSITION

3.1 Abstract

To effectively use measurements of $\delta^{13}\text{C}$ of atmospheric CH₄ to constrain emissions of CH₄ by source sector in atmospheric transport model studies, the spatial and temporal distribution of source isotopic signatures must be known. But currently, such information on $\delta^{13}\text{C}$ of CH₄ ($\delta^{13}\text{C}\text{-CH}_4$) emitted by wetlands is limited. Observations show a latitudinal gradient in wetland $\delta^{13}\text{C}\text{-CH}_4$ source signatures with heavier values in tropics and lighter values in the boreal region. Here we incorporated a carbon isotope-enabled module into an extant biogeochemistry model to mechanistically simulate the spatial and temporal variability of global wetland $\delta^{13}\text{C}\text{-CH}_4$. The new model explicitly considers isotopic fractionation during methane production, oxidation, and transport processes. The model is then parameterized for low and high pH conditions of boreal, temperate, and tropical wetland ecosystems using observed data from field studies and extrapolated to global wetland ecosystems from 1984 to 2016. We estimate a mean global wetland $\delta^{13}\text{C}\text{-CH}_4$ of -60.78‰ with its seasonal and inter-annual variability. We find that the new model matches field chamber observations 35% better in terms of RMSE compared to an empirical static wetland $\delta^{13}\text{C}\text{-CH}_4$ map. The model also reasonably reproduces the regional heterogeneity of wetland $\delta^{13}\text{C}\text{-CH}_4$ in Alaska, consistent with vertical profiles of $\delta^{13}\text{C}\text{-CH}_4$ from NOAA aircraft measurements. Furthermore, we show that the latitudinal gradient of atmospheric $\delta^{13}\text{C}\text{-CH}_4$ simulated by a chemical transport model using the new wetland $\delta^{13}\text{C}\text{-CH}_4$ map reproduces the observed latitudinal gradient based on NOAA/INSTAAR global flask-air measurements. We believe this study is among the first to use a process-based biogeochemistry model to map the global distribution of wetland $\delta^{13}\text{C}\text{-CH}_4$, which will significantly help atmospheric chemistry transport models partition global methane emissions from various sources.

3.2 Introduction

Methane (CH₄) is a powerful greenhouse gas, and its atmospheric abundance ($[\text{CH}_4]_{\text{atm}}$) has increased by about 150% since the 1750s (Etheridge et al. 1998; Dlugokencky et al. 2005). The

atmospheric burden is determined by the balance between sources and sinks (Saunio et al. 2016). Unlike the steady increase of atmospheric CO₂ and N₂O, [CH₄]_{atm} nearly stabilized from 1998 to 2006 followed by a rapid increase after 2007 with a growth rate of ~6 ppb/year in 2007-2013 and ~9 ppb/year in 2014-2018 (http://www.esrl.noaa.gov/gmd/ccgg/trends_ch4/). Especially since 2007, [CH₄]_{atm} has increased while its stable carbon isotopic composition ($\delta^{13}\text{C-CH}_4$) has shifted to significantly more negative values after increasing for 200 years (Nisbet et al. 2019; Dlugokencky et al. 2011). Diagnosing the mechanism behind these changes continues to generate considerable attention and controversy (Hausmann et al. 2016; Naus et al. 2019; Schaefer et al. 2016; Schwietzke et al. 2016; Worden et al. 2017). To understand how each sink and source contributes to the long-term trends of [CH₄]_{atm} and atmospheric $\delta^{13}\text{C-CH}_4$, diverse atmospheric transport models have been developed and applied to this problem (Feinberg et al. 2018; Strode et al. 2019).

The $\delta^{13}\text{C-CH}_4$ from different source sectors provides additional information on the global methane budget in atmospheric transport model studies as CH₄ produced from biogenic sources are lighter than the CH₄ from fossil fuel or biomass burning (Schwietzke et al. 2016; Sherwood et al. 2017). However, due to the wide spread of the distribution of $\delta^{13}\text{C-CH}_4$ in each source sector, the spatial and temporal distribution of source isotopic signatures must be known. Among the source sectors, wetlands are the largest single sources and have a strong impact on the atmospheric $\delta^{13}\text{C-CH}_4$ (Saunio et al. 2016). But currently, such spatial and temporal information on $\delta^{13}\text{C-CH}_4$ emitted by wetlands is limited, and many atmospheric transport modeling studies use a single uniform value for $\delta^{13}\text{C-CH}_4$ from wetlands (Strode et al. 2019).

Furthermore, recent studies addressed a distinct latitudinal gradient of the $\delta^{13}\text{C-CH}_4$ from wetlands, that the CH₄ emitted from Arctic wetlands is much lighter in $\delta^{13}\text{C-CH}_4$ than from tropics (Feinberg et al. 2018). Studies have proposed reasons behind the latitudinal gradients, such as differences in communities in CH₄ production archaea (methanogens), oxidation by bacteria (methanotrophs), abundance in C₄ plants in precursor plant materials (Chanton 2005; Fisher et al. 2017; Nakagawa et al. 2002; Brownlow et al. 2017). A recent study presented the first spatially resolved wetland $\delta^{13}\text{C-CH}_4$ map (Ganesan et al. 2018). However, without identifying the mechanisms of the latitudinal gradients, the static map represented an empirical relationship between wetland $\delta^{13}\text{C-CH}_4$ and global soil pH and C₄ plant distribution with an abrupt $\delta^{13}\text{C-CH}_4$ changes between 40°N and 45°N.

Here, we incorporate a carbon isotope module into a biogeochemistry model, Terrestrial Ecosystem Model (TEM) (Zhuang et al., 2004), to mechanistically understand $\delta^{13}\text{C}\text{-CH}_4$ from global wetlands. The model is then thoroughly validated using extensive site-level and regional observation data. We then use the model to understand the mechanisms behind the latitudinal and long-term variability of wetland $\delta^{13}\text{C}\text{-CH}_4$. Finally, we applied the model results as inputs for an atmospheric transport modeling to understand the effects of spatially and temporally resolved wetland isotope map on atmospheric $\delta^{13}\text{C}\text{-CH}_4$, compared to the uniform and static spatially resolved map from Ganesan *et al.* (2018).

3.3 Methods

The methane dynamics module of TEM simulates methane production, oxidation, and three transport processes (diffusion, ebullition and plant-mediated transport) between soil and the atmosphere (Liu et al. 2020; Oh et al. 2020; Zhuang et al. 2004, 2013). The new model, referred to as isoTEM, explicitly considers four main carbon isotopic fractionations in methane cycling processes (Fig. 3.1).

First, the initial $\delta^{13}\text{C}$ of soil organic carbon (SOC) is determined by the precursor global C3 and C4 plant distribution (Fig. 3.2) (Still et al. 2003), where C4 vegetation is isotopically heavier due to its photosynthetic pathways (Holmes et al. 2014). Second, methane is produced in the anaerobic soil zone by two distinct methanogen communities: hydrogenotrophic methanogens (HM) use H_2 and CO_2 and acetoclastic methanogens (AM) use acetate for methane production (Horn et al. 2003). The fractional contribution of two methanogen communities is important because HM produce isotopically lighter methane than AM (fractionation factor (α) for HM (α_{HM}) $\approx 0.920\text{-}0.970$ and for AM (α_{AM}) $\approx 0.960\text{-}1.000$) (McCalley et al. 2014; Holmes et al. 2015). Thus, we conducted a multiple regression analysis between the fraction of both methanogens and the main environmental factors, soil carbon, pH, and latitude, using a relatively large dataset from Holmes *et al.*, 2014 (Fig. 3.3, and Table 3.1). The regression showed a positive relationship between the HM fraction and latitudes with a breakpoint at 60°N , and a negative relationship between the HM fraction and soil pH and total carbon (R^2 0.41 and $p < 0.001$). The $\delta^{13}\text{C}$ of produced methane is then calculated using the binary mixing of methane pools of two methanogens.

Third, a fraction of CH₄ produced by methanogens is oxidized by methanotrophs in aerobic soils with preferably oxidized isotopically light CH₄ (α for methane oxidation (α_{MO}) \approx 1.015-1.035) (Le Mer and Roger 2001). Lastly, methane is transported to the atmosphere through three processes, where ebullition shows negligible fractionation, but diffusion and plant-mediated transport cause CH₄ to be lighter (α for plant-mediated transport (α_{TP}) \approx 0.970-1.000, α for diffusion (α_{TD}) \approx 0.990-1.000, and α for ebullition (α_{TE}) \approx 0.995-1.000) (Chanton 2005). The final $\delta^{13}\text{C-CH}_4$ emitted to the atmosphere is calculated by the mixing of the methane pools through three transport processes (see Section 3.3.1).

We optimized 6 fractionation factors (α_{HM} , α_{AM} , α_{MO} , α_{TP} , α_{TD} , α_{TE}) for low and high pH conditions in boreal, temperate, and tropical wetland ecosystems using observed data from field studies (McCalley et al. 2014; Kelly et al. 1992; Burke et al. 1988) and Shuffled Complex Evolution optimization (SCE-UA-R) with 10,000 maximum loops per parameter ensemble (Table 3.2-3.4 and Figure 3.4) (Duan et al. 1993). To quantify the uncertainty in the model simulations, we used one standard deviation of model results from 10 ensemble members of the SCE-UA-R optimization (see Section 3.3.2).

We used monthly meteorological inputs of the Gridded Climatic Research Unit (CRU) (Harris et al. 2014) to run global wetland simulations from 1984 to 2016 at a spatial resolution of 0.5°×0.5° with a 15-year of spin up to stabilize the carbon fractionation processes. Because various wetland inundation datasets exist (Melton et al. 2013), we first assumed that every global grid cell is fully saturated and set wetland $\delta^{13}\text{C-CH}_4$ values for all grid cells (Fig. 3.5), thus it can be used in conjunction with any flux and wetland area dataset for other studies. We then used a static upland and wetland inundation for our default simulation (Matthews and Fung, 1987) and conducted a sensitivity test using transient inundation data (Poulter et al. 2017) (see Section 3.3.3).

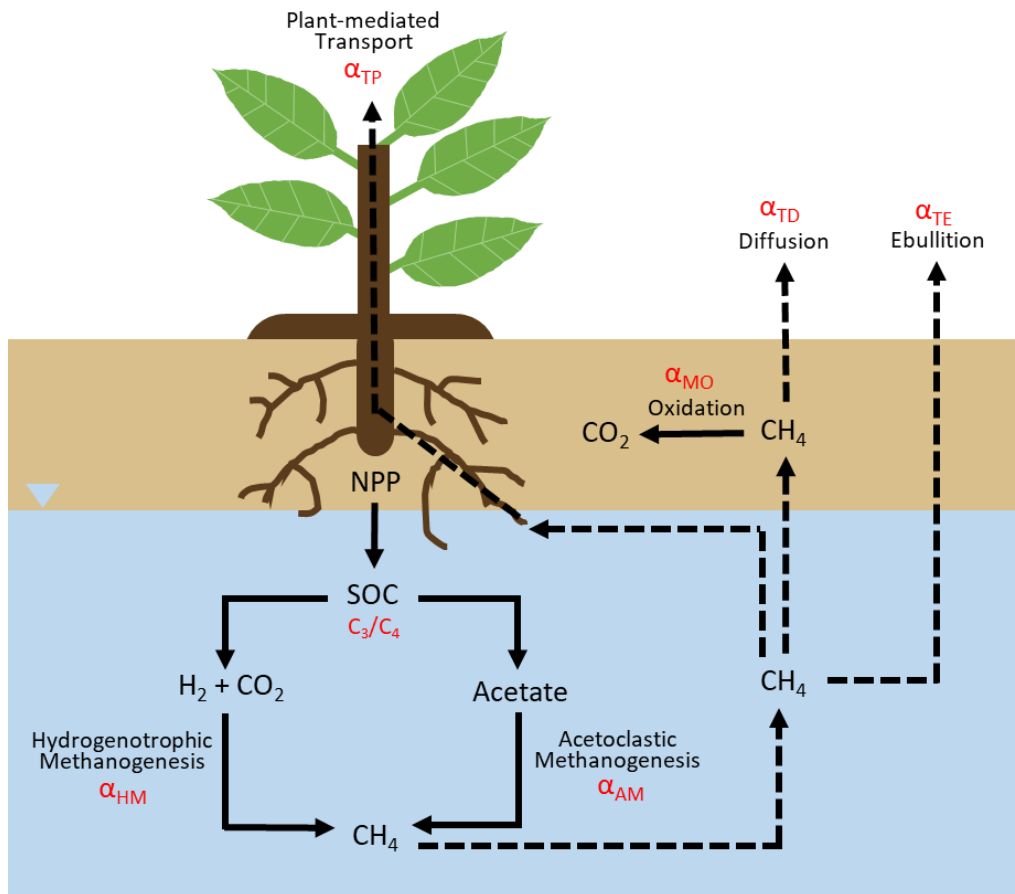


Figure 3.1 Main configuration of isoTEM. Bold and dashed lines refer to chemical and transport processes, respectively. Precursor C_3/C_4 plant distribution (C_3/C_4) and fractionation factors related to methane production, oxidation, and transport processes (α_{HM} , α_{AM} , α_{MO} , α_{TP} , α_{TE} , α_{TD}) were added for isoTEM.

3.3.1 Model development

We incorporated carbon isotope module of methane into a process-based biogeochemistry model, Terrestrial Ecosystem Model (TEM).

a. Terrestrial Ecosystem Model (TEM)

TEM is one of commonly used biogeochemistry models and its methane, soil thermal, and hydrological dynamics have been evaluated in previous studies (Zhuang et al. 2004, 2013). The methane dynamics module of TEM simulates methane production, oxidation, and three transport processes between soil and atmosphere. In a wetland system, changes in methane concentrations (C_M) at depth z and time t ($\partial C_M(z,t)/\partial t$) are governed by Equation 3.1, where $M_P(z,t)$, $M_O(z,t)$, $R_P(z,t)$, and $R_E(z,t)$ are methane production, oxidation, plant-mediated transport, and ebullition rates, respectively, and $\partial F_D(z,t)/\partial z$ represents flux divergence due to gaseous and aqueous diffusion.

$$\frac{\partial C_M(z,t)}{\partial t} = M_P(z,t) - M_O(z,t) - \frac{\partial F_D(z,t)}{\partial z} - R_P(z,t) - R_E(z,t) \dots \text{Equation 3.1}$$

Methane is produced (M_P) in anaerobic soils and is calculated by the product of maximum potential production rate (M_{GO}) and limiting functions of substrate, soil temperature, pH, and redox potentials (S_{OM} , M_{ST} , pH and R_x , respectively) (Equation 3.2). We used limiting factors of pH and R_x to consider enzymatic activity and the relative availability of electron acceptors (e.g., O_2 , NO_3^- , SO_4^{2-} , Fe^{+3} , Mn^{+4}) for methane production. The limiting function of substrate ($f(S_{OM}(z,t))$) is mainly dependent on soil organic carbon (SOC) derived from vegetation (Net Primary Productivity, NPP), where $NPP(mon)$ is monthly NPP ($gC\ m^{-2}\ month^{-1}$), NPP_{MAX} is ecosystem-specific maximum monthly NPP, and $f(C_{DIS}(z))$ describes the relative availability of organic carbon substrate at depth z (Equation 3.3). For the substrate availability, we calculated changes in vegetation carbon using atmospheric CO_2 concentrations, transient temperature, precipitation, vapor pressure and soil texture (Zhuang et al. 2003).

$$M_{P,TEM}(z,t) = M_{GO}f(S_{OM}(z,t))f(M_{ST}(z,t))f(pH(z,t))f(R_x(z,t)) \dots \text{Equation 3.2}$$

$$f(S_{OM}(z, t)) = \left(1 + \frac{NPP(mon)}{NPP_{max}}\right) f(C_{DIS}(z)) \dots \text{Equation 3.3}$$

The produced methane diffuses into aerobic soils and is oxidized by methanotrophs, calculated by the product of the maximum potential oxidation rate (O_{MAX}) and limiting functions of methane concentration, soil temperature, soil moisture, redox potential, nitrogen deposition, diffusion limited by high soil moisture, and oxygen concentration (C_M , T_{SOIL} , E_{SM} , R_{OX} , N_{DP} , D_{MS} , and C_{O_2} respectively) (Equation 3.4). The Michaelis-Menten constant for methane oxidation was set to 5 μM ($k_{CH_4,LAM}$) (Equation 3.5).

$$\begin{aligned} M_{O,TEM}(z, t) \\ = O_{MAX} f(C_M(z, t)) f(T_{SOIL}(z, t)) f(E_{SM}(z, t)) f(R_{OX}(z, t)) f(N_{dp}(z, t)) f(D_{ms}(z, t)) f(C_{O_2}(z)) \\ \dots \text{Equation 3.4} \end{aligned}$$

$$f(C_M(z, t)) = \frac{C_M(z,t)}{k_{CH_4} + C_M(z,t)} \dots \text{Equation 3.5}$$

The residual methane is emitted to the surface through three transport processes. First, gaseous and aqueous diffusion (F_D) occurs due to concentration gradients of methane ($\partial C_M(z,t)/\partial t$) following Fick's law through soil pores (Equation 3.6). The molecular diffusion coefficient (D) in different soil layers was calculated based on soil texture and soil moisture. We also have a simple limitation of temperature on diffusion, that there will be no diffusion when temperature is below 0 °C. Secondly, ebullition (R_E) occurs when methane bubble forms (i.e., when C_M is greater than 500 $\mu\text{mol L}^{-1}$ in saturated soils); C_M is multiplied by a constant rate of 1.0 h^{-1} (K_e) (Equation 3.7). Lastly, plant-mediated transport (R_p) occurs through the root systems of some plants that provide a direct conduit for methane to the atmosphere, and is functions of rate constant of 0.01 h^{-1} , vegetation type, root density, vegetation growth, and soil methane concentrations (K_p , TR_{veg} , f_{ROOT} , f_{GROW} , and C_M , respectively) (Equation 3.8) (Walter and Heimann 2000). R_p depends on ecosystem-specific plant functional types and increases in a warmer soil due to the increase in vegetation growth. In both wetland and upland ecosystems, the soil profile was divided into 1-cm layers, and

soil temperature, moisture, and methane dynamics of TEM were simulated at daily time steps (Zhuang et al. 2004).

$$F_D(z, t) = -D(z) \frac{\partial C_M(z, t)}{\partial t} \dots \text{Equation 3.6}$$

$$R_E(z, t) = K_e f(C_M(z, t)) \dots \text{Equation 3.7}$$

$$R_P(z, t) = K_P T R_{veg} f_{ROOT}(z) f_{GROW}(t) C_M(z, t) \dots \text{Equation 3.8}$$

b. Methane carbon isotope enabled TEM (isoTEM)

The isoTEM explicitly considers four main carbon isotopic fractionations during methane dynamics. First, the initial $\delta^{13}\text{C}$ of soil organic carbon (SOC) is determined by the global C3 and C4 vegetation distribution (Still et al., 2003). The initial $\delta^{13}\text{C}$ of soil organic carbon (SOC) is determined by the global C3 and C4 vegetation distribution (Still et al., 2003) and is set to -27 and -13 ‰ for C3- and C4-only vegetation area. The initial $\delta^{13}\text{C}$ of areas with mixed C3 and C4 vegetation is determined by the proportion of the vegetation (Fig. 3.2).

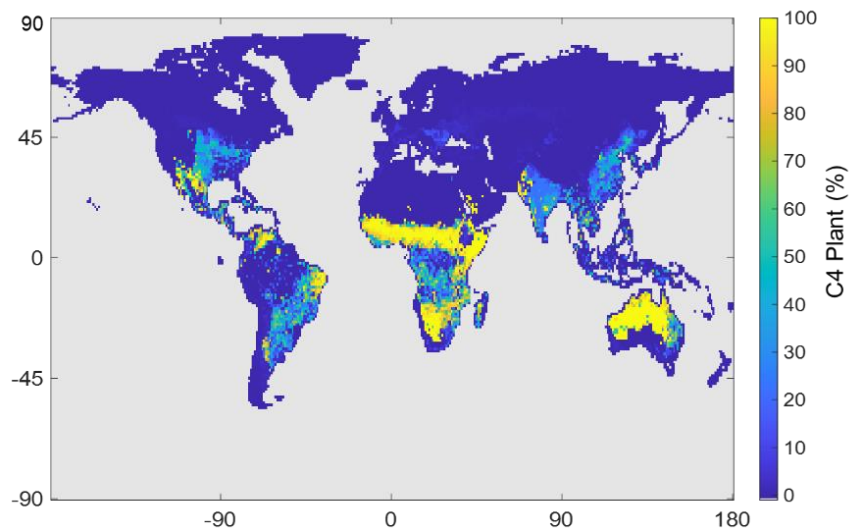


Figure 3.2 The C4 fraction of the vegetation (Still et al., 2003).

Second, methane is produced in the anaerobic soil zone by the two distinct methanogen communities: hydrogenotrophic (HM) use H₂ and CO₂ and acetoclastic methanogens (AM) use acetate for methane production (Horn et al., 2003). The fractional contribution of two methanogen communities is calculated based on a multiple regression analysis between the fraction of both methanogens and the main environmental factors, such as pH, total organic carbon, and latitude, using data from Holmes et al. (2015) (Equation 3.9). The regression results show that the fraction of HM is positively correlated with latitude with a steep increase at 60 °N (slope of 0.11 and 5.19 for latitudes below and above 60 °N, respectively) and negatively correlated with pH (slope of -9.23) and SOC (slope of -0.7) (R² of 0.41, p < 0.001) (Table 3.1 and Figure 3.3).

$$f_{HM} = \begin{cases} a_1 \times lat + b \times pH + c \times SOC + d \\ \dots \text{for } lat < lat_{step} \\ a_1 \times lat + a_2 \times (lat - lat_{step}) + b \times pH + c \times SOC + d \dots \text{Equation 3.9} \\ \dots \text{for } lat > lat_{step} \end{cases}$$

Table 3.1 Coefficients for multiple stepwise regression of the fraction of methanogenic community.

	a ₁	a ₂	b	c	d
Meaning	Latitudinal gradient	Latitudinal gradient for > 60N	pH gradient	SOC gradient	Intercept
Value	0.11	5.19	-9.23	-0.7	102.93
Significance		* 0.05	* 0.05		* 0.05

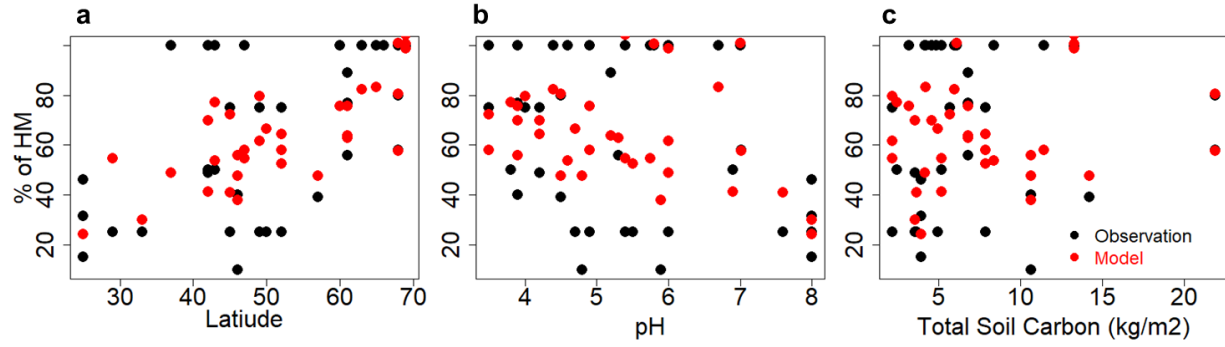


Figure 3.3 Multiple regression results between fraction of hydrogenotrophic methanogens (HM) and (a) step-wise latitude, (b) pH, and (c) total soils carbon.

The $\delta^{13}\text{C}$ of produced methane by HM and AM both makes methane lighter than the initial $\delta^{13}\text{C}$ of SOC and is calculated based on the fractionation factors ($\alpha_{\text{HM}} \approx 0.920-0.970$, $\alpha_{\text{AM}} \approx 0.960-1.000$) (Equation 3.10). The $\delta^{13}\text{C}$ of produced methane is calculated using the binary mixing of methane pools of two methanogens (Equation 3.11).

$$\begin{aligned} \delta^{13}\text{CH4}_{\text{prod, HM}} &= \delta^{13}\text{C}_{\text{initial}} - 1000 \times \ln(\alpha_{\text{HM}}) \\ \delta^{13}\text{CH4}_{\text{prod, AM}} &= \delta^{13}\text{C}_{\text{initial}} - 1000 \times \ln(\alpha_{\text{AM}}) \end{aligned} \dots \text{Equation 3.10}$$

$$\delta^{13}\text{CH4}_{\text{prod}} = f_{\text{HM}} \times \delta^{13}\text{CH4}_{\text{prod, HM}} + (1 - f_{\text{HM}}) \times \delta^{13}\text{CH4}_{\text{prod, AM}} \dots \text{Equation 3.11}$$

Next, methanotrophs oxidize methane in aerobic soils and preferably consume isotopically light methane (Le mer and Roger, 2001). Fraction of methane oxidation of total production (f_{ox}) is calculated by TEM (Equation 3.12), and Methane carbon isotope signatures after methane oxidation based on the fractionation of methane oxidation ($\alpha_{\text{MO}} \approx 1.015-1.035$) (Equation 3.13) (Zhang et al. 2016).

$$f_{\text{ox}} = \frac{\delta^{13}\text{CH4}_{\text{prod}} - \delta^{13}\text{CH4}_{\text{oxid}}}{\left(\frac{1}{\alpha_{\text{MO}}} - 1\right)(\delta^{13}\text{CH4}_{\text{oxid}} + 1000)} \dots \text{Equation 3.12}$$

$$\delta^{13}CH4_{oxid} = \frac{\delta^{13}CH4_{prod} - 1000 \times f_{ox} \left(\frac{1}{\alpha_{MO}} - 1 \right)}{f_{ox} \left(\frac{1}{\alpha_{MO}} - 1 \right) + 1} \dots \text{Equation 3.13}$$

Lastly, methane is transported to the atmosphere through three processes (plant-mediated transport, diffusion, and ebullition) with different fractionations ($\alpha_{TP} \approx 0.970-1.000$, $\alpha_{TD} \approx 0.990-1.000$, $\alpha_{TE} \approx 0.995-1.000$, respectively) (Equation 3.14). The final $\delta^{13}C-CH_4$ emitted to the atmosphere is calculated by the mixing of the methane pools through three transport processes (Equation 3.15) (Chanton et al., 2005).

$$\begin{aligned} \delta^{13}CH4_{final,TP} &= \delta^{13}C_{oxid} - 1000 \times \ln(\alpha_{TP}) \\ \delta^{13}CH4_{final,TE} &= \delta^{13}C_{oxid} - 1000 \times \ln(\alpha_{TE}) \\ \delta^{13}CH4_{final,TD} &= \delta^{13}C_{oxid} - 1000 \times \ln(\alpha_{TD}) \\ &\dots \text{Equation 3.14} \end{aligned}$$

$$\delta^{13}CH4_{final} = f_{TP} \times \delta^{13}CH4_{final,TP} + f_{TE} \times \delta^{13}CH4_{final,TE} + f_{TD} \times \delta^{13}CH4_{final,TD} \dots \text{Equation 3.15}$$

3.3.2 Model optimization

We optimized 6 fractionation factors (α_{HM} , α_{AM} , α_{MO} , α_{TP} , α_{TD} , α_{TE}) for low and high pH conditions in boreal, temperate, and tropical wetland ecosystems. All other parameters were set the same as in Liu et al. (2020). To optimize these parameters, we first collected observation data from six sites representing each ecosystem (Table 3.2-3.4) (Burke, Barber and Sackett, 1988; Kelly *et al.*, 1992; McCalley *et al.*, 2014a). Besides the observed meteorology from field sites, we also used CRU time-series data version 4.01 to fill missing meteorological inputs (Harris et al. 2014). We then used the Shuffled Complex Evolution Approach in R language (SCE-UA-R) to minimize the difference between simulated and observed methane emission and consumption rates (Duan et al. 1993). For each site, 10 ensembles were run using SCE-UA-R with 10,000 maximum loops per parameter ensemble, and all of them reached steady state before the end of the loops. Our optimization results show that isoTEM reasonably captures the magnitude and seasonality of observed soil methane fluxes (Fig. 3.4).

Table 3.2 Information about observation sites for model optimization.

Vegetation Types	Lat, Lon	Meteorological Inputs	Observation Data	References
Boreal low- and high- pH	68, 18.5	Site observed temperature and precipitation and CRU	CH ₄ flux and $\delta^{13}\text{C-CH}_4$ in 2012-2013	(McCalley et al. 2014)
Temperate low- and high - pH	48, -95	Site observed temperature and CRU	CH ₄ flux and $\delta^{13}\text{C-CH}_4$ in 1989-1990	Kelly <i>et al.</i> , 1992
Tropic low- and high- pH	27.5, -82.5	Site observed temperature and CRU	CH ₄ flux in 1986-1987	Burke, Barber and Sackett, 1988

Table 3.3 Upper and lower limits of parameter range of fractionation factors (α), where AM=acetoclastic methanogenesis, HM=hydrogenotrophic methanogenesis, MO=methane oxidation, TP=plant-mediated transport, TE=ebullition transport, TD=diffusion.

	Lower Bound	Upper Bound	Literature
α_{AM}	0.960	1.000	Conrad 2005; Vaughn 2016; Kruger 2002; Conrad 2010
α_{HM}	0.920	0.970	Conrad 2005; Vaughn 2016; Kruger 2002; Conrad 2010
α_{MO}	1.015	1.035	King 1989; Chanton 2005; Zhang 2016; Kinnaman 2006
α_{TP}	0.970	1.000	Chanton 2005 (review paper)
α_{TE}	0.995	1.000	Chanton 2005 (review paper)
α_{TD}	0.990	1.000	Chanton 2005 (review paper)

Table 3.4 Optimized Parameters related to methane fractionation factors in wetlands.

Latitude	Wetland Type	α_{AM}	α_{HM}	α_{MO}	α_{TP}	α_{TE}	α_{TD}
High (60 – 90°)	Low pH	0.9790 ±0.0103	0.9536 ±0.0006	1.0151 ±0.0001	0.9951 ±0.0002	0.9995 ±0.0007	0.9962 ±0.0008
	High pH	0.9659 ±0.0030	0.9595 ±0.0008	1.0150 ±0.0001	0.9951 ±0.0002	0.9975 ±0.0008	0.9914 ±0.0012
Middle (30 – 60°)	Low pH	0.9942 ±0.0033	0.9593 ±0.0091	1.0175 ±0.0031	0.9723 ±0.0039	0.9988 ±0.0010	0.9940 ±0.0029
	High pH	0.9800 ±0.0081	0.9350 ±0.0092	1.0311 ±0.0037	0.9924 ±0.0013	0.9975 ±0.0012	0.9959 ±0.0020
Low (0 to 30 °)	Low pH	0.9773 ±0.0036	0.9348 ±0.0101	1.0300 ±0.0008	0.9970 ±0.0032	0.9970 ±0.0015	0.9949 ±0.0023
	High pH	0.9864 ±0.0026	0.9587 ±0.0050	1.0350 ±0.0001	0.9825 ±0.0023	0.9963 ±0.0010	0.9982 ±0.0014
Average		0.9805 ±0.0140	0.9502 ±0.0129	1.0239 ±0.0085	0.9891 ±0.0092	0.9978 ±0.0015	0.9951 ±0.0028

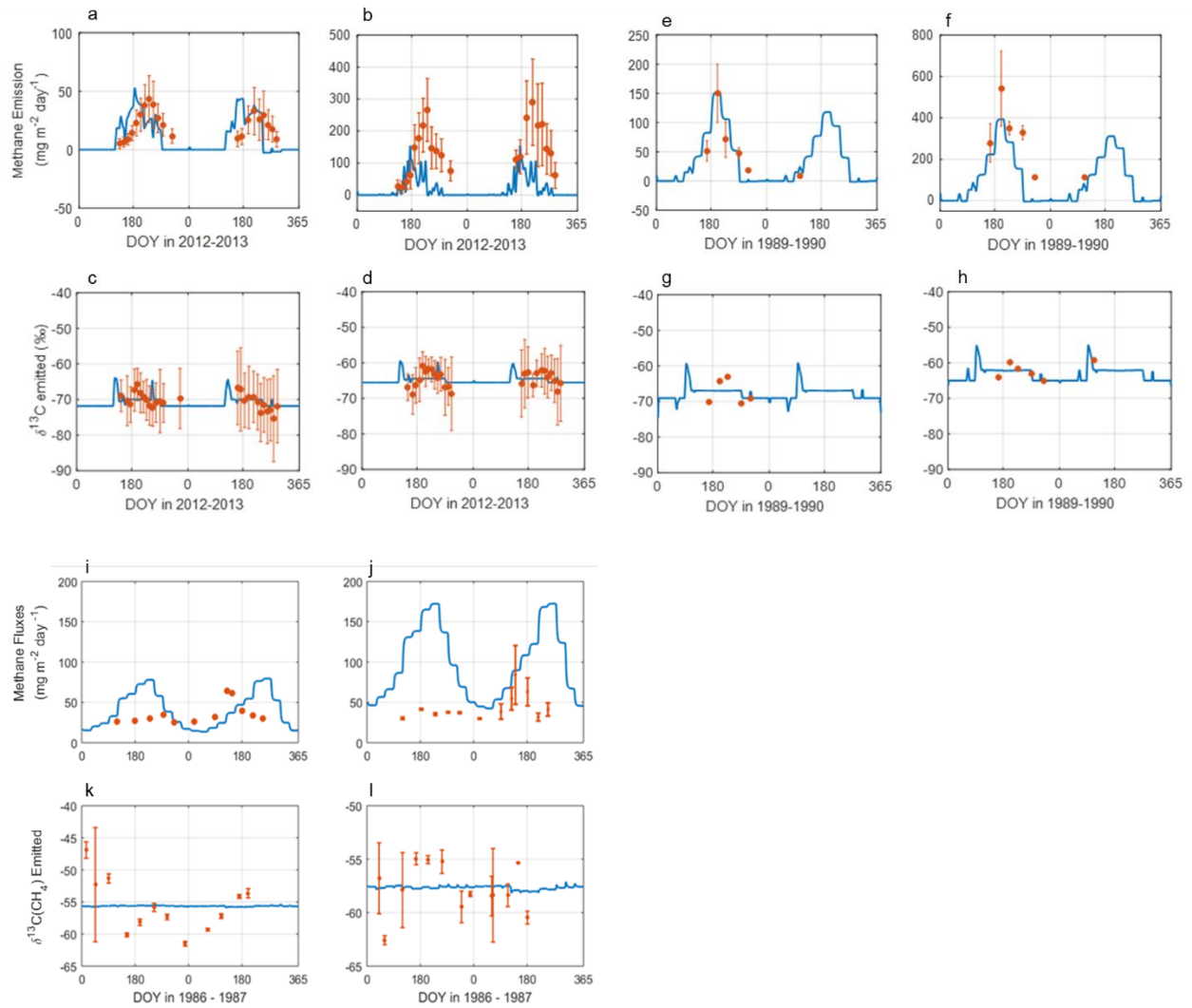


Figure 3.4 Calibration results of seasonal methane emissions in $\text{mg m}^{-2} \text{day}^{-1}$ (a,b,e,f,i,j) and its carbon isotope changes in $\delta^{13}\text{C}-\text{CH}_4$ (c,d,g,h,k,l) for low-pH (a,c,e,g,i,k) and high-pH (b,d,f,h,j,l) system in boreal (a-d), temperate (e-h), and tropic (i-l) regions. Red error bars represent observation with standard deviation, and blue lines represent simulation results.

3.3.3 Simulation setup

To make spatially- and temporally-varying estimates of methane emission and $\delta^{13}\text{C}\text{-CH}_4$ on the global scale, we used spatially explicit data of land cover, soil pH and textures, meteorology and leaf area index (LAI) (Zhuang et al. 2004). The vegetation and soil texture data sets were used to assign vegetation-specific and texture-specific parameters to a grid cell (Melillo et al. 1993; Zhuang et al. 2003). The soil-water pH dataset was used to estimate methane production across the study region (Carter and Scholes 2000). Meteorological inputs were derived from historical air temperature, precipitation, vapor pressure, and cloudiness from gridded CRU time-series data, version 4.01 (Harris et al. 2014). We used monthly LAI data derived from satellite imagery (Myneni et al. 2002) to prescribe LAI for each 0.5° latitude and longitude grid cell.

Because multiple wetland flux data sets exist (using different wetland inundated areas), we provide a source signature value for every grid cell globally by assuming wetland exists each grid cell. It can therefore be used in conjunction with any flux and wetland area dataset. The original wetland type from Matthews and Fung (1987) is in Fig. 3.5a. To fill the grid cells without wetland types, we set low-pH forested wetlands at acidic soil sites, and set high-pH non-forested wetlands at alkaline soil sites based on the pH 7 (Fig. 3.5b-c).

In our analyses, we used wetland fluxes defined over the static and time-varying inundated area from Matthews and Fung (1987) and Poulter et al. (2017), respectively. Simulated ecosystem-specific methane emissions from wetlands were then area weighted for each grid cell, as defined by the fractional inundation data. Finally, we used monthly meteorological inputs of the Gridded Climatic Research Unit (CRU) (Harris et al. 2014) to run a global wetland simulations with 10 ensemble members from 1984 to 2016 with a daily time-step at a spatial resolution of $0.5^\circ \times 0.5^\circ$. A 15-year of spin-up was used for methane and its isotope equilibrium in soils.

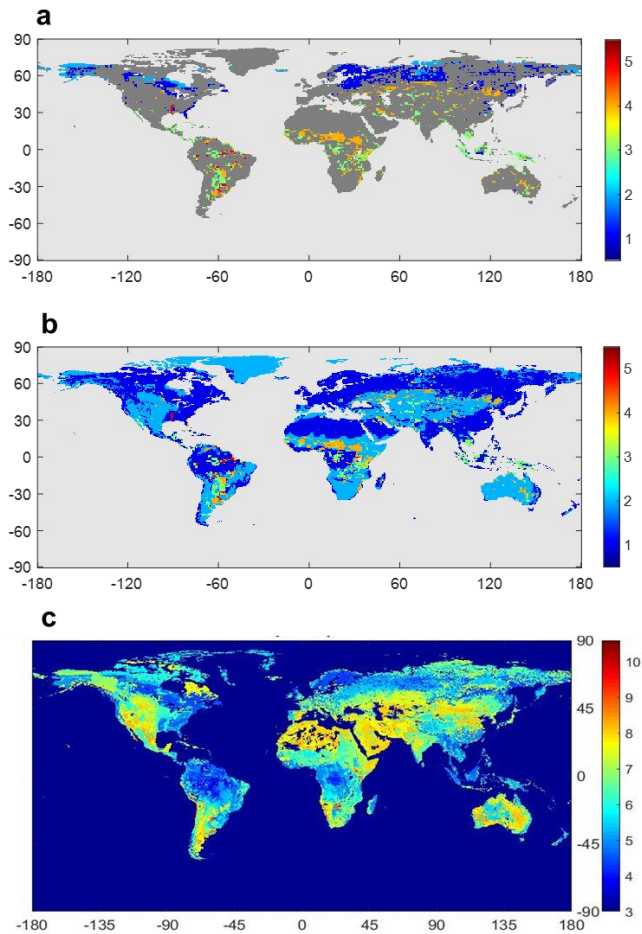


Figure 3.5 global soil wetland and pH map. (a) default wetland type map from Matthews and Fung (1987), where type 1 and 2 represent forested and non-forested bog, type 3 and 4 represent forested and non-forested swamp, and 5 represent alluvial wetlands. The wetland map was developed based on vegetation, soil properties, and fractional inundation, and yielded a global distribution of wetland sites identifies with in situ ecological and environmental characteristics. (b) filled wetland types assuming low-pH soils are in type 1 and high-pH soils are in type 2. (c) global soil pH map from (Carter and Scholes 2000).

3.3.4 Model data comparison

Site level

We compared our model results with previously published data from 58 in-situ measurements organized by Holmes et al. (2015) and 66 in-situ measurements Sherwood et al. (2017). (Table 3.5). Holmes et al. (2015) compiled data of latitude, fraction of HM and AM, pH, vegetation, $\delta^{13}\text{C-CH}_4$ from global wetlands to understand factors affecting the methanogenic pathway in different wetlands. This paper found that a combination of environmental parameters including pH, vegetation type, nutrient status, and latitude are correlated to the dominant methanogenic pathway from the principal component analysis. Sherwood et al. (2017) compiled database of $\delta^{13}\text{C-CH}_4$ from all methane sources including fossil fuel, microbial, and biomass burning sources. The wetland database of Sherwood et al. (2017) includes literature reference, latitude, wetland types, measurement methods.

After combining the overlapped data between Holmes et al. (2015) and Sherwood et al. (2017) and removing the data that we used for our model optimization (McCalley et al. 2014; Kelly et al. 1992; Burke et al. 1988), 71 sites remained for site-level validation. Due to a possible mismatch of soil and vegetation properties, and wetland distribution of grid cells between model and observation, we compared the observed $\delta^{13}\text{C-CH}_4$ with simulated data of the sampling year within two adjacent grid cells ($1^\circ \times 1^\circ$) of the observation.

Table 3.5 Site-level observations from Holmes *et al.* (2015) and Sherwood *et al.* (2017).

No.	Literature	Lat	Lon	$\delta^{13}\text{C}$- CH₄ mean	$\delta^{13}\text{C}$-CH₄ uncertainty
1	Brownlow et al. 2017	-16	-69.5	-59.7	1.0
2	Brownlow et al. 2017	-3.5	-62	-63.9	0.8
3	Tyler et al. 1987	-2.5	-62	-54	7.3
4	Quay et al. 1988	-2.5	-62.5	-58.47	9.0
5	Devol et al. 1996	0	39.5	-51.6	17.6
6	Tyler et al. 1988	0	29.5	-54.2	0.6
7	Tyler et al. 1988	0.5	36	-48	2.5
8	Tyler et al. 1988	1	33.5	-58.7	4.1
9	Brownlow et al. 2017	2	31.5	-53	0.4
10	Brownlow et al. 2017	5	118	-61.5	2.9
11	Brownlow et al. 2017	6	101	-65.9	5.6
12	Nakagawa et al. 2002a	8.5	-83.5	-73.9	3.8
13	Brownlow et al. 2017	9	-80	-61.9	3.2
14	Tyler 1989a	10.5	-85.5	-53.3	1.7
15	Brownlow et al. 2017	22	114	-55.7	3.3
16	Brownlow et al. 2017	25	-80.5	-60.97	3.0
17	Stevens and Engelkemeir 1988; Chanton and Martens 1988; Holmes 2014	25.5	-80.5	-61.7	3.6
18	Burke et al. 1988	28	-81.5	-63.6	6.1
19	Burke and Sacket 1986	29	97	-68.3	5.0
20	Liu et al., 2013	29.5	-90	-60.1	0.2
21	Burke and Sacket 1986	33	80	-51.1	5.0
22	Liu et al., 2013	34	-81	-53.5	1.6
23	Burke and Sacket 1986	34.5	-78.5	-65.27	1.0
24	Martens et al. 1986; Chanton and Martens 1988	39	-80	-56.7	3.3

Table 3.5 continued

25	Wahlen et al. 1989	40	-106	-50.7	1.1
26	Tyler 1986	41	-89.5	-50.4	0.8
27	Stevens and Engelkemeir 1988	41.5	-72.5	-64.06	5.2
28	Oana and Deevey 1960	42	-83	-64.4	7.9
29	Hornibrook et al., 1997; Hornibrook et al., 2000; Mayer et al., 1998	43	-73.5	-58.3	2.4
30	Wahlen et al. 1989	43	-81	-52.5	13.5
31	Hornibrook et al., 1997; Hornibrook et al., 2000	45	-76	-75	5.0
32	Alstad and Whiticar, 2011	47	-94	-66	6.0
33	Quay et al. 1988	47	-122	-74	0.5
34	Conrad, 1999; Lansdown et al., 1992	48	-94	-67.2	5.0
35	Stevens and Engelkemeir 1988	49	-79	-60	3.2
36	Kuhlmann et al. 1998	49	-95	-65.1	1.0
37	Chasar et al., 2000	49.5	9.5	-57.4	2.1
38	Levin et al. 1993	50	12	-56	6.0
39	Hädrich et al., 2012; Kuesel et al., 2008; Paul et al., 2006; Reiche et al., 2008	52	-4	-63.9	15.0
40	Hornibrook and Bowes, 2007	52.5	10.5	-58.4	2.4
41	Woltemate 1982	55	-113	-67.5	3.0
42	Alstad and Whiticar, 2011	57	83	-60	15.0
43	Kotsyurbenko et al., 2004	59	-99	-62.9	1.9
44	Wahlen et al. 1989	60	-149	-67.9	5.0
45	Chanton et al., 2006; Duddleston et al., 2002; Hines et al., 2001	60.5	-155.5	-66	2.4
46	Martens et al. 1992	60.5	-145.5	-51.3	14.2
47	Douglas et al. 2016	61	74	-63.8	5.4
48	Nisbet 2013	61	24	-70.63	15.0
49	Galand et al., 2010	62	129	-61.45	4.4

Table 3.5 continued

50	Nakagawa et al. 2002b	64.5	-153	-73.1	0.8
51	Walter et al. 2008	65	-148	-56.6	11.3
52	Douglas et al. 2016	66	-151	-65.5	5.0
53	Chanton et al., 2006; Hines et al., 2008; Rooney-Varga et al., 2007	66	-150	-62.8	5.0
54	Chanton et al., 2006; Hines et al., 2008; Rooney-Varga et al., 2007	67.5	26	-69.75	2.8
55	Fisher et al. 2017	68	-153.5	-72.5	2.9
56	Walter et al. 2008	68	18.5	-72.95	2.0
57	Fisher et al. 2017	68	25	-70.15	5.3
58	Hines et al., 2008; Levine and Whalen, 2001; Rooney-Varga et al., 2007	68	-149	-62.9	5.0
59	Fisher et al. 2017	68.5	19	-68.6	4.1
60	Quay et al. 1988	68.5	-154.5	-62.6	5.0
61	Walter et al. 2006, Walter et al. 2008	69	129	-70.3	6.0
62	Douglas et al. 2016	69	19	-64.6	12.1
63	Chanton et al., 2006; Hines et al., 2008; Rooney-Varga et al., 2007	69	-150	-65.9	5.0
64	Bowden et al., 2008; Chanton et al., 2006; Hines et al., 2008; Rooney-Varga et al., 2007	69	-149	-62.3	5.0
65	Chanton et al., 2006; Hines et al., 2008; Rooney-Varga et al., 2007	69	-148	-57.8	5.0
66	Fisher et al. 2017	69	27	-71.7	2.5
67	Fisher et al. 2017	69.5	29	-72	1.1
68	Chanton et al., 2006; Hines et al., 2008; Rooney-Varga et al., 2007	70	-149	-58.1	5.0
69	Douglas et al. 2016	71	-156.5	-56.5	7.5
70	Bouchard et al. 2015	73	-79.5	-60.5	4.0
71	Fisher et al. 2011	78	98.5	-68.7	2.4

Regional level

We used aircraft air samples for 3 regions in Alaska from Carbon in Arctic Reservoirs Vulnerability Experiment (CARVE) (Miller et al. 2016; Chang et al. 2014). From 2012 to 2015, CARVE collected airborne measurements of atmospheric carbon dioxide, methane, and carbon monoxide and relevant land surface parameters in the Alaskan Arctic to provide insights into Arctic carbon cycling. During the airborne measurements, flask samples were collected to send them to NOAA ESRL GMD for 50 trace gas analysis including CO₂, CH₄, CO, OCS, HC's and their isotopic signatures. After screening aircraft data with flags, total data points are 1,476 during the measurement period.

To compare the spatial variability wetland $\delta^{13}\text{C-CH}_4$, we divided the Alaskan continent into three regions: North slope, interior, and southwest Alaska based on the latitudes (62-68, 57-62, 52-57 °N for North slope, interior, and southwest, respectively). We used Keeling and Miller-Tans (M-T) plots to identify the source signatures of $\delta^{13}\text{C}$ of methane from wetlands (Keeling 1960; Miller and Tans 2003). To identify wetland isotopic signatures, we removed data that may have effects from fossil fuel emission ($\text{C}_3\text{H}_8 < 300$ ppt), biomass burning ($\text{CO} < 300$ ppb), and transport influence (Altitude $< 1500\text{m}$). For M-T plots, we set the background altitude to be $> 5000\text{m}$. After plotting the data, year 2014 was screened out due to the limited data points with low R^2 for both Keeling and M-T plots (Table 3.6).

Table 3.6 Regional-level observation of Alaska airborne measurements from North-slope (N), interior (IN), and southwest (SW) Alaska in 2012-2013, and 2015.

	Keeling plot			Miller-Tans plot		
	N	IN	SW	N	IN	SW
Year 2012	-65.75	-66.50	-62.37	-65.90	-66.43	-62.61
Year 2013	-65.53	-74.81	-54.73	-65.92	-75.47	-54.67
Year 2015	-63.71	-64.42	-59.83	-63.65	-64.31	-59.74
Mean	-65.00	-68.58	-58.98	-65.16	-68.74	-59.01
Standard Deviation	1.12	5.50	3.89	1.30	5.93	4.02

3.3.5 Forward modeling using TM5 chemical transport model

3.3.5.1 Isotope mass balance and bottom-up inventory

We first set up the bottom-up inventory for each emission scenario using isotope mass balance. Considering the global atmosphere as one box with mass conservation, the global mass balance of CH₄ can be expressed on a yearly time scale (t=1 yr) as Equation 3.16, where [CH₄] is the global burden, τ is the atmospheric lifetime, Q_{ATM} is total emissions to the atmosphere, and $\frac{[\text{CH}_4]}{\tau}$ is total sinks. Total emissions to the atmosphere Q_{Atm} include sub-categories of emissions (Q) from microbial (Mic), fossil emission (FE, including FF and natural geological seeps) and biomass/biofuel burning (BB) sources as Equation 3.17. A similar equation can also be written for $\delta^{13}\text{C}_{\text{atm}}$ in Equation 3.18, where $\delta^{13}\text{C}_x$ in the right-hand side is the emission-weighted source signature of a specific category of emissions, $\delta^{13}\text{C}_Q$ in the left-hand side is the combined signal of $\delta^{13}\text{C}$ emitted to the atmosphere. Atmospheric $\delta^{13}\text{C}_{\text{atm}}$ also sees the combined effects of emissions and sinks on the ¹³C/¹²C ratio. All sink processes enrich the atmosphere with ¹³C due to their faster reactions with ¹²C. In Equation 3.19, ε is defined as the sink-weighted average fractionation factor due to reactions with OH, Cl, and O(¹D) and the soil sink, each with different fractionation.

$$\frac{d[\text{CH}_4]}{dt} = Q_{\text{Atm}} - \frac{[\text{CH}_4]}{\tau} \dots \text{Equation 3.16}$$

$$Q_{\text{Atm}} = Q_{\text{Mic}} + Q_{\text{FE}} + Q_{\text{BB}} \dots \text{Equation 3.17}$$

$$\delta^{13}\text{C}_Q \cdot Q_{\text{Atm}} = \delta^{13}\text{C}_{\text{Mic}} \cdot Q_{\text{Mic}} + \delta^{13}\text{C}_{\text{FE}} \cdot Q_{\text{FE}} + \delta^{13}\text{C}_{\text{BB}} \cdot Q_{\text{BB}} \dots \text{Equation 3.18}$$

$$\delta^{13}\text{C}_Q = \alpha \cdot \delta^{13}\text{C}_{\text{atm}} + \varepsilon \dots \text{Equation 3.19}$$

The emission scenarios covering 1984-2016 were constructed for 3D model runs. We first estimated top-down total emissions using Eq. 3.16 with observed global atmospheric CH₄ growth

rate $\frac{d[\text{CH}_4]}{dt}$ and $[\text{CH}_4]$, and modelled lifetime τ . A conversion factor of 2.763 Tg/ppb, based on TM5 atmospheric mass, is used to convert dry mole fraction to Tg of CH_4 .

The top-down estimates show step increases in emissions in 2007 and 2014, which sum up to a ~40 Tg/yr increase in annual emissions at 2016 compared with those during the 1999-2006 stable period. To satisfy the global mass balance of CH_4 , all candidate emission scenarios are designed to have the same total emissions as the top-down estimates. Specifically, we assumed wetland increases are fully responsible for the global emission increase since 2007. Thus the 40 Tg/yr additional increase with inter-annual variability is assigned to wetland emissions, and ruminant and oil/gas emissions are adjusted to fit the top-down total (Table 3.7 and Fig. 3.6-3.7).

Table 3.7 Data sources for total emissions and their spatiotemporal patterns used in building different emission scenarios for model simulations.

Source	Total emissions	Spatial distribution	Seasonal cycle
Fossil Emission (FE)	EDGAR 4.3.2 for coal, oil and natural gas, and other energy/industry (Janssens-Maenhout et al., 2017). ONG and coal are disaggregated because their $\delta^{13}\text{CH}_4$ signatures are different.		n/a (annual resolution)
	Etiopie et al. (2019) for geological seeps.		Time invariant
Biomass and biofuel burning (BB)	Biomass burning fluxes between 1997-2016 are from GFED 4.1s with monthly resolution (Van der Werf et al., 2017)		
	Biomass burning fluxes before 1997 are from Reanalysis of the Tropospheric chemical composition project (Schultz et al., 2008)	GFED 4.1s for 2000	GFED 4.1s for 2000
	Biofuel fluxes are from EDGAR 4.3.2		n/a (annual resolution)
Modern Microbial (Mic)	Ruminants and waste/landfills fluxes are from EDGAR 4.3.2		n/a (annual resolution)
	Rice fluxes are from EDGAR 4.3.2		Matthews et al. (1991) with monthly resolution
	Wild animals and termites fluxes are from Bergamaschi et al. (2007), with daily resolution but without inter-annual variability		
	Wetland (positive) and soil sink (negative) fluxes are from a process-based model with monthly resolution (Liu et al., 2019)		

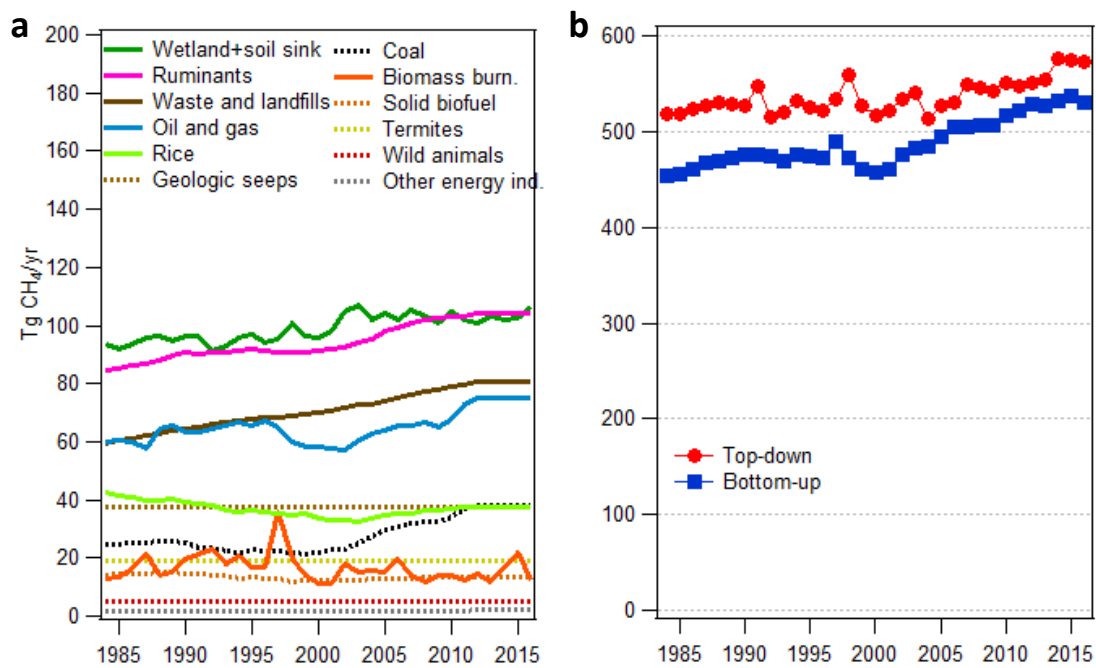


Figure 3.6 (a) Bottom-up emissions for each category and (b) total emissions including soil sinks (negative) estimated by bottom-up (i.e., the total of a) and top-down approaches. The data sources can be found in Table 3.7.

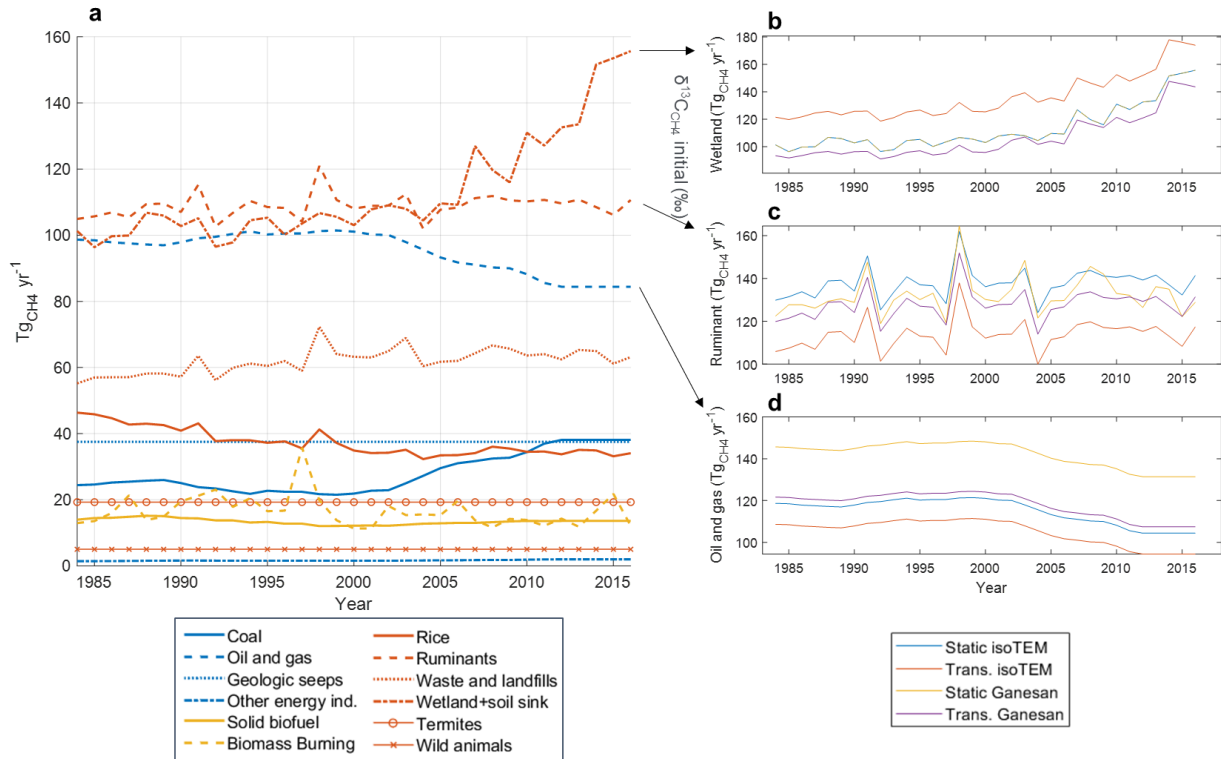


Figure 3.7 Bottom-up emissions for each category and scenario. (a) Bottom-up emissions for each category for static isoTEM scenario. Changes of emissions in (b) wetland, (c) ruminant, and (d) oil/gas for different scenarios of isoTEM with static inundation (blue), isoTEM with transient inundation (red), Ganesan *et al.* (2018) with static inundation (yellow), and Ganesan *et al.* (2018) with transient inundation (purple). The data sources can be found in Table 3.7.

3.3.5.2 TM5 Model setup

Atmospheric CH₄ mole fractions and $\delta^{13}\text{C-CH}_4$ were simulated from January 1, 1984 to January 1, 2017 by coupling the surface fluxes and isotope source signatures with the TM5 tracer transport model driven by ECMWF ERA Interim meteorology with the 4DVAR branch of the TM5 model (Basu et al. 2013; Meirink et al. 2008). TM5 was run globally at $6^\circ \times 4^\circ$ over 25 vertical sigma-pressure hybrid levels, for total CH₄ and $^{13}\text{CH}_4$. For each source type, $^{13}\text{CH}_4$ fluxes were derived from total CH₄ fluxes and source-specific isotope source signatures. Our model setup consists of the OH field from Spivakovsky et al (2000) scaled by 0.901, tropospheric Cl field from Hossaini et al (2016), and fractionation factors for $^{13}\text{CH}_4$ for the atmospheric loss reactions from Saueressig et al (2001). For this setup, we calculated the CH₄ lifetime from the decay of a CH₄ tracer with a realistic initial field in 1984 and no sources. Despite the climatological OH, Cl and O¹D fields, the CH₄ lifetime is not a constant every year from 1984 to 2016 due to changes in meteorology.

We constructed the initial CH₄ mole fraction field on January 1, 1984 as follows. First, we took the 3D CH₄ mole fraction field from CarbonTracker-CH₄ (CT-CH₄) on January 1, 2003 (<https://www.esrl.noaa.gov/gmd/ccgg/carbontracker-ch4/>). Since CT-CH₄ started assimilation on January 1, 2000, its posterior mole fraction field after 3 years is expected to have spatial gradients consistent with CH₄ observations globally. Next, we calculated the average Pacific Ocean marine boundary layer (MBL) CH₄ mole fraction from this field by considering the lowest ~160 hPa between 180°W and 174°W, and derived a scaling factor between this calculated quantity and the January 1984 observed MBL average CH₄ from NOAA's global network (https://www.esrl.noaa.gov/gmd/ccgg/trends_ch4/). We scaled the January 1, 2003 CT-CH₄ field by this factor to reach a CH₄ field for January 1984 that was consistent with observed MBL CH₄ and its latitudinal gradient and had vertical gradients consistent with the TM5 model. We then calculated the initial $^{13}\text{CH}_4$ field in January 1984 from this initial CH₄ field and the estimated global average $\delta^{13}\text{CH}_4$ of -47.501 ‰ in 1984 (Schwietzke et al. 2016).

3.3.5.3 Measurements and Marine Boundary Layer references

Observational data used to evaluate model results are from flask-air measurements from NOAA's Cooperative Global Air Sampling Network (Dlugokencky et al., 2019). Weekly samples were collected in pairs of 2.5 L borosilicate glass flasks with a portable sampler and sent to NOAA in Boulder, Colorado for CH₄ analysis by gas chromatography with flame ionization detection. All CH₄ data are reported on the WMO X2004A mole fraction scale (Dlugokencky et al. 2005) and reported in units of nmol mol⁻¹ dry air (abbreviated as ppb for parts per billion by moles). A subset of the flask-air samples were then analyzed for δ¹³C-CH₄ at the Institute of Arctic and Alpine Research (INSTAAR), University of Colorado, Boulder. Isotope-ratio mass spectrometry is used for δ¹³C-CH₄ analysis, and more details are described in Miller *et al.* (2002).

A subset of the network air sampling sites predominantly influenced by well-mixed background air is used to construct Marine Boundary Layer (MBL) zonally averaged surfaces using methods developed by Masarie and Tans (1995), to represent the observational-based global trend and latitude gradient. More details on the MBL data products and uncertainties can be found at <https://www.esrl.noaa.gov/gmd/ccgg/mbl/mbl.html>. For model-observation comparisons, model results from the same set of MBL sites are sampled, and the same calculation methods are applied to model results and observations for global mean and latitude gradient.

3.4 Results

3.4.1 Modeling global isotopic signatures of wetland δ¹³C-CH₄ and its model-data comparison

We estimated that total wetland CH₄ emissions range from 120 to 150 TgCH₄yr⁻¹ and a mean global wetland δ¹³C-CH₄ is -60.78‰ with its spatial and temporal variability in 1984-2016 (Fig. 3.8). Since not all grid cells contain wetlands, Fig. 3.9 shows the wetland δ¹³C-CH₄ map masked for the wetland grid cells based on the static inundation in Fig. 3.8. The histogram of flux-weighted global wetland δ¹³C-CH₄ by isoTEM shows more variance than δ¹³C-CH₄ from Ganesan *et al.* (2018) (Fig. 3.10), as Ganesan *et al.* (2018) set the maximum, minimum, and the mean value

of wetland $\delta^{13}\text{C-CH}_4$ empirically. Our mean global source signature is heavier than the mean wetland signature of -62.25 and -61.5‰ reported in Ganesan *et al.* (2018) and Sherwood *et al.* (2017) (Fig. 3.11), respectively, and similar to the one derived by Feinberg *et al.* (2018) (approximately -60.5‰). We also showed the latitudinal gradients of flux-weighted $\delta^{13}\text{C-CH}_4$ range from a mean of -55.60‰ from the tropics to -64.11‰ from the boreal region (Fig. 3.8b). The new model also simulated a seasonal variation of $\delta^{13}\text{C-CH}_4$ with a relatively consistent value throughout the growing season for boreal and tropic regions, and with a lower value in temperate regions when methane flux is higher due to high fractionation during plant-mediated transport (mean α_{TP} of 0.982 for temperate ecosystems) (Fig. 3.12). We did not find a clear long-term change of flux-weighted wetland $\delta^{13}\text{C-CH}_4$ as it showed a consistent value during 1984-2016 (Fig. 3.13b).

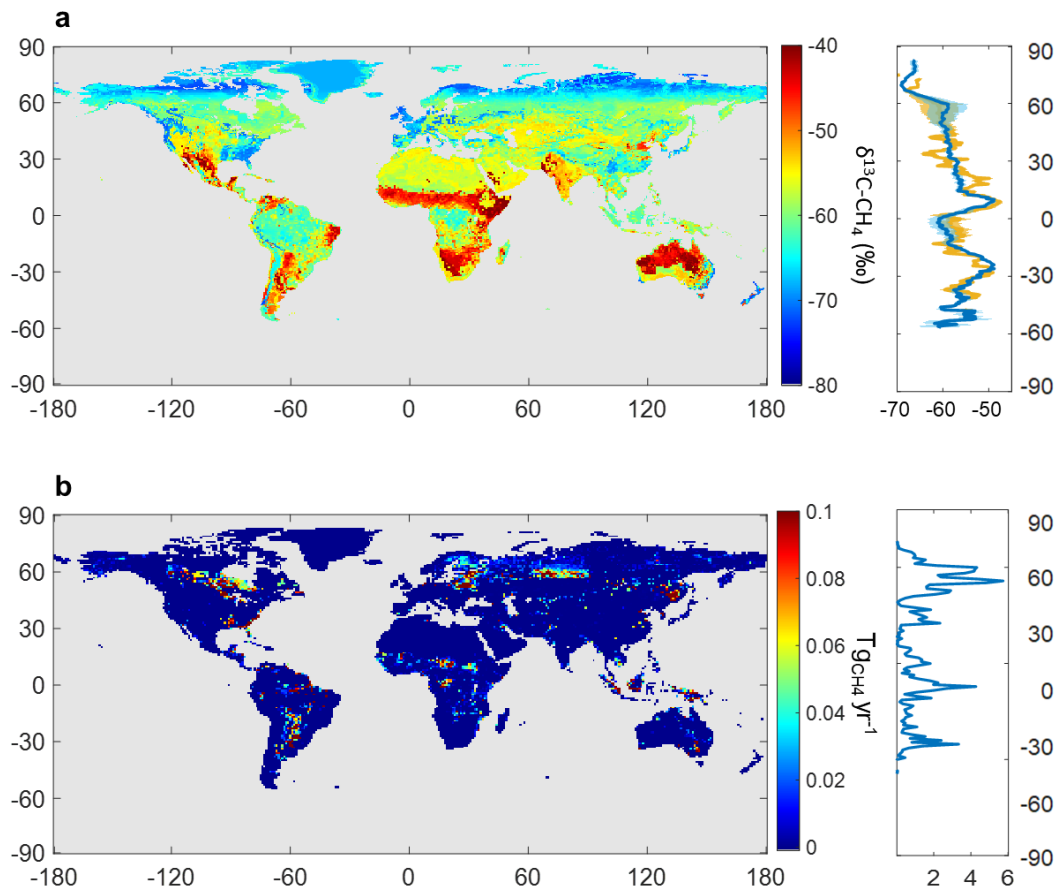


Figure 3.8 Global map of wetland methane carbon isotopic signatures ($\delta^{13}\text{C-CH}_4$) and its emissions. (a) (left) Modeled global wetland $\delta^{13}\text{C-CH}_4$ and (right) its latitudinal mean by flux not weighted (blue) and flux weighted (yellow). (b) (left) Modeled global wetland methane emissions by static inundation data from Matthews and Fung (1987) in $\text{Tg}_{\text{CH}_4} \text{yr}^{-1}$ and (right) its latitudinal sum. The error bars represent one standard deviation by varying the optimized parameters from ensemble simulations.

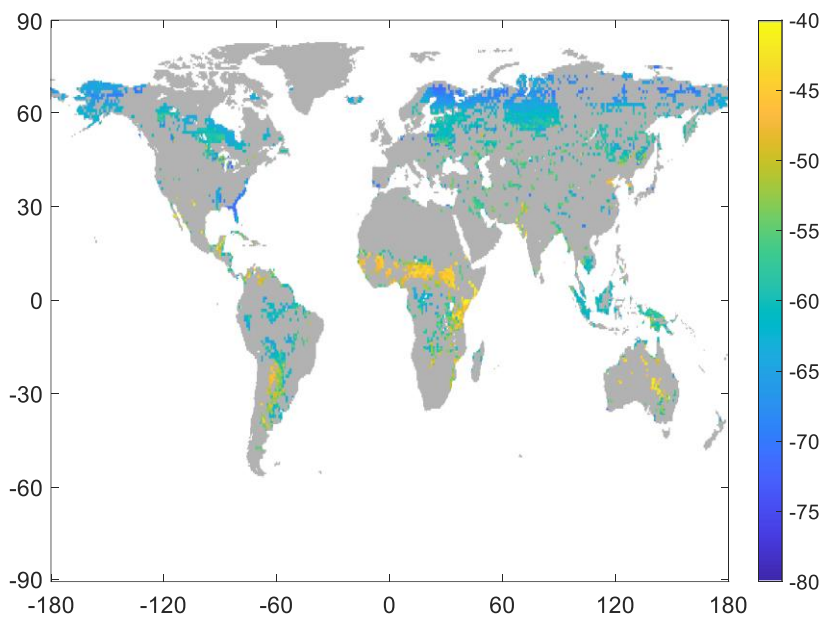


Figure 3.9 Wetland $\delta^{13}\text{C-CH}_4$ masked for grid cells using static inundation from Matthews and Fung (1987).

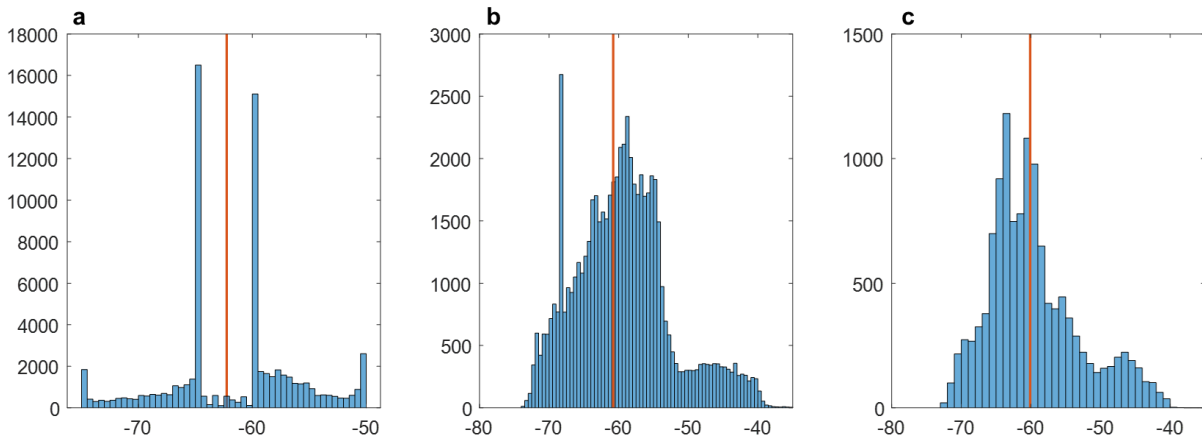


Figure 3.10 Histogram of modeled global isotopic signatures of wetland $\delta^{13}\text{C-CH}_4$ by (a) Ganesan et al. (2018), and isoTEM with (b) flux not weighted and (c) weighted.

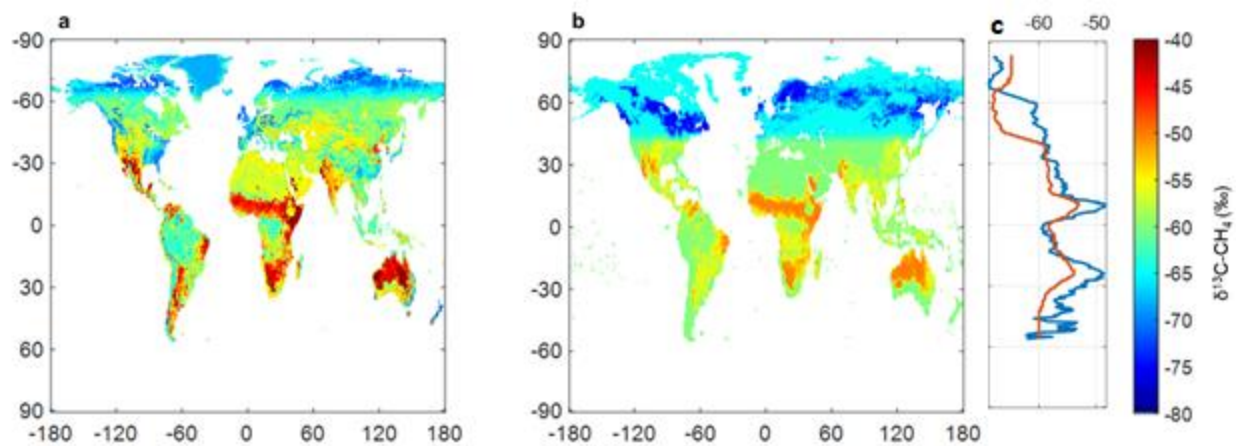


Figure 3.11 Global map of wetland $\delta^{13}\text{C-CH}_4$. Wetland $\delta^{13}\text{C-CH}_4$ by (a) isoTEM in July, 2000 and (b) Ganesan *et al.* (2018), and (c) their latitudinal gradients mean of wetland $\delta^{13}\text{C-CH}_4$ by isoTEM (blue) and Ganesan *et al.* (2018) (red).

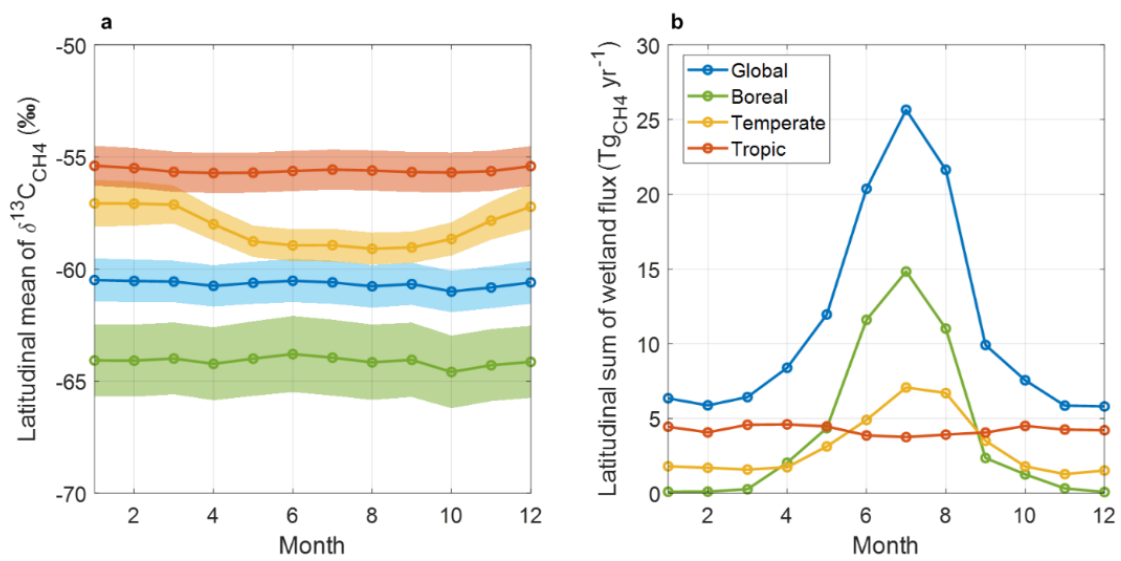


Figure 3.12 Seasonality of (a) mean $\delta^{13}\text{C}\text{-CH}_4$ and (b) sum of methane fluxes for global (blue), boreal (green), temperate (yellow), and tropic (red) regions. The error bars represent one standard deviation by varying the optimized parameters from ensemble simulations.

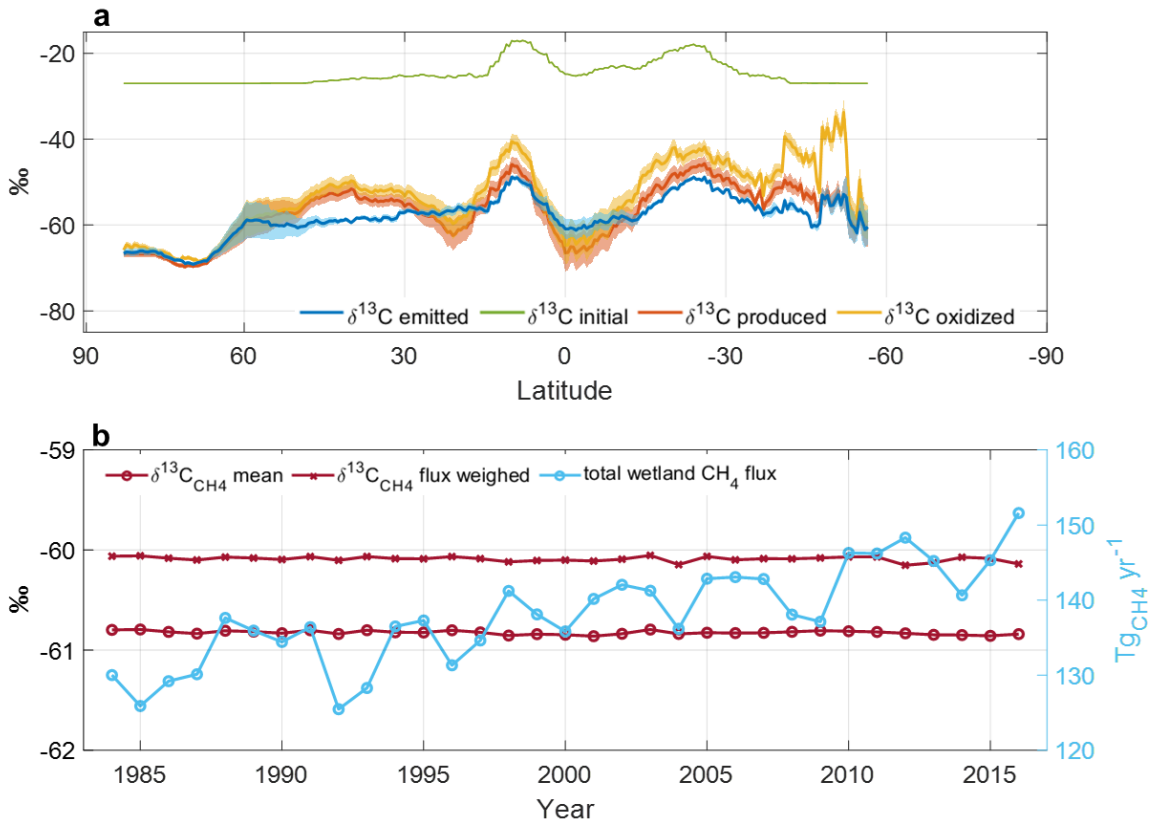


Figure 3.13 Latitudinal gradients of simulated $\delta^{13}\text{C}\text{-CH}_4$ and inter-annual variability of wetland emissions and $\delta^{13}\text{C}\text{-CH}_4$. (a) Flux-weighted mean latitudinal gradients of $\delta^{13}\text{C}$ of SOC (green), produced methane (red), methane after oxidized (yellow), and methane after transported to the soil surface (blue). The error bars represent one standard deviation by varying the optimized parameters from ensemble simulations. (b) inter-annual variability of global wetland emissions (skyblue), global mean wetland $\delta^{13}\text{C}\text{-CH}_4$ with flux weighted (maroon with cross symbol) and not weighted (maroon with circle symbol).

We validated the magnitude and spatial variability of isoTEM model comparing with Ganesan *et al.* (2018) using site-level and regional observations. First, we conducted a site-level comparison of wetland $\delta^{13}\text{C-CH}_4$ using 71 independent in situ measurements from previous studies (Table 3.5) (Holmes *et al.* 2015; Sherwood *et al.* 2017). We showed that isoTEM reduced root mean square error (RMSE) 35% compared to Ganesan *et al.* (2018) (2.33 vs. 3.60), but both Ganesan *et al.*, 2018 and isoTEM show a positive mean bias in the tropic but a negative mean bias in the temperate and arctic regions (Fig. 3.14). In specific, Ganesan *et al.* (2018) showed a mean of 1.88 ± 4.15 , -2.50 ± 4.75 , and $-1.63\pm 4.75\text{‰}$ bias of observation and model for tropical, temperate, and Arctic regions, respectively, whereas the bias for isoTEM was 0.87 ± 3.38 , -0.69 ± 4.18 , and $-1.27\pm 4.19\text{‰}$, respectively.

Furthermore, we compared the spatial variability of the simulated wetland source isotopic signatures with inferred signatures from Keeling and Miller-Tans (M-T) plots of vertical aircraft air samples for 3 regions in Alaska during 2012-2013 and 2015 (Fig. 3.15-3.16) (Miller and Tans 2003; Keeling 1960). A collected series of *in situ* samples along a N-S transect across Alaska from 60-70°N showed an average of -65.31‰ but a large variance of 8.96‰ , due to the complex vegetation and soil properties in Alaska (Chanton *et al.* 2006). The Keeling and M-T plots of observation from aircraft data also showed the spatial variability, that the $\delta^{13}\text{C-CH}_4$ from North slope Alaska is heavier ($-65\pm 1.12\text{‰}$) than the CH_4 from interior (-68.58 ± 5.50) but lighter than southwest Alaska ($-58.98\pm 3.89\text{‰}$) (Fig. 3.16, and Table 3.6). The isoTEM simulated the spatial variability (-65.53 ± 1.50 , -66.92 ± 1.51 , and $-63.65\pm 1.44\text{‰}$ for north slope, interior, and southwest Alaska, respectively), whereas Ganesan *et al.* (2018) simulated no spatial variability ($-65.07\pm 0.20\text{‰}$) (Fig. 3.15). We did not fully represent the enriched $\delta^{13}\text{C-CH}_4$ from southwest Alaska (-58.98 ± 3.89 and $-63.65\pm 1.44\text{‰}$ for observation and isoTEM, respectively), which may explain the negative bias for boreal regions from site-level comparison (Fig. 3.14). In summary, the site-level and regional model-data comparison shows that isoTEM improves the spatial variability of wetland $\delta^{13}\text{C-CH}_4$ than the previous static map.

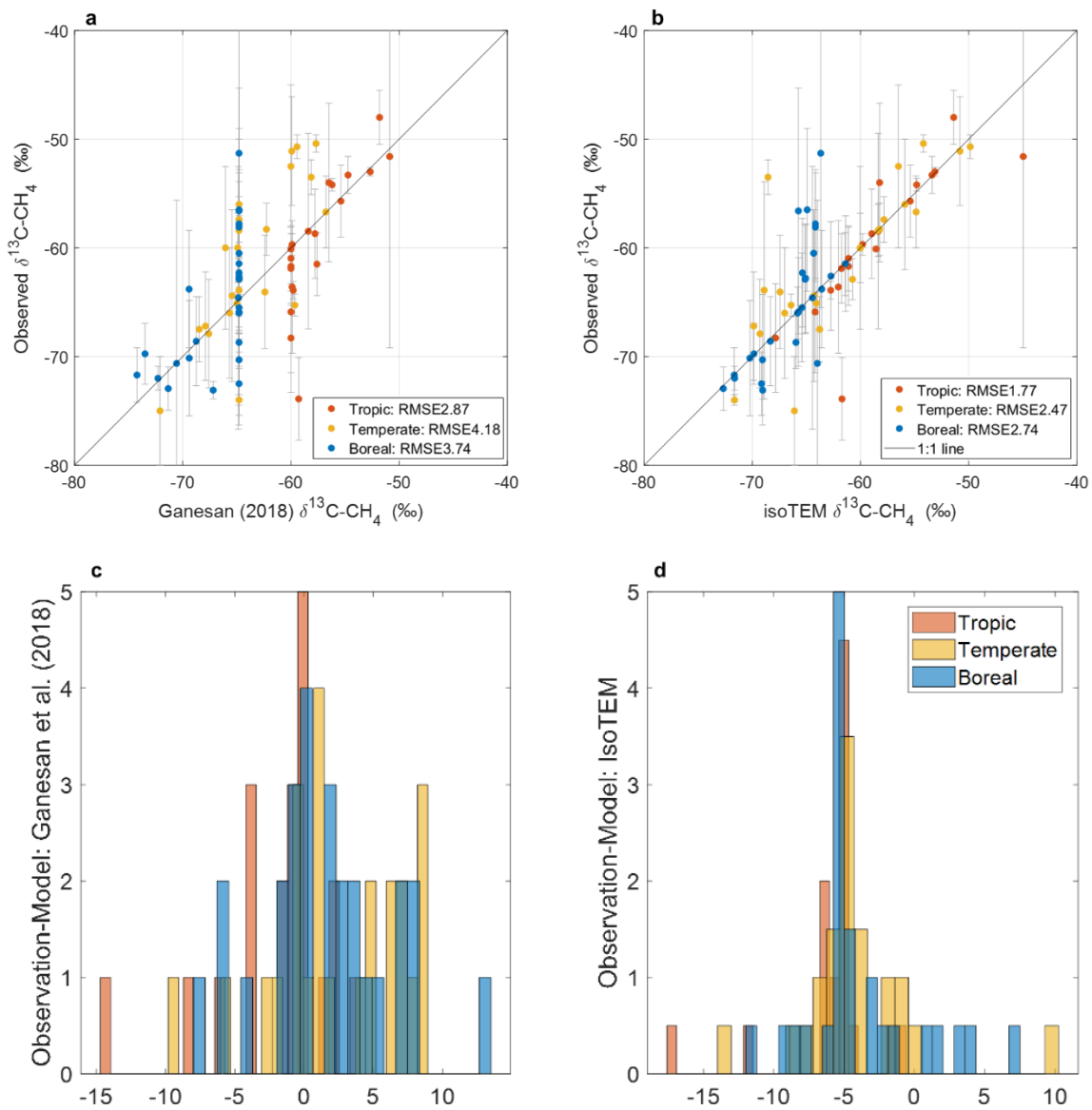


Figure 3.14 Site-level model-data comparison. (a-b) Comparison between observation and Ganesan et al. (2018) using 1:1 line with observation and (c-d) histogram of the difference between model and observation from the tropic (red), temperate (yellow), and boreal (blue) region.

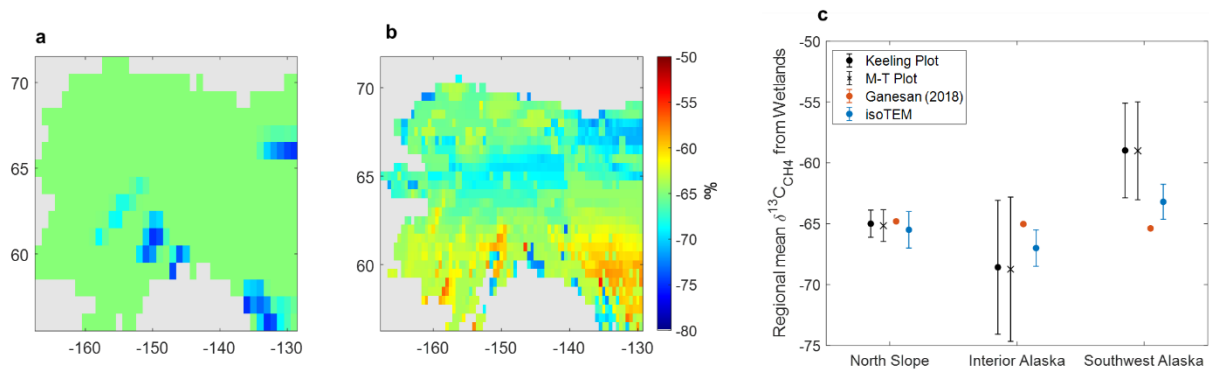


Figure 3.15 Regional model-data comparison. Simulated wetland $\delta^{13}\text{C}$ (CH₄) by (a) Ganesan *et al.* (2018) and (b) isoTEM, and (c) their comparison with observation from NOAA Alaska aircraft data using Keeling and Miller-Tans plots.

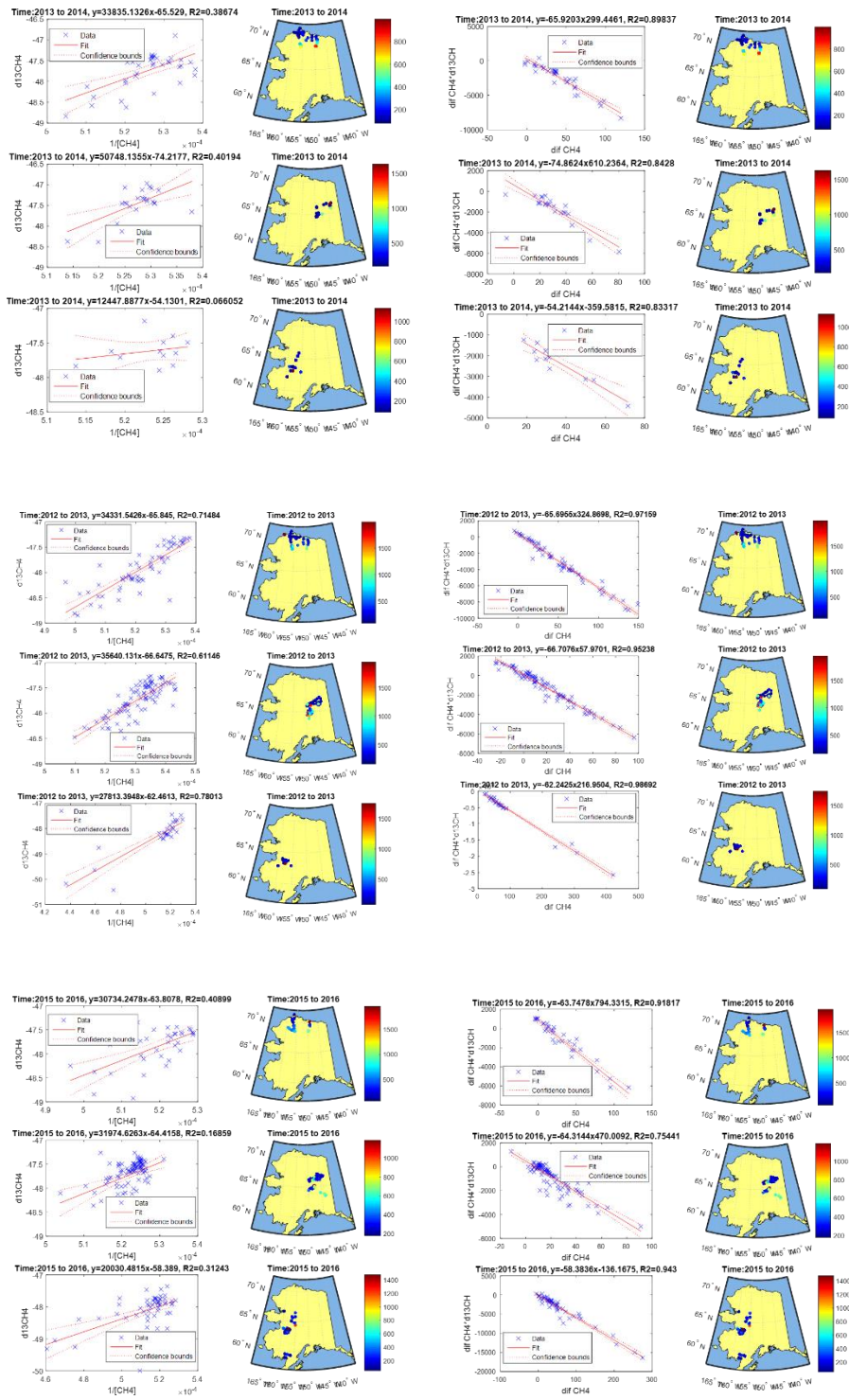


Figure 3.16 Keeling and Miller-Tans plots of airborne measurements in 2012, 2013, and 2015 for North slope, interior, and southwest Alaska.

3.4.2 Latitudinal and long-term variability of wetland $\delta^{13}\text{C-CH}_4$

After validating the simulations, we used the isoTEM results to identify the mechanisms behind the distinct latitudinal gradients of $\delta^{13}\text{C-CH}_4$ from wetlands (Fig. 3.13a), where Figure 3.17 shows how four carbon isotopic fractionations during methane dynamics affect the latitudinal gradients. First, since C4 plants are more prevalent in the tropics (Fig. 3.1), their $\delta^{13}\text{C}$ of soil organic carbon is heavier (Fig. 3.17a). Second, due to higher fraction of AM in the tropics (Fig. 3.2), the $\delta^{13}\text{C-CH}_4$ produced by methanogens is heavier (Fig. 3.17b). Third, methane oxidation is more prevalent in the tropics due to thicker oxic zone (Chanton, 2005), which makes the residual methane from the oxidation heavier (Fig. 3.17c). Lastly, due to high fraction of plant-mediated transport in the tropics (Fig. 3.18), their final methane release to the atmosphere becomes lighter (Fig. 3.17d). In summary, in our simulation, the higher $\delta^{13}\text{C-CH}_4$ from tropic wetlands are strengthened due to distribution of C3/C4 plant (40%), methanogen community (60%), methane oxidation (50%), and weakened due to plant mediated transport (-50%) (Fig. 3.13a).

Furthermore, the simulated long-term trends of wetland $\delta^{13}\text{C-CH}_4$ in 1984-2016 shows that the wetland $\delta^{13}\text{C-CH}_4$ did not change significantly during the simulation period (Fig. 3.13b). The simulation showed that increased temperature increases plant productivity and plant-mediated transport. Since $\delta^{13}\text{C-CH}_4$ becomes lighter during the plant-mediated transport (α_{TP}), the wetland $\delta^{13}\text{C-CH}_4$ showed a decreasing trend during 1984-2016 (Fig. 3.18). However, the change was not significant when applying uncertainties of the ensemble simulations (0.95‰). We acknowledge that the latitudinal and long-term variability of wetland $\delta^{13}\text{C-CH}_4$ are simulation results based on the mechanistic processes and parameters of our model. More atmospheric and field measurements are necessary to verify these results and better understand the mechanisms.

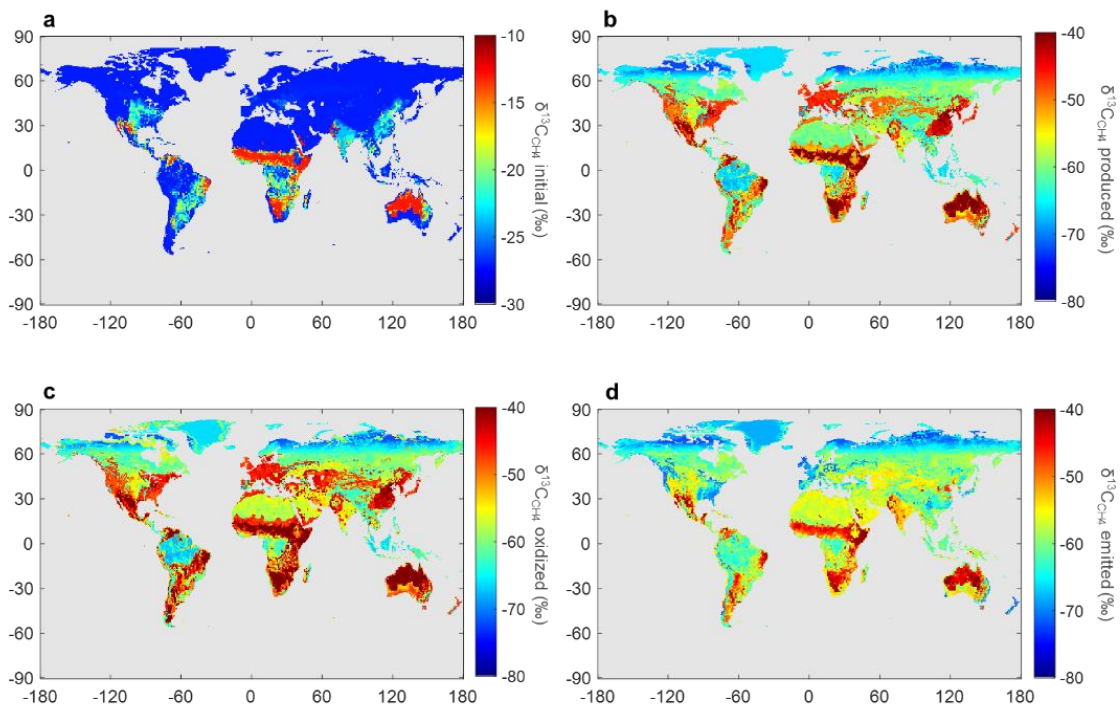


Figure 3.17 Spatial map of $\delta^{13}\text{C}$ simulated in isoTEM. Map of $\delta^{13}\text{C}$ of (a) SOC, (b) produced methane, (c) methane after oxidized, and (d) methane after transported to the soil surface.

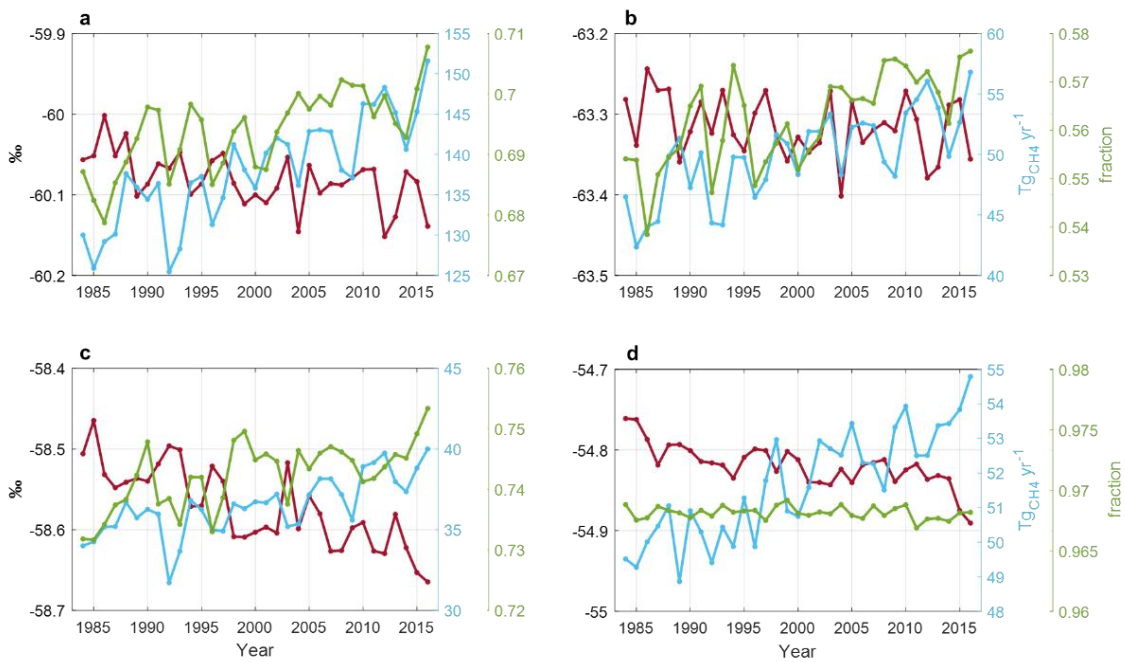


Figure 3.18 Inter-annual variability of wetland emissions (skyblue), flux-integrated wetland $\delta^{13}\text{C-CH}_4$ (Maroon), and fraction of plant-mediated transport over all three transport processes (green) for (a) global scale, (b) boreal, (c) temperate, and (d) tropic regions.

3.4.3 Implication for global methane cycling

Finally, we applied the isoTEM results as inputs for atmospheric transport modeling to understand the effects of spatially and temporally resolved wetland isotope distribution on atmospheric $\delta^{13}\text{C-CH}_4$, compared to the previous maps. We used the global atmospheric chemical transport model TM5 tracer transport model with the 4DVAR branch driven by ECMWF ERA Interim meteorology (Meirink et al. 2008; Basu et al. 2013; Krol et al. 2005). We conducted the TM5 forward run from 1984 to 2016 globally at $6^\circ \times 4^\circ$ over 25 vertical sigma-pressure hybrid levels by coupling the surface CH_4 fluxes and isotope source signatures for each source type of biogenic, fossil fuel, and biomass burning (Table 3.7 and Fig. 3.6). We spun up our model for 16 years from 1984 to 1999 and selected 2000-2016 as our analysis period with observation to ensure that our spin-up period was significantly longer than equilibration of inter-hemispheric $\delta^{13}\text{CH}_4$ gradients (Tans 1997).

We set up eight emission scenarios in total, four of them using static (Matthews, E., and Fung 1987) and another four using transient inundation data (Poulter et al. 2017). First scenario uses a globally uniform wetland signature of -62.25‰ (referred to as uniform) and the second scenario uses the static spatially-resolved wetland $\delta^{13}\text{C-CH}_4$ map from Ganesan *et al.*, 2018 (referred to as Ganesan). The third and fourth scenarios use new spatially-resolved wetland $\delta^{13}\text{C-CH}_4$ map from this study using a static map from July, 2000, and time-varying maps from 1984 to 2016 (referred to as isoTEM-static and isoTEM-dynamic, respectively). We set the bottom-up inventory for the eight emission scenarios by varying the annual wetland, ruminants, and oil and gas emissions up to $50 \text{ Tg}_{\text{CH}_4} \text{ yr}^{-1}$ (Fig. 3.7). In particular, since the flux-weighted mean of wetland $\delta^{13}\text{C-CH}_4$ is 1.5‰ enriched for isoTEM maps (-62.25 vs. -60.78‰), we reduced the oil and gas emissions by $25 \text{ Tg}_{\text{CH}_4} \text{ yr}^{-1}$ and adjusted ruminant emissions to meet the isotope mass balance (Fig 3.7c-d and Eq. 3.16-19). We compared the long-term variability and inter-hemispheric CH_4 and $\delta^{13}\text{C-CH}_4$ gradients by calculating the average Pacific Ocean marine boundary layer (MBL) between the scenarios and observation from NOAA/INSTAAR global flask-air measurements (Dlugokencky et al., 2011).

The comparison with observation showed that all scenarios reproduce the long-term variability of CH_4 reasonably well, since all scenarios satisfy the atmospheric top-down constraints when setting up the bottom-up inventory (Fig. 3.19). However, for scenarios using static

inundation, isoTEM wetland $\delta^{13}\text{C-CH}_4$ map reproduces the observed inter-hemispheric $\delta^{13}\text{C-CH}_4$ 72 and 89% better when compared with uniform and Ganesan scenarios, respectively, in terms of RMSE in 2000-2016 (Fig. 3.21). Compared with observation, uniform and Ganesan scenarios under- and over-estimated the inter-hemispheric $\delta^{13}\text{C-CH}_4$ (0.47, 0.17, and 0.58‰ for observation, uniform, and Ganesan, respectively). The inter-hemispheric $\delta^{13}\text{C-CH}_4$ between isoTEM-static and isoTEM-dynamic scenarios was similar, as isoTEM does not show a significant temporal variability (Fig. 3.21). When using transient inundation data, the inter-hemispheric CH_4 matched better compared with scenarios using static inundation data (Fig. 3.20). However, all four scenarios underestimate the inter-hemispheric $\delta^{13}\text{C-CH}_4$ compared with observation (Fig. 3.22), implying that the transient inundation data from Poulter *et al.* (2017) may need more wetland emissions from the boreal region as static inundation data (Fig. 3.23) and other satellite-driven inundated data from Prigent, Jimenez and Bousquet (2020).

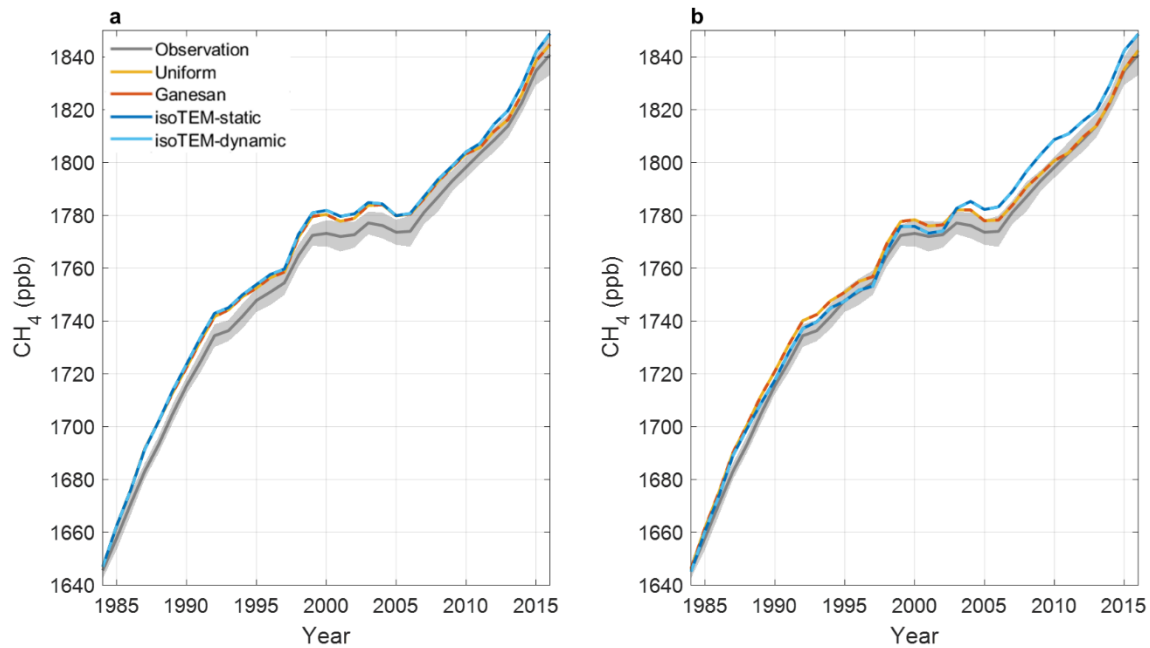


Figure 3.19 Long-term variability of atmospheric $[\text{CH}_4]$. Model-data comparison of long-term variability of atmospheric $[\text{CH}_4]$ (in ppb) by observation (grey) and simulations from uniform (yellow), Ganesan (red), isoTEM-static (blue), isoTEM-dynamic (skyblue) from 1984 to 2016 for scenarios using (a) static inundation from Matthews and Fung (1987) and (b) transient inundation from Poulter et al. (2017).

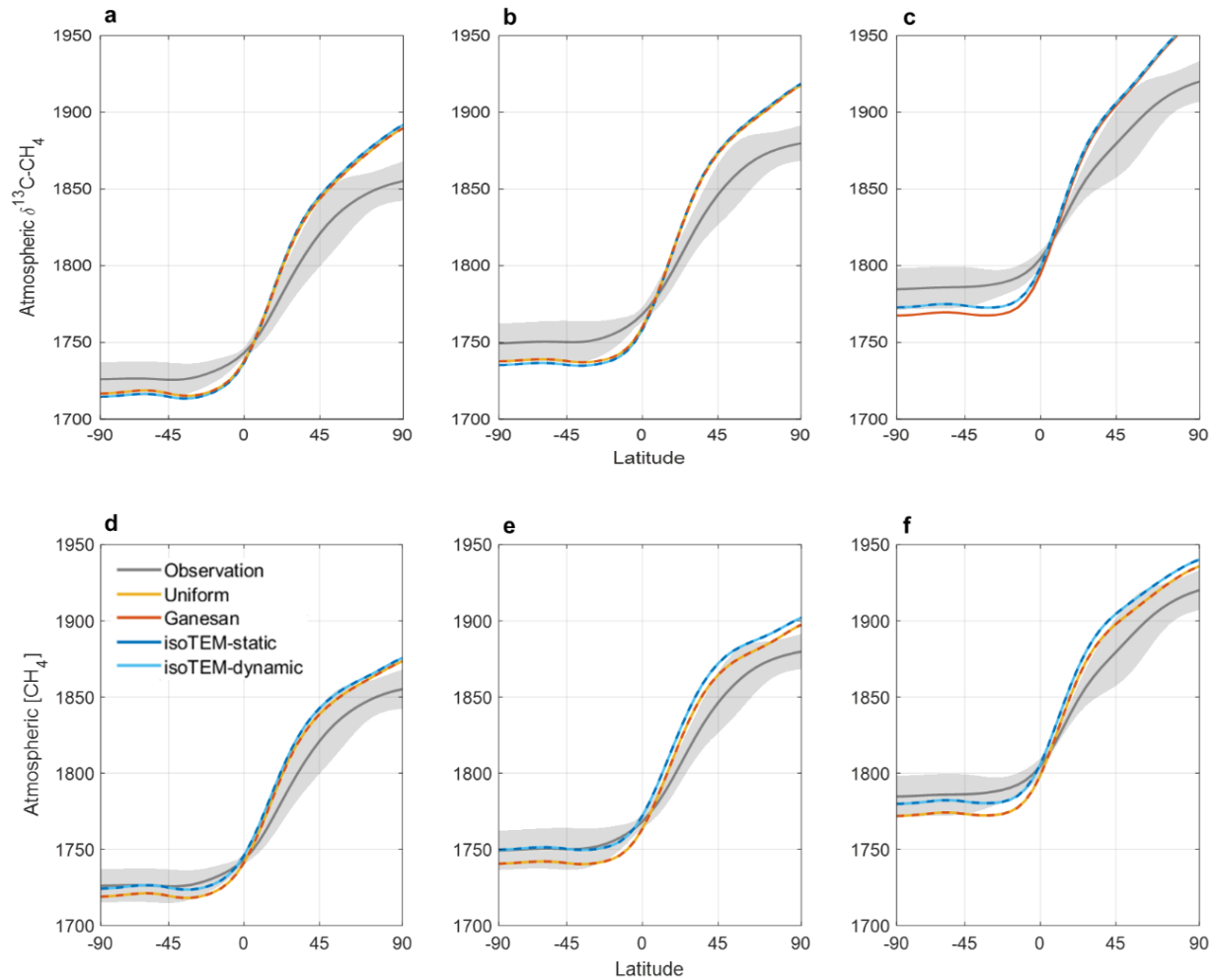


Figure 3.20 Inter-hemispheric gradients of atmospheric $[\text{CH}_4]$. Model-data comparison of global inter-hemispheric gradients of atmospheric $[\text{CH}_4]$ by observation (grey) and simulations from uniform (yellow), Ganesan (red), isoTEM-static (blue), isoTEM-dynamic (skyblue) scenarios in (a, d) 2005, (b, e) 2010, and (c, f) 2015 using (a-c) static and (d-f) dynamic inundation data from Matthews and Fung (1987) and Poulter et al. (2017), respectively.

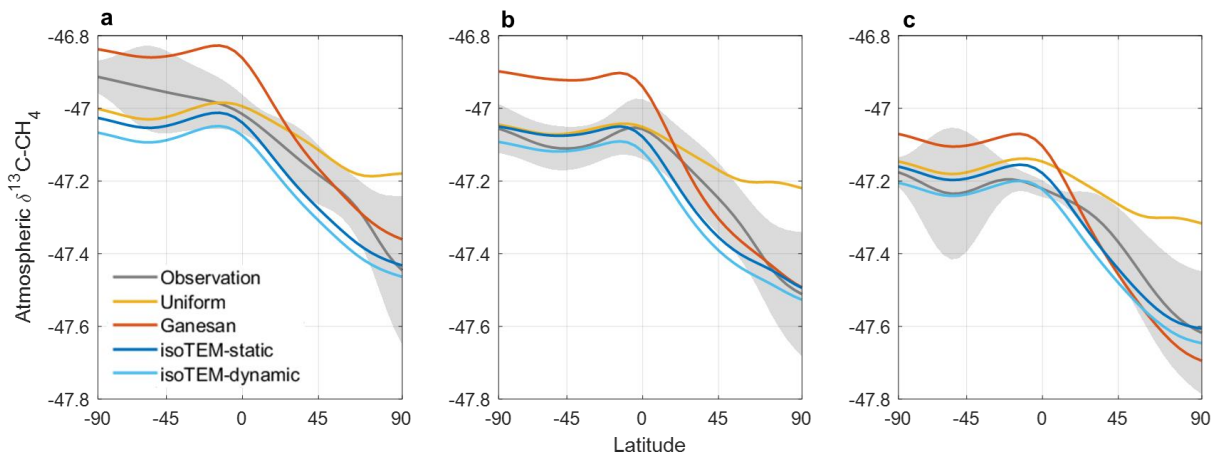


Figure 3.21 Inter-hemispheric gradients of atmospheric $\delta^{13}\text{C-CH}_4$ using static inundation. Model-data comparison of global inter-hemispheric gradients of atmospheric $\delta^{13}\text{C-CH}_4$ by observation (grey) and simulations from uniform (yellow), Ganesan (red), isoTEM-static (blue), isoTEM-dynamic (skyblue) scenarios in (a) 2005, (b) 2010, and (c) 2015 using static inundation data from Matthews and Fung (1987).

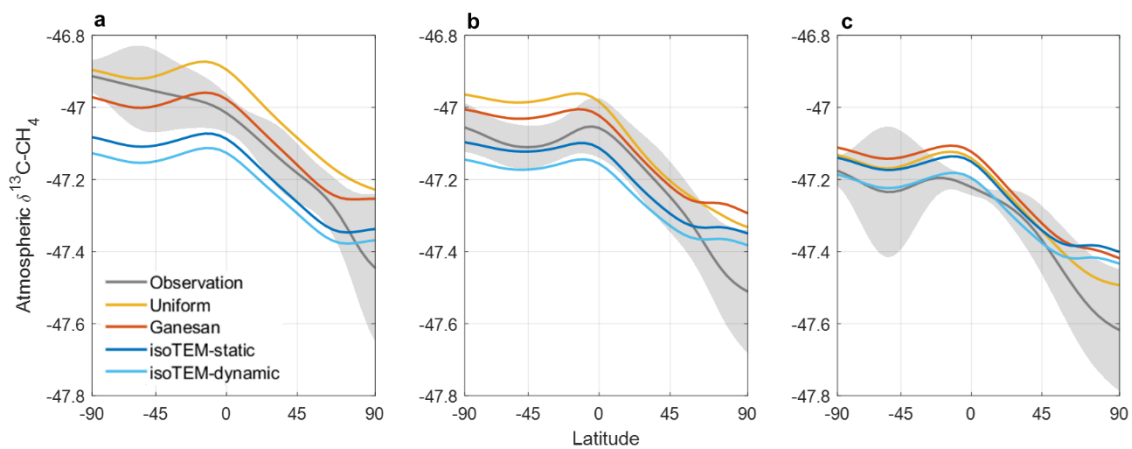


Figure 3.22 Inter-hemispheric gradients of atmospheric $\delta^{13}\text{C-CH}_4$ using dynamic inundation. Model-data comparison of global inter-hemispheric gradients of atmospheric $\delta^{13}\text{C-CH}_4$ by observation (grey) and simulations from uniform (yellow), Ganesan (red), isoTEM-static (blue), isoTEM-dynamic (skyblue) scenarios in (a) 2005, (b) 2010, and (c) 2015 using dynamic inundation data from Poulter et al. (2017).

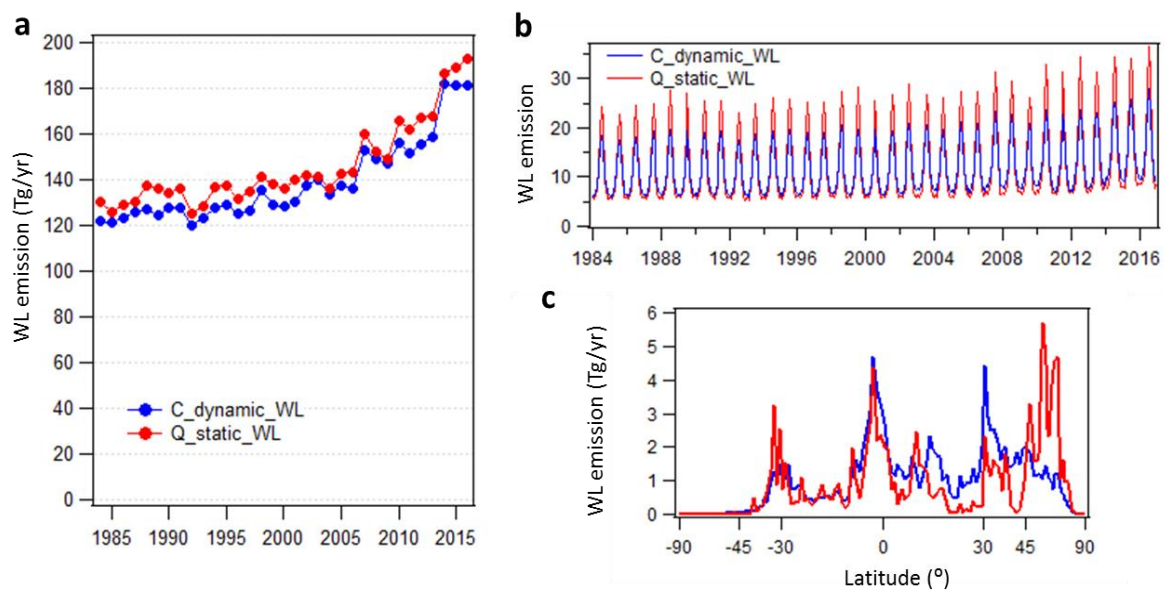


Figure 3.23 Comparisons of wetland (WL) emissions between static (red) and dynamic WL (blue) area maps for (a) annual emissions in Tg yr⁻¹, (b) seasonal cycle in Tg yr⁻¹ and (c) latitude distribution in Tg yr⁻¹.

3.5 Discussion and Conclusion

Although the new model significantly improved our understanding of the spatial and temporal variability of global wetland $\delta^{13}\text{C-CH}_4$ and global CH_4 budgets, there are still a few limitations of this study. First, we need more field and atmospheric measurements of wetland $\delta^{13}\text{C-CH}_4$ to further constrain model parameters. Our optimization of fractionation factors (α_{HM} , α_{AM} , α_{MO} , α_{TP} , α_{TD} , α_{TE}) was based on a limited amount of observations, which increases the uncertainty of our model results. Also, since we set the fraction of two methanogen communities (HM and AM) using multiple regression analysis, the fraction changes spatially but not temporally, we need a better understanding of the temporal microbial community changes as they occur when permafrost thaws and disturbance happens (McCalley et al. 2014). Finally, various methanogenic and non-methanogenic processes will change $\delta^{13}\text{C}$ of CH_4 and CO_2 , and the CO_2/CH_4 ratios, thus $\delta^{13}\text{C-CH}_4$ emitted from wetlands. We need to identify detailed vertical subsurface methane processes using isotopic labeling analysis and inhibitor techniques to include those fractionation processes in the model.

In conclusion, we developed the first-of-its-kind process-based biogeochemistry model that maps the global distribution of wetland $\delta^{13}\text{C-CH}_4$ and thoroughly validated the model using site-level and regional observations. The new model isoTEM explains latitudinal and long-term variability of $\delta^{13}\text{C-CH}_4$ from wetlands. The latitudinal gradients of $\delta^{13}\text{C}$ of methane from wetlands strengthen due to distribution of C3/C4 plant, methanogen community, methane oxidation, but weaken due to plant mediated transport. Also, the long-term trends in $\delta^{13}\text{C-CH}_4$ from wetlands may be related to increased plant-mediated transport due to increasing temperature, but the changes were within the uncertainty range of our ensemble simulations. We applied the model results as inputs for an atmospheric transport modeling and showed that the spatially and temporally resolved wetland isotope map better matches observed inter-hemispheric $\delta^{13}\text{C-CH}_4$ compared to the previous uniform and static maps.

CHAPTER 4. CARBON ALLOCATION AFFECTS SEASONAL LEAF CARBON ISOTOPIC SIGNATURES AND INFERRED WATER USE EFFICIENCY OF TEMPERATE DECIDUOUS TREES

4.1 Abstract

Temperate deciduous trees remobilize stored carbon early in the growing season to produce new leaves and xylem vessels. The use of remobilized carbon for building leaf tissue dampens the link between environmental stomatal response and inferred intrinsic water use efficiency (iWUE) using leaf carbon isotopic signatures ($\delta^{13}\text{C}$). So far, few studies consider carbon allocation processes in interpreting leaf $\delta^{13}\text{C}$ signals. To understand effects of carbon allocation on $\delta^{13}\text{C}$ and iWUE estimates, we analyzed and modeled the seasonal leaf $\delta^{13}\text{C}$ of four temperate deciduous species (*Acer saccharum*, *Liriodendron tulipifera*, *Sassafras albidum*, and *Quercus alba*) and compared the iWUE estimates from different methods, species, and drought conditions. At the start of the growing season, leaf $\delta^{13}\text{C}$ values were more enriched, due to remobilized carbon during leaf-out. The bias towards enriched leaf $\delta^{13}\text{C}$ values explains the higher iWUE from leaf isotopic methods compared with iWUE from leaf gas exchange measurements. We further showed that the discrepancy of iWUE estimates between methods may be species-specific and drought sensitive. The use of $\delta^{13}\text{C}$ of plant tissues as a proxy for stomatal response to environmental processes, through iWUE, is complicated due to carbon allocation and care must be taken when interpreting estimates to avoid proxy bias.

4.2 Introduction

Globally, temperate forests account for 25% of carbon stored as biomass and remove a significant amount of increasing anthropogenic carbon dioxide (CO_2) from the atmosphere annually (Bonan 2008). Drought has been a key disturbance agent in temperate forests, and it is predicted that droughts will occur more frequently in the future and significantly reduce forest carbon uptake capacity (Ciais et al. 2005; Stocker et al. 2013; Millar and Stephenson 2015). To understand how trees respond to water stress and how increased atmospheric CO_2 may ameliorate

the effects, water use efficiency (WUE) has been used as a key measure to link terrestrial carbon and water cycles (Frank et al. 2015; Baldocchi et al. 1997; Hoffmann et al. 2011). The responses of WUE to water stress depend on biome types and tree species in temperate forests (Yi et al. 2019; Charney et al. 2016; Yang et al. 2016), emphasizing the importance of understanding WUE to predict future forest demographics and adaptation to climate change (Fei et al. 2011, 2017).

The intrinsic WUE (iWUE), defined as the photosynthetic rate (A) divided by stomatal conductance (g_s) (Eq. 4.1), represents the trade-off between new carbon uptake and the ease with which water vapor is lost through leaf stomata in terms of internal and atmospheric CO₂ concentrations (c_i and c_a , respectively). Unlike the total WUE, defined as the ratio of A to transpiration, the iWUE is not sensitive to abiotic controls on water loss that do not affect photosynthesis (specifically, enhanced transpiration as vapor pressure deficit (VPD) rises). Thus, iWUE is a measure of WUE that more clearly reflects physiological (or biotic) responses to changing environmental conditions.

$$iWUE = \frac{A}{g_s} = \frac{(c_a - c_i)}{1.6} = \frac{c_a}{1.6} \left(1 - \left(\frac{c_i}{c_a} \right) \right) \dots \text{Equation 4.1}$$

To estimate a long-term changes in iWUE, studies have used the ratio of stable carbon isotopes (¹³C/¹²C) of plant tissues, such as tree rings and leaves (e.g. Linares & Camarero, 2012; Belmecheri *et al.*, 2014; Frank *et al.*, 2015; Cornwell *et al.*, 2018) and residual effects on atmospheric CO₂ (e.g. Keeling *et al.*, 2017). The stable carbon isotope ratio is expressed in delta notation ($\delta^{13}\text{C}$) (Eq. 4.2) (McCarroll and Loader 2004). The isotopic method of estimating iWUE is based on photosynthetic fractionation, where gas diffusion and enzymes discriminate against heavier ¹³C during photosynthesis (Farquhar and Sharkey 1982). When plants close their stomata, it causes smaller photosynthetic fractionation, higher $\delta^{13}\text{C}$ of plant tissues, smaller ratios of internal to atmospheric CO₂ concentrations (c_i/c_a), and thus higher iWUE (Eq. 4.1). Land surface models have incorporated stable carbon isotope tracers to improve model representation and prediction of terrestrial water and carbon fluxes (Raczka et al. 2016; Graven et al. 2017; Van Der Velde et al. 2013; Suits et al. 2005).

$$\delta^{13}\text{C} (\text{‰}) = \left(\frac{(^{13}\text{C}/^{12}\text{C})_{\text{sample}}}{(^{13}\text{C}/^{12}\text{C})_{\text{standard}}} - 1 \right) \times 1000 \dots \text{Equation 4.2}$$

However, the $\delta^{13}\text{C}$ of plant tissues may not be explained solely by stomatal-controlled photosynthetic fractionation. For example, the $\delta^{13}\text{C}$ of plant tissues have been found to vary across different tissue types within the same plant, where stem and root tissues are generally enriched in $\delta^{13}\text{C}$ than leaf tissue (Badeck et al. 2005; Bowling et al. 2008). The offsets vary by tree species, and reflect post-photosynthetic fractionation during construction of plant tissues and storage pools and allocation processes moving carbon between pools (Linares and Camarero 2012; Gessler et al. 2014; Cernusak et al. 2009). Post-photosynthetic processes leading to variability in $\delta^{13}\text{C}$ of internal carbon pools may cause a discrepancy of iWUE among different measurement methods for temperate forests. Isotope-based estimates of iWUE tend to be higher than estimates based on non-isotopic methods, such as gas exchange and eddy covariance (Medlyn et al. 2017; Yi et al. 2019).

The discrepancy of isotope-based iWUE may be resolved by improved understanding of seasonal dynamics of $\delta^{13}\text{C}$ in plant tissues. Some studies have shown an enrichment in $\delta^{13}\text{C}$ in leaf tissues early in the growing season of temperate deciduous trees compared to the peak growing season, which leads to higher inferred iWUE during the early period and lower iWUE during the peak season (Helle and Schleser 2004; Stokes et al. 2010; Ogée et al. 2009). This cannot be explained by the photosynthetic fractionation only, as fractionation due to leaf gas diffusion and resulting c_i/c_a often decreases resulting in higher iWUE during the peak growing season when VPD is high and trees close their stomata to avoid xylem cavitation and hydraulic failure (Farquhar and Sharkey 1982; Farquhar et al. 1989; Yi et al. 2019).

A conceptual illustration of how the observed seasonal $\delta^{13}\text{C}$ of leaf tissues may be related to post-photosynthetic carbon allocation processes is given in Figure 4.1. After carbon is assimilated in the leaf (Fig. 4.1a), it can be stored in structural or non-structural carbon pools, lost through respiration, or transported to the other parts of tree (Fig. 4.1b, 4.1c, and 4.1d) (Brüggemann et al. 2011; Fatichi et al. 2014; Savage et al. 2016). Among the carbon pools, non-structural carbohydrates (NSC) exist as a form of sugar or starch and are used to regulate plant metabolism or stored for later use. The stored NSC often shows enriched values (high $\delta^{13}\text{C}$) compared to new NSC from photosynthetic fractionation due to additional fractionation during post-photosynthetic carbon allocation processes (Bowling et al. 2008; Cernusak et al. 2009; Gessler et al. 2014). Temperate deciduous trees remobilize stored NSC every spring to produce new xylem vessels and leaves until new carbon can be supplied from photosynthesis (Fig. 4.1e) (Kuptz et al. 2011; Carbone et al. 2013; De Kauwe et al. 2014). They also remobilize stored NSC to avoid carbon

starvation when environmental conditions are unfavorable for productivity, for example during drought (Hasibeder et al. 2015; Gessler and Treydte 2016).

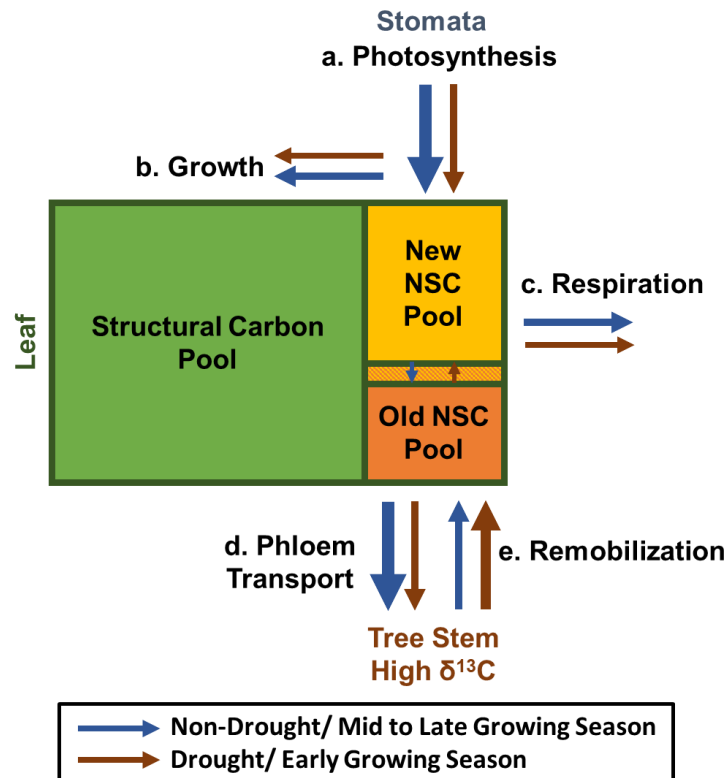


Figure 4.1 A conceptual illustration of leaf carbon allocation processes. Trees produce newly assimilated carbon by photosynthesis (a) and input the new carbon to the non-structural carbon (NSC) pool in leaves. The NSC can be used for leaf growth and structural carbon pool (b), growth and maintenance respiration (c), or transported to stems through phloem (d). When leaf respiration costs outpace photosynthetic fluxes, the NSC from stems and roots is transported back to leaf (e). The color of the arrows represents drought/early growing season (red) and non-drought/mid to late growing season (blue) conditions and the size of arrows represents relative annual fluxes.

This remobilization of stored NSC for use in new tissues, and later mixing of stored carbon with new carbon pools, can therefore contribute to the seasonal variability of $\delta^{13}\text{C}$ of leaf tissues for temperate deciduous trees. Remobilizing old NSC from stem and root tissues which tend to have higher $\delta^{13}\text{C}$ values to build xylem vessels and new leaves early in the growing season is a proposed explanation for leaf $\delta^{13}\text{C}$ enrichment (Hoch et al. 2003; Stokes et al. 2010; Gessler et al. 2014). As photosynthesis continues to increase, the leaf NSC pool (i.e., mixture of old and new NSCs) gradually increases the fraction of new carbon, causing the $\delta^{13}\text{C}$ to gradually decrease (Helle and Schleser 2004; Gessler et al. 2009; Stokes et al. 2010). The fraction of new carbon in leaf tissues may depend on the minimum size of NSC pools in temperate deciduous species as trees use different strategies of carbon allocation for early-season growth (Brüggemann et al. 2011; Stokes et al. 2010).

In summary, the use of remobilized NSC early in the growing season for different species and environmental conditions can dampen the link between stomatal response to climate, photosynthesis, and tree growth (Kagawa et al. 2006; Eglin et al. 2010; Brüggemann et al. 2011; Gessler et al. 2014). So far, few studies have considered the role of the carbon allocation in interpreting the high iWUE by isotopic methods due to enriched $\delta^{13}\text{C}$ signals from remobilized NSC. The uncertainty leads to a potential for bias for studying carbon and water fluxes when using different iWUE measures to parameterize or validate models (Battipaglia et al. 2013; Frank et al. 2015; Monclus et al. 2006; Keller et al. 2017).

The objective of this paper is to quantify the effects of carbon allocation on seasonal leaf $\delta^{13}\text{C}$ and iWUE estimates of temperate deciduous trees. We specifically investigate (1) the role of remobilized NSC early in the growing season in explaining the discrepancy in iWUE between isotope-based and other measurements, and (2) the effects of species-specific and drought-sensitive remobilized NSC on the variations in iWUE among different species and environmental conditions. We studied four tree species (*Acer saccharum*, *Liriodendron tulipifera*, *Sassafras albidum*, and *Quercus alba*) that vary in stomatal responses and carbon allocation strategies. To address these objectives, we modelled species-specific photosynthesis, carbon allocation, and isotopic fractionation processes. We then used this model framework to estimate iWUE using different methods (isotopic and non-isotopic), for each species and environmental conditions, which helps to isolate the role of remobilized NSC in iWUE estimates.

4.3 Materials and Methods

4.3.1 Study site and materials

Our study was conducted at the Morgan-Monroe State Forest (MMSF) in southcentral Indiana, USA (Latitude 39.119°N, Longitude 86.125°W). MMSF is a core-site affiliated in the AmeriFlux network (US-MMS), and a 46 m eddy covariance tower has been operating since 1998 to measure CO₂, water, and energy fluxes along with other ecophysiological measurements (Yi et al. 2017; Roman et al. 2015; Brzostek et al. 2014). As a secondary successional temperate deciduous forest, the mean age of trees in MMSF is 80-90 years. About 70% of the basal area is comprised of *Acer saccharum* (sugar maple), *Liriodendron tulipifera* (tulip poplar), *Sassafras albidum* (sassafras), and *Quercus alba* (white oak) (Ehman et al. 2002).

During our study period in 2011-2013 and 2017-2018, the mean annual temperature at MMSF was 14.42°C and the mean annual precipitation as 1,069 mm based on meteorological observations from the tower (Fig. 4.2). In 2012, MMSF experienced an extreme drought event that affected much of the Midwestern US, and received only 23 mm of rainfall during the peak of the growing season in June and July (Yi et al. 2019; Roman et al. 2015). The drought reduced soil moisture and increased VPD significantly (Fig. 4.2c and 4.2d). As a result, the absolute value of net ecosystem exchange (NEE) during the peak growing season in 2012 (DOY 182–218) was reduced by 55% relative to mean NEE during typical weather conditions in 1999–2010 (Yi et al., 2019). However, since the growing season started several weeks early in 2012, the drought caused only about a 30% reduction in the absolute value of NEE during the entire growing season in 2012 relative to the NEE in wetter 2013 (Fig. 4.2b).

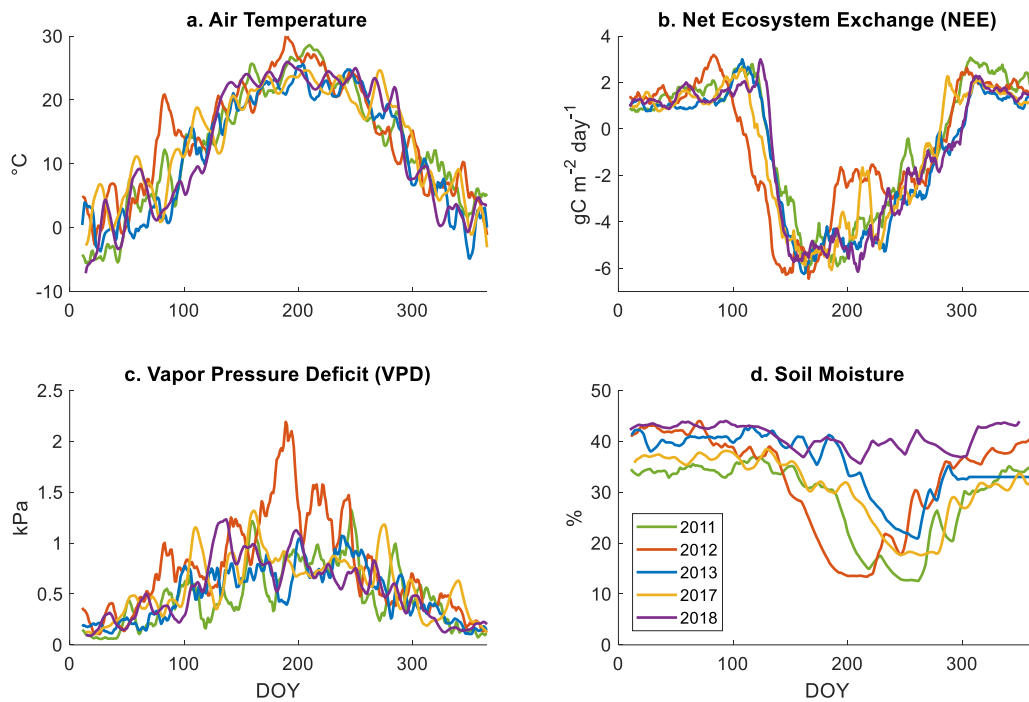


Figure 4.2 Inter- and intra-annual variability of environmental conditions in 2011–2013, 2017–2018. Seasonal changes of 10-day moving average of (a) air temperature, (b) net ecosystem CO₂ exchange (NEE), (c) vapor pressure deficit, and (d) soil moisture in the first 30 cm depth measured at the MMSF AmeriFlux site in 2011–2013, 2017–2018.

We collected seasonal leaf samples from three individuals each tree species in 2011–2013. During the growing seasons, at least two sunlit leaves of maximum maturity for that time for each tree were collected every 2 weeks (day of year (DOY) 195–235 in 2011, DOY 123–286 in 2012 and DOY 135–270 in 2013) by accessing to the top of the canopy using a boom-lift. During the bi-weekly collections, leaf gas exchange and ancillary data, including mid-day atmospheric and intercellular CO₂ concentrations (c_a and c_i , respectively), net assimilation (A_n), and stomatal conductance (g_s) were measured using a portable photosynthesis system (LI-6400; Li-COR) (Roman *et al.*, 2015; Yi *et al.*, 2019). Additional samples were collected in 2017–2018 using a sling-shot method from one individual of the four tree species to sample at least two sunlit leaves for each tree at the top-to-middle canopy range (every 1–2 weeks during DOY 111–307 in 2017 and four times during DOY 145–298 in 2018).

Tree cores were sampled using a 5 mm diameter increment borer at breast height. The growth-rings were available in 2011–2012 for all species and additional samples in 2013 for sassafras only (Yi *et al.*, 2019). Tree core samples were not collected in 2017 or 2018 to minimize the damage of the heavily-sampled target trees.

4.3.2 Carbon isotope analysis

Carbon isotope ratios ($\delta^{13}\text{C}$) of the seasonal leaf and annual tree core samples were measured using a continuous flow elemental analyzer-isotopic ratio mass spectrometer (EA-IRMS) (PDZ Europa ANCA-GSL EA interfaced with a Sercon 20-22 IRMS). Before leaf samples were ground using a mixer mill (Restech MM 200), samples in 2011–2013 were dried passively at room temperature during storage of 3 years or longer and samples in 2017–2018 were oven-dried within 3 days. For the tree core samples, alpha-cellulose was extracted from late-wood annual rings following the modified Soxhlet method at Indiana University (see more details about the tree cores sample preparation in Yi *et al.*, 2019). The tree core samples of sassafras and all leaf samples were then analyzed by Purdue Stable Isotope (PSI) facility at Purdue University, and the tree ring samples of other species were analyzed by Stable Isotope Research Facility (SIRF) at Indiana University. Peach Leaf standard reference material (NIST 1547) was used as a quality control in the PSI lab, and USGS 40 and acetanilide #1 (CAS 103-84-4) were further used to check the accuracy of the one-point standard correction. Analytical precision was better than 0.2‰.

Leaf $\delta^{13}\text{C}$ values are known to vary with height due to differences in solar irradiance and hydraulic conductance affecting leaf water potential, photosynthesis rates, and c_i/c_a values (McDowell et al. 2011; Suh and Diefendorf 2018). To account for sampling height differences in leaves collected by the sling-shot method at a lower height in 2017–2018 compared to the upper-canopy leaves collected by the boom-lift in 2011–2013, we added a constant offset of +3‰ for sugar maple and +2‰ for all other species to leaf $\delta^{13}\text{C}$ values in 2017–2018. The offsets were in the observation range of relationships between tree height and leaf $\delta^{13}\text{C}$ and brought the mean values for each in line with previous years (McDowell et al. 2011).

To quantify differences in the seasonal variability of leaf $\delta^{13}\text{C}$ among species, we averaged leaf $\delta^{13}\text{C}$ for early and late growing seasons separately, defined by before and after DOY 150, for four species from four years of data (2012, 2013, 2017 and 2018). We excluded the data from the year 2011 in this seasonal analysis due to the lack of sample collection prior to DOY 150 in this year.

4.3.3 Modeling species-specific carbon allocation processes

Photosynthetic rate and stomatal conductance

We implemented the photosynthesis equations from the Community Land Model version 4.5 (CLM 4.5) (Bonan et al. 2012, 2014). In specific, we directly referred chapters 8.2 – 8.5 of technical description of CLM 4.5 to calculate leaf-level net assimilation (A_n) and intercellular CO_2 concentrations (c_i) for the C_3 photosynthesis module. The A_n was calculated by subtracting autotrophic respiration (R_d) from the minimum of Rubisco-, light, and product- limited assimilation rates (A_c , A_j , and A_p , respectively) (Eq. 4.3). The rubisco-limited rates are a function of the maximum carboxylation rate ($V_{c,max}$), CO_2 compensation point (Γ^*), Michaelis-Menten constants for CO_2 and O_2 (K_c and K_o), and oxygen partial pressure (o_i) (Eq. 4.4). The c_i was calculated by considering diffusion of atmospheric CO_2 (c_a) controlled by boundary layer and stomata conductance (g_b and g_s , respectively), and atmospheric pressure (P_{atm}) (Eq. 4.5). The A_n , c_i and g_s were solved iteratively using Brent’s method until c_i converges (Brent 1976). Additionally, phenology was prescribed by setting the initiation and termination of photosynthesis using seasonal leaf growth derived from the PhenoCam imagery (Table 4.1) (Richardson et al. 2018) and species-specific phenology recorded at MMSF (Table 4.2).

$$A_n = \min(A_c, A_j, A_p) - R_d \dots \text{Equation 4.3}$$

$$A_c = (V_{c,max}(c_i - \Gamma^*)) / (c_i + K_c(1 + o_i/K_o)) \dots \text{Equation 4.4}$$

$$c_i = c_a - (1.4/g_b + 1.6/g_s)P_{atm}A_n \dots \text{Equation 4.5}$$

Table 4.1 Species-specific model parameters for four tree species of this study.

		Tulip Poplar	Sugar Maple	Sassafras	White Oak	References
Offset between Tree ring cellulose and leaf NSC		+2.5‰	+2.0‰	+0.5‰	+1.0‰	Badeck et al. (2005)
Species-specific Wood Anatomy	Porosity	Diffuse Porous		Ring Porous		Yi et al. (2017)
	Minimum NSC pool	20 mg/g _{DM}		40 mg/g _{DM}		Barbaroux & Bréda (2002)
Species-specific Isohydrlicity		Isohydrlic			Anisohydrlic	Medlyn et al. (2011)
		Stomatal model optimized using leaf gas exchange data				
Spring Phenology based on Table S1		Shifted 5 days earlier	Shifted 5 days earlier	Shifted 15 days later	No Shift	This study

Table 4.2 Phenology of Morgan Monroe State Forest in 2011 – 2013.

Day of Year (DOY)	2011	2012	2013
Leaf Out (LA_0)	125	115	125
Maximum LAI (LA_{max})	210	200	210
Start of Senescence	245	245	260
Full Senescence	310	310	320

We implemented species-specific stomatal conductance (g_s) using a linear relationship between g_s and the term $A_n/(c_a D^{1/2})$, where c_a is atmospheric CO₂ and D is VPD (Eq. 4.6) (Medlyn et al. 2011). Compared to the empirical stomatal conductance model, the Medlyn model provides a theoretical interpretation for stomatal optimization of carbon gain per water loss. Equation 3 predicts a close linear relationship between g_s and the term $A/(c_a D^{1/2})$, where D is VPD. Here, the parameter g_1 (kPa^{0.5}) is shown to vary with growth temperature and is species-specific, and g_0 is assumed to be small (< 0.1) (Medlyn et al. 2017).

We optimized the parameters g_1 and g_0 in Eq. 4.6 using leaf-gas exchange measurements for each species to account for trees response to VPD at the stomatal level along the species-specific gradients of isohydric and anisohydric traits (Roman et al., 2015; Yi et al., 2019). To filter leaf gas exchange data, we applied the same criteria as Wolz et al., 2017 by screening data from sun leaves with no precipitation, and when photosynthetic photon flux density (PPFD) $> 1400 \mu\text{mol m}^{-2} \text{s}^{-1}$. During a drought, isohydric trees close their stomata to sustain relatively stationary leaf water potential, which reduces the risk of xylem embolism. Anisohydric trees leave the stomata open, which sustains gas exchange but at greater risk of hydraulic damage by decreasing leaf water potential. Among the species considered here, tulip poplar is known to be very isohydric, sugar maple and sassafras are intermediate isohydric, and white oak is very anisohydric (Brzostek et al. 2014; Roman et al. 2015) (Table 4.1).

$$g_s \approx g_0 + 1.6 \left(1 + \left(\frac{g_1}{\sqrt{D}} \right) \right) \frac{A}{c_a} \dots \text{Equation 4.6}$$

For each simulation time-step of one hour, the interdependent variables A_n and g_s were solved iteratively. Initial A_n for each species was set to be equal to the gross primary productivity from eddy flux measurements and intercellular CO₂ concentration (c_i) was set as a function of g_s (Eq. 4.5). Calculation of A_n and g_s was iterated until the previous and updated c_i converged to a constant (Brent 1976).

Post-photosynthetic carbon allocation to/from leaves

The carbon budget within leaves was simulated based on respiration fluxes, phloem export, and remobilization processes in addition to photosynthesis (Fig. 4.1). We used equations of the

post-photosynthetic carbon allocation processes from the ISOCASTANEA model (Eglin et al. 2010). Note that we did not track carbon pools in other parts of the tree like stems and roots, but only the carbon entering (import) or leaving (export) the leaves was considered. Thus, we assume in our simulation that an infinite supply of stored NSC is available when leaf respiration costs outpace photosynthetic fluxes.

The leaf carbon pool consists of structural and non-structural carbon (NSC) pools (Figure 4.1). The size of the NSC pool in the leaf is determined by the balance between the new NSC and stored NSC. The new NSC refers to the freshly produced NSC via photosynthesis, and the stored NSC refers to the NSC that has been stored before it was remobilized into the leaf NSC pool. Both new and stored NSC pools are the carbon sources of the structural carbon pool during the period of leaf growth. The leaf structural carbon pool was simulated using stored and new NSC proportionally from leaf NSC pools during periods of leaf growth. Both new and stored carbon contributions were tracked separately in the structural and NSC leaf pools in order to account for differences in the $\delta^{13}\text{C}$ values of each.

Leaf carbon fluxes include the input of new NSC as a result of photosynthesis, export of new and stored NSC for respiration and phloem transport proportionally, and import of stored NSC from remobilization. In the ISOCASTANEA model, the carbon allocation is simulated by leaf growth, respiration, phloem transport, and remobilization processes (Fig. 4.1b, 4.1c, 4.1d and 4.1e).

First, the leaf area growth (LA) was calculated as a function of accumulated temperature (T) between day of year (DOY) of leaf out (LA_0) and maximum LAI (LA_{max}), where S_{frCLA} is the state of forcing for leaf growth (Eq. 4.7-8 and Table 4.2) (Dufrêne et al. 2005)

$$S_{frCLA} = \sum_{DOY_{LA_0}}^{DOY_{LA_{max}}} T, \text{ if } T > 0^\circ\text{C} \dots \text{Equation 4.7}$$

$$\frac{dLA}{dt} = \begin{cases} \frac{LA_{max} \times T}{S_{frCLA}}, & \text{if } LA < LA_{max} \\ 0, & \text{if } LA = LA_{max} \end{cases} \dots \text{Equation 4.8}$$

We then calculated growth respiration (RG) as a function of growth rate (GB) and construction cost (CR) of leaf growth from Eq. 4.9, and maintenance respiration (RM) as a function of temperature (T_{suf}) and nitrogen content (N_m), where B is biomass, MRN is nitrogen dependency,

N_m is nitrogen contents, Q_{10} is temperature effect for leaves, and T_{mr} is base temperature for maintenance respiration (Eq. 4.10) (Dufrêne et al. 2005).

$$RG = GB(CR - 1) \dots \text{Equation 4.9}$$

$$RM = B \times MRN \times N_m \times Q_{10}^{(T_{suf} - T_{mr})/10} \dots \text{Equation 4.10}$$

The phloem transport followed a Michaelis-Menten equation of the leaf NSC pool, where L and S are the export rate and the NSC pool size, respectively, and L_{max} and K_m^{export} are the Michaelis-Menten constants for NSC pool (Eq. 4.11). S_{min} is the minimum leaf NSC pool size that was set to be species-specific (Table 4.1). Lastly, the remobilization of NSC was simulated to occur when the NSC pool size becomes smaller than S_{min} in leaves (Eglin et al. 2010).

$$L = \frac{L_{max}(S - S_{min})}{K_m^{export} + (S - S_{min})} \dots \text{Equation 4.11}$$

We assigned different leaf S_{min} depending on wood porosity of each species. Ring porous species build wider and longer xylem vessels that are more susceptible to xylem cavitation during winter (Barbaroux and Bréda 2002; Barbaroux et al. 2003). Ring porous species are known to have larger S_{min} than diffuse porous species do in order to reserve NSC to repair vulnerable xylem vessels (Heizmann et al. 2001; Mayrhofer et al. 2004; Palacio et al. 2011; Dietze et al. 2014). On the other hand, diffuse porous species have smaller xylem vessels, which are less susceptible to damage from freezing, and therefore smaller S_{min} is observed (Barbaroux and Bréda 2002; Furze et al. 2019). In this model, we assume that S_{min} follows the tree-level minimum NSC pool size and set S_{min} for diffuse porous species (tulip poplar and sugar maple) to be 50% lower than ring porous species (white oak and sassafras) (Table 4.1).

Modeling carbon isotope values of leaf carbon fluxes and pools

We simulated $\delta^{13}\text{C}$ values of leaf NSC and structural carbon pools using photosynthetic isotopic fractionation and mixing between the new and remobilized stored NSC pools (Seibt et al. 2008; Eglin et al. 2010). We trained the model in 2011–2013 using observed leaf phenology and

tree ring $\delta^{13}\text{C}$, and tested the model in 2017–2018 using the mean leaf phenology and tree ring $\delta^{13}\text{C}$.

First, using the time-varying simulated A_n and c_i in the model, we calculated the time-varying $\delta^{13}\text{C}$ of newly assimilated NSC by photosynthetic fractionation using Equation 4.12a, where a is the fractionation during CO_2 diffusion through the stomata (4.4‰), b is the fractionation during carboxylation (29‰), a_m is the fractionation during the mesophyll CO_2 transfer (1.8‰), f is the fractionation during photorespiration (Eq. 4.13), Γ^* is the CO_2 compensation point in the absence of dark respiration (Eq. 4.14), and mesophyll conductance (g_m) is assumed to be $0.2 \text{ mol m}^{-2} \text{ s}^{-1}$ within the range of limited observations (Seibt et al. 2008). We also test a common simplification presented in Equation 4.12b not accounting for g_m , where b' (27‰) is the net carboxylation fractionation reduced to account for the terms omitted from Equation 4.12a (Farquhar et al. 1989).

$$\delta^{13}\text{C}_{photo} = \delta^{13}\text{C}_{atm} - (a + (b - a) \frac{c_i}{c_a} - (b - a_m) \frac{A_n}{g_m c_a} - f \frac{\Gamma^*}{c_a}) \dots \text{Equation 4.12a}$$

$$\delta^{13}\text{C}_{photo} = \delta^{13}\text{C}_{atm} - a + (b' - a) \frac{c_i}{c_a} \dots \text{Equation 4.12b}$$

$$f = 8 - \left(\frac{350 - c_a}{25} \right) \dots \text{Equation 4.13}$$

$$\Gamma^* = 1.54 \times 1.05 \times (T + 2.5) \dots \text{Equation 4.14}$$

Second, due to observational constraints, the $\delta^{13}\text{C}$ of stored NSC was not modeled in a time-dependent way but assumed to be a constant value set by the stored carbon of the previous year. We estimated $\delta^{13}\text{C}$ of stored NSC from the isotopic signatures of tree ring cellulose of the previous year in 2011–2012 and subtracted a species-specific fractionation factor within the observed range of +0.5 to +2.5‰ to consider differences in post-photosynthetic enrichment of tree ring cellulose compared to leaf NSC material ($\Delta_{stem-leafNSC}$) (Gessler et al. 2014; Badeck et al. 2005). The different $\Delta_{stem-leafNSC}$ fractionations were used for each species in order to best fit the leaf $\delta^{13}\text{C}$

observations (Table 4.1). We further conducted a sensitivity test including $\Delta_{stem-leafNSC}$ to quantify the importance of $\Delta_{stem-leafNSC}$ on our simulation results.

Within the leaf, the binary mixing of stored and new carbon pools was calculated using the fraction of stored and new carbon and their respective isotopic signatures (Eq. 4.15a). In Equation 4.15a and 4.15b, the isotopic signatures of the resulting mixture of NSC and structural carbon pool ($\delta^{13}C_{NSC}$ and $\delta^{13}C_{struct}$, respectively) at a timestep t vary systematically depending on the relative fraction of new carbon (f_{new}) and the isotopic signatures of new and old carbon pools ($\delta^{13}C_{new}$ and $\delta^{13}C_{old}$). We set the isotopic fractionation between leaf structural and NSC (Δ_{NSC-SC}) to be +1.5‰, where structural is more enriched than NSC. We do not consider different chemical compounds within the structural pool (e.g. Collister *et al.*, 1994). For the leaf respiration and phloem transport fluxes removing carbon from the leaf, we assumed that there was no isotopic fractionation and they have the mixed $\delta^{13}C$ value of the leaf NSC at each time step.

$$\delta^{13}C_{NSC,t} = \delta^{13}C_{new,t} \times f_{new,NSC,t} + \delta^{13}C_{old,t} \times (1 - f_{new,NSC,t}) \quad \dots \text{Equation 4.15a}$$

$$\delta^{13}C_{struct,t} = \delta^{13}C_{new,t} \times f_{new,struct,t} + \delta^{13}C_{old,t} \times (1 - f_{new,struct,t}) \quad \dots \text{Equation 4.15b}$$

Uncertainty tests

To quantify the uncertainty in the model simulations of leaf carbon fluxes and $\delta^{13}C$, we varied six key parameters mentioned in section 4.3.3: $V_{c,max}$, L_{max} , K_m^{export} , CR_{leaf} , $Q_{10,leaf}$, and Δ_{NSC-SC} (Table 4.3). We sampled the six parameters 20 times using a random distribution of minimum and maximum of parameters based on reported literature ranges and used these samples to define 20 different model ensemble members. We found that the ensemble mean and ensemble variance of leaf $\delta^{13}C$ values stabilized at around 10 members, so we ultimately chose to include 20 ensemble members to be conservative.

Table 4.3 Details of parameter uncertainty tests.

No.	Parameter	Minimum	Maximum	References
1	Maximum rate of carboxylation ($V_{c,max}$)	52.4 $\text{mol m}^{-2}\text{s}^{-1}$	57.7 $\text{mol m}^{-2}\text{s}^{-1}$	Bonan <i>et al.</i> , 2012
2	Maximum phloem transport rate (L_{max})	6 $\text{mol m}^{-2}\text{s}^{-1}$	14 $\text{mol m}^{-2}\text{s}^{-1}$	Moing, Escobar-Gutierrez and Gaudillere, 1994; Eglin <i>et al.</i> , 2010
3	Half-saturation point for Michaelis-Menten parameter for phloem transport (K_m^{export})	3.6 $\text{mol m}^{-2}\text{s}^{-1}$	4.4 $\text{mol m}^{-2}\text{s}^{-1}$	Moing, Escobar-Gutierrez and Gaudillere, 1994; Eglin <i>et al.</i> , 2010
4	Construction cost of leaves (CR_{leaf})	1.2	1.4	Niinemets, 1999; Dufrêne <i>et al.</i> , 2005
5	Temperature effect for leaves ($Q_{10,leaf}$)	2.0	2.4	Bolstad, Mitchell and Vose, 1999
6	Offset between leaf non- structural and structural carbon pools (Δ_{NSC-SC})	+1.4‰	+1.6‰	Badeck <i>et al.</i> , 2005; Gessler <i>et al.</i> , 2014

Model sensitivity test

We conducted seven sensitivity tests to identify the relative importance of various model parameterization choices (Table 4.4). Test 1 clarifies the importance of carbon allocation to bulk leaf material by considering photosynthetic discrimination only. Tests 2 and 3 address the importance of mesophyll conductance and offsets of $\delta^{13}\text{C}$ between tree ring cellulose and leaf NSC pool. Test 4 elucidates the importance of species-specific carbon allocation processes by switching the NSC pool size and timing of vessel growth of ring- and diffuse-porous species. Test 5 switches the species-specific stomatal response between the isohydric and anisohydric species. Lastly, test 6 neglects the species-specific phenology and test 7 changed maximum phloem loading rates. We ran seven independent simulations for the sensitivity tests and calculated the RMSE between the observations and the model.

We present two types of error analysis. First, testing how close the model results are to the mean observations by the RMSE from the 1:1 line, and second, how close the model captures the within season variability by the RMSE from the least squares linear fit to the model-observation comparison. This second error analysis acknowledges that some constant parameters are optimized to the observation means, but do not contribute to within season variability. We present the RMSE values from the sensitivity tests relative to the optimized model.

Table 4.4 Details of sensitivity tests.

No.	Sensitivity Test	Assumption	Variable Change
1	No Carbon allocation	Leaf bulk $\delta^{13}\text{C}$ is solely controlled by photosynthetic fractionation	Turn off post-photosynthetic carbon allocation processes
2	Varied mesophyll conductance	Mesophyll conductance varies in the observation range	0.20 to 0.25 mol m ⁻² s ⁻¹
3	Same fractionation factor of tree ring cellulose – bulk leaf $\delta^{13}\text{C}$ ($\Delta_{stem-leafNSC}$)	$\Delta_{stem-leafNSC}$ does not vary between species	+1.5 ‰
4	Species-specific wood anatomy and minimum leaf NSC pool size (S_{min})	Switched between ring and diffuse porous species	S_{min} for ring porous species to be 50% lower than diffuse porous species
5	Species-specific isohydricity	Switched between isohydric and anisohydric species	Switched Medlyn relationship between isohydric and anisohydric species
6	Same phenology	Phenology does not vary between species and between years	Same leaf out and maximum LAI dates
7	Varied maximum phloem loading rates	Maximum phloem loading rates vary in the observation range	6 to 10 $\mu\text{mol m}^{-2} \text{s}^{-1}$

4.3.4 Estimation of iWUE using multiple methods

We compared iWUE in equation 4.1 from five different methods using the observations and model results in our study. These include direct leaf gas exchange measurements, carbon isotope measurements of leaves and tree rings, and our modeled fluxes sampled in two different ways. The iWUE estimated by leaf gas exchange measurements is the most direct measurement, but is limited as an instantaneous measurement of constantly changing gas exchange (*Instantaneous Licor A/g_s*) (Yi et al. 2019). In order to examine the influence of temporal variability, we sampled our model at the same times that the leaf gas exchange was measured (*Instantaneous Model A/g_s*) and also averaged the iWUE of the modeled fluxes using GPP-weighting over the entire season (*GPP weighed Model A/g_s*). The iWUE estimates from leaf and tree ring $\delta^{13}\text{C}$ (*Leaf and Tree ring $\delta^{13}\text{C}$*) were calculated using equation 4.1 after calculating c_i/c_a using both Eq. 4.12a and 4.12b, with and without considering g_m , respectively. For tree ring $\delta^{13}\text{C}$, we accounted for the well-known $\delta^{13}\text{C}$ offset of 1.0‰ between cellulose and bulk wood (Badeck et al. 2005; Gessler et al. 2014). We compared the iWUE calculated using the five methods, across species, and between relatively unstressed conditions in 2011 to drought conditions in 2012. The iWUE for other years were not calculated due to lack of tree ring $\delta^{13}\text{C}$ measurements.

4.4 Results

4.4.1 Observed bulk leaf and tree ring cellulose $\delta^{13}\text{C}$ variability

The bulk leaf $\delta^{13}\text{C}$ values generally started high in the spring and then decreased as the growing season proceeded (circle symbols in Fig. 4.3). The average early-late season difference was statistically significant over the study period in 2012–2013 and 2017–2018 for sassafras and white oak ($p < 0.05$), with a larger difference for sassafras (2.43‰) than white oak (1.43‰) (triangle symbols in Fig. 3c-d). The averaged early-late season difference was smaller for sugar maple (1.24‰) and tulip poplar (0.70‰) over the study period and was significant only in 2017–2018 for sugar maple (2.16‰) and in 2013 for tulip poplar (0.95‰) ($p < 0.05$) (triangle symbols in Fig. 4.3a-b).

We observed a species-specific variability of mean tree ring cellulose $\delta^{13}\text{C}$ in 2011–2012 with the highest $\delta^{13}\text{C}$ for sugar maple (an average of -24.02‰), followed by tulip poplar, sassafras, and white oak (-24.46, -24.99, and -26.41‰, respectively) (asterisk symbols in Fig. 4.3). The tree

ring $\delta^{13}\text{C}$ in 2012 was higher than 2011 in all species (0.40, 0.52, 1.06, and 0.27 for sugar maple, tulip poplar, sassafras, and white oak, respectively), although the difference was not statistically significant ($p > 0.05$). A clear species-specific offset between bulk leaf and tree ring cellulose $\delta^{13}\text{C}$ was observed, where the average offset was larger for diffuse porous tulip poplar (3.54‰) and sugar maple (2.83‰) and smaller for ring porous sassafras (1.61‰) and white oak (1.05‰).

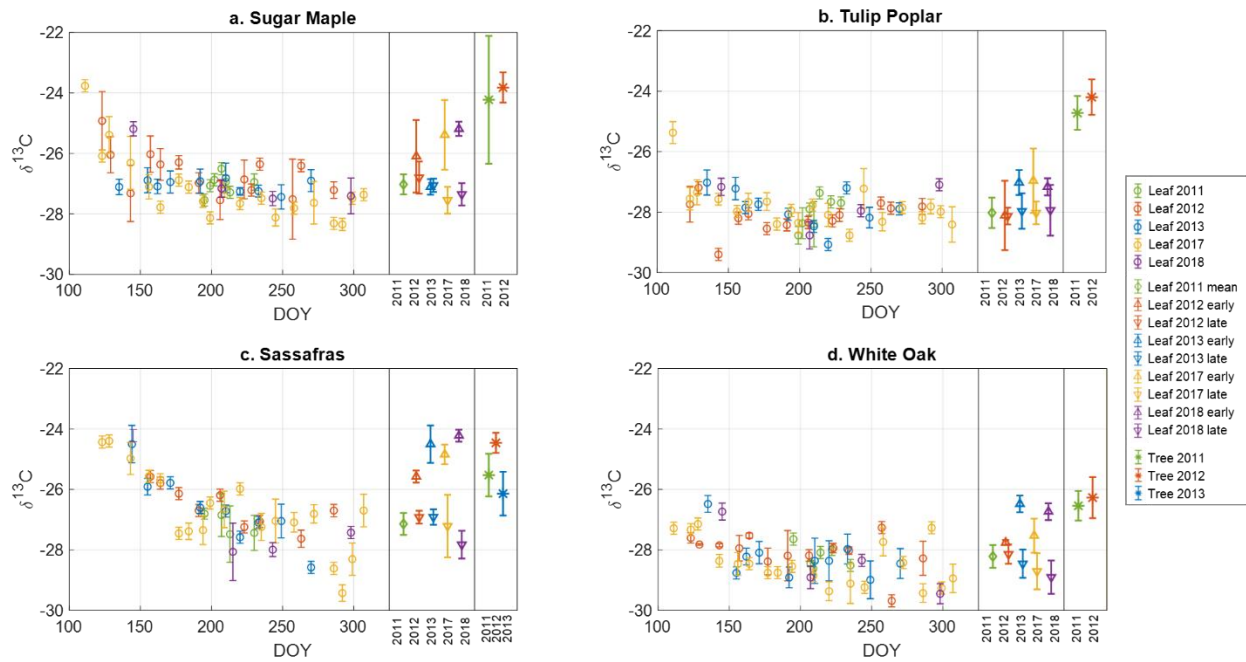


Figure 4.3 Observed seasonal leaf and annual tree ring $\delta^{13}\text{C}$ in 2011–2013, 2017–2018. Observed seasonal changes of bulk leaf $\delta^{13}\text{C}$ (‰) (open circles), early- and late-season averages of bulk leaf $\delta^{13}\text{C}$ (‰) (up and down triangles), and annual tree ring cellulose (asterisk symbol) for (a) sugar maple, (b) tulip poplar, (c) sassafras, and (d) white oak in 2011–2013, 2017–2018. Left panels show bulk leaf $\delta^{13}\text{C}$ (‰) sampled throughout the growing season. Middle panels show early- and late-season averages of bulk leaf $\delta^{13}\text{C}$ (‰) based on the DOY 150 cutoff. Right panels show tree ring cellulose $\delta^{13}\text{C}$ plotted in 2011–2013. Error bars represent one standard deviation of each sampling/average period.

4.4.2 Modeling of photosynthesis, stomatal conductance, and photosynthetic fractionation

The empirical fit of the Medlyn *et al.* (2011) relationship of g_s to the leaf gas exchange data showed the species-specific stomatal response to environmental changes (Eq. 4.6) (Fig. 4.4). The three-year averaged g_1 , sensitivity of g_s to D , during 2011-2013 was lowest for sugar maple, 2.36 $\text{kPa}^{0.5}$, followed by 3.26, 3.76, and 4.36 $\text{kPa}^{0.5}$ for white oak, sassafras, and tulip poplar. The annual averaged g_s of anisohydric white oak species did not decrease (an average of 10% reduction) as much during drought as other isohydric species (an average of 40% reduction) during the drought year in 2012 (Fig. 4.4). The simulated annual photosynthesis (A_n) agreed reasonably well with the leaf gas exchange measurements with an averaged root mean square error (RMSE) of 1.80 $\mu\text{mol}_c \text{m}^{-2}\text{s}^{-1}$ for all species (Fig. 4.5). The seasonal variation in A_n started at the prescribed leaf-out date and increased gradually in DOY 100–200 and stayed high until the prescribed leaf senescence (Table 4.2).

The simulated seasonal bulk leaf $\delta^{13}\text{C}$ based on the photosynthetic fractionation using A_n and g_s not accounting for stored carbon reallocation failed to match the early season enrichment of the observed bulk leaf $\delta^{13}\text{C}$ (dashed lines in Fig. 4.6). The simulated seasonal bulk leaf $\delta^{13}\text{C}$ considering photosynthetic fractionation started from low values (an average of -28.64‰) and increased gradually as the growing season proceeded. This was driven by stomatal response to high mid-summer VPD resulting in less photosynthetic fractionation (Figure. 4.2c). The simulated $\delta^{13}\text{C}$ was higher in 2012 (an average of -27.76‰) than other years (an average of -28.43‰) as the drought caused a reduction in modeled g_s and less ^{13}C fractionation. The modeled final leaf $\delta^{13}\text{C}$ averaged in 2011-2013 was more enriched for sugar maple (-27.00‰) than other species (-28.03‰) as sugar maple showed the lowest mean g_s and g_1 for Medlyn relationship than other species (Fig. 4.4) (Medlyn *et al.* 2011).

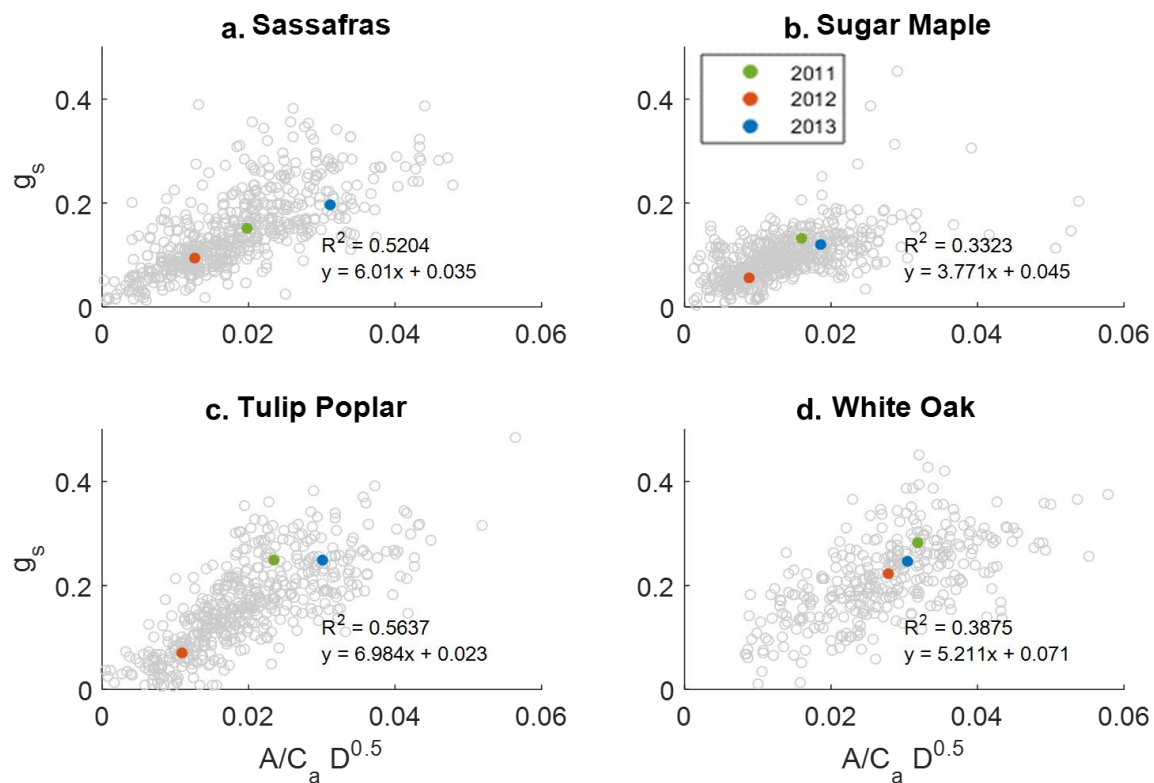


Figure 4.4 *Medlyn* stomatal conductance relationship using leaf gas exchange measurements in 2011–2013. The optimized linear relationship between g_s and $A/c_a D^{0.5}$, where A is photosynthesis rates in $\mu\text{mol m}^{-2} \text{s}^{-1}$, c_a is atmospheric CO_2 concentrations in $\mu\text{mol mol}^{-1}$, and D is VPD in kPa with R^2 for (a) sugar maple, (b) tulip poplar, (c) sassafras, and (d) white oak using leaf gas exchange measurements (open circles) (Medlyn et al. 2011). The filled circles represent average values of g_s and $A/c_a D^{0.5}$ in 2011 (green), 2012 (red), and 2013 (blue).

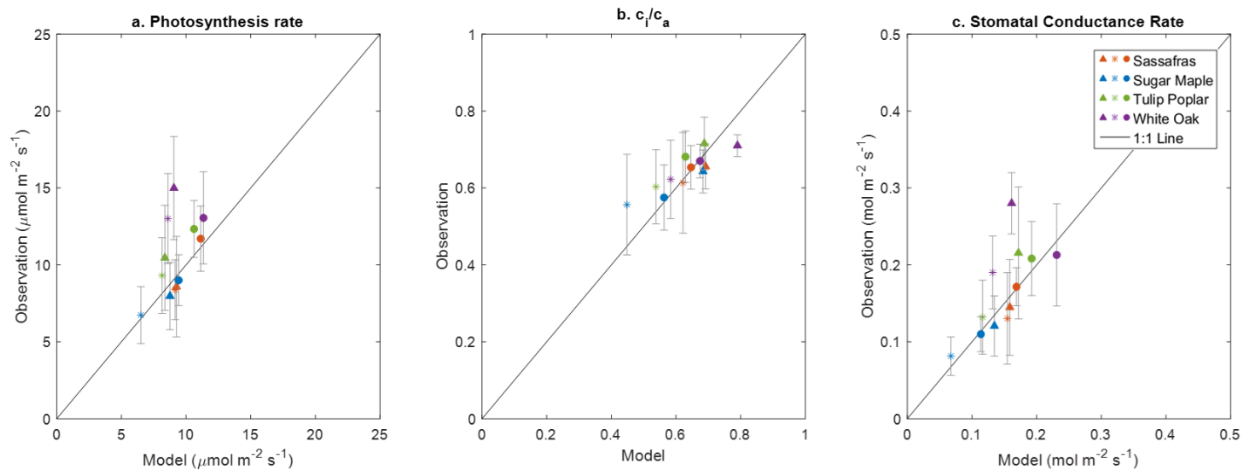


Figure 4.5 Model-data comparison of photosynthesis-related parameters. The model-data comparison of annual averages of (a) photosynthesis rate, (b) fraction of intercellular and atmospheric CO_2 concentrations (c_i/c_a), and (c) stomatal conductance rate during observation period of day of year (DOY) 195–235 in 2011 (Δ), DOY 123–286 in 2012 (\times), and DOY 135–270 in 2013 (\circ) for sassafras (red), sugar maple (blue), tulip poplar (green), and white oak (purple). Error bars represent one standard deviation of each measurement point, and an averaged root mean square error (RMSE) represents an absolute difference of the annual averages between model and observation.

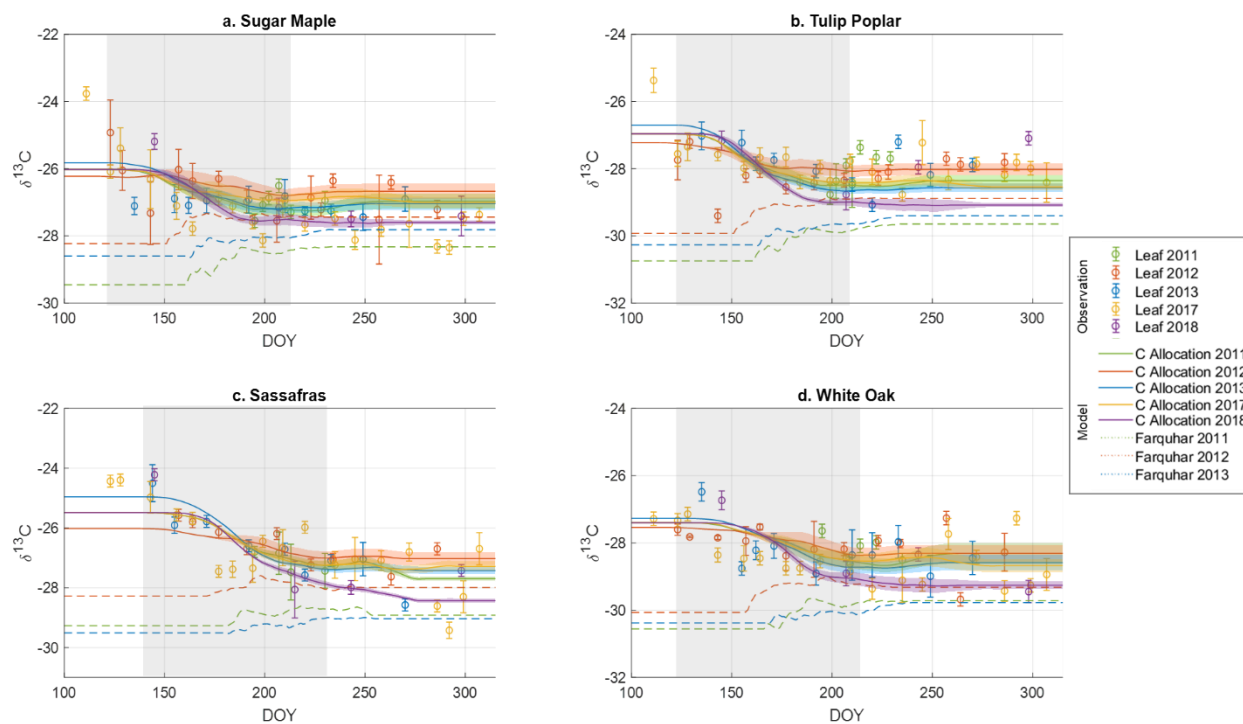


Figure 4.6 Observed and simulated seasonal bulk leaf $\delta^{13}\text{C}$ in 2011–2013, 2017–2018. Observed (open circles) and simulated (lines) seasonal changes of bulk leaf $\delta^{13}\text{C}$ (‰) for (a) sugar maple, (b) tulip poplar, (c) sassafras, and (d) white oak, with carbon allocation in 2011–2013, 2017–2018 (solid lines) and with photosynthetic fractionation only in 2011–2013 (dashed lines) overlaid the observed bulk leaf $\delta^{13}\text{C}$ (open circle). The grey highlight represents the mean leaf growth period in 2011–2013. Shaded error bars represent one standard deviation of parameter uncertainty from 20 ensemble simulations.

4.4.3 Modeling of leaf carbon allocation and mixing among leaf carbon pools

Our simulation including leaf post-photosynthetic carbon allocation showed that the leaf carbon pools were initially fueled by remobilized stored NSC but gradually increased the fraction of new carbon (Fig. 4.7). The simulated fraction of new carbon in the leaf NSC pool (solid lines Fig. 4.7) and the leaf structural carbon pool (dashed lines Fig. 4.7) showed the fraction of new carbon increases as photosynthesis rates increase during the growing season (Fig. 4.9). This increase in the fraction of new carbon occurred during the leaf growth periods (grey highlight in Fig. 4.6) when the newly assimilated carbon was partially consumed by leaf growth respiration (Fig. 4.9-10). The phloem transport also gradually increased as more carbon was available in leaf NSC pool from photosynthesis (Fig. 4.11). The structural carbon pool was also initially fully fueled by the remobilized carbon and gradually increased the fraction of new carbon (Fig. 4.12). The pattern of new carbon fraction in structural carbon pools followed the pattern of its carbon source, the leaf NSC pool (Fig. 4.6).

There were responses to drought and species-specific differences in carbon allocation. In the mid-growing season (DOY 200), the fraction of new carbon decreased significantly in 2012 due to the stomatal closure and consequential reduction of photosynthesis in response to drought (Red solid lines in Fig. 4.7 and Fig. 4.9). The final fraction of new carbon in the structural pool was thus smaller by 15% in 2012 than in 2013 (Dashed lines in Fig. 4.7 and Table 4.5). Furthermore, the larger amount of remobilized carbon caused smaller fraction of new carbon by 10% in structural carbon pools for ring porous white oak and sassafras (Table 4.5), which is attributable to their assumed larger S_{min} than diffuse porous species (Table 4.1) (Heizmann et al. 2001; Mayrhofer et al. 2004; Palacio et al. 2011; Dietze et al. 2014).

The simulated bulk leaf $\delta^{13}\text{C}$ using species-specific carbon allocation showed a better match of early season enrichment (solid lines in Fig. 4.6). During the model-trained period in 2011–2013, the carbon allocation model agreed well with the observed seasonal leaf $\delta^{13}\text{C}$ throughout the growing season with an average R^2 of 0.54 and RMSE of 0.55 across the four species (green, red, and blue solid lines in Fig. 4.6 and black markers in Fig. 4.8). Sassafras showed the highest R^2 of 0.78 and tulip poplar showed the lowest R^2 of 0.43. The R^2 for tulip poplar was the lowest partly due to the extremely low $\delta^{13}\text{C}$ of -29.40‰ in DOY 143 in 2012 (R^2 of 0.5 after removing the outlier). The model also agreed well with the observations for the model-testing

years (2017–2018) with an average R^2 of 0.40 for all species (yellow and purple solid lines in Fig. 4.6 and gray markers in Fig. 4.8).

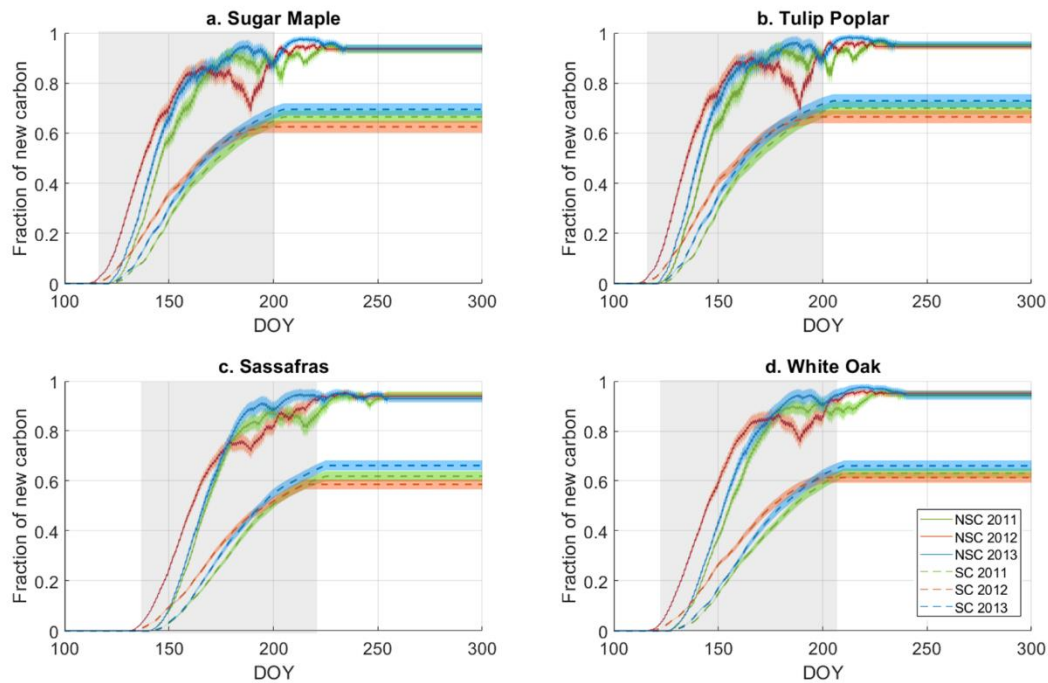


Figure 4.7 Fraction of new carbon in the leaf NSC and structural pool. The simulated fraction of new carbon in the leaf NSC pool (solid lines) and structural carbon (SC) pool (dashed lines) for (a) sugar maple, (b) tulip poplar, (c) sassafras, and (d) white oak in 2011–2013. The grey highlight represents the leaf growth period. Shaded error bars represent one standard deviation of parameter uncertainty from 20 ensemble simulations.

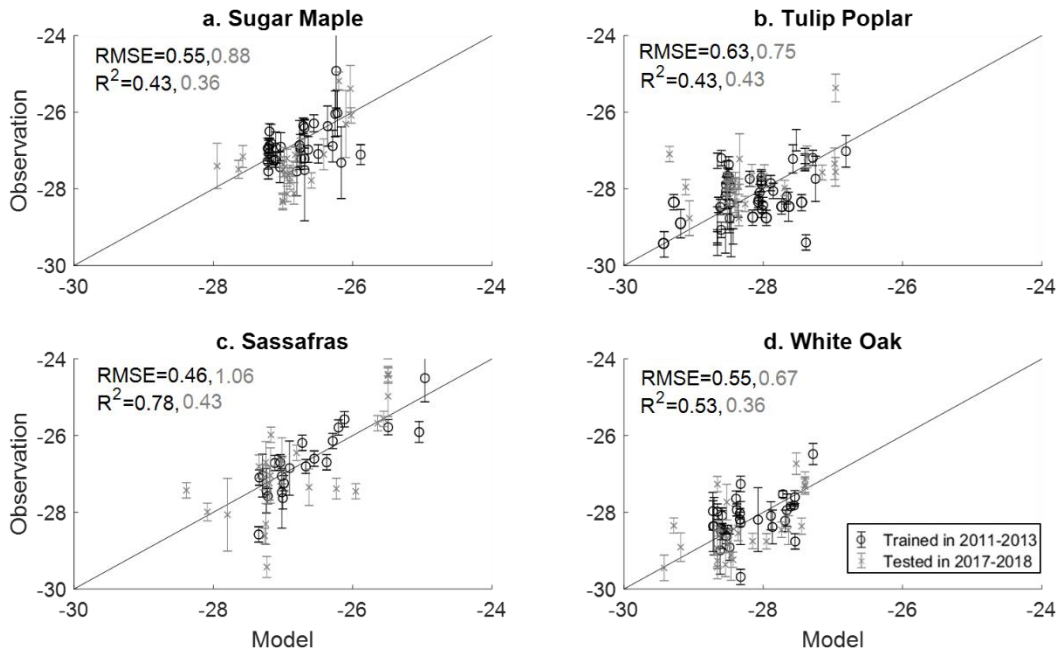


Figure 4.8 Model-data comparison of leaf $\delta^{13}\text{C}$ in 2011–2013 and 2017–2018. The model-data comparison of the observed and carbon allocation simulated seasonal changes of bulk leaf $\delta^{13}\text{C}$ (‰) (a) sugar maple, (b) tulip poplar, (c) sassafras, and (d) white oak for trained years in 2011–2013 (black lines with circle symbols) and for tested years in 2017–2018 (grey lines with cross symbols).

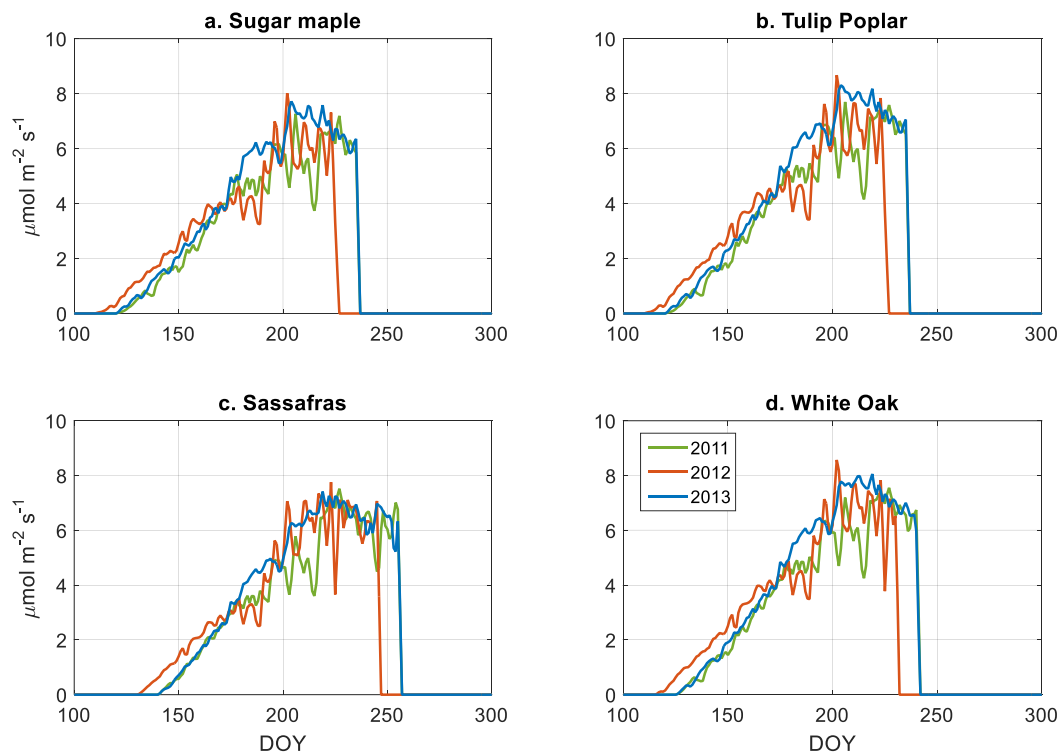


Figure 4.9 Simulated photosynthesis rates in 2011 – 2013. The simulated daily-averaged photosynthesis rates ($\mu\text{mol m}^{-2} \text{s}^{-1}$) for (a) sugar maple, (b) tulip poplar, (c) sassafras, and (d) white oak in 2011 – 2013.

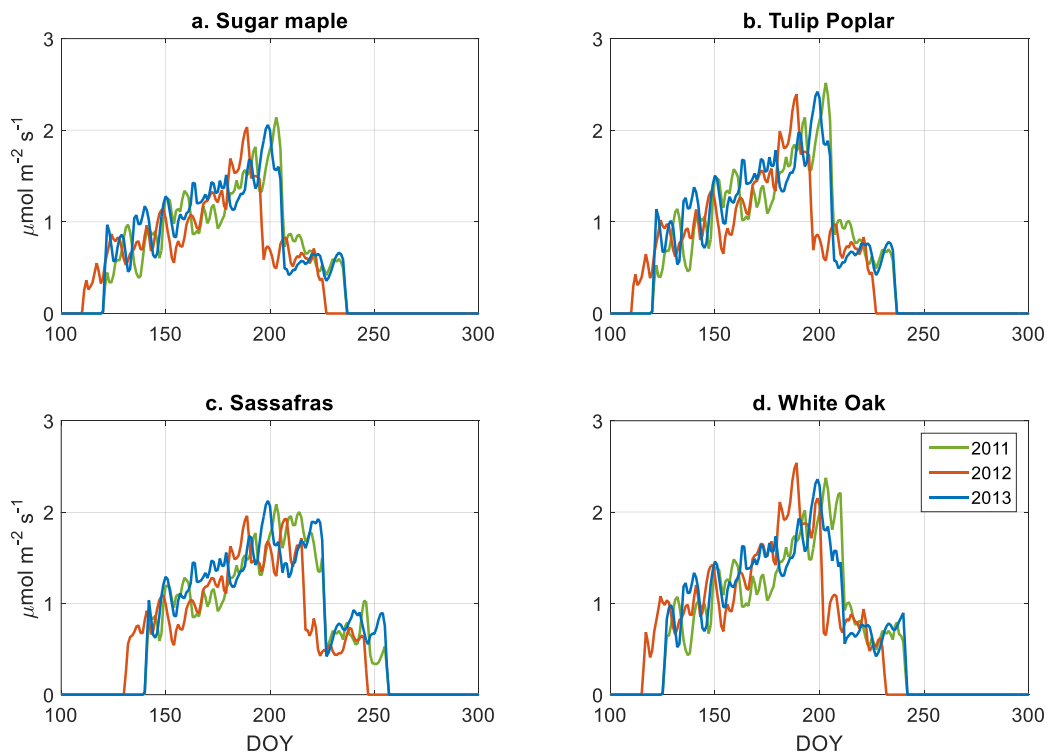


Figure 4.10 Simulated respiration rates in 2011 – 2013. The simulated daily-averaged respiration rates ($\mu\text{mol m}^{-2} \text{s}^{-1}$) for (a) sugar maple, (b) tulip poplar, (c) sassafras, and (d) white oak in 2011 – 2013.

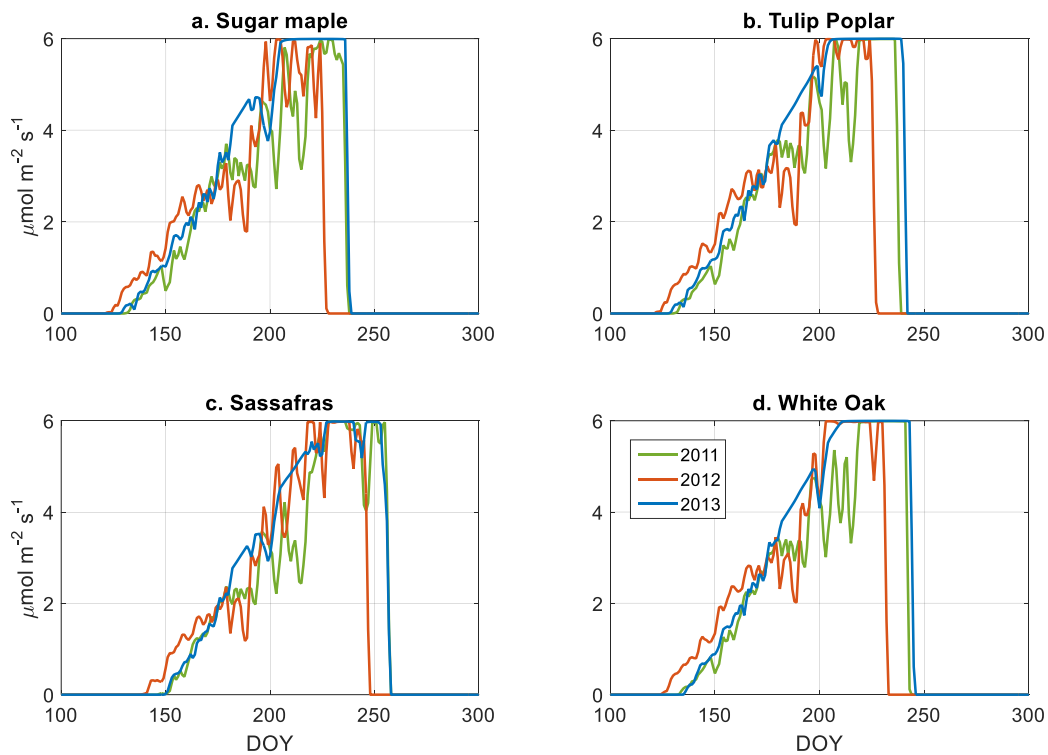


Figure 4.11 Simulated phloem loading rates in 2011 – 2013. The simulated daily-averaged phloem loading rates ($\mu\text{mol m}^{-2} \text{s}^{-1}$) for (a) sugar maple, (b) tulip poplar, (c) sassafras, and (d) white oak in 2011 – 2013.

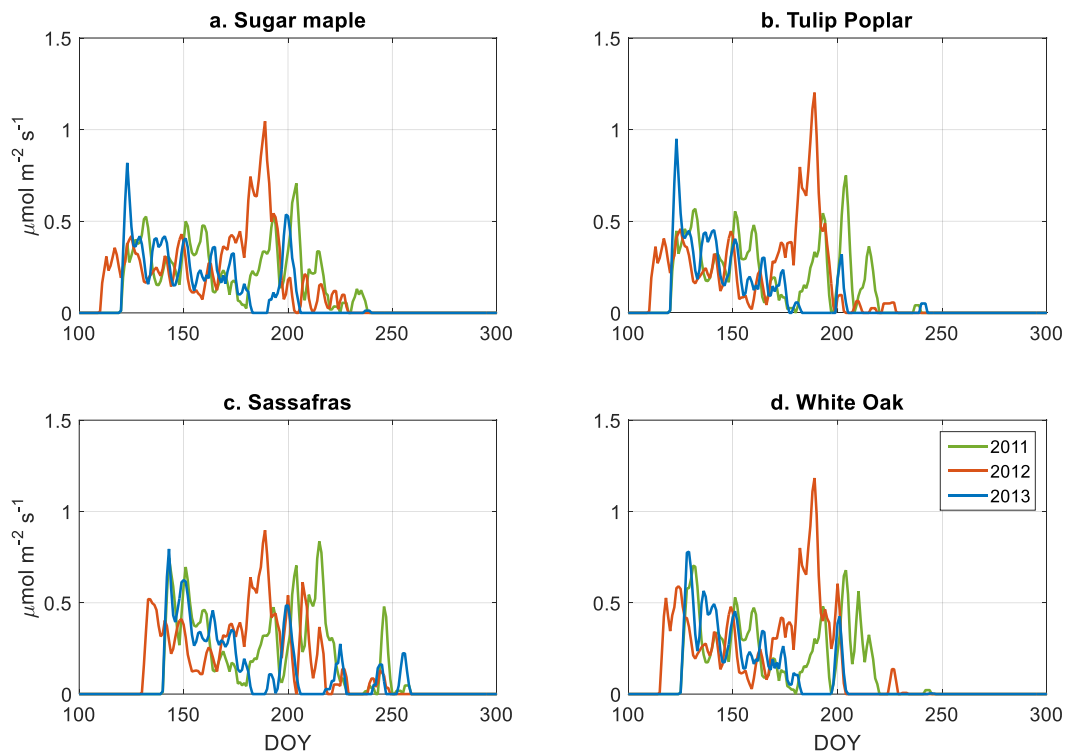


Figure 4.12 Simulated remobilization rates in 2011 – 2013. The simulated daily-averaged remobilization rates ($\mu\text{mol m}^{-2} \text{s}^{-1}$) for (a) sugar maple, (b) tulip poplar, (c) sassafras, and (d) white oak in 2011 – 2013.

Table 4.5 A final fraction of new carbon in leaf structural pool weighted by time-varying leaf growth in 2011-2013. Uncertainty represents one standard deviation of parameter uncertainty from 20 ensemble simulations.

	2011	2012	2013
Sugar Maple	0.71±0.05	0.67±0.05	0.74±0.05
Tulip Poplar	0.74±0.05	0.70±0.05	0.77±0.05
Sassafras	0.65±0.04	0.61±0.04	0.70±0.04
White Oak	0.66±0.04	0.65±0.04	0.69±0.04

4.4.4 iWUE across different methods, species, and drought conditions

Sampling the model at the same time as the leaf gas measurements showed good agreement in iWUE estimates within 2% difference (Fig. 4.13a, *Instantaneous Model A/g_s* and *Instantaneous Licor A/g_s*), showing that our model reasonably captures photosynthetic rates and stomatal conductance (Fig. 4.5). However, when we simulated the iWUE over the entire growing season weighted by GPP (*GPP-weighted Model A/g_s*), the iWUE estimates were 15-20% smaller compared to the leaf gas exchange measurements. This can be explained by mid-day leaf gas exchange measurements biased toward periods of high photosynthesis rates (Long and Bernacchi 2003). The estimated iWUE from tree ring and leaf isotopes (*Tree-ring* and *Leaf δ¹³C*) was significantly higher than iWUE from leaf gas exchange measurements (*Instantaneous Licor A/g_s*) by 35 and 20% respectively when mesophyll conductance (g_m) was not taken into account (Eq. 4.12b), and by 31 and 13% when g_m was considered (Eq. 4.12a) respectively. The decrease in iWUE after considering g_m is largest for white oak (decrease by 21 %), followed by tulip poplar, sassafras, and white oak (18, 14, and 8%, respectively), due to high photosynthetic rates that cause higher g_m limitation and less photosynthetic fractionation (Eq. 4.12a and Fig. 4.5). When the difference between the iWUEs based on leaf and tree ring δ¹³C was compared across species, the ring porous species (sassafras and white oak) showed lower difference (12.5%) than the diffuse porous species (sugar maple and tulip poplar, 25%) (Fig. 4.13a).

The estimated iWUE among the different methods and species also showed differences of drought response of iWUE (Fig. 4.13b). The iWUE was significantly higher for 2012 than 2011 using model and leaf gas exchange averaged across all species (9.03, 10.55, and 11.51 μmol_cmol_{H₂O}⁻¹ for *GPP-weighted Model A/g_s*, *instantaneous Model A/g_s*, and *Instantaneous Licor A/g_s*, respectively). The difference was smaller when using leaf and tree ring δ¹³C for all species except Sassafras (an averaged difference of 5.67 and 5.89 μmol_cmol_{H₂O}⁻¹ for all species except Sassafras, and 11.4 and 13.2 μmol_cmol_{H₂O}⁻¹ for sassafras for *Tree-ring* and *Leaf δ¹³C*, respectively), indicating dampened stomatal-response signals in the carbon isotope proxies. Sassafras exceptionally showed comparable drought iWUE response from all estimation methods, possibly related to its physiological traits as an isohydric and ring porous species (Table 4.1).

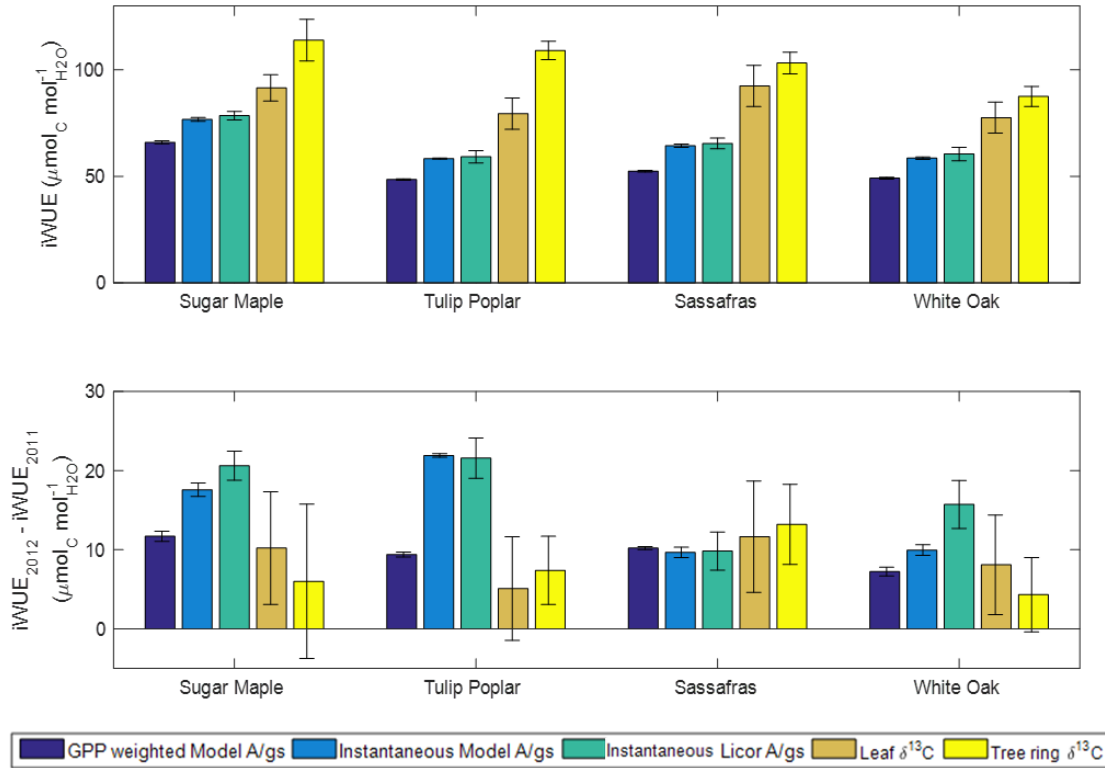


Figure 4.13 Estimation of iWUE. (a) Mean annual iWUE using five different methods in 2011–2012 for each of the 4 species studied with error bars. The horizontal bar in the middle of the *leaf* and *tree ring* $\delta^{13}\text{C}$ represents the adjustment in calculated iWUE between using the full Eq. 4.12a considering mesophyll conductance (g_m) rather than the simplified Eq. 4.12b (full bar height).

This shows that the model derived from Licor observations (*Instantaneous Licor A/g_s*) can be partially reconciled with isotopic observations, but the ‘true’ iWUE, *GPP-weighted model A/g_s*, is lower than all the methods. (b) The difference in annual iWUE using five different methods between 2012 and 2011 showing that drought iWUE response varies by species and method.

Error bars represent one standard deviation of parameter uncertainty from 20 ensemble simulations for *GPP-weighted* and *Instantaneous model A/g_s*, and one standard deviation of each sampling/average period for other methods.

4.5 Discussion

4.5.1 Processes affecting seasonal leaf $\delta^{13}\text{C}$

We observed an early-season enrichment in bulk leaf $\delta^{13}\text{C}$ that cannot be explained by photosynthetic fractionation alone (dashed lines in Fig. 4.6). The simulation without considering carbon allocation underestimated bulk leaf $\delta^{13}\text{C}$ early in the growing season, which implied the early-season leaf growth was fueled mainly by remobilized NSC (solid lines in Fig. 4.6 and Fig. 4.7). Previous leaf carbon isotope studies also observed this decreasing seasonal trend and explained it by a progressive shift from ^{13}C enriched remobilized carbon from root and stem storage pools (stored NSC) to carbon from recent assimilation (new NSC) (Damesin et al. 1998; Helle and Schleser 2004; Gessler et al. 2009; Stokes et al. 2010; Damesin and Lelarge 2003; Li et al. 2007).

There are some additional processes besides carbon allocation that may play a role in changing bulk leaf $\delta^{13}\text{C}$ through the growing season. First, an increase in cell membranes rich in lipids as leaves mature could make bulk leaf $\delta^{13}\text{C}$ more depleted because lipids have been shown to be ~4‰ lighter than synthesized sugars (Collister et al. 1994; Sachse et al. 2015). Second, leaf respiration could reduce leaf $\delta^{13}\text{C}$ over time because respiration has been shown to be more enriched in ^{13}C than the bulk leaf (Xu et al. 2004; Ubierna and Marshall 2011). Third, exported phloem sugars have also been found to be enriched in ^{13}C compared to leaf sugars (Bögelein et al. 2019) which could also result in lighter $\delta^{13}\text{C}$ leaf carbon values over time. According to Eglin *et al.* (2009), the remobilized NSC is most likely the main driver of the early-season enrichment in bulk leaf $\delta^{13}\text{C}$, which fuels both leaf and stem growth. This is supported by other studies showing similar enrichment patterns in the bulk leaf and tree-ring cellulose (Helle and Schleser 2004; Gessler et al. 2009, 2014; Eglin et al. 2010, 2009). The covariation of $\delta^{13}\text{C}$ of leaf tissue and stem cellulose growth increments suggests that the seasonal variability is driven by changes in the $\delta^{13}\text{C}$ of the leaf and stem NSC pools. The possibility of refining this model to reflect all of these processes is discussed in section 4.5.3.

We conducted model-fitting exercises to explore sensitivity of model parameters influencing the seasonal variability of modeled bulk leaf $\delta^{13}\text{C}$ (Fig. 4.14, Table 4.4). When remobilization of stored carbon was ignored, the RMSE increased by 100% (dashed line in Fig. 4), highlighting allocation as one of the most important factors in our model (Test 1 in Fig. 4.14).

We found that the mesophyll conductance (g_m), the offset between bulk leaf NSC and tree ring cellulose $\delta^{13}\text{C}$ ($\Delta_{stem-leafNSC}$), and species-specific minimum NSC pool size (S_{min}) are important to accurately simulate mean leaf $\delta^{13}\text{C}$ of the four species (27, 25 and 24% RMSE differences for Tests 2, 3, and 4, respectively) but did not contribute strongly to the seasonal variability (1, 7, and 4% of RMSE difference in mean bias, respectively, in Fig. 4.14). Switching species-specific stomatal response between isohydric and anisohydric species by changing the g_l value used in the photosynthesis calculations increased RMSE by 17% suggesting that incorporating isohydricity into our model, while important, has a smaller impact than allocation (Test 5 in Fig. 4.14). Lastly, removing species-specific phenology increased RMSE by 8% by changing the seasonal variability (Test 6 in Fig. 4.14). To sum up, these results illustrate that carbon allocation was one of the most important processes to explain the observed seasonal variability of bulk leaf $\delta^{13}\text{C}$ and therefore iWUE estimate biases.

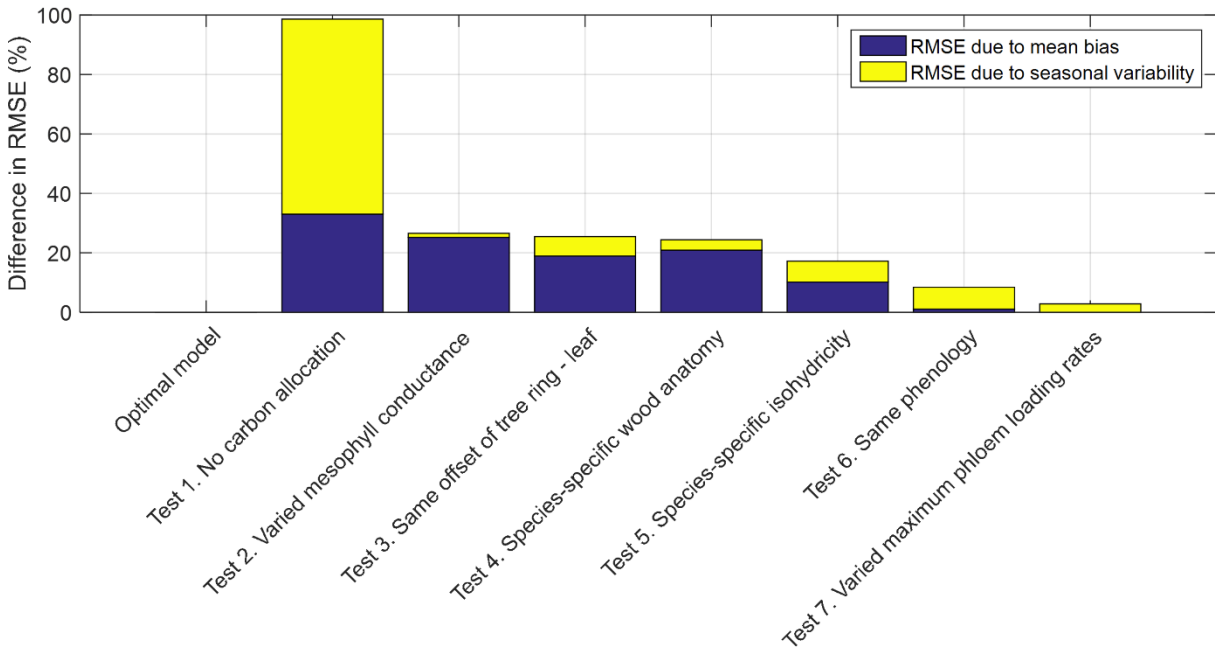


Figure 4.14 Model sensitivity test. Bar plot of the difference in RMSE between the observations and the model fits using the 1:1 line fit and the linear fit, compared to the RMSE of the optimal model (Table S2 and Supplementary Method 4).

4.5.2 Implications for the estimation of iWUE

From global compilations of leaf gas exchange, leaf $\delta^{13}\text{C}$, and eddy covariance data, Medlyn *et al.* (2017) investigated variations in iWUE across plant functional types (PFTs) using the g_1 proxy (Eq. 4.6). In their results, the leaf $\delta^{13}\text{C}$ based estimates of iWUE were higher than estimates based on gas exchange for most PFTs, including temperate deciduous trees. Medlyn *et al.* (2017) hypothesized that the discrepancy may be explained by neglected mesophyll conductance (g_m) in the isotopic calculations, although the magnitude of this discrepancy was more substantial than they expected in most PFTs.

Our results suggest that considering g_m may not fully explain the magnitude of the discrepancy of iWUE between isotopic and non-isotopic methods (Fig. 4.13). The higher iWUE inferred from leaf and tree ring $\delta^{13}\text{C}$ compared with leaf gas measurements could be due to the bias towards higher $\delta^{13}\text{C}$ values of remobilized stored NSC used in the spring leaf flush (Hoch, Richter and Körner, 2003; Stokes, Morecroft and Morison, 2010; Gessler *et al.*, 2014). One recent study also explained a discrepancy of iWUE between isotopic and non-isotopic methods by stored NSC remobilization during dry periods (Tarin *et al.* 2019). The iWUE overestimation we observed was smaller when using leaf $\delta^{13}\text{C}$ compared to tree ring $\delta^{13}\text{C}$, as the leaf $\delta^{13}\text{C}$ is likely affected less by stored NSC compared to tree ring $\delta^{13}\text{C}$ (Gessler *et al.* 2014).

Our findings emphasize that care must be taken when using plant tissue $\delta^{13}\text{C}$ as a proxy for iWUE. This supports the warning by Barbaroux and Bréda (2002) about using the $\delta^{13}\text{C}$ of plant tissues to estimate stomatal response to environmental changes as carbon allocation processes lead to species-specific biases and dampening of the signals between leaf- and tree-level responses. Our results also show that the stomatal iWUE $\delta^{13}\text{C}$ signal is altered in the leaf and tree ring tissues, suggesting that a direct comparison between isotope- and non-isotope-based iWUE estimation may be misleading to understand the plant stomatal responses. We acknowledge that these biases do not call into question long-term trends of iWUE estimates using a single measurement technique like tree rings, but will likely affect the interpretation of interannual variability (Lavergne *et al.* 2019; Gessler *et al.* 2014).

4.5.3 Suggested future work

Due to observational constraints, we did not simulate chemical composition changes within leaf tissues or the carbon pools in other plant tissues, like stems and roots. This limits the ability

of our model to track changes in stored NSC and post-photosynthetic fractionation through the entire tree. For a comprehensive understanding of the internal carbon allocation processes, future research should target tracking the $\delta^{13}\text{C}$ of the leaf respiration, structural, and NSC carbon pools in the trees over time, including sugars and starches, in leaves, intra-annual tree rings, and roots. Moreover, the relative contributions of different pathways, including maintenance and growth respiration (Xu *et al.*, 2004) and sugar export through phloem (Bögelein *et al.*, 2019) as well as dilution with recently assimilated sugars discussed here, leading to a decrease in bulk leaf $\delta^{13}\text{C}$ as the growing season progresses is not clear (Eglin *et al.* 2009). These types of detailed studies will yield further insight into how stored NSC contributes to each of these pools (Barbaroux and Bréda 2002; Furze *et al.* 2019).

The analysis of carbon isotope signatures of the different parts of tree tissues and fluxes will further improve our understanding of the offsets between tree ring cellulose and bulk leaf $\delta^{13}\text{C}$ that our sensitivity test showed to be critical (Fig. 4.14) and will help to improve models of carbon allocation and $\delta^{13}\text{C}$ fractionation. We also need more studies to understand the discrepancy in iWUE estimation between isotopic and non-isotopic methods for diverse PFTs that cover longer seasons and years and capture the full range of environmental conditions (Medlyn *et al.* 2011, 2017).

4.5.4 Conclusion

The observed and simulated seasonal leaf $\delta^{13}\text{C}$ variability showed that leaf tissues rely on stored NSC for their growth in the beginning of the growing season. As the growing season proceeds, the enriched leaf $\delta^{13}\text{C}$ decreases when leaf tissues make the switch from relying on remobilized stored NSC to new assimilates. This early season reliance on stored carbon with more enriched $\delta^{13}\text{C}$ values provides an explanation for the observed bias between isotopic and non-isotopic estimates for measuring iWUE. The different magnitudes of stored NSC for ring and diffuse porous species and under drought conditions may also play a role in the discrepancy of iWUE estimates. Therefore, the use of $\delta^{13}\text{C}$ of leaves and tree rings as a proxy for stomatal response to environmental processes, through iWUE, is complicated due to species-specific internal carbon allocation.

CHAPTER 5. SUMMARY AND FUTURE WORK

From the first article and Chapter 2 of the thesis, I showed that HAM microbial dynamics are an important component of the current Arctic methane budget as the new estimate more than doubles upland sinks. I also found revised estimates with microbial and permafrost SOC dynamics better match site-level and regional observations and observation-based inversions. This model projected a smaller increase of net methane emission than previous models by 2100 as the increase in wetland emission due to more accessible permafrost SOC is mostly offset by the increase in upland consumption by HAM. A potential decrease in future net methane emission was projected after including microbial physiology of HAM and MG. The first article highlighted the need to incorporate more detailed microbial dynamics into process-based methane models to better constrain the Arctic methane budget.

Although the new model significantly revises estimates of net Arctic methane emission, there are processes that current models, including mine, have not considered. I do not capture the complex Arctic hydrological and vegetation dynamics (Liljedahl et al. 2016; Nauta et al. 2015), which may influence estimates of both methane production and consumption. I focused on terrestrial ecosystems without considering potential large methane emissions from aquatic systems, whose magnitude and spatial distribution may change (Sepulveda-Jauregui et al. 2015; Wik et al. 2016). I used observed wetland methane emissions to optimize methane production and oxidation where the fraction of each is uncertain (Segers 1998). More observations of subsurface vertical processes using isotopic labeling analysis and inhibitor techniques will better constrain future models (Pedersen et al. 2018).

In the second article and Chapter 3 of the thesis, I developed the first process-based biogeochemistry model that maps the global distribution of wetland $\delta^{13}\text{C-CH}_4$ and thoroughly validated the model using site-level and regional observations. The new model isoTEM explained latitudinal and long-term variability of $\delta^{13}\text{C-CH}_4$ from wetlands. The latitudinal gradients of $\delta^{13}\text{C}$ of methane from wetlands strengthen due to distribution of C3/C4 plant, methanogen community, methane oxidation, but weaken due to plant mediated transport. Also, the long-term trends in $\delta^{13}\text{C-CH}_4$ from wetlands may be related to increased plant-mediated transport due to increasing temperature, but the changes were within the uncertainty range of our ensemble simulations. I

applied the model results as priors for an atmospheric transport modeling and showed that the spatially and temporally resolved wetland isotope map better matches observed inter-hemispheric $\delta^{13}\text{C-CH}_4$ compared to the previous uniform and static maps.

Although the new model significantly improved the understanding of the spatial and temporal variability of global wetland $\delta^{13}\text{C-CH}_4$ and global CH_4 budgets, there are still a few limitations of this study. First, I need more field and atmospheric measurements of wetland $\delta^{13}\text{C-CH}_4$ to further constrain model parameters. The optimization of fractionation factors (α_{HM} , α_{AM} , α_{MO} , α_{TP} , α_{TD} , α_{TE}) was based on a limited amount of observations, which increases the uncertainty of our model results. Also, since I set the fraction of two methanogen communities (HM and AM) using multiple regression analysis, the fraction changes spatially but not temporally, I need a better understanding of the temporal microbial community changes as they occur when permafrost thaws and disturbance happens (McCalley et al. 2014). Finally, various methanogenic and non-methanogenic processes will change $\delta^{13}\text{C}$ of CH_4 and CO_2 , and the CO_2/CH_4 ratios, thus $\delta^{13}\text{C-CH}_4$ emitted from wetlands. I need to identify detailed vertical subsurface methane processes using isotopic labeling analysis and inhibitor techniques to include those fractionation processes in the model.

In the third article and Chapter 4 of the thesis, the observed and simulated seasonal leaf $\delta^{13}\text{C}$ variability showed that leaf tissues rely on stored NSC for their growth in the beginning of the growing season. As the growing season proceeds, the enriched leaf $\delta^{13}\text{C}$ decreases when leaf tissues make the switch from relying on remobilized stored NSC to new assimilates. This early season reliance on stored carbon with more enriched $\delta^{13}\text{C}$ values provides an explanation for the observed bias between isotopic and non-isotopic estimates for measuring $i\text{WUE}$. The different magnitudes of stored NSC for ring and diffuse porous species and under drought conditions may also play a role in the discrepancy of $i\text{WUE}$ estimates. Therefore, the use of $\delta^{13}\text{C}$ of leaves and tree rings as a proxy for stomatal response to environmental processes, through $i\text{WUE}$, is complicated due to species-specific internal carbon allocation.

Due to observational constraints, I did not simulate chemical composition changes within leaf tissues or the carbon pools in other plant tissues, like stems and roots. This limits the ability of the model to track changes in stored NSC and post-photosynthetic fractionation through the entire tree. For a comprehensive understanding of the internal carbon allocation processes, future

research should target tracking the $\delta^{13}\text{C}$ of the leaf respiration, structural, and NSC carbon pools in the trees over time, including sugars and starches, in leaves, intra-annual tree rings, and roots. Moreover, the relative contributions of different pathways, including maintenance and growth respiration (Xu *et al.*, 2004) and sugar export through phloem (Bögelein *et al.*, 2019) as well as dilution with recently assimilated sugars discussed here, leading to a decrease in bulk leaf $\delta^{13}\text{C}$ as the growing season progresses is not clear (Eglin *et al.* 2009). These types of detailed studies will yield further insight into how stored NSC contributes to each of these pools (Barbaroux and Bréda 2002; Furze *et al.* 2019).

The analysis of carbon isotope signatures of the different parts of tree tissues and fluxes will further improve the understanding of the offsets between tree ring cellulose and bulk leaf $\delta^{13}\text{C}$ that our sensitivity test showed to be critical (Fig. 4.14) and will help to improve models of carbon allocation and $\delta^{13}\text{C}$ fractionation. I also need more studies to understand the discrepancy in iWUE estimation between isotopic and non-isotopic methods for diverse PFTs that cover longer seasons and years and capture the full range of environmental conditions (Medlyn *et al.* 2011, 2017).

REFERENCES

- Baani, M., and W. Liesack, 2008: Two isozymes of particulate methane monooxygenase with different methane oxidation kinetics are found in *Methylocystis* sp. strain SC2. *Proc. Natl. Acad. Sci. U. S. A.*, **105**, 10203–10208, <https://doi.org/10.1073/pnas.0702643105>.
- Badeck, F. W., G. Tcherkez, S. Nogués, C. Piel, and J. Ghashghaie, 2005: Post-photosynthetic fractionation of stable carbon isotopes between plant organs - A widespread phenomenon. *Rapid Commun. Mass Spectrom.*, **19**, 1381–1391, <https://doi.org/10.1002/rcm.1912>.
- Baldocchi, D. D., C. A. Vogel, and B. Hall, 1997: Seasonal variation of energy and water vapor exchange rates above and below a boreal jack pine forest canopy. *J. Geophys. Res. Atmos.*, **102**, 28939–28951.
- Barbaroux, C., and N. Bréda, 2002: Contrasting distribution and seasonal dynamics of carbohydrate reserves in stem wood of adult ring-porous sessile oak and diffuse-porous beech trees. *Tree Physiol.*, **22**, 1201–1210, <https://doi.org/10.1093/treephys/22.17.1201>.
- , N. Bréda, and E. Dufrêne, 2003: Distribution of above-ground and below-ground carbohydrate reserves in adult trees of two contrasting broad-leaved species (*Quercus petraea* and *Fagus sylvatica*). *New Phytol.*, **157**, 605–615, <https://doi.org/10.1046/j.1469-8137.2003.00681.x>.
- Basu, S., and Coauthors, 2013: Global CO₂ fluxes estimated from GOSAT retrievals of total column CO₂. *Atmos. Chem. Phys. Discuss.*, **13**.
- Battipaglia, G., M. Saurer, P. Cherubini, C. Calfapietra, H. R. McCarthy, R. J. Norby, and M. Francesca Cotrufo, 2013: Elevated CO₂ increases tree-level intrinsic water use efficiency: insights from carbon and oxygen isotope analyses in tree rings across three forest FACE sites. *New Phytol.*, **197**, 544–554.
- Belmecheri, S., R. S. Maxwell, A. H. Taylor, K. J. Davis, K. H. Freeman, and W. J. Munger, 2014: Tree-ring $\delta^{13}\text{C}$ tracks flux tower ecosystem productivity estimates in a NE temperate forest. *Environ. Res. Lett.*, **9**, 74011.
- Bloom, A. A., P. I. Palmer, A. Fraser, D. S. Reay, and C. Frankenberg, 2010: Large-scale controls of methanogenesis inferred from methane and gravity spaceborne data. *Science (80-.)*, **327**, 322–325.
- Bögelein, R., M. M. Lehmann, and F. M. Thomas, 2019: Differences in carbon isotope leaf-to-phloem fractionation and mixing patterns along a vertical gradient in mature European beech and Douglas fir. *New Phytol.*, **222**, 1803–1815, <https://doi.org/10.1111/nph.15735>.
- Bohn, T. J., and Coauthors, 2015: WETCHIMP-WSL: Intercomparison of wetland methane emissions models over West Siberia. *Biogeosciences*, **12**, 3321–3349, <https://doi.org/10.5194/bg-12-3321-2015>.

- Bolstad, P. V., K. Mitchell, and J. M. Vose, 1999: Foliar temperature–respiration response functions for broad-leaved tree species in the southern Appalachians. *Tree Physiol.*, **19**, 871–878.
- Bonan, G., K. W. Oleson, R. A. Fisher, G. Lasslop, and M. Reichstein, 2012: Reconciling leaf physiological traits and canopy flux data: Use of the TRY and FLUXNET databases in the Community Land Model version 4. *J. Geophys. Res. Biogeosciences*, **117**.
- Bonan, G. B., 2008: Forests and climate change: Forcings, feedbacks, and the climate benefits of forests. *Science (80-.)*, **320**, 1444–1449, <https://doi.org/10.1126/science.1155121>.
- , M. Williams, R. A. Fisher, and K. W. Oleson, 2014: Modeling stomatal conductance in the earth system: Linking leaf water-use efficiency and water transport along the soil-plant-atmosphere continuum. *Geosci. Model Dev.*, **7**, 2193–2222, <https://doi.org/10.5194/gmd-7-2193-2014>.
- Bowling, D. R., D. E. Pataki, and J. T. Randerson, 2008: Carbon isotopes in terrestrial ecosystem pools and CO₂ fluxes. *New Phytol.*, **178**, 24–40, <https://doi.org/10.1111/j.1469-8137.2007.02342.x>.
- Brent, R. P., 1976: Fast multiple-precision evaluation of elementary functions. *J. ACM*, **23**, 242–251.
- Brownlow, R., and Coauthors, 2017: Isotopic Ratios of Tropical Methane Emissions by Atmospheric Measurement. *Global Biogeochem. Cycles*, **31**, 1408–1419, <https://doi.org/10.1002/2017GB005689>.
- Brüggemann, N., and Coauthors, 2011: Carbon allocation and carbon isotope fluxes in the plant-soil-atmosphere continuum: A review. *Biogeosciences*, **8**, 3457–3489, <https://doi.org/10.5194/bg-8-3457-2011>.
- Bruhwyler, L., and Coauthors, 2014: CarbonTracker-CH₄: An assimilation system for estimating emissions of atmospheric methane. *Atmos. Chem. Phys.*, **14**, 8269–8293, <https://doi.org/10.5194/acp-14-8269-2014>.
- Brzostek, E. R., D. Dragoni, H. P. Schmid, A. F. Rahman, D. Sims, C. A. Wayson, D. J. Johnson, and R. P. Phillips, 2014: Chronic water stress reduces tree growth and the carbon sink of deciduous hardwood forests. *Glob. Chang. Biol.*, **20**, 2531–2539, <https://doi.org/10.1111/gcb.12528>.
- Burke, R. A., T. R. Barber, and W. M. Sackett, 1988: Methane flux and stable hydrogen and carbon isotope composition of sedimentary methane from the Florida Everglades. *Global Biogeochem. Cycles*, **2**, 329–340, <https://doi.org/10.1029/GB002i004p00329>.
- Carbone, M. S., C. I. Czimczik, T. F. Keenan, P. F. Murakami, N. Pederson, P. G. Schaberg, X. Xu, and A. D. Richardson, 2013: Age, allocation and availability of nonstructural carbon in mature red maple trees. *New Phytol.*, **200**, 1145–1155, <https://doi.org/10.1111/nph.12448>.

- Carter, A. J., and R. J. Scholes, 2000: Spatial global database of soil properties. *IGBP Glob. Soil Data Task CD-ROM. Int. Geosphere-biosph. Program. Data Inf. Syst. Toulouse, Fr.,.*
- Cernusak, L. A., and Coauthors, 2009: Why are non-photosynthetic tissues generally ^{13}C enriched compared with leaves in C3 plants? Review and synthesis of current hypotheses. *Funct. Plant Biol.*, **36**, 199–213, <https://doi.org/10.1071/FP08216>.
- Chang, R. Y. W., and Coauthors, 2014: Methane emissions from Alaska in 2012 from CARVE airborne observations. *Proc. Natl. Acad. Sci. U. S. A.*, **111**, 16694–16699, <https://doi.org/10.1073/pnas.1412953111>.
- Chanton, J. P., 2005: The effect of gas transport on the isotope signature of methane in wetlands. *Org. Geochem.*, **36**, 753–768, <https://doi.org/10.1016/j.orggeochem.2004.10.007>.
- , D. Fields, and M. E. Hines, 2006: Controls on the hydrogen isotopic composition of biogenic methane from high-latitude terrestrial wetlands. *J. Geophys. Res. Biogeosciences*, **111**, 1–9, <https://doi.org/10.1029/2005JG000134>.
- Charney, N. D., F. Babst, B. Poulter, S. Record, V. M. Trouet, D. Frank, B. J. Enquist, and M. E. K. Evans, 2016: Observed forest sensitivity to climate implies large changes in 21st century North American forest growth. *Ecol. Lett.*, **19**, 1119–1128, <https://doi.org/10.1111/ele.12650>.
- Christiansen, J. R., A. J. B. Romero, N. O. G. Jørgensen, M. A. Glaring, C. J. Jørgensen, L. K. Berg, and B. Elberling, 2015: Methane fluxes and the functional groups of methanotrophs and methanogens in a young Arctic landscape on Disko Island, West Greenland. *Biogeochemistry*, **122**, 15–33, <https://doi.org/10.1007/s10533-014-0026-7>.
- Ciais, P., and Coauthors, 2005: Europe-wide reduction in primary productivity caused by the heat and drought in 2003. *Nature*, **437**, 529–533, <https://doi.org/10.1038/nature03972>.
- Collister, J. W., G. Rieley, B. Stern, G. Eglinton, and B. Fry, 1994: Compound-specific $\delta^{13}\text{C}$ analyses of leaf lipids from plants with differing carbon dioxide metabolisms. *Org. Geochem.*, **21**, 619–627, [https://doi.org/10.1016/0146-6380\(94\)90008-6](https://doi.org/10.1016/0146-6380(94)90008-6).
- Conrad, R., 2007: Microbial Ecology of Methanogens and Methanotrophs. *Adv. Agron.*, **96**, 1–63, [https://doi.org/10.1016/S0065-2113\(07\)96005-8](https://doi.org/10.1016/S0065-2113(07)96005-8).
- , 2009: The global methane cycle: Recent advances in understanding the microbial processes involved. *Environ. Microbiol. Rep.*, **1**, 285–292, <https://doi.org/10.1111/j.1758-2229.2009.00038.x>.
- Cornwell, W. K., and Coauthors, 2018: Climate and soils together regulate photosynthetic carbon isotope discrimination within C3 plants worldwide. *Glob. Ecol. Biogeogr.*, **27**, 1056–1067, <https://doi.org/10.1111/geb.12764>.
- Curry, C. L., 2007: Modeling the soil consumption at atmospheric methane at the global scale. *Global Biogeochem. Cycles*, **21**, 1–15, <https://doi.org/10.1029/2006GB002818>.

- D'Imperio, L., C. S. Nielsen, A. Westergaard-Nielsen, A. Michelsen, and B. Elberling, 2017: Methane oxidation in contrasting soil types: responses to experimental warming with implication for landscape-integrated CH₄ budget. *Glob. Chang. Biol.*, **23**, 966–976, <https://doi.org/10.1111/gcb.13400>.
- Damesin, C., and C. Lelarge, 2003: Carbon isotope composition of current-year shoots from *Fagus sylvatica* in relation to growth, respiration and use of reserves. *Plant, Cell Environ.*, **26**, 207–219, <https://doi.org/10.1046/j.1365-3040.2003.00951.x>.
- , S. Rambal, and R. Joffre, 1998: Seasonal and annual changes in leaf $\delta^{13}\text{C}$ in two co-occurring Mediterranean oaks: Relations to leaf growth and drought progression. *Funct. Ecol.*, **12**, 778–785, <https://doi.org/10.1046/j.1365-2435.1998.00259.x>.
- DelSontro, T., J. J. Beaulieu, and J. A. Downing, 2018: Greenhouse gas emissions from lakes and impoundments: Upscaling in the face of global change. *Limnol. Oceanogr. Lett.*, **3**, 64–75, <https://doi.org/10.1002/lol2.10073>.
- Dietze, M. C., A. Sala, M. S. Carbone, C. I. Czimczik, J. A. Mantooth, A. D. Richardson, and R. Vargas, 2014: Nonstructural Carbon in Woody Plants. *Annu. Rev. Plant Biol.*, **65**, 667–687, <https://doi.org/10.1146/annurev-arplant-050213-040054>.
- Dinsmore, K. J., J. Drewer, P. E. Levy, C. George, A. Lohila, M. Aurela, and U. M. Skiba, 2017: Growing season CH₄ and N₂O fluxes from a subarctic landscape in northern Finland; From chamber to landscape scale. *Biogeosciences*, **14**, 799–815, <https://doi.org/10.5194/bg-14-799-2017>.
- Dlugokencky, E. J., and Coauthors, 2005: Conversion of NOAA atmospheric dry air CH₄ mole fractions to a gravimetrically prepared standard scale. *J. Geophys. Res. Atmos.*, **110**.
- Dlugokencky, E. J., E. G. Nisbet, R. Fisher, and D. Lowry, 2011: Global atmospheric methane: budget, changes and dangers. *Philos. Trans. R. Soc. A Math. Phys. Eng. Sci.*, **369**, 2058–2072.
- Duan, Q. Y., V. K. Gupta, and S. Sorooshian, 1993: Shuffled complex evolution approach for effective and efficient global minimization. *J. Optim. Theory Appl.*, **76**, 501–521.
- Dufrêne, E., H. Davi, C. François, G. Le Maire, V. Le Dantec, and A. Granier, 2005: Modelling carbon and water cycles in a beech forest. Part I: Model description and uncertainty analysis on modelled NEE. *Ecol. Modell.*, **185**, 407–436, <https://doi.org/10.1016/j.ecolmodel.2005.01.004>.
- Eglin, T., C. Fresneau, C. Lelarge-Trouverie, C. Francois, and C. Damesin, 2009: Leaf and twig $\delta^{13}\text{C}$ during growth in relation to biochemical composition and respired CO₂. *Tree Physiol.*, **29**, 777–788, <https://doi.org/10.1093/treephys/tpp013>.
- , C. Francois, A. Michelot, N. Delpierre, and C. Damesin, 2010: Linking intra-seasonal variations in climate and tree-ring $\delta^{13}\text{C}$: A functional modelling approach. *Ecol. Modell.*, **221**, 1779–1797, <https://doi.org/10.1016/j.ecolmodel.2010.04.007>.

- Ehman, J. L., H. P. Schmid, C. S. B. Grimmond, J. C. Randolph, P. J. Hanson, C. A. Wayson, and F. D. Cropley, 2002: An initial intercomparison of micrometeorological and ecological inventory estimates of carbon exchange in a mid-latitude deciduous forest. *Glob. Chang. Biol.*, **8**, 575–589.
- Emmerton, C. A., V. L. St. Louis, I. Lehnherr, E. R. Humphreys, E. Rydz, and H. R. Kosolofski, 2014: The net exchange of methane with high Arctic landscapes during the summer growing season. *Biogeosciences*, **11**, 3095–3106, <https://doi.org/10.5194/bg-11-3095-2014>.
- Etheridge, D. M., L. Steele, R. J. Francey, and R. L. Langenfelds, 1998: Atmospheric methane between 1000 AD and present: Evidence of anthropogenic emissions and climatic variability. *J. Geophys. Res. Atmos.*, **103**, 15979–15993.
- Farquhar, G. D., and T. D. Sharkey, 1982: Stomatal conductance and photosynthesis. *Annu. Rev. Plant Physiol.*, **33**, 317–345.
- , J. R. Ehleringer, and K. T. Hubick, 1989: Carbon isotope discrimination and photosynthesis. *Annu. Rev. Plant Biol.*, **40**, 503–537.
- Fatichi, S., S. Leuzinger, and C. Körner, 2014: Moving beyond photosynthesis: From carbon source to sink-driven vegetation modeling. *New Phytol.*, **201**, 1086–1095, <https://doi.org/10.1111/nph.12614>.
- Fei, S., N. Kong, K. C. Steiner, W. K. Moser, and E. B. Steiner, 2011: Change in oak abundance in the eastern United States from 1980 to 2008. *For. Ecol. Manage.*, **262**, 1370–1377, <https://doi.org/10.1016/j.foreco.2011.06.030>.
- , J. M. Desprez, K. M. Potter, I. Jo, J. A. Knott, and C. M. Oswalt, 2017: Divergence of species responses to climate change. *Sci. Adv.*, **3**, <https://doi.org/10.1126/sciadv.1603055>.
- Feinberg, A. I., A. Coulon, A. Stenke, S. Schwietzke, and T. Peter, 2018: Isotopic source signatures: Impact of regional variability on the $\Delta^{13}\text{CH}_4$ trend and spatial distribution. *Atmos. Environ.*, **174**, 99–111, <https://doi.org/10.1016/j.atmosenv.2017.11.037>.
- Fisher, R. E., and Coauthors, 2017: Measurement of the ^{13}C isotopic signature of methane emissions from northern European wetlands. *Global Biogeochem. Cycles*, **31**, 605–623, <https://doi.org/10.1002/2016GB005504>.
- Frank, D. C., and Coauthors, 2015: Water-use efficiency and transpiration across European forests during the Anthropocene. *Nat. Clim. Chang.*, **5**, 579–583, <https://doi.org/10.1038/nclimate2614>.
- Friedlingstein, P., and Coauthors, 2019: Global carbon budget 2019. *Earth Syst. Sci. Data*, **11**, 1783–1838, <https://doi.org/10.5194/essd-11-1783-2019>.
- Furze, M. E., B. A. Huggett, D. M. Aubrecht, C. D. Stolz, M. S. Carbone, and A. D. Richardson, 2019: Whole-tree nonstructural carbohydrate storage and seasonal dynamics in five temperate species. *New Phytol.*, **221**, 1466–1477, <https://doi.org/10.1111/nph.15462>.

- Ganesan, A. L., A. C. Stell, N. Gedney, E. Comyn-Platt, G. Hayman, M. Rigby, B. Poulter, and E. R. C. Hornibrook, 2018: Spatially Resolved Isotopic Source Signatures of Wetland Methane Emissions. *Geophys. Res. Lett.*, **45**, 3737–3745, <https://doi.org/10.1002/2018GL077536>.
- Gessler, A., and K. Treydte, 2016: The fate and age of carbon - insights into the storage and remobilization dynamics in trees. *New Phytol.*, **209**, 1338–1340, <https://doi.org/10.1111/nph.13863>.
- , E. Brandes, N. Buchmann, G. Helle, H. Rennenberg, and R. L. Barnard, 2009: Tracing carbon and oxygen isotope signals from newly assimilated sugars in the leaves to the tree-ring archive. *Plant, Cell Environ.*, **32**, 780–795, <https://doi.org/10.1111/j.1365-3040.2009.01957.x>.
- , J. P. Ferrio, R. Hommel, K. Treydte, R. A. Werner, and R. K. Monson, 2014: Stable isotopes in tree rings: Towards a mechanistic understanding of isotope fractionation and mixing processes from the leaves to the wood. *Tree Physiol.*, **34**, 796–818, <https://doi.org/10.1093/treephys/tpu040>.
- Gottschalk, G., 2012: *Bacterial metabolism*. Springer Science & Business Media,.
- Graven, H., and Coauthors, 2017: Compiled records of carbon isotopes in atmospheric CO₂ for historical simulations in CMIP6. *Geosci. Model Dev.*, **10**, 4405–4417, <https://doi.org/10.5194/gmd-10-4405-2017>.
- Hagerty, S. B., K. J. Van Groenigen, S. D. Allison, B. A. Hungate, E. Schwartz, G. W. Koch, R. K. Kolka, and P. Dijkstra, 2014: Accelerated microbial turnover but constant growth efficiency with warming in soil. *Nat. Clim. Chang.*, **4**, 903–906, <https://doi.org/10.1038/nclimate2361>.
- Harazono, Y., M. Mano, and A. Miyata, Temporal and spatial differences of methane flux at arctic tundra in Alaska.
- Harris, I., P. D. Jones, T. J. Osborn, and D. H. Lister, 2014: Updated high-resolution grids of monthly climatic observations - the CRU TS3.10 Dataset. *Int. J. Climatol.*, **34**, 623–642, <https://doi.org/10.1002/joc.3711>.
- Hasibeder, R., L. Fuchslueger, A. Richter, and M. Bahn, 2015: Summer drought alters carbon allocation to roots and root respiration in mountain grassland. *New Phytol.*, **205**, 1117–1127, <https://doi.org/10.1111/nph.13146>.
- Hausmann, P., R. Sussmann, and D. Smale, 2016: Contribution of oil and natural gas production to renewed increase in atmospheric methane (2007–2014): top-down estimate from ethane and methane column observations. *Atmos. Chem. Phys.*, **16**, 3227–3244.
- Heizmann, U., J. Kreuzwieser, J. P. Schnitzler, N. Brüggemann, and H. Rennenberg, 2001: Assimilate transport in the xylem sap of pedunculate oak (*Quercus robur*) saplings. *Plant Biol.*, **3**, 132–138, <https://doi.org/10.1055/s-2001-12898>.

- Helle, G., and G. H. Schleser, 2004: Beyond CO₂-fixation by Rubisco - An interpretation of ¹³C/¹²C variations in tree rings from novel intra-seasonal studies on broad-leaf trees. *Plant, Cell Environ.*, **27**, 367–380, <https://doi.org/10.1111/j.0016-8025.2003.01159.x>.
- Higham, D. J., and N. J. Higham, 2016: *MATLAB guide*. Siam,.
- Hoch, G., A. Richter, and C. Körner, 2003: Hoch, Richter, Körner - 2003 - Non-structural carbon compounds in temperate forest trees.pdf. *Plant, Cell Environ.*, 1067–1081.
- Hoffmann, W. A., R. M. Marchin, P. Abit, and O. L. Lau, 2011: Hydraulic failure and tree dieback are associated with high wood density in a temperate forest under extreme drought. *Glob. Chang. Biol.*, **17**, 2731–2742.
- Holmes, M. E., J. P. Chanton, H. S. Bae, and A. Ogram, 2014: Effect of nutrient enrichment on $\delta^{13}\text{CH}_4$ and the methane production pathway in the Florida Everglades. *J. Geophys. Res. Biogeosciences*, **119**, 1267–1280, <https://doi.org/10.1002/jgrg.20122>.
- Holmes, M. E., J. P. Chanton, M. M. Tfaily, and A. Ogram, 2015: CO₂ and CH₄ isotope compositions and production pathways in a tropical peatland. *Global Biogeochem. Cycles*, **29**, 1–18.
- Horn, M. A., C. Matthies, K. Küsel, A. Schramm, and H. L. Drake, 2003: Hydrogenotrophic methanogenesis by moderately acid-tolerant methanogens of a methane-emitting acidic peat. *Appl. Environ. Microbiol.*, **69**, 74–83, <https://doi.org/10.1128/AEM.69.1.74-83.2003>.
- Hugelius, G., and Coauthors, 2013: A new data set for estimating organic carbon storage to 3 m depth in soils of the northern circumpolar permafrost region. *Earth Syst. Sci. Data*, **5**, 393–402, <https://doi.org/10.5194/essd-5-393-2013>.
- Juncher Jørgensen, C., K. M. Lund Johansen, A. Westergaard-Nielsen, and B. Elberling, 2015: Net regional methane sink in High Arctic soils of northeast Greenland. *Nat. Geosci.*, **8**, 20–23, <https://doi.org/10.1038/ngeo2305>.
- Kagawa, A., A. Sugimoto, and T. C. Maximov, 2006: Seasonal course of translocation, storage and remobilization of ¹³C pulse-labeled photoassimilate in naturally growing *Larix gmelinii* saplings. *New Phytol.*, **171**, 793–804, <https://doi.org/10.1111/j.1469-8137.2006.01780.x>.
- De Kauwe, M. G., and Coauthors, 2014: Where does the carbon go? A model-data intercomparison of vegetation carbon allocation and turnover processes at two temperate forest free-air CO₂ enrichment sites. *New Phytol.*, **203**, 883–899, <https://doi.org/10.1111/nph.12847>.
- Keeling, C. D., 1960: The concentration and isotopic abundances of carbon dioxide in the atmosphere. *Tellus*, **12**, 200–203.
- Keeling, R. F., and Coauthors, 2017: Atmospheric evidence for a global secular increase in carbon isotopic discrimination of land photosynthesis. *Proc. Natl. Acad. Sci. U. S. A.*, **114**, 10361–10366, <https://doi.org/10.1073/pnas.1619240114>.

- Keller, K. M., and Coauthors, 2017: 20th century changes in carbon isotopes and water-use efficiency: Tree-ring-based evaluation of the CLM4.5 and LPX-Bern models. *Biogeosciences*, **14**, 2641–2673, <https://doi.org/10.5194/bg-14-2641-2017>.
- Kelly, C. a, N. Carolina, C. Hill, B. Dise, and C. S. Martens, 1992: Temporal variations in the stable carbon isotopic composition of methane emitted from Minnesota peatlands. **6**, 263–269.
- Knoblauch, C., O. Spott, S. Evgrafova, L. Kutzbach, and E. Pfeiffer, 2015: Regulation of methane production, oxidation, and emission by vascular plants and bryophytes in ponds of the northeast Siberian polygonal tundra. *J. Geophys. Res. Biogeosciences*, **120**, 2525–2541.
- Koven, C. D., B. Ringeval, P. Friedlingstein, P. Ciais, P. Cadule, D. Khvorostyanov, G. Krinner, and C. Tarnocai, 2011: Permafrost carbon-climate feedbacks accelerate global warming. *Proc. Natl. Acad. Sci. U. S. A.*, **108**, 14769–14774, <https://doi.org/10.1073/pnas.1103910108>.
- Krol, M., and Coauthors, 2005: The two-way nested global chemistry-transport zoom model TM5: algorithm and applications. *Atmos. Chem. Phys.*, **5**, 417–432.
- Kuptz, D., F. Fleischmann, R. Matyssek, and T. E. E. Grams, 2011: Seasonal patterns of carbon allocation to respiratory pools in 60-yr-old deciduous (*Fagus sylvatica*) and evergreen (*Picea abies*) trees assessed via whole-tree stable carbon isotope labeling. *New Phytol.*, **191**, 160–172, <https://doi.org/10.1111/j.1469-8137.2011.03676.x>.
- Lau, M. C. Y., and Coauthors, 2015: An active atmospheric methane sink in high Arctic mineral cryosols. *ISME J.*, **9**, 1880–1891, <https://doi.org/10.1038/ismej.2015.13>.
- , and Coauthors, 2016: An oligotrophic deep-subsurface community dependent on syntrophy is dominated by sulfur-driven autotrophic denitrifiers. *Proc. Natl. Acad. Sci. U. S. A.*, **113**, E7927–E7936, <https://doi.org/10.1073/pnas.1612244113>.
- Lavergne, A., H. Graven, M. G. De Kauwe, T. F. Keenan, B. E. Medlyn, and I. C. Prentice, 2019: Observed and modelled historical trends in the water-use efficiency of plants and ecosystems. *Glob. Chang. Biol.*, **25**, 2242–2257.
- Lawrence, D., R. Fisher, C. Koven, K. Oleson, S. Swenson, and M. Vertenstein, 2018: Technical Description of version 5.0 of the Community Land Model (CLM). *Natl. Cent. Atmos. Res. (NCAR), NCAR Tech. Note NCARTN-478+ STR*, **257**.
- Lawrence, D. M., C. D. Koven, S. C. Swenson, W. J. Riley, and A. G. Slater, 2015: Permafrost thaw and resulting soil moisture changes regulate projected high-latitude CO₂ and CH₄ emissions. *Environ. Res. Lett.*, **10**, <https://doi.org/10.1088/1748-9326/10/9/094011>.
- Li, Y., T. Chen, Y. Zhang, and L. An, 2007: The relation of seasonal pattern in stable carbon compositions to meteorological variables in the leaves of *Sabina przewalskii* Kom. and *Sabina chinensis* (Lin.) Ant. *Environ. Geol.*, **51**, 1279–1284, <https://doi.org/10.1007/s00254-006-0421-z>.

- Liljedahl, A. K., and Coauthors, 2016: Pan-Arctic ice-wedge degradation in warming permafrost and its influence on tundra hydrology. *Nat. Geosci.*, **9**, 312–318, <https://doi.org/10.1038/ngeo2674>.
- Linares, J. C., and J. J. Camarero, 2012: From pattern to process: Linking intrinsic water-use efficiency to drought-induced forest decline. *Glob. Chang. Biol.*, **18**, 1000–1015, <https://doi.org/10.1111/j.1365-2486.2011.02566.x>.
- Liu, L., Q. Zhuang, Y. Oh, N. J. Shurpali, S. Kim, and B. Poulter, 2020: Uncertainty Quantification of Global Net Methane Emissions from Terrestrial Ecosystems Using a Mechanistically-based Biogeochemistry Model. *J. Geophys. Res.*, **In Review**.
- Long, S. P., and C. J. Bernacchi, 2003: Gas exchange measurements, what can they tell us about the underlying limitations to photosynthesis? Procedures and sources of error. *J. Exp. Bot.*, **54**, 2393–2401.
- Masarie, K. A., and P. P. Tans, 1995: Extension and integration of atmospheric carbon dioxide data into a globally consistent measurement record. *J. Geophys. Res. Atmos.*, **100**, 11593–11610.
- Matthews, E., and Fung, I., 1987: Methane emission from natural wetlands: Global distribution, area, and environmental characteristics of sources. *Global Biogeochem. Cycles*, **1**, 61–86.
- Mayrhofer, S., and Coauthors, 2004: Carbon balance in leaves of young poplar trees. *Plant Biol.*, **6**, 730–739, <https://doi.org/10.1055/s-2004-821268>.
- McCalley, C. K., and Coauthors, 2014: Methane dynamics regulated by microbial community response to permafrost thaw. *Nature*, **514**, 478–481, <https://doi.org/10.1038/nature13798>.
- McCarroll, D., and N. J. Loader, 2004: Stable isotopes in tree rings. *Quat. Sci. Rev.*, **23**, 771–801, <https://doi.org/10.1016/j.quascirev.2003.06.017>.
- McDowell, N. G., B. J. Bond, L. T. Dickman, M. G. Ryan, and D. Whitehead, 2011: Relationships between tree height and carbon isotope discrimination. *Size-and age-related changes in tree structure and function*, Springer, 255–286.
- McGuire, A. D., and Coauthors, 2009: Sensitivity of the carbon cycle in the Arctic to climate change. *Ecol. Monogr.*, **79**, 523–555, <https://doi.org/10.1890/08-2025.1>.
- McGuire, A. D., and Coauthors, 2012: An assessment of the carbon balance of Arctic tundra: Comparisons among observations, process models, and atmospheric inversions. *Biogeosciences*, **9**, 3185–3204, <https://doi.org/10.5194/bg-9-3185-2012>.
- McGuire, A. D., and Coauthors, 2018: Dependence of the evolution of carbon dynamics in the northern permafrost region on the trajectory of climate change. *Proc. Natl. Acad. Sci. U. S. A.*, **115**, 3882–3887, <https://doi.org/10.1073/pnas.1719903115>.
- Medlyn, B. E., and Coauthors, 2011: Reconciling the optimal and empirical approaches to

- modelling stomatal conductance. *Glob. Chang. Biol.*, **17**, 2134–2144, <https://doi.org/10.1111/j.1365-2486.2010.02375.x>.
- , and Coauthors, 2017: How do leaf and ecosystem measures of water-use efficiency compare? *New Phytol.*, <https://doi.org/10.1111/nph.14626>.
- Meinshausen, M., and Coauthors, 2011: The RCP greenhouse gas concentrations and their extensions from 1765 to 2300. *Clim. Change*, **109**, 213–241, <https://doi.org/10.1007/s10584-011-0156-z>.
- Meirink, J. F., P. Bergamaschi, and M. C. Krol, 2008: Four-dimensional variational data assimilation for inverse modelling of atmospheric methane emissions: method and comparison with synthesis inversion. *Atmos. Chem. Phys.*, **8**, 6341–6353.
- Melillo, J. M., A. D. McGuire, D. W. Kicklighter, B. Moore, C. J. Vorosmarty, and A. L. Schloss, 1993: Global climate change and terrestrial net primary production. *Nature*, **363**, 234.
- Melton, J. R., and Coauthors, 2013: Present state of global wetland extent and wetland methane modelling: Conclusions from a model inter-comparison project (WETCHIMP). *Biogeosciences*, **10**, 753–788, <https://doi.org/10.5194/bg-10-753-2013>.
- Le Mer, J., and P. Roger, 2001: Production, oxidation, emission and consumption of methane by soils: a review. *Eur. J. Soil Biol.*, **37**, 25–50.
- Millar, C. I., and N. L. Stephenson, 2015: Temperate forest health in an era of emerging megadisturbance. *Science (80-.)*, **349**, 823–826, <https://doi.org/10.1126/science.aaa9933>.
- Miller, J. B., and P. P. Tans, 2003: Calculating isotopic fractionation from atmospheric measurements at various scales. *Tellus, Ser. B Chem. Phys. Meteorol.*, **55**, 207–214, <https://doi.org/10.1034/j.1600-0889.2003.00020.x>.
- , K. A. Mack, R. Dissly, J. W. C. White, E. J. Dlugokencky, and P. P. Tans, 2002: Development of analytical methods and measurements of $^{13}\text{C}/^{12}\text{C}$ in atmospheric CH_4 from the NOAA Climate Monitoring and Diagnostics Laboratory Global Air Sampling Network. *J. Geophys. Res. Atmos.*, **107**.
- Miller, S. M., and Coauthors, 2016: A multiyear estimate of methane fluxes in Alaska from CARVE atmospheric observations. *Global Biogeochem. Cycles*, **30**, 1441–1453, <https://doi.org/10.1002/2016GB005419>.
- Moing, A., A. Escobar-Gutierrez, and J. P. Gaudillere, 1994: Modeling carbon export out of mature peach leaves. *Plant Physiol.*, **106**, 591–600.
- Monclus, R., and Coauthors, 2006: Impact of drought on productivity and water use efficiency in 29 genotypes of *Populus deltoides* × *Populus nigra*. *New Phytol.*, **169**, 765–777.
- Myneni, R. B., and Coauthors, 2002: Global products of vegetation leaf area and fraction absorbed PAR from year one of MODIS data. *Remote Sens. Environ.*, **83**, 214–231.

- Nakagawa, F., N. Yoshida, Y. Nojiri, and V. Makarov, 2002: Production of methane from alasses in eastern Siberia: Implications from its ^{14}C and stable isotopic compositions. *Global Biogeochem. Cycles*, **16**, 14-1-14–15, <https://doi.org/10.1029/2000gb001384>.
- Naus, S., S. A. Montzka, S. Pandey, S. Basu, E. J. Dlugokencky, and M. Krol, 2019: Constraints and biases in a tropospheric two-box model of OH. *Atmos. Chem. Phys.*, **19**, 407–424.
- Nauta, A. L., and Coauthors, 2015: Permafrost collapse after shrub removal shifts tundra ecosystem to a methane source. *Nat. Clim. Chang.*, **5**, 67–70, <https://doi.org/10.1038/nclimate2446>.
- Niinemets, Ü., 1999: Research review. Components of leaf dry mass per area–thickness and density–alter leaf photosynthetic capacity in reverse directions in woody plants. *New Phytol.*, **144**, 35–47.
- Nisbet, E. G., and Coauthors, 2019: Very Strong Atmospheric Methane Growth in the 4 Years 2014–2017: Implications for the Paris Agreement. *Global Biogeochem. Cycles*, **33**, 318–342, <https://doi.org/10.1029/2018GB006009>.
- Ogée, J., and Coauthors, 2009: A single-substrate model to interpret intra-annual stable isotope signals in tree-ring cellulose. *Plant, Cell Environ.*, **32**, 1071–1090, <https://doi.org/10.1111/j.1365-3040.2009.01989.x>.
- Oh, Y., and Coauthors, 2016: A scalable model for methane consumption in arctic mineral soils. *Geophys. Res. Lett.*, 2289–2296, <https://doi.org/10.1002/2014GL059380>.
- , and Coauthors, 2020: Reduced net methane emissions due to microbial methane oxidation in a warmer Arctic. *Nat. Clim. Chang.*, **10**, 317–321, <https://doi.org/10.1038/s41558-020-0734-z>.
- Palacio, S., E. Paterson, A. Sim, A. J. Hester, and P. Millard, 2011: Browsing affects intra-ring carbon allocation in species with contrasting wood anatomy. *Tree Physiol.*, **31**, 150–159, <https://doi.org/10.1093/treephys/tpq110>.
- Pedersen, E. P., A. Michelsen, and B. Elberling, 2018: In situ CH_4 oxidation inhibition and $^{13}\text{CH}_4$ labeling reveal methane oxidation and emission patterns in a subarctic heath ecosystem. *Biogeochemistry*, **138**, 197–213, <https://doi.org/10.1007/s10533-018-0441-2>.
- Peters, W., and Coauthors, 2005: An ensemble data assimilation system to estimate CO_2 surface fluxes from atmospheric trace gas observations. *J. Geophys. Res. Atmos.*, **110**.
- Poulter, B., and Coauthors, 2017: Global wetland contribution to 2000 – 2012 atmospheric methane growth rate dynamics. *Environ. Res. Lett.*, **12**.
- Prigent, C., C. Jimenez, and P. Bousquet, 2020: Satellite-derived global surface water extent and dynamics over the last 25 years (GIEMS-2). *J. Geophys. Res. Atmos.*, **125**, e2019JD030711.
- Raczka, B., H. F. Duarte, C. D. Koven, D. Ricciuto, P. E. Thornton, J. C. Lin, and D. R. Bowling,

- 2016: An observational constraint on stomatal function in forests: Evaluating coupled carbon and water vapor exchange with carbon isotopes in the Community Land Model (CLM4.5). *Biogeosciences*, **13**, 5183–5204, <https://doi.org/10.5194/bg-13-5183-2016>.
- Richardson, A. D., and Coauthors, 2018: Tracking vegetation phenology across diverse North American biomes using PhenoCam imagery. *Sci. data*, **5**, 180028.
- Riley, W. J., Z. M. Subin, D. M. Lawrence, S. C. Swenson, M. S. Torn, L. Meng, N. M. Mahowald, and P. Hess, 2011: Barriers to predicting changes in global terrestrial methane fluxes: Analyses using CLM4Me, a methane biogeochemistry model integrated in CESM. *Biogeosciences*, **8**, 1925–1953, <https://doi.org/10.5194/bg-8-1925-2011>.
- Roman, D. T., K. A. Novick, E. R. Brzostek, D. Dragoni, F. Rahman, and R. P. Phillips, 2015: The role of isohydric and anisohydric species in determining ecosystem-scale response to severe drought. *Oecologia*, **179**, 641–654, <https://doi.org/10.1007/s00442-015-3380-9>.
- Roy C., T., E. M. Herndon, T. J. Phelps, D. A. Elias, B. Gu, L. Liang, S. D. Wullschleger, and D. E. Graham, 2015: Stoichiometry and temperature sensitivity of methanogenesis and CO₂ production from saturated polygonal tundra in Barrow, Alaska. *Glob. Chang. Biol.*, **21**, 722–737, <https://doi.org/10.1111/gcb.12762>.
- Sachse, D., T. E. Dawson, and A. Kahmen, 2015: Seasonal variation of leaf wax n-alkane production and $\delta^2\text{H}$ values from the evergreen oak tree, *Quercus agrifolia*. *Isotopes Environ. Health Stud.*, **51**, 124–142, <https://doi.org/10.1080/10256016.2015.1011636>.
- Saunio, M., and Coauthors, 2016: The global methane budget 2000–2012. *Earth Syst. Sci. Data*, **8**, 697–751, <https://doi.org/10.5194/essd-8-697-2016>.
- , and Coauthors, 2020: The Global Methane Budget 2000 – 2017. 1561–1623.
- Savage, J. A., M. J. Clearwater, D. F. Haines, T. Klein, M. Mencuccini, S. Sevanto, R. Turgeon, and C. Zhang, 2016: Allocation, stress tolerance and carbon transport in plants: How does phloem physiology affect plant ecology? *Plant Cell Environ.*, **39**, 709–725, <https://doi.org/10.1111/pce.12602>.
- Schaefer, H., and Coauthors, 2016: A 21st-century shift from fossil-fuel to biogenic methane emissions indicated by $^{13}\text{CH}_4$. *Science* (80-.), **352**, 80–84, <https://doi.org/10.1126/science.aad2705>.
- Schlesinger, W. H., and S. Jasechko, 2014: Transpiration in the global water cycle. *Agric. For. Meteorol.*, **189**, 115–117.
- Schuur, E. A. G., J. G. Vogel, K. G. Crummer, H. Lee, J. O. Sickman, and T. E. Osterkamp, 2009: The effect of permafrost thaw on old carbon release and net carbon exchange from tundra. *Nature*, **459**, 556–559, <https://doi.org/10.1038/nature08031>.
- Schuur, E. A. G., and Coauthors, 2013: Expert assessment of vulnerability of permafrost carbon to climate change. *Clim. Change*, **119**, 359–374, <https://doi.org/10.1007/s10584-013-0730-7>.

- , and Coauthors, 2015: Climate change and the permafrost carbon feedback. *Nature*, **520**, 171–179, <https://doi.org/10.1038/nature14338>.
- Schwietzke, S., and Coauthors, 2016: Upward revision of global fossil fuel methane emissions based on isotope database. *Nature*, **538**, 88–91, <https://doi.org/10.1038/nature19797>.
- Segers, R., 1998: Methane production and methane consumption: A review of processes underlying wetland methane fluxes. *Biogeochemistry*, **41**, 23–51, <https://doi.org/10.1023/A:1005929032764>.
- Seibt, U., A. Rajabi, H. Griffiths, and J. A. Berry, 2008: Carbon isotopes and water use efficiency: Sense and sensitivity. *Oecologia*, **155**, 441–454, <https://doi.org/10.1007/s00442-007-0932-7>.
- Seinfeld, J. H., S. N. Pandis, and K. Noone, 1998: Atmospheric chemistry and physics: from air pollution to climate change. *Phys. Today*, **51**, 88.
- Sellers, P. J., and Coauthors, 1997: BOREAS in 1997: Experiment overview, scientific results, and future directions. *J. Geophys. Res. Atmos.*, **102**, 28731–28769.
- Sepulveda-Jauregui, A., K. M. Walter Anthony, K. Martinez-Cruz, S. Greene, and F. Thalasso, 2015: Methane and carbon dioxide emissions from 40 lakes along a north-south latitudinal transect in Alaska. *Biogeosciences*, **12**, 3197–3223, <https://doi.org/10.5194/bg-12-3197-2015>.
- Sherwood, O. A., S. Schwietzke, V. A. Arling, and G. Etiope, 2017: Global inventory of gas geochemistry data from fossil fuel, microbial and burning sources, version 2017. *Earth Syst. Sci. Data*, **9**, 639–656, <https://doi.org/10.5194/essd-9-639-2017>.
- Stackhouse, B., M. C. Y. Lau, T. Vishnivetskaya, N. Burton, R. Wang, A. Southworth, L. Whyte, and T. C. Onstott, 2017: Atmospheric CH₄ oxidation by Arctic permafrost and mineral cryosols as a function of water saturation and temperature. *Geobiology*, **15**, 94–111, <https://doi.org/10.1111/gbi.12193>.
- Stackhouse, B. T., and Coauthors, 2015: Effects of simulated spring thaw of permafrost from mineral cryosol on CO₂ emissions and atmospheric CH₄ uptake. *J. Geophys. Res. Biogeosciences*, **120**, 1764–1784, <https://doi.org/10.1002/2015JG003004>.Received.
- Still, C. J., J. A. Berry, G. J. Collatz, and R. S. DeFries, 2003: Global distribution of C₃ and C₄ vegetation: Carbon cycle implications . *Global Biogeochem. Cycles*, **17**, 6-1-6–14, <https://doi.org/10.1029/2001gb001807>.
- Von Stockar, U., and J. S. Liu, 1999: Does microbial life always feed on negative entropy? Thermodynamic analysis of microbial growth. *Biochim. Biophys. Acta - Bioenerg.*, **1412**, 191–211, [https://doi.org/10.1016/S0005-2728\(99\)00065-1](https://doi.org/10.1016/S0005-2728(99)00065-1).
- Von Stockar, U., T. Maskow, J. Liu, I. W. Marison, and R. Patiño, 2006: Thermodynamics of microbial growth and metabolism: An analysis of the current situation. *J. Biotechnol.*, **121**, 517–533, <https://doi.org/10.1016/j.jbiotec.2005.08.012>.

- Stocker, T. F., and Coauthors, 2013: Climate change 2013: The physical science basis.
- Stokes, V. J., M. D. Morecroft, and J. I. L. Morison, 2010: Comparison of leaf water use efficiency of oak and sycamore in the canopy over two growing seasons. *Trees - Struct. Funct.*, **24**, 297–306, <https://doi.org/10.1007/s00468-009-0399-8>.
- Strode, S., J. Wang, M. Manyin, B. Duncan, R. Hossaini, C. Keller, S. Michel, and J. W. White, 2019: Strong Sensitivity of the Isotopic Composition of Methane to the Plausible Range of Tropospheric Chlorine. *Atmos. Chem. Phys. Discuss.*, **2007**, 1–24, <https://doi.org/10.5194/acp-2019-1047>.
- Suh, Y. J., and A. F. Diefendorf, 2018: Seasonal and canopy height variation in n-alkanes and their carbon isotopes in a temperate forest. *Org. Geochem.*, **116**, 23–34, <https://doi.org/10.1016/j.orggeochem.2017.10.015>.
- Suits, N. S., A. S. Denning, J. A. Berry, C. J. Still, J. Kaduk, J. B. Miller, and I. T. Baker, 2005: Simulation of carbon isotope discrimination of the terrestrial biosphere. *Global Biogeochem. Cycles*, **19**, 1–15, <https://doi.org/10.1029/2003GB002141>.
- Tans, P. P., 1997: A note on isotopic ratios and the global atmospheric methane budget. *Global Biogeochem. Cycles*, **11**, 77–81.
- Tarin, T., R. H. Nolan, B. E. Medlyn, J. Cleverly, and D. Eamus, 2019: Water-use efficiency in a semi-arid woodland with high rainfall variability. *Glob. Chang. Biol.*, 1–13, <https://doi.org/10.1111/gcb.14866>.
- Thauer, R. K., A. K. Kaster, H. Seedorf, W. Buckel, and R. Hedderich, 2008: Methanogenic archaea: Ecologically relevant differences in energy conservation. *Nat. Rev. Microbiol.*, **6**, 579–591, <https://doi.org/10.1038/nrmicro1931>.
- Throckmorton, H. M., and Coauthors, 2016: Active layer hydrology in an arctic tundra ecosystem: quantifying water sources and cycling using water stable isotopes. *Hydrol. Process.*, **30**, 4972–4986.
- Tijhuis, L., M. C. M. Van Loosdrecht, and J. J. Heijnen, 1993: A thermodynamically based correlation for maintenance gibbs energy requirements in aerobic and anaerobic chemotrophic growth. *Biotechnol. Bioeng.*, **42**, 509–519, <https://doi.org/10.1002/bit.260420415>.
- Trimmer, M., F. C. Shelley, K. J. Purdy, S. T. Maanoja, P. M. Chronopoulou, and J. Grey, 2015: Riverbed methanotrophy sustained by high carbon conversion efficiency. *ISME J.*, **9**, 2304–2314, <https://doi.org/10.1038/ismej.2015.98>.
- Turetsky, M. R., and Coauthors, 2020: Carbon release through abrupt permafrost thaw. *Nat. Geosci.*, **13**, 138–143, <https://doi.org/10.1038/s41561-019-0526-0>.
- Tveit, A. T., and Coauthors, 2019: Widespread soil bacterium that oxidizes atmospheric methane. *Proc. Natl. Acad. Sci. U. S. A.*, **116**, 8515–8524, <https://doi.org/10.1073/pnas.1817812116>.

- Ubierna, N., and J. D. Marshall, 2011: Vertical and seasonal variation in the $\delta^{13}\text{C}$ of leaf-respired CO_2 in a mixed conifer forest. *Tree Physiol.*, **31**, 414–427, <https://doi.org/10.1093/treephys/tpr026>.
- Van Der Velde, I. R., and Coauthors, 2013: Biosphere model simulations of interannual variability in terrestrial $^{13}\text{C}/^{12}\text{C}$ exchange. *Global Biogeochem. Cycles*, **27**, 637–649, <https://doi.org/10.1002/gbc.20048>.
- Walter, B. P., and M. Heimann, 2000: A process-based, climate-sensitive model to derive methane emissions from natural wetlands: Application to five wetland sites, sensitivity to model parameters, and climate. *Global Biogeochem. Cycles*, **14**, 745–765.
- Wania, R., and Coauthors, 2013: Present state of global wetland extent and wetland methane modelling: Methodology of a model inter-comparison project (WETCHIMP). *Geosci. Model Dev.*, **6**, 617–641, <https://doi.org/10.5194/gmd-6-617-2013>.
- Whalen, S. C., and W. S. Reeburgh, 1996: Moisture and temperature sensitivity of CH_4 oxidation in boreal soils. *Soil Biol. Biochem.*, **28**, 1271–1281, [https://doi.org/10.1016/S0038-0717\(96\)00139-3](https://doi.org/10.1016/S0038-0717(96)00139-3).
- Wieder, W. R., G. B. Bonan, and S. D. Allison, 2013: Global soil carbon projections are improved by modelling microbial processes. *Nat. Clim. Chang.*, **3**, 909–912, <https://doi.org/10.1038/nclimate1951>.
- Wik, M., R. K. Varner, K. W. Anthony, S. MacIntyre, and D. Bastviken, 2016: Climate-sensitive northern lakes and ponds are critical components of methane release. *Nat. Geosci.*, **9**, 99–105, <https://doi.org/10.1038/ngeo2578>.
- Wolz, K. J., T. M. Wertin, M. Abordo, D. Wang, and A. D. B. Leakey, 2017: Diversity in stomatal function is integral to modelling plant carbon and water fluxes. *Nat. Ecol. Evol.*, **1**, 1292–1298, <https://doi.org/10.1038/s41559-017-0238-z>.
- Worden, J. R., A. A. Bloom, S. Pandey, Z. Jiang, H. M. Worden, T. W. Walker, S. Houweling, and T. Röckmann, 2017: Reduced biomass burning emissions reconcile conflicting estimates of the post-2006 atmospheric methane budget. *Nat. Commun.*, **8**, 1–11, <https://doi.org/10.1038/s41467-017-02246-0>.
- Xu, C. Y., G. H. Lin, K. L. Griffin, and R. N. Sambrotto, 2004: Leaf respiratory CO_2 is ^{13}C -enriched relative to leaf organic components in five species of C_3 plants. *New Phytol.*, **163**, 499–505, <https://doi.org/10.1111/j.1469-8137.2004.01153.x>.
- Xu, X., and Coauthors, 2016: Reviews and syntheses: Four decades of modeling methane cycling in terrestrial ecosystems. *Biogeosciences*, **13**, 3735–3755, <https://doi.org/10.5194/bg-13-3735-2016>.
- Yang, Y., and Coauthors, 2016: Contrasting responses of water use efficiency to drought across global terrestrial ecosystems. *Sci. Rep.*, **6**, 1–8, <https://doi.org/10.1038/srep23284>.

- Yi, K., D. Dragoni, R. P. Phillips, D. T. Roman, and K. A. Novick, 2017: Erratum: Dynamics of stem water uptake among isohydric and anisohydric species experiencing a severe drought. *Tree Physiol.*, **37**, 1393, <https://doi.org/10.1093/treephys/tpx014>.
- , J. T. Maxwell, M. K. Wenzel, D. T. Roman, P. E. Sauer, R. P. Phillips, and K. A. Novick, 2019: Linking variation in intrinsic water-use efficiency to isohydricity: a comparison at multiple spatiotemporal scales. *New Phytol.*, **221**, 195–208, <https://doi.org/10.1111/nph.15384>.
- Zhang, G., H. Yu, X. Fan, J. Ma, and H. Xu, 2016: Carbon isotope fractionation reveals distinct process of CH₄ emission from different compartments of paddy ecosystem. *Sci. Rep.*, **6**, 1–10, <https://doi.org/10.1038/srep27065>.
- Zhuang, Q., A. D. McGuire, K. P. O’Neill, J. W. Harden, V. E. Romanovsky, and J. Yarie, 2003: Modeling soil thermal and carbon dynamics of a fire chronosequence in interior Alaska. *J. Geophys. Res. D Atmos.*, **108**, <https://doi.org/10.1029/2001JD001244>.
- , J. M. Melillo, D. W. Kicklighter, R. G. Prinn, A. D. McGuire, P. A. Steudler, B. S. Felzer, and S. Hu, 2004: Methane fluxes between terrestrial ecosystems and the atmosphere at northern high latitudes during the past century: A retrospective analysis with a process-based biogeochemistry model. *Global Biogeochem. Cycles*, **18**, <https://doi.org/10.1029/2004GB002239>.
- Zhuang, Q., K. Xu, J. Tang, E. Saikawa, Y. Lu, J. M. Melillo, R. G. Prinn, and A. D. McGuire, 2013: Response of global soil consumption of atmospheric methane to changes in atmospheric climate and nitrogen deposition. *Global Biogeochem. Cycles*, **27**, 650–663, <https://doi.org/10.1002/gbc.20057>.
- Zimov, S. A., E. A. G. Schuur, and F. S. Chapin III, 2006: Permafrost and the global carbon budget. *Science(Washington)*, **312**, 1612–1613.

VITA

1. Education

– **Purdue University, West Lafayette, IN, Aug 2016 – present**

Ph.D. in Earth, Atmospheric, and Planetary Sciences

Cumulative GPA: 4.00

Princeton University, Princeton, NJ, Sep 2013 – Jul 2015

M.A. in Atmospheric and Oceanic Sciences

Dissertation topic: Development of Arctic Microbial Methane Model, eXplicit High Affinity Methanotroph model (XHAM)

– **University of California, Davis, Davis, CA, Sep 2010 – Jun 2011**

Global Exchange Student

– **Ewha Womans University, Seoul, South Korea, Mar 2009 – Jun 2013**

B.S. in Environmental Science and Engineering

Double Major in Biological Sciences, Certification in ABEEK Advanced Engineering Program

Magna cum laude. Cumulative GPA: 3.71

2. Research Experience

– **Visiting Scholar, NOAA ESRL Global Monitoring Division, Nov 2018 – Aug 2019**

Advisor: Dr. Edward J. Dlugokencky and Dr. Lori Bruhwiler

Forward modeling of Arctic and global methane budget using TM5 atmospheric chemistry model. Also, wetland isotope modeling to understand spatial and temporal variability of carbon isotopic signatures of methane emitted from wetlands.

– **NASA Earth and Space Science Fellow, Purdue University, Sep 2017 – present**

Advisor: Dr. Qianlai Zhuang and Dr. Lisa Welp

Understanding importance of High Affinity Methanotroph (HAM) in arctic methane budget by simulating methane fluxes and atmospheric concentrations using global ecosystem model (TEM-XHAM) and atmospheric transport model, and evaluating simulations using in-situ, aircraft and satellite data.

- **Graduate Research Assistant, Purdue University, Jul 2016 – present**
 Advisor: Dr. Lisa Welp
 Species-specific seasonal stable carbon isotope variation in temperate deciduous leaves and implications for carbon allocation phenology and water use efficiency estimates in Morgan Monroe State Forest, IN using Elemental Analyzer Isotope Ratio Mass Spectrometry
- **Graduate Advisor, Princeton University, Sep 2016 – May 2017**
 Advisor: Dr. Tullis Onstott and Dr. Maggie Lau
 Senior Thesis Students Co-Advised: Christianese Kaiser, Princeton Class of 2017
 Estimating annual methane sinks in the Arctic of the 2000s using regional-level XHAM model.
- **Graduate Research Assistant, Princeton University, Aug 2013 – Apr 2016**
 Advisor: Dr. David Medvigy
 Developing XHAM model of Arctic soils to elucidate the importance of high affinity methanotrophy. The scalable model was constrained by microcosm experiment and tested against laboratory and field measurements.
- **Undergraduate Research Assistant, Ewha Womans University, Sep 2011 – Aug 2013**
 Advisor: Dr. Yong-Sang Choi
 Senior Thesis: Impact of Tropical Pacific and Atlantic Sea Surface Temperature (SST) on Vegetative Phenology in Amazon Statistical analysis to study how El Nino-Southern Oscillation and Tropical North Atlantic affect vegetation activity in the Amazon.

3. Selected presentation

- Oh, Y. et al., Dec 2019: The role of microbial dynamics of methanogens and high affinity methanotrophs in current and future net land methane emissions in the Arctic. American Geophysical Union Fall Meeting, San Francisco, CA ORAL.
- Oh, Y. et al., May 2019: High Affinity Methanotrophs Are an Important Overlooked Methane Sink in Arctic and Global Methane Budget. NOAA ESRL Global Monitoring Annual Conference, Boulder, CO. ORAL.
- Oh, Y. et al., Mar 2019: Reduced net methane emissions due to microbial methane oxidation in a warmer Arctic. Center for Permafrost, University of Copenhagen, Copenhagen, Denmark. INVITED.

- Oh, Y. et al., Apr 2018: Impacts of Permafrost Dynamics and Nitrogen Deposition on High Affinity Methanotrophy and Net Methane Fluxes in the Pan-Arctic Terrestrial Ecosystems. European Geosciences Union General Assembly, Vienna, Austria. ORAL.
- Oh, Y. et al., Jun 2016: A Scalable Model for Methane Consumption in Arctic Mineral Soils. Korea Polar Research Institute Workshop, Incheon, South Korea. INVITED.
- Oh, Y. et al., May 2016: A Scalable Model for Methane Consumption in Arctic Mineral Soils. South University of Science and Technology Workshop, Shenzhen, China. INVITED.
- Oh, Y. et al., Feb 2016: An underestimated methane sink in Arctic mineral soils. Lawrence Berkeley National Laboratory, Berkeley, CA. ORAL.

4. Awards & Honor

- NASA Earth and Space Science Fellowship, Sep 2017 – present
- CESM Polar Modeling Workshop and Tutorial, NCAR, Boulder, CO, Aug 2018
- Henry Silver Graduate Scholarship, Purdue University, May 2018
- Ross Fellowship in Natural Sciences and Engineering, Purdue University, Aug 2016 – Jul 2017
- Purdue Climate Change Research Center Award, Aug 2016
- Research Fellowship in Natural Science and Engineering, Princeton University, Sep 2013 – Feb 2016
- Best Poster at 4th International Winter School on Climate Change, Seoul, South Korea, Dec 2012
- Minister’s Award at Paper Contest hosted by the Korea Water Resources, May 2012
- Leadership Award, University of California, Davis, Aug 2011
- Fellowship for Global Exchange Student, Ewha Womans University, Sep 2010 – Jun 2011
- Provost’s Honors, Ewha Womans University Sep 2009, 2010, 2012, and Mar 2011, 2012

5. Community activities

- **Education Volunteer, Earth Science Program, Purdue University, Aug 2016 – present**
Outreach program to local elementary school where Purdue graduates host scientific programs.

- **Session Liaison, American Geophysical Union Fall Meeting 2018, Dec 2018**
Organizing a session about Terrestrial and Aquatic Methane Sinks: New Discoveries and Revisions, from Molecular to Global Perspectives.
- **Mentee, Women in GeoScience Program, Princeton University, Sep 2014 – Aug 2016**
Mentorship program where Princeton graduate students meet senior scientists every week to get advice on successful career as women scientists.
- **Founder and Leader, Ewha Water, Ewha Womans University, Sep 2011 – Aug 2013**
Collaboration with government, companies and local cafes to address environmental water use and encourage publics to drink tap water.
- **Mentor, Korea Women in Science and Engineering Program, Sep 2009 – Aug 2010**
Outreach program where undergraduates meet high school students twice a month for science paper writing.

6. Et cetera

- Academic Associations: American Geophysical Union and European Geophysical Union
- Computers: Running Terrestrial Ecosystem Model (TEM), TM5 Atmospheric Chemistry Model, and Other Earth System Models (CESM, ORCHIDEE, LPJ-WhyMe) and analyzing their output with Matlab, Python, Fortran, IDL, C, C++, LATEX(experienced)
- Laboratory Skills: Elemental Analysis-Isotope Ratio Mass Spectrometry
- Language: English (Fluent), Korean (Fluent), Chinese (Conversational), Japanese (Conversational)

PUBLICATIONS

Published / Accepted

- **Oh, Y.**, Zhuang, Q., Liu, L., Welp, L.R., Lau, M.C., Onstott, T.C., Medvigy, D., Bruhwiler, L., Dlugokencky, E.J., Hugelius, G. and D’Imperio, L., 2020. Reduced net methane emissions due to microbial methane oxidation in a warmer Arctic. *Nature Climate Change*, 10(4), pp.317-321.
- Liu, L., Zhuang, Q., **Oh, Y.**, Shurpali, N.J., Kim, S. and Poulter, B., 2020. Uncertainty Quantification of Global Net Methane Emissions from Terrestrial Ecosystems Using a Mechanistically-based Biogeochemistry Model. *Journal of Geophysical Research: Biogeosciences*, p.e2019JG005428.
- Abbasi, A. O., A. Salazar, **Y. Oh**, S. Reinsch, M. D. R. Uribe, J. Li, I. Rashid, and J. S. Dukes. “Soil responses to manipulated precipitation changes: A synthesis of meta-analyses.” *Biogeosciences*, Accepted.
- Lau, M.C., Harris, R.L., **Oh, Y.**, Yi, M.J., Behmard, A. and Onstott, T.C., 2018. Taxonomic and functional compositions impacted by the quality of metatranscriptomic assemblies. *Frontiers in microbiology*, 9, p.1235.
- Lau, M., T. L. Kieft, O. Kuloyo, B. Linage, E. Heerden, M. R. Lindsay, C. Magnabosco, W. Wang, J. B. Wiggins, L. Guo, D. H. Perlman, S. Kyin, H. H. Shwe, R. L. Harris, **Y. Oh**, M. J. Yi, R. Purtschert, G. F. Slater, S. Ono, S. Wei, L. Li, B. S. Lollar and T. C. Onstott, 2016. An oligotrophic deep-subsurface community dependent on syntrophy is dominated by sulfur-driven autotrophic denitrifiers. *Proceedings of the National Academy of Sciences*, 113(49), pp.E7927-E7936.
- **Oh, Y.**, Stackhouse, B., Lau, M.C., Xu, X., Trugman, A.T., Moch, J., Onstott, T.C., Jørgensen, C.J., D’Imperio, L., Elberling, B. and Emmerton, C.A., 2016. A scalable model for methane consumption in arctic mineral soils. *Geophysical Research Letters*, 43(10), pp.5143-5150.

In review / In preparation

- **Oh, Y.**, L. R. Welp, K. Yi, M. C. Benson, K. A. Novick, Q. Zhuang, and D. Lombardozzi. Leaf Carbon Allocation Affects Seasonal Isotopic Signatures and Water Use Efficiency of Temperate Deciduous Trees. *New Phytologist*, In Review.
- **Oh, Y.**, Q. Zhuang, L. Liu, L. R. Welp, X. Lan, S. Basu, E. J. Dlugokencky, L. Bruhwiler, J. B. Miller, S. E. Michel, S. Schwietzke, P. Tans, P. Ciais, and J. P. Chanton. Process-based mapping of global wetland carbon isotopic signatures of methane. *Nature Geoscience*, In Preparation.